

**DEVELOPMENT OF AN EFFICIENT COMPACT  
WIDEBAND METAMATERIAL-BASED RECTENNA**

**SOBHAN SARAVANI**

**COLLEGE OF GRADUATE STUDIES  
UNIVERSITI TENAGA NASIONAL**

**2020**

**DEVELOPMENT OF AN EFFICIENT COMPACT WIDEBAND  
METAMATERIAL-BASED RECTENNA**

**SOBHAN SARAVANI**

**A Thesis Submitted to the College of Graduate Studies, Universiti  
Tenaga Nasional in Fulfilment of the Requirements for the Degree of**

**Doctor of Philosophy (Engineering)**

**JANUARY 2020**

## **DECLARATION**

I hereby declare that the thesis is my original work except for quotations and citations which have been duly acknowledged. I also declare that it has not been previously, and is not concurrently submitted for any other degree at Universiti Tenaga Nasional or at any other institutions. This thesis may be made available within the university library and may be photocopied and loaned to other libraries for the purpose of consultation.

---

(Signature)

**SOBHAN SARAVANI**

Date :

## ABSTRACT

This thesis focuses on a design methodology for RF energy harvesting systems and far-field wireless powering of low-power devices. The energy harvesting system composed of an antenna which scavenges plane waves transmitted by the powering source, and delivers the captured RF power to a rectifying element. The generated DC power is used to empower low power devices independent of their electronic applications including IoT and wireless sensor nodes. For a quality energy harvesting system the role of antenna and rectifier are critical that work interactively for the optimum performance. To date, most works in the literature focus on the design of high gain antennas via traditional methods which requires large space area, thus, restricting their applications. Furthermore, there are only few broadband rectennas in the literature and most of them perform well only at the high power levels (i.e. 20mW). This PhD thesis focuses on design and implementation of a more reliable and practical energy harvesting system for space-restricted applications. To achieve this goal, a wideband and miniaturized zeroth-order resonance (ZOR) antenna loaded by parasitic element is presented. The measured operational bandwidth of the designed antenna is about 1.6 GHz from 1.715 to 3.318 GHz corresponding to 87.1% of the fractional bandwidth with excellent radiation efficiency up to 95.7%. Moreover, the design and implementation of a low power rectifier operating at 2.45 GHz with increased output tolerance is presented. The efficiency of the rectifier is maximized by properly terminating the harmonics generated by non-linear diode and reaches to 61.9% at 3 dBm power level. Additionally, design of compact dual output broadband rectifier is detailed, with the highest measured efficiency of 70.3%. At the very low input power level of -17 dBm, an efficiency better than 10% from 1.85 to 2.5 GHz is obtained. Several combination of rectifiers and antenna as well as compact integrated rectenna are designed, simulated and tested. It has been demonstrated that for a broadband rectenna, under multi-tone condition, the efficiency considerably improves and exceeds 50% at only  $3.16 \mu W/cm^2$  while for the mono-tone case, the best recorded efficiency remains below 50% even at the power density level as high as  $5.13 \mu W/cm^2$  for almost all measured frequency points. Measurement results clearly demonstrate the advantage of this broadband energy harvesting system and its potential for space-restricted applications where the use of bulky and high gain antennas are impractical.

## ACKNOWLEDGEMENTS

First of all, I would like to acknowledge my deepest gratitude to my thesis advisor, Professor Chandan Kumar Chakrabarty, for his valuable contribution and guidance towards my Ph.D. thesis. He provided me supportive and engaging environment to pursue Ph.D. but also offered me freedom in pursuing my own ideas for the research. His remarkable leadership gave me lessons on how to become an expert, leader, and respectful person. I have been extremely privileged to have Professor Norashida Md Din as my co-supervisor. I would like to acknowledge my sincere appreciation for all her insightful suggestions, continuous supports and, most importantly, never giving up on me. I could not have imagined having better advisors and mentors for my Ph.D study.

A very special thank you to Professor Mohd Tarmizi Ali, a truly inspiring, knowledgeable and generous person who has guided and helped me with most of my measurements. As of the writing of this thesis, he had been granted a professor status at UITM University, and the honor could not have been more deserved. Much of the work presented in this thesis would have not been possible without his generous supports.

My sincere thank you to my family, my parents, Gholamreza and Fatemeh (Sedigheh). Everything good about me came from my extraordinary mom and dad. Words cannot express my deep gratitude and love towards them. I would also like to thank my brothers, Saeed and Soroush, for supporting me spiritually throughout my Ph.D study and my life in general.

Last but most certainly not the least, I would like to whole heartedly thank the love of my life, my dear Mun Hoong (Wendy). Without her sacrifices, unconditional love, and supports, I would not had been able to complete my studies. Words cannot express my deep gratitude and love towards her.

## TABLE OF CONTENTS

	<b>Page</b>
<b>DECLARATION</b>	<b>ii</b>
<b>ABSTRACT</b>	<b>iii</b>
<b>ACKNOWLEDGEMENTS</b>	<b>iv</b>
<b>TABLE OF CONTENTS</b>	<b>v</b>
<b>LIST OF TABLES</b>	<b>ix</b>
<b>LIST OF FIGURES</b>	<b>x</b>
<b>LIST OF ABBREVIATIONS</b>	<b>xviii</b>
<b>LIST OF SYMBOLS</b>	<b>xx</b>
<b>LIST OF PUBLICATIONS</b>	<b>xxiii</b>
<b>CHAPTER 1            INTRODUCTION</b>	<b>1</b>
1.1    Overview	1
1.2    Wireless Power Transmission Techniques	2
1.3    Energy Harvesting Challenges	5
1.3.1    Free Space Path Loss	5
1.3.2    Antenna Miniaturization Challenges	5
1.3.3    Power Availability	6
1.4    Problem Statement	9
1.5    Objectives of this Research	12
1.6    General Methodology and Achievements	13
1.7    Organization	14
<b>CHAPTER 2            LITERATURE REVIEW</b>	<b>16</b>
2.1    Brief History and Background Survey	16
2.2    Rectennas for Power Harvesting Applications	18

2.3	Literature Review of Recent Metamaterial-Inspired Antennas	18
2.4	Literature Review of Recent Rectennas	26
2.4.1	Stacked Rectenna for Low Power Application	27
2.4.2	Decoupled Dual-dipole Rectennas for Wireless Battery Charging	28
2.4.3	Compact Fractal Loop Rectenna	29
2.4.4	Circularly Polarized Shorted Ring-Slot Rectenna	30
2.4.5	Rectennas with All Polarization Reception Properties	30
2.4.6	Broadband and Multiband Rectennas	33
2.4.7	Array Configuration for Energy Harvester	35
2.4.8	Broadband Bent Triangular Omnidirectional	38
2.5	Literature Review Summary	40
<b>CHAPTER 3 RESEARCH METHODOLOGY</b>		<b>49</b>
3.1	Introduction	49
3.2	Schottky Diode Characteristics	49
3.2.1	Schottky Diode Circuit Model	51
3.2.2	Current versus Voltage Relation	52
3.2.3	Diode Series Resistance ( $R_s$ )	53
3.2.4	Diode Junction Capacitance ( $C_j$ )	53
3.2.5	Harmonic Generation in Non-Linear Devices	57
3.2.6	Analytical Model of Non-Linear Rectifier	58
3.3	Microwave Rectifiers	68
3.3.2	Rectifier Efficiency	76
3.3.3	Rectifier Design	79
3.3.4	Design of Voltage Doubler Rectifier for Microwave Energy Harvesting System	82
3.3.5	Modified Rectifier with Increased Output Load Tolerance	85
3.3.6	High Efficiency and Broadband Rectifier for Energy Harvesting System	91

3.4	Metamaterial-Based Miniaturized Wideband Antennae for Energy Harvesting Systems	100
3.4.1	Composite Left/Right-Handed (CRLH) Transmission Line	102
3.4.2	CRLH Leaky-Wave Antenna	105
3.4.3	CRLH Zeroth Order Resonant Antenna	115
3.4.4	Miniaturized Antenna Design for Integrated Energy Harvesting System	121
3.5	Summary	124
 <b>CHAPTER 4 RESULTS AND ANALYSIS</b>		<b>125</b>
4.1	Modified Rectifier with Increased Output Tolerance Results	125
4.2	Broadband Rectifier Results and Analysis	127
4.3	CRLH LWA Results and Analysis	131
4.4	ZOR Antenna Experimental Results	138
4.5	Miniaturized Antenna Design for Integrated Energy Harvesting System Results and Analysis	144
4.6	Rectenna Measurements Setup	149
4.7	Antenna and Modified Rectifier Combination Measurement Results	151
4.8	Antenna and Broadband Rectifier Combination Measurement Results	153
4.9	Miniaturized Integrated Rectenna Results	156
4.10	Broadband Rectenna performance on the open Field	162
4.11	Multi-Tone Analysis and Measurement Results	163
4.12	Summary	166
 <b>CHAPTER 5 CONCLUSION AND RECOMMENDATIONS FOR FUTURE WORK</b>		<b>168</b>
5.1	Conclusion	168
5.2	Contribution of this Research Work	169
5.3	Future Works	170

<b>REFERENCES</b>	<b>172</b>
<b>APPENDIX</b>	<b>189</b>

## LIST OF TABLES

Table 1.1	The power density levels measured in London [14].	7
Table 2.1	A summary of some recent works available in the literature.	25
Table 2.2	Overview of integrated rectifier antennas and rectifiers described	40
Table 2.3	Summary of the reviewed works in the literature	43
Table 3.1	A comparison between p-n and Schottky diode characteristics.	51
Table 3.2	Comparison of typical Schottky diode values from HSMS-28XX family.	78
Table 3.3	A summary of the performance of rectifier with different topologies.	85
Table 3.4	The optimal dimensions of the designed rectifier	86
Table 3.5	The optimal parameter values of the proposed rectifier design.	99
Table 3.6	The SIW unit cell parameter values.	112
Table 3.7	The optimized parameter values of the designed ZOR antenna.	118
Table 3.8	The optimized parameters of the ZOR HTA.	123
Table 4.1	Comparison results of the proposed and reference antennas.	144
Table 4.2	Performance comparison of the presented rectenna combinations.	160
Table 4.3	The range of measured available power at approximately 30 m away from cell tower.	162

## LIST OF FIGURES

Figure 1.1	Experimental test setup used in [10]. Notice that both coils have a diameter of 50 cm and the spacing between the coils is 1.5 m powering a 60W light bulb.	3
Figure 1.2	A simple RF energy harvesting receiving end.	4
Figure 1.3	RF power measured at a residential area in Shunde, China [13].	7
Figure 1.4	(a) Maximum allowable exposure limits for general public, (b) Maximum permissible exposure limits for controlled RF environments [18].	8
Figure 1.5	Flowchart of the methodology undertaken.	13
Figure 2.1	The rectenna made by William C. Brown in 1963 at Raytheon Company operating at 2.45 GHz [22].	16
Figure 2.2	(a) SHARP project concept (b) flight experiment in 1987 [83].	17
Figure 2.3	Configuration of ZOR antenna composed of four cascaded unit cells presented in [89].	19
Figure 2.4	(a) Conventional patch antenna and (b) Four-cell ZOR antenna operating at 4.88 GHz in [89].	19
Figure 2.5	Configuration of compact and wideband two MTM-TL arm antenna presented in [57].	20
Figure 2.6	Configurations and photographs of 2-D isotropically arranged slot loaded ZOR antenna proposed in [90]. (a) Nine rectangular patches with 16 square slots. (b) Seven hexagonal patches with 24 triangular slots.	21
Figure 2.7	Miniaturized dual-arm spiral ZOR antenna (a) Antenna configuration and (b) Photograph of fabricated antenna proposed in [54].	21
Figure 2.8	Compact and efficiency enhanced ZOR antenna (a) Top view; (b) Bottom view geometry and (c) Photograph of the fabricated antenna presented in [91].	22

Figure 2.9	Compact bandwidth-enhanced ZOR antenna proposed in [58].	23
Figure 2.10	The fabricated bandwidth and efficiency enhanced antenna presented in [62].	23
Figure 2.11	Compact and bandwidth-enhanced asymmetrical CPW-fed antenna (a) Top view geometry; (b) Bottom view geometry and (c) Photograph of fabricated antenna by Lee et al. from [61].	24
Figure 2.12	General block diagram of an energy harvesting for powering low power sensors.	27
Figure 2.13	Configuration of the stacked rectenna designed by Akkermans et al. [23].	28
Figure 2.14	Decoupled Dual-dipole Rectennas layout presented in [94].	29
Figure 2.15	Compact fractal loop antenna by Zeng et al. [41]	29
Figure 2.16	Circularly polarized shorted ring-slot rectenna [33].	30
Figure 2.17	Circularly polarized all polarization receiving rectenna with harmonic rejection property [24].	31
Figure 2.18	Rectenna with all-polarization-receiving capability[31].	32
Figure 2.19	The photograph of fabricated rectenna and its dual shunt rectifier circuit employed in [31].	32
Figure 2.20	Dual band energy harvester proposed in [74].	33
Figure 2.21	(a) the configuration of the dual port stacked antenna and (b) the rectifier topology employed in [96].	34
Figure 2.22	(a) The configuration of quasi-Yagi array rectenna and (b) dual band rectifier from [39].	35
Figure 2.23	Beamwidth-enhanced rectenna (a) antenna array structure with two axillary antenna for beamwidth enhancement (b) single shunt rectifier proposed by Sun et al. in [32].	36
Figure 2.24	Rectenna array of 64 elements presented in [16].	37
Figure 2.25	Broadband bent triangular monopole presented in [77].	38
Figure 2.26	The configuration of broadband GCPW rectenna presented in [78], (a) antenna structure; (b) rectifier circuit and (c) photograph of the fabricated prototype.	39

Figure 3.1	Common semiconductor junction types (a) p-n diode and (b) metal-semiconductor junction used in Schottky diodes.	50
Figure 3.2	(a) Cross section view of a schottky diode, (b) graphical symbol of a diode.	52
Figure 3.3	Equivalent circuit model of a Schottky diode.	52
Figure 3.4	Simulated I-V curve of diode model HSMS2850 extracted from vendor model in Advanced Design System (ADS) components library.	54
Figure 3.5	Diode junction resistance versus voltage for diode model HSMS-2850.	55
Figure 3.6	The junction capacitance of diode model HSMS-2850 derived from Equation (3.4).	56
Figure 3.7	The impact of junction capacitance on the output voltage using Equation (3.6).	57
Figure 3.8	Circuit schematic of a detector circuit.	59
Figure 3.9	Simplified diode detector circuit with an ideal zero-bias diode.	60
Figure 3.10	Comparison between calculated and simulated conversion efficiency. (a) Conversion efficiency and (b) output DC voltage. The outputs are for different cases using Equation (3.18).	66
Figure 3.11	Impact of different diode's parameters on the overall efficiency; (a) series resistance, (b) breakdown voltage, (c) frequency and (d) output load.	67
Figure 3.12	General block diagram of the rectification circuit.	69
Figure 3.13	Rectenna topologies, rectenna with single shunt (a), single serial (b), voltage doubler (c) and bridge rectifier (d).	70
Figure 3.14	Some commonly used voltage multiplier topologies (a) single stage Dickson charge pump, (b) Villard charge pump, (c) Multi-stage Dickson charge pump, (d) modified Greinacher voltage quadrupler.	71
Figure 3.15	Principle of operation of a voltage doubler at (a) positive cycle, (b) negative cycle.	72

Figure 3.16	Schematic of a N stage voltage doubler in the form of Dickson charge pump.	73
Figure 3.17	(a) The impact of output voltage on the harmonic current generation of a voltage multiplier. (b) Comparison of the third to the fundamental harmonic currents of a voltage multiplier in a logarithmic scale.	75
Figure 3.18	The methodology flowchart for the design of rectifiers.	80
Figure 3.19	Load/Source pull simulation setup of the half-wave rectifier.	81
Figure 3.20	Maximum power conversion efficiency as a function of output load at 2.45 GHz and -15 dBm power level.	81
Figure 3.21	The simulated load/source pull contours on the Smith chart at 2.45 GHz and for power level of -15 dBm extracted from ADS.	82
Figure 3.22	Power conversion efficiency for different output load values.	83
Figure 3.23	Output voltage results for various output load values.	84
Figure 3.24	The configuration of the modified rectifier.	85
Figure 3.25	Simulated return loss of the DC pass filter providing short to the fundamental and harmonic frequencies.	87
Figure 3.26	The basic test setup used for the source/load pull measurement in ADS software.	87
Figure 3.27	The efficiency contours obtained from source/load pull analysis to realize efficiency higher than 40% for the load values of: (a) 4.3 k $\Omega$ and (b) 10 k $\Omega$ . The dark cyan, black, red and blue colour lines indicate the power levels of -10, -5, 0 and 5 dBm, respectively.	88
Figure 3.28	Simulated 40% efficiency contours for the output values of 4.3 k $\Omega$ (dotted lines) and 10 k $\Omega$ (dash-dotted lines). For the better demonstration, the values are normalized to $Z_0 \times (0.8 \times -j 2.81)$ on the Smith chart. The dark cyan, dark gray, red and blue color lines indicate the power levels of -10, -5, 0 and 5 dBm, respectively.	89

Figure 3.29	Simulated power conversion efficiency as a function of output load value.	90
Figure 3.30	The photograph of the fabricated modified rectifier.	91
Figure 3.31	The methodology flowchart for the design of broadband rectifiers.	93
Figure 3.32	General block diagram of the proposed broadband rectifier.	94
Figure 3.33	Simulated return loss of a single L-matched rectifier at different power levels for $RL = 10 \text{ k}\Omega$ .	96
Figure 3.34	The simulated input impedance $Z_L$ seen at the input of the matching network. The matching network provides matching at 2.45 GHz to the $100 \Omega$ line. All the values are normalized to $100 \Omega$ .	96
Figure 3.35	Layout of the broadband dual output rectifier.	98
Figure 3.36	The transmission and return loss responses of the designed harmonic rejection filter.	98
Figure 3.37	Simulated 3-D view of the return loss versus frequency and power level.	99
Figure 3.38	Equivalent circuit model corresponding to a small section of traditional TL.	101
Figure 3.39	Equivalent circuit model for (a) purely left-handed; (b) purely right-handed transmission lines and (c) homogenized CRLH transmission line.	103
Figure 3.40	Generalized circuit model of CRLH-TL unit-cell.	103
Figure 3.41	Dispersion diagram of CRLH transmission line (a) unbalanced and (b) balanced case.	104
Figure 3.42	Back-fire to end-fire radiating characteristics of the CRLH LWA. Notice the backward radiation of LWA occurring at $\beta < 0$ that is unique to left-handed property of metamaterials.	106
Figure 3.43	Design methodology flowchart of metamaterial-based antenna.	109
Figure 3.44	(a) The layout of proposed SIW unit cell. (b) The equivalent circuit model of the structure.	110
Figure 3.45	Dispersion diagram of the proposed unit cell.	114

Figure 3.46	Simulated transmission coefficient of the four-stage CRLH SIW and its equivalent SIW structure.	114
Figure 3.47	The photograph of the fabricated LWA.	115
Figure 3.48	CPW-CRLH unit cell design setup in CST software.	118
Figure 3.49	Configuration of the proposed bandwidth-enhanced dual CRLH-TL ZOR antenna.	119
Figure 3.50	Dispersion diagram of the proposed CRLH unit cell.	120
Figure 3.51	Photograph of the fabricated antenna.	121
Figure 3.52	The layout of harmonic terminating ZOR antenna (HTA).	122
Figure 3.53	(a) Photograph of the fabricated HTA and (b) HTA under the test.	123
Figure 3.54	The layout of compact broadband rectifier.	124
Figure 4.1	Comparison between the simulated results of modified rectifier and the rectifier without HRF.	125
Figure 4.2	Simulated and measured return loss of the modified rectifier at the input power of -10 dBm and the load of 4.3 k $\Omega$ .	126
Figure 4.3	Simulated and measured results of the proposed modified rectifier.	126
Figure 4.4	Simulated and measured RF-to-DC power conversion efficiency of the modified rectifier as a function of output load.	127
Figure 4.5	Photograph of the fabricated broadband rectifier.	128
Figure 4.6	Simulated and measured return loss of the fabricated broadband rectifier under various power conditions.	129
Figure 4.7	Measured and simulated power conversion efficiency as a function of frequency at three power levels of 3, -7 and -17 dBm.	129
Figure 4.8	Measured and simulated power conversion efficiency as a function of power at different frequencies.	130
Figure 4.9	Measured output DC voltage versus frequency of the broadband rectifier for an incident power levels of (a) 3 dBm and (b) -17 dBm.	131
Figure 4.10	Simulated and measured return loss of the proposed design.	132

Figure 4.11	E-field distribution of the LWA for different time instants on the x-y plane. (a) Transient E-field at 2.7 GHz, (b) transient E-field at 2.45 GHz, (c) transient E-field at 2.3GHz.	134
Figure 4.12	(a) 3-D farfield view at 2.55GHz and (b) normalized radiation patterns of the antenna at E-plane (zy-plane).	135
Figure 4.13	Normalized simulated radiation patterns at (a) H-plane (zx-plane) and (b) Elevation plane (zy-plane).	136
Figure 4.14	Simulated scanning angle (black solid line) and antenna gain (red dashed line) versus frequency.	137
Figure 4.15	Measured gain and efficiency of the designed LWA.	137
Figure 4.16	Simulated and measured reflection coefficients of the proposed antenna.	139
Figure 4.17	Simulated results of surface current distribution at (a) $f = 1.84$ GHz and (b) $f = 3.1$ GHz obtained from CST software.	140
Figure 4.18	Simulated and measured radiation patterns of the proposed antenna: (a) zy-plane (E-plane) at 1.84 GHz; (b) xz-plane (H-plane) at 1.84 GHz; (c) zy-plane (E-plane) at 3.08 GHz; (d) xz-plane (H-plane) at 3.08 GHz. Symbol lines indicate the simulated results where the blue and red colour lines show the co-pol and X-pol, respectively.	143
Figure 4.19	Measured Gain and radiation efficiency of the proposed antenna.	143
Figure 4.20	Measured and simulated reflection coefficient of the proposed HTA and the reference modified ZOR antenna without the harmonic rejecting filter.	144
Figure 4.21	Simulated and measured radiation patterns of the HTA: (a) zy-plane (E-plane) at 1.85 GHz; (b) xz-plane (H-plane) at 1.85 GHz; (c) zy-plane (E-plane) at 2.45 GHz; (d) xz-plane (H-plane) at 2.45 GHz; (e) zy-plane (E-plane) at 3 GHz; (f) xz-plane (H-plane) at 3 GHz.	148
Figure 4.22	Measured and simulated gain of the HTA.	148

Figure 4.23	The ad hoc measurement test setup used for rectenna performance evaluation inside an anechoic chamber.	149
Figure 4.24	Photograph of rectenna from combination of modified rectifier and ZOR antenna.	152
Figure 4.25	Measured RF-to-DC power conversion efficiency of the modified rectifier.	152
Figure 4.26	Measured RF-to-DC efficiency as a function of output load.	153
Figure 4.27	Measures RF-to-DC power conversion efficiency of the broadband rectenna versus power density.	154
Figure 4.28	Photograph of rectenna from combination of broadband rectifier and ZOR antenna.	155
Figure 4.29	Measured DC output voltage at each port as a function of power density.	155
Figure 4.30	Measured received RF power and rectified DC power at 2.15 (Red lines), 2.3 (Green lines) and 2.45 GHz (Blue lines) for different power density levels.	157
Figure 4.31	Fabricated prototype of compact integrated rectenna.	158
Figure 4.32	Measured RF-to-DC efficiency of the integrated Rectenna.	158
Figure 4.33	Measured output DC voltage at different power density levels.	159
Figure 4.34	Rectenna under test inside an anechoic chamber.	159
Figure 4.35	Measured harvested (a) DC power and (b) achieved output DC voltage as a function of distance.	161
Figure 4.36	The general test setup used for multi-tone measurements inside anechoic chamber.	163
Figure 4.37	The two and three-tone performance measurements of the broadband integrated rectenna (a) 2.45 & 2.3GHz; (b) 2.45 & 2.15 GHz; (c) 2.3 & 2.15 GHz; (d) 2.45 & 2.3 & 2.15 GHz.	166

## LIST OF ABBREVIATIONS

IoT	Internet of Things
WPT	Wireless power transmission
RFID	Radio Frequency Identification
MIT	Massachusetts Institute of Technology
NASA	National Aeronautics and Space Administration
LOS	line-of-sight
MWPT	Microwave wireless power transmission
RF	radio frequency
DC	direct current
JPL	Jet propulsion laboratory
FSPL	free space path loss
UHF	ultra high frequency
ISM	industrial–scientific–medical
IEEE	Institute of Electrical and Electronics Engineers
ICNIRP	International Commission on Non-Ionizing Radiation Protection
RIS	reactive impedance surfaces
CSRR	complimentary split ring resonator
SRR	split ring resonator
CRLH	composite right-/left- handed
ZOR	Zeroth-order resonance
CPW	Coplanar-waveguide
LED	light emitting diode
SHARP	Stationary High Altitude Relay Platform
UAV	unmanned aerial vehicles
LP	linearly polarized
CP	circularly polarized
DLP	dual-linearly polarized
DCP	dual-circularly polarized
FR4	flame retardant 4
LCD	liquid crystal display
AR	axial ratio

GSM	Global System for Mobile communications
UMTS	Universal Mobile Telecommunications System
3G	Third Generation
SMD	Surface-mounted device
LHCP	Left-hand circularly polarized
RHCP	Right-hand circularly polarized
GCPW	Grounded coplanar waveguide
ADS	Advanced Design System
CST	Computer Simulation Technology
BPF	Band pass Filter
IC	Integrated circuit
HB	Harmonic balanced
HRF	Harmonic rejection filter
WiMAX	Worldwide Interoperability for Microwave Access
LTE	Long-Term Evolution
DPS	Double-positive
MNG	mu-negative
ENG	Epsilon-negative
DNG	Double-negative
RH	Right-handed material
LH	Left-handed material
LWA	Leaky-wave antenna
EM	Electromagnetic
TL	Transmission line
PLH	Purely left-handed
PRH	Purely right-handed
P.E	Parasitic element
HTA	Harmonic terminating antenna
CMOS	Complementary metal–oxide–semiconductor
SIW	Substrate integrated waveguide
IDC	Interdigital capacitor
MIRA	Metamaterial-inspired resonant antenna
PCE	Power conversion efficiency

## LIST OF SYMBOLS

$L_0$	Free space path loss
$d$	Distance
$\lambda$	Wavelength
$P_r$	Received power
$P_t$	Transmitted power
$G_t$	Transmitting gain
$G_r$	Receiving gain
$\epsilon_r$	Relative permittivity/Dielectric constant
$R_j$	Diode non-linear resistance
$C_j$	Diode junction capacitance
$R_s$	Diode series resistance
$L_p$	Diode parasitic inductance
$C_p$	Diode parasitic capacitance
$V_d$	Diode voltage
$I_s$	Diode saturation current
$q$	Electron charge ( $1.6 \times 10^{-16}$ Coulomb)
$n_i$	Ideality factor/emission coefficient
$T$	Absolute temperature in Kelvins
$U$	Contact junction area
$U^*$	Modified Richardson constant
$\Phi_B$	Barrier height in volt
$A_u$	Cross section junction area of the diode
$m_g$	Grading coefficient
$C_{j0}$	Junction capacitance at zero bias voltage
$N_D$	Donor density in n-layer and

$V_f$	Forward voltage of diode
$M$	Multiplication factor
$\omega$	Radial frequency
$R_g$	Source resistance
$C_{lo}$	Output capacitor
$R_L$	Load resistance
$v$	Voltage across non-linear diode
$x$	Forcing function
$y$	Video output
$I_0$	Bias current
$v_g$	Source voltage
$Y_{(N)}$	Amplitude of harmonic terms
$\theta$	Signal phase
$f$	Frequency
$V_{DC}$	DC voltage
$V_{br}$	Diodes breakdown voltage
$\eta$	Efficiency
$\eta_{EH}$	Energy harvester efficiency
$P_{RF-Acc}$	Power accepted
$P_{DC}$	DC power
$P_{inEH}$	Total power delivered to the harvester
$P_{outDC}$	DC output power
$P_{inc}$	Incident power
$\Gamma$	Reflection coefficient
$\lambda_0$	free space wavelength
$v_p$	Phase velocity
$Z_0$	Characteristic Impedance

$\beta$	Propagation constant
$v_g$	Group velocity
$\alpha$	Attenuation constant
$p$	Unit cell physical length
$C_L$	Left-handed capacitance
$L_R$	Right-handed inductance
$L_L$	Left-handed inductance
$C_R$	Right-handed capacitance
$Z_{in}$	Input impedance
$W_m$	Stored magnetic energy
$W_e$	Stored electrical energy
$G$	Conductance
$Q$	Quality factor
$f_{se}$	Series resonant frequency
$f_{sh}$	Shunt resonant frequency
$f_{-1}$	First negative order resonance
$\lambda_g$	Guided wavelength
$G_{Cal}$	Calibrating gain
$P_{Cal}$	Calibrating power
$P_{RX}$	Power received at reference antenna
$A_{eff}$	Antenna effective aperture area

## LIST OF PUBLICATIONS

1. Saravani, Sobhan, Chandan Kumar Chakrabarty, Norashidah Bt Md Din, and K. K. A. Devi. "A compact substrate integrated waveguide CRLH leaky-wave antenna for S-band applications." In *2015 IEEE International RF and Microwave Conference (RFM)*, pp. 175-179, 2015.
2. Saravani, S., Chakrabarty, C.K. and Md Din, N. "Compact bandwidth-enhanced center-fed CPW zeroth-order resonant antenna loaded by parasitic element." *Progress In Electromagnetics Research*, 66, pp.1-8, 2017.
3. Saravani, S., Chakrabarty, C.K. and Md Din, N., Syamimi Mohd Norzeli, Mohamad Halil Haron "Broadband and high efficiency rectifier design based on dual-mode operation for RF ambient energy harvesting" **Accepted** and to be published in *International Journal on Advanced Science, Engineering and Information Technology (IJASEIT)*, 2019.
4. Saravani, S., Chakrabarty, C.K. and Md Din, N., Syamimi Mohd Norzeli, Mohamad Halil Haron "A novel sensitive rectifier with increased output load tolerance for ambient RF energy harvesting" **Accepted** and to be published in *International Journal on Advanced Science, Engineering and Information Technology (IJASEIT)*, 2019.
5. Norzeli, Syamimi Mohd, Ismarani Ismail, Norashidah Md Din, Mohd Tarmizi Ali, Sobhan Saravani, and Ali Abd Almisreb. "Design of high gain microstrip Patch Reader array antenna with parasitic elements for UHF RFID application." *International Journal of Engineering and Technology (UAE)* 7, no. 4, pp. 463-467, 2018.

# CHAPTER 1

## INTRODUCTION

### 1.1 Overview

The limited remaining of the natural energy resources such as fossil fuels and their negative impact on the nature and human lives has driven many researchers to look more into an alternative solution. Recently, by the expansion of the technology and reduced power requirement of modern electronic devices, the use and recycle of new and clean sources of energy, commonly referred as “Green Energies”, as a reliable source of power has become more possible.

Energy harvesting is the process of capturing and accumulating residual energy often released into the environment as waste and converting it into usable energy and, therefore, it is free energy. The harvested power can be used to either empower the consumer device directly or store it into a storage element for later use. The energy can be captured from a variety of natural sources such as wind, fluid, thermal, solar as well as artificially generated ones like radio frequency (RF) energy in the environment provided from ubiquitous radio transmitters and television broadcasting stations. The natural based energy harvesters such as fluid, wind and solar are matured enough for generating power in large scales [1]. Moreover, while the latter one is considered integrated circuit-compatible technology with potentially long-life-cycle than other energy-harvesting mechanisms it is limited to applications where sufficient sunlight is available [2]. Natural source of energy may not be available continuously depending on the circumstances, location and also weather condition. Therefore, harvesting RF energy from the ambience can be an encouraging solution in providing long-lasting energy supply for energy-constraint low-power devices. This transparent, human non-sensible energy source becomes more appealing as it does not require any direct contact with the harvester, thus, the harvester can be sealed and most importantly the power source is always available and controllable.

During the last decade the number of portable wireless electronic devices has increased dramatically in military, industry and commercial applications. These devices are

operated by batteries as it provides a simple design approach for the powering of autonomous sensors and hand-held devices. However, batteries must be replaced when depleted, which can lead to unacceptable maintenance costs whenever the number of autonomous sensors is very large or their accessibility is difficult or impractical.

A good example for the large scale usage of autonomous sensors is connecting things, i.e. physical components, to create an Internet of Things (IoT) which is predicted to have great impact in daily life and is likely to make many novel applications possible. The world of IoT has already merged with variety of applications such as health care tracking[3], smart homes [4], smart industrial plants [5], logistics and many other examples both in the public and private sectors within [6].

As connected devices are becoming progressively smaller and getting more out on the edge, powering them with batteries becomes more of a problem. The prospect of replacing the drained batteries, even as infrequently as every five to ten years, is simply a non-starter (i.e. sensors embedded within structural members or walls). On the other hand, according to a research work carried out by D. Lund et al. [7], as of 2013, 9.1 billion IoT units have been employed and is expected to grow over 28.1 billion by 2020. On the other hand the expected revenue growth is from 1.9\$ trillion in 2013 to be 7.1\$ trillion in 2020 visualizing the brilliant future of energy harvesters.

## **1.2 Wireless Power Transmission Techniques**

Wireless power transmission (WPT) is generally done through four major techniques of short-range induction, mid-range magnetically coupled resonance, microwave wireless power transfer and distributed laser techniques [8, 9]. The inductive coupling technique is the simplest for the implementation which uses the mutual induction phenomena between coils. The alternating current at the transmitting side generates magnetic field around the primary coil. Once the secondary coil is placed close enough, a current stream is generated from the interaction between the secondary coil and the existing magnetic field. The inductive coupling is widely used in variety of applications such as Radio Frequency Identification (RFID) tags and even in readily available electric toothbrushes. However, in the case of inductive coupling, tight alignment between the primary and secondary coils is necessary and the effective

power transfer distance does not exceed from few millimeters to few centimeters. An improvement on the power transfer distance is achieved following an experiment conducted by Soljačić et al. in Massachusetts Institute of Technology (MIT) in which two coils were forced to resonate at the same frequency referred as magnetically resonant technique [10]. Figure 1.1 shows the test setup used to power up a 60 W light bulb at the distance of 1.5 m with an object between the coils to block direct line of sight demonstrating the potential of this technique.

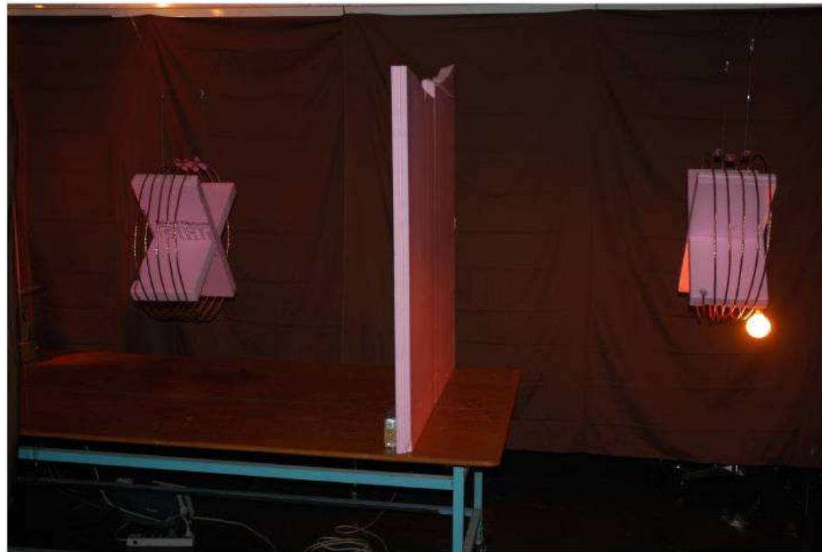


Figure 1.1. Experimental test setup used in [10]. Notice that both coils have a diameter of 50 cm and the spacing between the coils is 1.5 m powering a 60W light bulb.

As a consequence, the power transfer over larger distance of up to few meters with reduced sensitivity to the coil positions was possible. The new contactless charging of smart phones and electric vehicle charging is benefited from this technique as it can provide a fairly high efficiency at different power levels. However, similar to inductive coupling, these techniques are non-radiative and not suitable for the mobile application due to the short range of power transfer.

Distributed laser technique is a new method of power transfer over a distance. Unlike the previously mentioned methods above, it is a long range power transfer technique relying on the high intensity laser beam at the transmitter side and a highly sensitive

photovoltaic cells at the receiving end. This idea was initially suggested by The National Aeronautics and Space Administration (NASA) in a project for transferring power to a rover exploring inside a crater on the moon through a two stage power conversion where the preliminary power is realized from solar power and then converted into the laser beam and transferred to the rover at a location where no sunlight could reach [11]. With all being said, distributed laser technique is still at infancy stage and some major drawbacks of short range transfer, high attenuation caused by atmospheric and weather changes, low efficiency and direct line-of-sight (LOS) requirement makes it undesirable for many applications [8].

Microwave wireless power transmission (MWPT) is the most popular method amongst all other aforementioned techniques as it allows for long-range power transmission. Rectifying antenna, also known as rectenna, is the most important module for MWPT and RF energy harvesting applications. Figure 1.2 shows a simple RF energy harvesting receiving end. As is observed, it composed of a receiving antenna that captures the power from the ambience. The collected power passes through a matching network to a rectifier circuit where the power is converted into usable DC form. The provided DC power is then used to drive a device or conserved into a storage element for a later usage. In an experimental work done by Jet propulsion laboratory (JPL) sponsored by NASA, 100 kW of power successfully transferred over 1.54 km. In that work, the power captured and converted by a rectenna array consist of 270 elements operating at 2.388 GHz. It is reported that over 30 kW of DC power and an efficiency of 80% has been achieved [12]. The focus of this thesis is on this type of WPT.

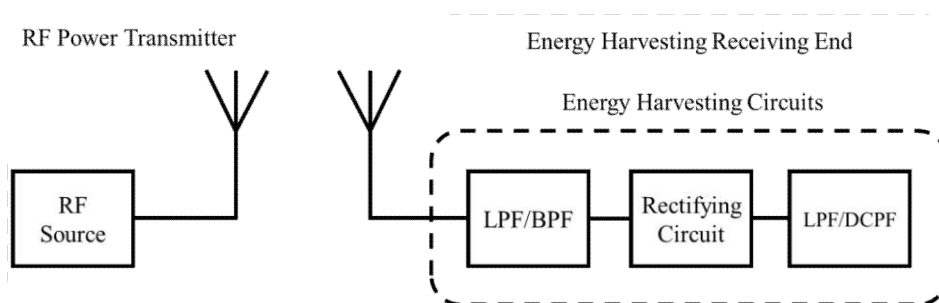


Figure 1.2. A simple RF energy harvesting receiving end.

### 1.3 Energy Harvesting Challenges

The overall efficiency of energy harvesting system is the product of the several individual efficiencies associated with the energy transmitted, receiving antenna and converting processes of the rectifier. High conversion efficiency of the rectifying circuit for a specified input power level and the overall size are two important factors to be considered when rectenna systems are designed. The rectifying circuit is often constructed using Schottky diodes at the low power levels owing to their low built-in voltage and fast switching speed. The antenna dimensions is also critical in the design of rectenna systems as it can directly impact the overall size of the energy harvester. As a consequence, harvesting power from ambient RF energy faces with several conflicting requirements and trade-offs that will be briefly explained in the following sections.

#### 1.3.1 Free Space Path Loss

A challenge involved on the design of RF energy harvesting is the inevitable trade-off between antenna size, power and distance. For any WPT system, the free space path loss (FSPL) of a transmission link is the major loss mechanism which can be calculated following the equation:

$$L_0 = \left( \frac{4\pi d}{\lambda} \right)^2 \quad \text{Equation (1.1)}$$

In the above equation,  $d$  and  $\lambda$  are the distance and free space wave-length at the frequency of operation, respectively. For instance, the value of loss for 2.4 GHz and 5.5 GHz are 46 and 53 dBm at the distance of only 2 meters away from the transmitter. Hence, if we transmit 1W power, the amount of received power at the distance of 10 m is around 1  $\mu\text{W}$  and 190 nW at 2.4 and 5.5 GHz, respectively.

#### 1.3.2 Antenna Miniaturization Challenges

In order to compensate for the FSPL effect and capture more power from ambience, high gain antennas are needed in RF energy harvesting modules. According to the Friis transmission equation, employing high gain antennas at both transmitting and receiving ends can pay-off for the existing FSPL as:

$$P_r = P_t G_t G_r \left( \frac{\lambda}{4\pi d} \right)^2 \quad \text{Equation (1.2)}$$

where  $P_r$  and  $P_t$  are the received and transmitted power;  $G_t$  and  $G_r$  are the gain of transmitting and receiving antennas, respectively. However, the problem with trade-off between antenna gain and antenna size remains unsolved as high gain antenna, means the electrical area of antenna to be large which is directly proportional to the physical size and its achieved efficiency. This makes the design of antenna for energy harvesting systems extremely challenging as the system requires to be portable and efficient, simultaneously.

### 1.3.3 Power Availability

Nowadays our living environment is pervaded with ubiquitous electromagnetic energy sources as wireless communication is involved with almost every aspect of our lives. Several recent studies have investigated the availability of RF power and its density level at various locations, i.e. Shunde, China [13], London, U.K. [14] and Tokyo, Japan [15]. Table 1.1 and Figure 1.3 present the measured power levels in some of these works. According to these studies, the range of measured power densities are within  $0.1\text{--}10 \mu\text{W}/\text{cm}^2$  in the UHF and some of industrial–scientific–medical (ISM) bands. In some other publications [16, 17], it has been shown that the amount of available power at a range of 50 meter away from a cell tower can reach up to  $1 \mu\text{W}/\text{cm}^2$ . However, it should be kept in mind that this value of power density can vary widely depending on the location, time and type of base stations.

Table 1.1. The power density levels measured in London [14].

Band	Frequencies (MHz)	Average $S_{BA}^2$ (nW/cm <sup>2</sup> )	Maximum $S_{BA}^2$ (nW/cm <sup>2</sup> )
DTV (during switch over)	470–610	0.89	460
GSM900 (MTx)	880–915	0.45	39
GSM900 (BTx)	925–960	36	1930
GSM1800 (MTx)	1710–1785	0.5	20
GSM1800 (BTx)	1805–1880	84	6390
3G (MTx)	1920–1980	0.46	66
3G (BTx)	2110–2170	12	240
Wi-Fi	2400–2500	0.18	6

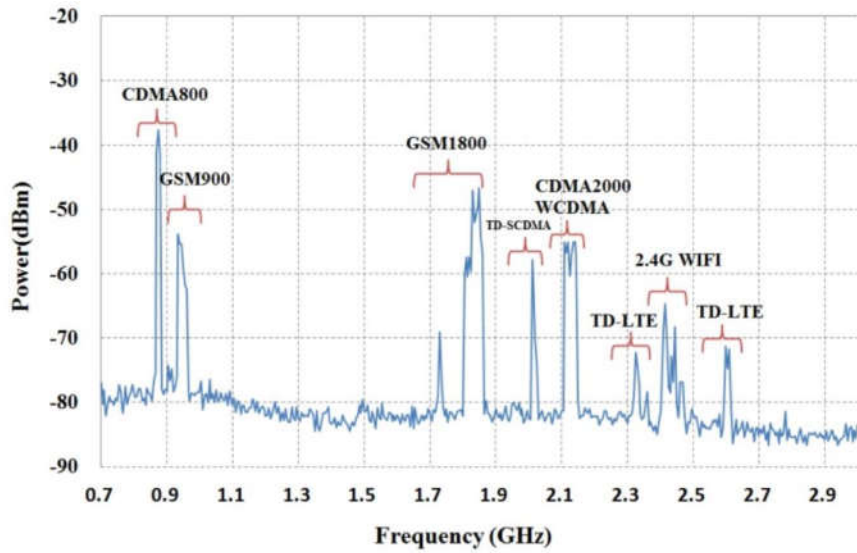
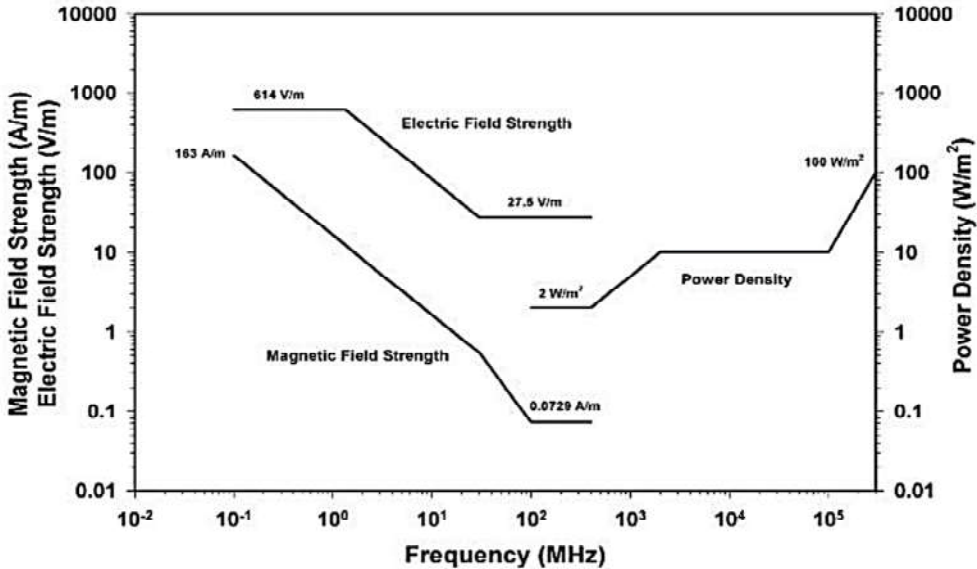


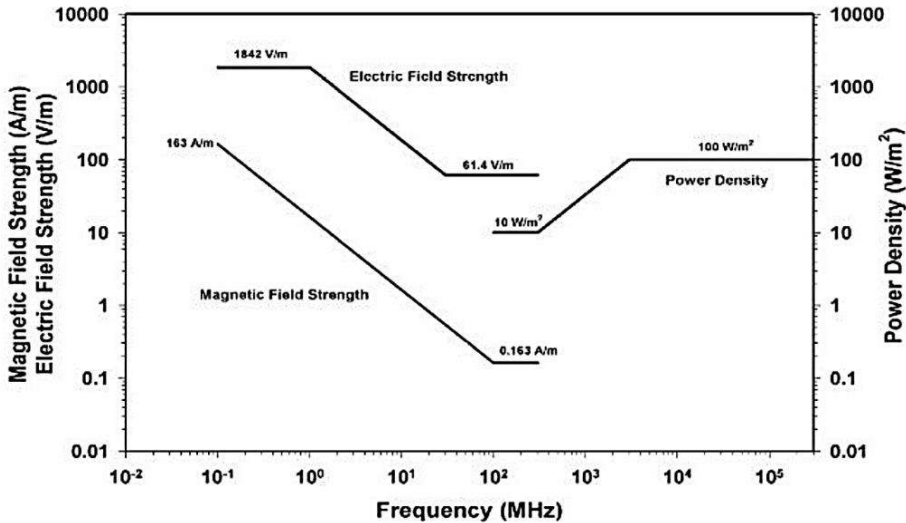
Figure 1.3. RF power measured at a residential area in Shunde, China [13].

An energy harvesting system should operate over large range of frequencies including the versatile and unlicensed ISM bands (902–928 MHz and 2.435–2.465, 5.785–5.815, 10.5–10.550, and 24.075–24.175 GHz). In such a manner, not only the energy harvester can benefit from wide range of available RF spectrum but also the system can be powered intentionally if required which can significantly increase the reliability of the energy harvester. Nevertheless, the maximum level of transmitted power must follow regulatory and safety standards.

According to the new IEEE standard for safety levels with respect to human exposure to RF radiation, the maximum allowable exposures are  $2 \text{ W/m}^2$  for frequencies between 30 and 400 MHz and  $10 \text{ W/m}^2$  between 400 and 2000 MHz. For frequencies greater than 2000 MHz, the maximum permitted exposure is  $10 \text{ W/m}^2$  [18, 19]. Figure 1.4 (a) and (b) show the maximum allowable power exposure limits at different environments assigned by IEEE standard society [18].



(a)



(b)

Figure 1.4. (a) Maximum allowable exposure limits for general public, (b) Maximum permissible exposure limits for controlled RF environments [18].

Moreover, the International Commission on Non-Ionizing Radiation Protection (ICNIRP) exposure guidelines, published in 1998, indicates the power density levels to be  $0.45 \text{ mW} / \text{cm}^2$  at 900 MHz,  $0.9 \text{ mW} / \text{cm}^2$  for mobile phone base stations at 1.8 GHz, and  $1 \text{ mW} / \text{cm}^2$  at 2.45 GHz [20]. Additionally, ICNIRP reconfirmed its previously published guidelines as the scientific literature published since 1998 has provided no evidence of any adverse effect below the basic restrictions of ICNIRP [21].

#### **1.4 Problem Statement**

The modern free-space power transmission needs to achieve the combined objectives of high efficiency, low cost, high reliability, and low mass at the transmitting and receiving ends of the system [22]. Hence, considering a rectenna consisting of two main parts of antenna and rectifier, the problem statement is divided into two section.

For the antenna element, various antenna types have been utilized for the realization of rectenna and rectenna arrays such as patch antennas [23-36]; spiral antennas [37, 38], Quasi-Yagi antenna [39] fractal antennas [40, 41]; bow-tie antennas [42] and even reconfigurable antenna [43]. For these resonant type antennas, the size of antenna is determined by frequency of operation. For example the size of a microstrip patch antenna needs to be half a wavelength at the frequency of operation. However, half-wavelength size of conventional antennas is relatively large in modern portable communication devices particularly at the frequencies below 3 GHz. However, taking into account the extensive deployment of commercial applications for the frequency bands below 3 GHz, ambient electromagnetic power density is relatively high at these commonly used wireless frequency bands and the cost of wireless power source generators at these frequencies are relatively low.

Therefore, different approaches have been introduced to overcome this problem by employing the shorting pins [44], etching slots [45] and even utilization of high dielectric materials. Nevertheless, miniaturizing antenna size via traditional miniaturization methods often results in narrow bandwidth, low radiation efficiencies and undesired radiation patterns.

Since there is an inherent need for compact rectennas in such applications, especially as their size decreases, the metamaterial-inspired miniaturized antennas with broad bandwidth and high radiation efficiency become the promising candidates for rectenna systems. Several types of metamaterials has shown promising opportunities for antenna miniaturization such as reactive impedance surfaces (RIS), magneto-dielectrics, and left-handed metamaterials [46-52]. For example, in [49], it is reported that both antenna bandwidth (10%) and efficiency (96%) can be improved using RIS and the antenna size reduced to one-tenth of wavelength ( $\lambda_0$ ). Nevertheless, this structure requires high permittivity substrate ( $\epsilon_r=25$ ) which is costly and increases the thickness of overall structure. In [53], complimentary split ring resonator (CSRR) was used where the CSRR is sandwiched between two circuit boards in which a microstrip-line-fed circular patch is placed at the top and the ground plane is at the bottom side of structure. The level of miniaturization achieved at this work is up to 1/16 of the traditional patch antenna but at the cost of reduction in both bandwidth (0.4%) and efficiency (28.1%). Additionally, a type of artificially developed transmission line called composite right-/left- handed (CRLH) material exhibited the capability of supporting both backward and forward waves within the structure. An interesting feature of CRLH structure is the operation at zeroth order resonance (ZOR) where the physical limits imposed by frequency of operation is vanished. However, ZOR antennas suffer from narrow bandwidth and low radiation efficiency [54-57]. Various ZOR antennas with enhanced bandwidth and efficiency have been proposed in [58-64]. In [62] the bandwidth was improved up to 67.4% by merging first order resonance to the ZOR antenna and an efficiency of 90.08% was achieved. In [61] a wideband asymmetrical coplanar-waveguide (CPW) antenna with modified ground plane has been proposed that employs several resonances to increase the bandwidth. However, there is a severe inconsistency on the achieved efficiency over the large range of frequency. In [63], a CPW-fed ZOR antenna with enhanced bandwidth was reported in which, a resonating ring was utilized. However, the gain and efficiency were dropped significantly around the split ring resonance and large cross-polarization was observed that would make it undesirable for some applications. Hence, considering the stringent requirements of many applications for energy harvesting, there is an inevitable need for the miniaturized high efficiency and broadband antenna.

So far, most of the presented rectenna systems in the literature operate only within a single narrowband and with the main concentration on the overall achieved efficiency [23-25, 30, 31, 33-36, 41, 65-73]. As an example, a low cost and efficient rectenna operating at 2.45 GHz using bridge rectifier network is reported in [34] and an efficiency of 61% is obtained over a load of 1050 ohm at 10 dBm. Furthermore, a dual circularly polarized rectenna at 2.45 GHz has been presented in [24], in which, the antenna has a gain of 10 dBic and the maximum efficiency of 81% at the power level of 22 dBm has been obtained. In another work, a high gain antenna array and three-stage Dickson charge pump is used to lit-on a light emitting diode (LED) which is used as the load of rectenna system operating at 915 MHz [36]. The maximum efficiency achieved is 40% at 10 dBm. However, since the design of these rectennas is typically performed under some predefined power and load conditions, even slight deviation on output load values can downgrade the performance due to sensitive non-linear behavior of diode. This is a serious bottleneck for many practical applications as the type of external circuitry may vary depending on the types of applications. Hence, the design of a rectenna with increased output load tolerance can greatly expand its usability over much wider applications.

Moreover, for the energy harvesting applications, the power density at a single frequency band may not be adequate to guarantee the operation of the most rectennas. As a consequence, several designs with the intention of harvesting energy from dual or multiple bands, thus, achieving higher amount of output DC power has also been proposed in the literature [28, 39, 74-76]. Most of these designs are based on dual/multiband antennas incorporated with the complex matching networks to mitigate the low power issue. Unfortunately, there are several major drawbacks with the current designs. First, most of these designs are constrained with narrow band operation in some of bands, if not all, which severely restricts the amount of power captured before the rectification process. Second, due to inconsistency on the power available at each frequency during a period of time the energy harvesting operates at single dominant frequency only. For example, in [74], the dual band rectenna efficiency is 37% and 20% at 0.915 and 2.45 GHz, respectively, under the same power density of  $1 \mu\text{W} / \text{cm}^2$ . A broadband rectenna can be less sensitive to the aforementioned drawbacks as it can substantially provide larger power dynamic range and output voltage. There are only

a few broadband rectennas in the literature [38, 77-81]. For example, in [38] a broadband rectenna array, operating from 2 to 18 GHz, with dual circularly polarized characteristic is presented where the total efficiency is only 20% at power density of  $63 \mu W/cm^2$ . In [81] a rectenna using grounded co-planar waveguide structure is presented achieving 72.5% efficiency at 20 mW incident power. However, almost all of them neglect the overall dimensions of final design and, more importantly, they all present the good efficiency only at high power levels that is far from the realistic scenarios ( $P_{inc} \leq 10 \mu W/cm^2$ ). No special attention have been paid for the simultaneous achievement of system reliability, overall sensitivity and dimensions which are crucial requirements of energy harvesting systems. Therefore, it is essential to design a sensitive and high efficiency broadband rectenna for the low power level operation while preserving its compact form to be used for autonomous sensor network and IoT applications.

### **1.5 Objectives of this Research**

Therefore, according to the mentioned backgrounds, the need for a broadband high efficiency rectenna operating at microwave range of frequency is necessary. Additionally, design of miniaturized size antenna structure with wide bandwidth and high efficiency characteristics have motivated our research to realize a compact and quality energy harvesting system. To be more specific, there are four main objectives as follows:

- i. To design a compact, wideband and miniaturized metamaterial-based antenna with high efficiency to be used for energy harvesting applications under low/medium RF power level.
- ii. To develop a high efficiency harmonically terminated rectifier with increased output load tolerance to maintain the high performance over large range of power and output loads.
- iii. To design a broadband rectifier possessing high RF-to-DC conversion efficiency over a large range of frequency under very low RF power levels.

- iv. Development of miniaturized fully integrated broadband energy harvester operating over wide range of frequency and power levels for space-restricted applications.

## 1.6 General Methodology and Scope of This Work

This work reports the design process of efficient, miniaturized and broadband RF energy harvesting systems. Figure 1.5 demonstrates the flowchart of general methodology undertaken in this thesis.

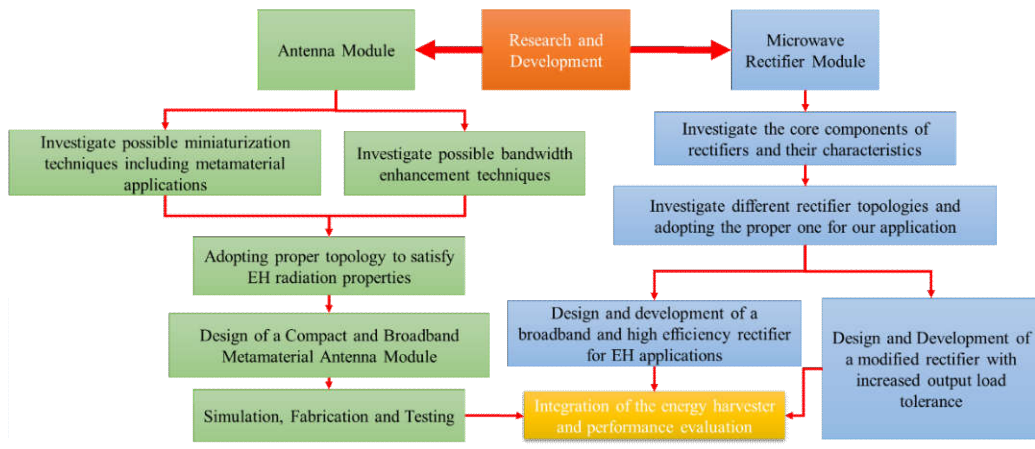


Figure 1.5. Flowchart of the methodology undertaken.

For the antenna design, a miniaturized symmetrically oriented CPW-fed ZOR antenna is presented. In order to extend the bandwidth of the proposed antenna a thin folded microstrip line as a parasitic element is loaded to the structure. The purpose of using the parasitic element is twofold. One is to provide an additional resonance to overcome the low bandwidth drawback of the antenna. The other is to provide a path for the trapped power on the square signal patch caused by the high impedance within the band-gap region of CRLH-TL that, in turn, effectively improves the efficiency of the proposed antenna. Moreover, two essential harmonic terminated rectifier design have been presented aiming to improve the output load tolerance and bandwidth performance of rectifiers. To compensate for the narrow bandwidth of the rectifier, we introduce a secondary rectifier operating at a frequency around the primary rectifier. By adjusting the resonance frequencies to be close enough, while taking into account

the power level condition, the performance bandwidth can be effectively improved. Such a technique allows for much smaller rectifier footprint which is critical to energy harvesting applications while avoiding highly complex matching network in which even slight deviation from the targeted resonant frequencies can result in large power leakage and deteriorating the rectifier performance. To increase the system reliability, the energy harvester covers 1.8 to 2.7 GHz frequency range encompassed by GSM-1800 (1805.2 – 1879.8 GHz), UMTS-3G (2110 – 2170 GHz), WiMAX (2.3 GHz), ISM-2.4 GHz (2.4-2.5 GHz, including Wi-Fi channels) and LTE- 4G (2.5-2.69 GHz) at the upper band. Several combinations of the rectennas are presented and a compact and high efficiency integrated rectenna with broadband performance is developed. Lastly, the advantage of broadband rectifier is emphasised by performing multi-tone measurements.

## **1.7 Organization**

The contents of this thesis are organized as follows:

Chapter 2 reviews the literature of rectennas in the past decades and identifies objectives and presents the state of art achievements on rectenna designs.

Chapter 3 provides complete methodology undertaken in this thesis work and is divided into three main sections. At the first section, a general description of the Schottky diodes as of core component of rectification process. It begins with the basic diode operating principle, and further discusses the impact of different components on the diode and its nonlinear behavior. At the end, an analytical model of basic rectifier is presented where the importance of harmonic consideration is emphasized.

The second section deals with the design procedure of microwave rectifiers. It initiates by introducing general rectifier topologies and their components. An efficient rectifier with reduced output load sensitivity is presented. Following that, the design of a novel efficient and broadband rectifier for the low power operation is discussed.

Finally, the problems involved with the performance of miniaturized antennas are addressed. Next, the theory of composite right-/left-handed transmission line is

primarily provided. Subsequently, the design procedure of a miniaturized high efficiency and broadband zeroth order resonant and the fabricated antenna is presented.

Chapter 4 presents the simulation and experimental results obtained at each part of this work including rectifiers, antennas and also discusses the integration challenges of the rectenna. The performance evaluation of the rectennas are provided.

Chapter 5 finalizes this thesis work, reviews the works undertaken and gives some directions for future research in this interesting area of microwave engineering.

## CHAPTER 2

### LITERATURE REVIEW

#### 2.1 Brief History and Background Survey

The context of wireless power transfer dates back to the late 19<sup>th</sup> century following the theory of wireless power transfer proposed by Nikola Tesla and Heinrich Hertz [22]. However, the Tesla project led to a failure due to several reasons such as performing the experiment at a very low frequency of 150 KHz with a very large beam wavelength, the low cost of power transmission using the copper wires, lack of investors and also the required equipment for the wireless power transmission. By development of radar technology, high power and high efficiency microwave tubes were developed allowing to concentrate power on the receivers. As a consequence, Tesla's dream was perused by William C. Brown with the invention of the first ever rectenna (rectifying antenna) in early 1960s. The Brown's rectenna composed of 28 half-wave dipole elements in which each element was terminated to a bridge rectifier made from four point-contact diodes model 1N82G [22]. A photograph of Brown's rectenna is demonstrated in Figure 2.1.

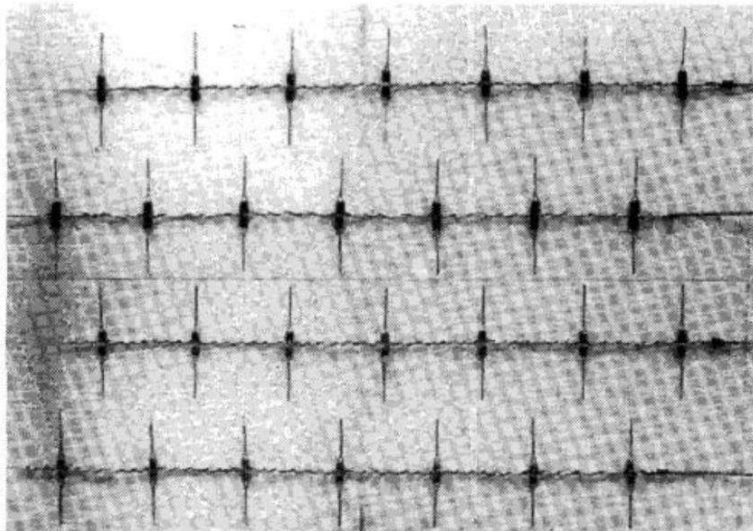


Figure 2.1. The rectenna made by William C. Brown in 1963 at Raytheon Company operating at 2.45 GHz [22].

The reported measured efficiency of the rectenna for 4 and 7 WDC are 50% and 40%, respectively.

In his work, Brown could successfully power up a flying vehicle (Helicopter) from the ground by introducing a matching network to the rectenna structure raising the output power up to 270 W. The highest power rectification efficiency reported by Brown is 90.6% for the input power level of 8W [22, 65, 82]. In 1982, Brown from Raytheon Company along with James F. Trimer from the NASA successfully developed the first rectenna using printed circuit board (PCB) technology [82]. Following these achievements a project was launched by Canadian ministry of communication called “SHARP” which stands for Stationary High Altitude Relay Platform [83]. As shown in Figure 2.2, the SHARP project was intended to develop unmanned aircraft that would maintain a circular trajectory above a ground terminals.

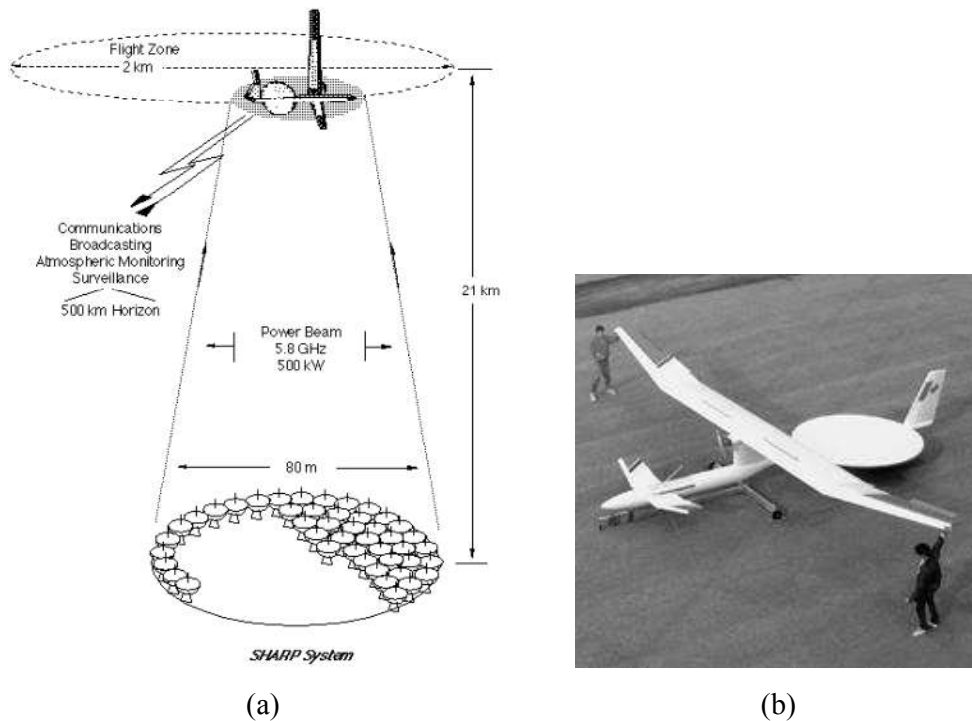


Figure 2.2. (a) SHARP project concept (b) flight experiment in 1987 [83].

While most of these works centered on high power transmission systems, in 1991, Brown investigated the possibility of collecting low microwave power by developing a large  $8 \times 6$  dipole array corporate feeding to a single rectifier [65]. A maximum

power conversion efficiency of 50% for an input RF power level of 20 mW has been reported.

## **2.2 Rectennas for Power Harvesting Applications**

For the energy harvesting applications, the rectifying efficiency for a specified input power level (typically less than 5 dBm), overall size and broad bandwidth of operation are critical figures of merit considered when rectenna systems are evaluated. Furthermore, while most laboratory and commercially available sensor nodes concentrate on the employment of traditional battery or other energy storage device technologies, which require periodic recharging or power supply replacement, WPT technologies are being actively pursued for future sensor networks and IoT applications. The bio-implanted devices [84, 85], unmanned aerial vehicles (UAVs) [86], aircraft and reinforced concrete structural health monitoring [87, 88] are some of interesting recent applications. For a low power harvesting system, a Schottky diode with low built-in voltage is often utilized to increase the rectifying efficiency.

## **2.3 Literature Review of Recent Metamaterial-Inspired Antennas**

Recently, metamaterial-inspired resonant antennas (MIRA's) have become an interesting field of study as they provide novel design approach into the design of conventional antennas. By taking advantage from exotic properties of metamaterials, the designers are benefited from additional degree of freedom on some of the critical properties of antennas such as antenna radiation properties (i.e. gain, radiation efficiency..., etc.) and size miniaturization. Composite right-/left handed (CRLH) has been widely used for the purpose of MIRA's due to its capability of supporting both backward and forward waves within the structure. Some of the advantages of CRLH materials over other types of metamaterials are their broadband characteristic, strictly planar structure, lower loss and also they allow for integration of passive elements. The background theory of CRLH transmission line is presented in Chapter 5.

The earliest design of CRLH antenna proposed by Sanada et al. in [89] and presented in Figure 2.3. As is observed, each unit cell is composed of an interdigital capacitor (IDC) and a meandered line connected to a rectangular patch that is a virtual ground plane. The antenna is fed using microstrip line through an impedance transformer

section with the zeroth impedance ( $m = 0$ ) occurring at 4.88 GHz. It has also been shown that the lowest negative order mode ( $m < 0$ ) is around 3.2 GHz achieving a miniaturization of 75% compared to conventional patch antenna as illustrated in Figure 2.4.

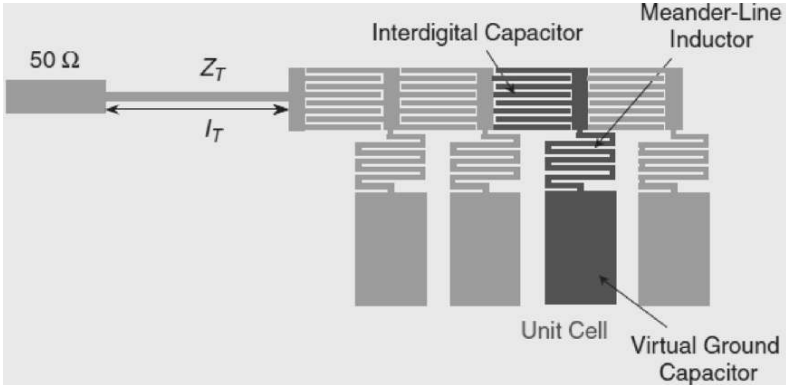


Figure 2.3. Configuration of ZOR antenna composed of four cascaded unit cells presented in [89].

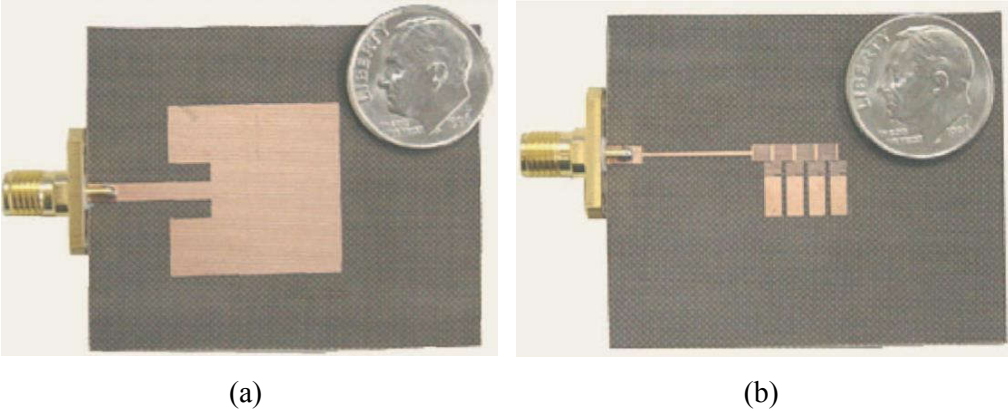


Figure 2.4. (a) Conventional patch antenna and (b) Four-cell ZOR antenna operating at 4.88 GHz in [89].

In [57], a wideband and compact resonant transmission-line metamaterial (TL-MTM) antenna is proposed based on the principle of double resonance. Figure 2.5 shows a photograph of fabricated antenna. The antenna is composed of two TL-MTM arms, each consisting of five spiral-inductor-loaded transmission-lines in microstrip. In order to obtain the wideband characteristic, the resonance of each arm is controlled by adjusting the spiral inductor turns. The antenna is fabricated on a Rogers RT/duriod

5880 substrate with a thickness of 125 mil. The fabricated prototype operating at 3.3 GHz exhibits a bandwidth of 100 MHz corresponding to fractional bandwidth of 3.1% with a maximum measured efficiency of 65.8%.

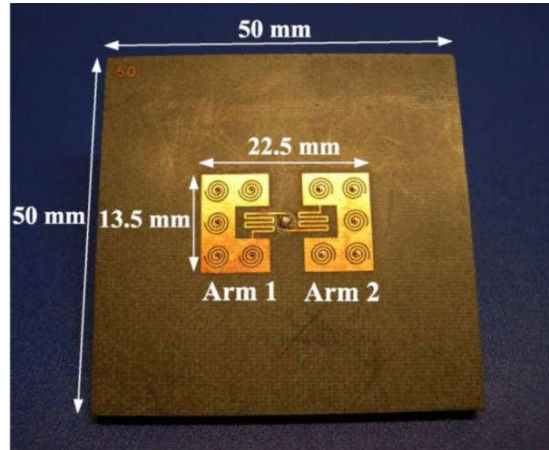


Figure 2.5. Configuration of compact and wideband two MTM-TL arm antenna presented in [57].

In [90], a two-dimensional resonator based on CRLH theory is presented comprised of well-known mushroom-like structures. In order to increase the efficiency, two structures composed of array of square and hexagonal patch have been considered in which each structure is loaded with slots to reduce the quality factor of the resonators. Figure 2.6 demonstrates the configuration of the proposed antennas. It has been reported that an increment of 7.56 dB for the nine-rectangular patches and 6.31 dB for the seven-hexagonal patches are obtained without any degradation of the radiation pattern.

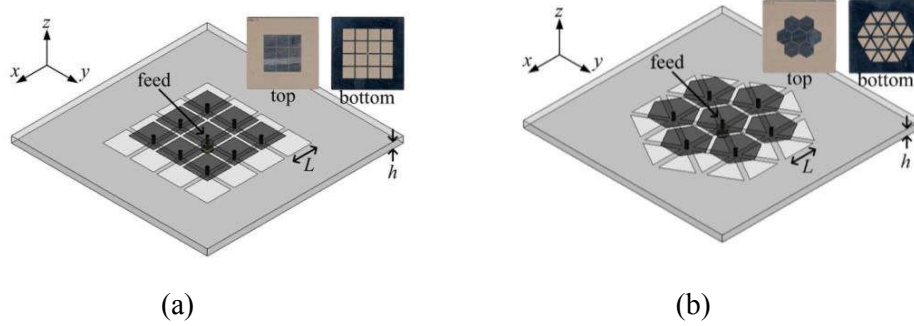


Figure 2.6. Configurations and photographs of 2-D isotropically arranged slot loaded ZOR antenna proposed in [90]. (a) Nine rectangular patches with 16 square slots. (b) Seven hexagonal patches with 24 triangular slots.

A miniaturized dual-arm spiral ZOR antenna based on CRLH theory is presented in [54]. The antenna structure and a photograph of the fabricated antenna is presented in Figure 2.7. The proposed ZOR antenna consists of two unit cells in which each unit cell forms from spiral conductors providing the series capacitance and shunt inductance from the edge coupling of spiral arms and grounded via at the center of each unit cells, respectively. Moreover, an IDC is used to provide the matching between the antenna structure and microstrip feeding. The footprint of presented antenna is  $26.4 \times 10 \text{ mm}^2$  with a fractional bandwidth of 1% operating at 2.42 GHz. The reported measured radiation efficiency and realized gain of the antenna are 53% and -0.53 dBi, respectively.

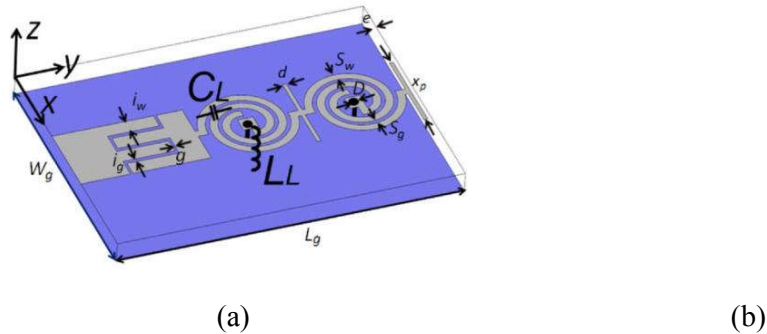


Figure 2.7. Miniaturized dual-arm spiral ZOR antenna (a) Antenna configuration and (b) Photograph of fabricated antenna proposed in [54].

In order to improve the gain and radiation efficiency of the ZOR antenna, a compact antenna based on novel CRLH transmission line unit cell structure is proposed in [91]. The antenna composed of two unit cells in which each unit cell realized from two

metallic layers isolated by a dielectric substrate; and each layer is made with a common ground plane, patch elements, and shunt stubs. The commonly used IDC is replaced by rectangular patches at either sides of substrate resulting in increased series capacitance from parallel capacitive planes and shunt inductance shorted by via holes to the CPW ground plane. The antenna presents a -10 dB-impedance bandwidth of 100 MHz from 2.25 to 2.35 GHz, and a gain and radiation efficiency of 2.3 dBi and 79%, respectively. The overall dimensions of the antenna is  $18 \times 26 \times 0.8 \text{ mm}^3$ .

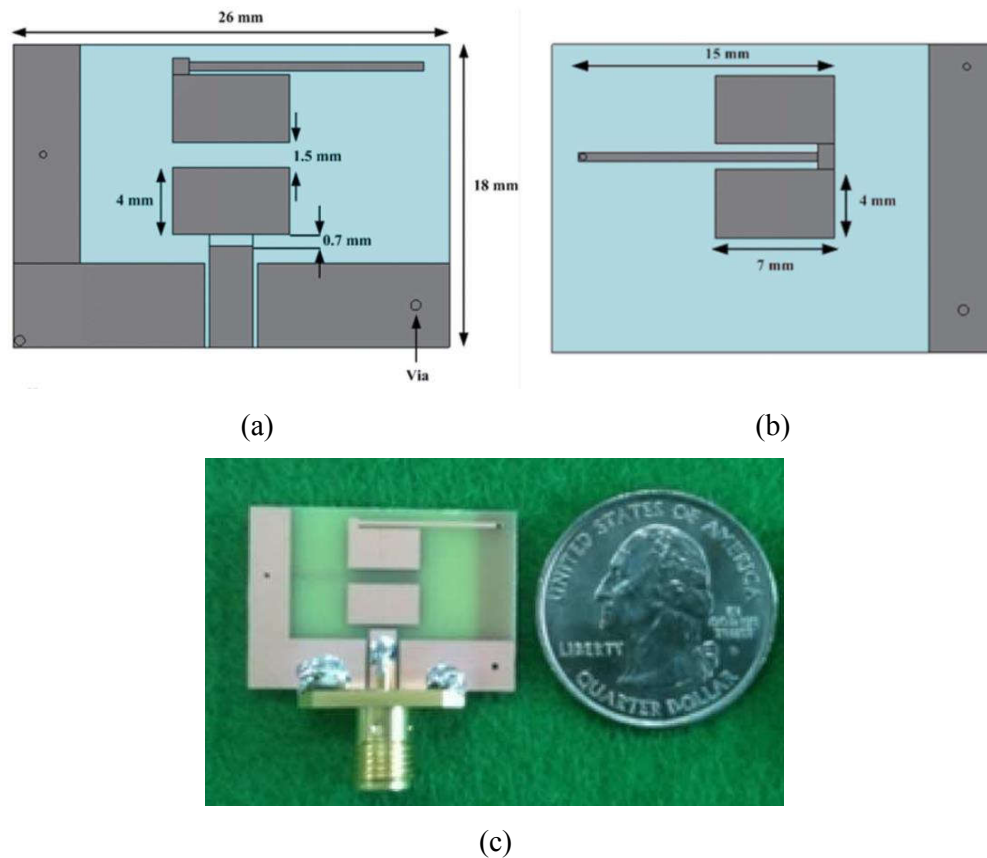


Figure 2.8. Compact and efficiency enhanced ZOR antenna (a) Top view; (b) Bottom view geometry and (c) Photograph of the fabricated antenna presented in [91].

In [58], a compact and via-less ZOR antenna with enhanced bandwidth performance is presented. The antenna layout is shown in Figure 2.9. The antenna composed of two unit cell fed through an IDC where the CPW feeding topology allows for the integration of entire antenna on the same plane. The design of the unit cell is accomplished by carefully controlling the quality factor to achieve the wideband

characteristic of the antenna. The optimized antenna has been developed on the Rogers RT/Duroid 5880 substrate of thickness 1.57 mm and dielectric constant 2.2 where the overall footprint area is  $0.14 \lambda_0 \times 0.22 \lambda_0$  operating at 2.16 GHz. The measured gain and efficiency of the antenna are 1.62 dBi and 72%, respectively.

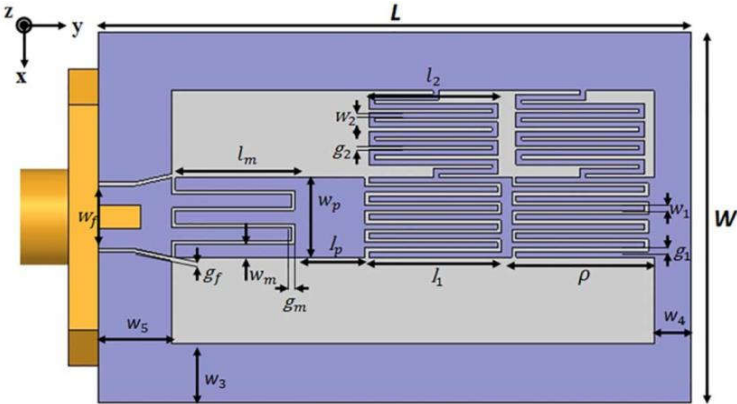


Figure 2.9. Compact bandwidth-enhanced ZOR antenna proposed in [58].

In [62], an epsilon-negative (ENG) transmission line is utilized for the realization of ZOR antenna with extended bandwidth and high efficiency. In order to increase the bandwidth the zeroth- and first-order resonances of the antenna, composed of three unit cells, have been merged resulting in a large bandwidth of 1.8 GHz with the zeroth- and first-order resonance frequencies occurring at 1.99 GHz and 3 GHz, respectively. The photograph of the fabricated antenna is depicted in Figure 2.10. The measured gains are 2.21 and 2.77 dBi at the zeroth- and first-order resonances where the

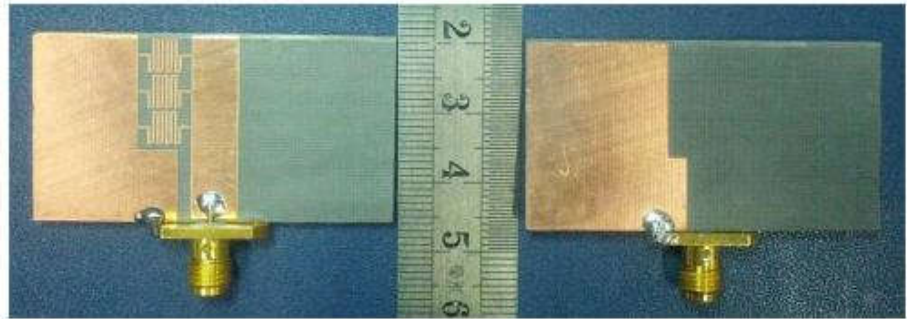


Figure 2.10. The fabricated bandwidth and efficiency enhanced antenna presented in [62].

maximum measured efficiency is 90.8%. The good efficiency and large bandwidth obtained from this antenna makes it potential for many application operating within its coverage band. The total dimensions of the antenna are  $0.173 \lambda_0 \times 0.332 \lambda_0 \times 0.011 \lambda_0$  at 1.99 GHz.

In [61], a method to extend the bandwidth of a metamaterial-inspired antenna based on CRLH transmission line theory and a modified ground plane is proposed. The ACPW antenna has a broadband characteristic by placing the ZOR, first-positive-order resonance (FPOR) of short-ended CRLH-TL and merging them with the modified ground plane's two resonances, which are half and one lambda resonances, at all different frequencies with proper frequency intervals. The configuration and photograph of the fabricated antenna are demonstrated in Figure 2.11. The measured achieved bandwidth is nearly 6.46 GHz (2.69–9.15 GHz), corresponding to a 109.1% fractional bandwidth. The measured efficiency remains above 65.91% over the band with the maximum efficiency of 94.64% occurring at 3.8 GHz.

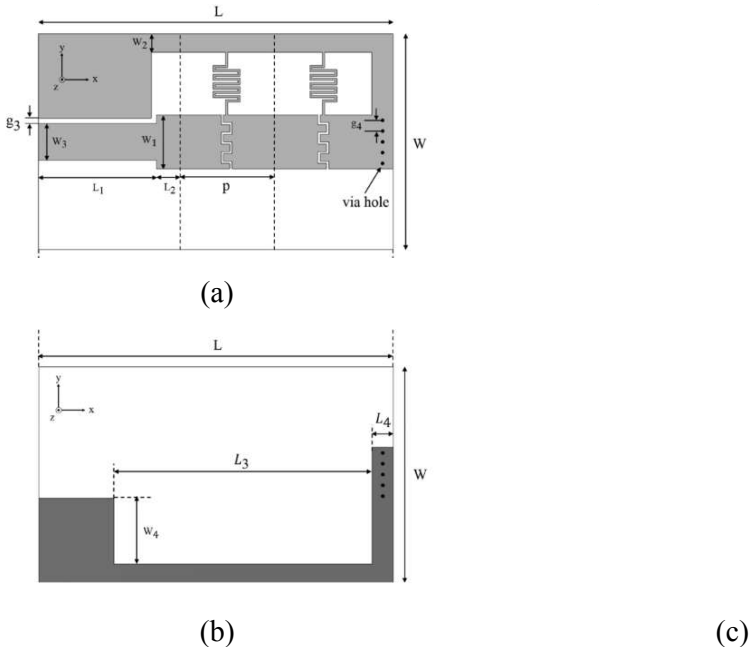


Figure 2.11. Compact and bandwidth-enhanced asymmetrical CPW-fed antenna (a) Top view geometry; (b) Bottom view geometry and (c) Photograph of fabricated antenna by Lee et al. from [61].

A summary of several recent works and their advantages are given in Table 2.1. While zeroth-order resonance have shown a great potential for the purpose of miniaturization, however, there are still some major drawbacks to be addressed such as low efficiency and narrow bandwidth. Most of these designs are narrowband and operating only in a single band. In [58], the bandwidth has been improved by 15.1%, however, such a bandwidth would not satisfy the requirement of modern communication systems. On the other hand, while the antennas presented in [61] and [62] exhibit decent bandwidth performance by merging different resonances, both structures are restricted with the resonances that are highly dependent on the physical dimensions of the main structure. Hence, achieving the additional resonances from an external element would allow for an additional degree of freedom without any

Table 2.1. A summary of some recent works available in the literature.

Ref.	F.B.W (%)	Antenna electrical size ( $\lambda_0$ )	ZOR freq. (GHz)	Gain @ ZOR	Eff. @ ZOR	Antenna Features
[89]	0.002	$0.16 \times 0.16$	4.88	N.A	N.A	75% of size miniaturization
[57]	3.1	$0.25 \times 0.14$	3.3	0.79	65.8	Miniaturization and efficiency improvement
[90]	< 1	Square patches N.A	4.94	0.08	45.6	Slot loading efficiency enhancement
	< 1	Hexagonal patches N.A	4.32	-3.39	27.4	
[54]	1	$0.218 \times 0.082$	2.42	-0.53	53	Miniaturization using novel unit cell
[91]	4.3	$0.2 \times 0.14$	2.3	2.3	79	Miniaturization and efficiency enhancement
[58]	15.1	$0.14 \times 0.22$	2.16	1.62	72	Bandwidth enhancement, Simple implementation
[62]	67.4	$0.33 \times 0.172$	1.99	2.2	90.08	Bandwidth and efficiency

						enhancement using ENG-TL
[61]	109.1	$0.41 \times 0.25$	2.9	2.59	86.2	Bandwidth and efficiency enhancement
This work	87.1	$0.30 \times 0.24$	1.84	2.1	91.6	Bandwidth and efficiency enhancement, Miniaturization

N.A: Not available.

F.B.W: Fractional bandwidth.

considerable impact on the operation of the main design.

## 2.4 Literature Review of Recent Rectennas

Nowadays, with the drop on the circuit sizes, low fabrication costs and reduced power requirements of modern electronics, wireless power transmission and energy harvesting systems have become a hot field of interest. The research is ongoing with main concentration on the performance improvement of rectennas. The two vital parts of energy harvesters are antennas and RF-to-DC rectification circuits that work interactively for the optimum overall efficiency of the energy harvesting system.

A general block diagram of an energy harvesting for empowering low power sensors is demonstrated in Figure 2.12. Reviewing recent literature on the subject, various antennas such as monopole [77], dipole antennas [69, 74, 92-94], linearly polarized (LP) antennas [28, 32, 34, 35, 39, 43, 71, 74, 77, 78, 92, 95], dual-linearly polarized (DLP) [25, 31, 72], circularly polarized (CP) [30, 33, 66, 73] and also dual circularly polarized (DCP) [24, 26, 38] have been utilized. Each of these works adopted different rectifier topologies aiming to improve the overall system efficiency.

In [34], a rectenna using conventional rectangular patch antenna was incorporated with a modified bridge rectifier. The advantage of this work was the elimination of harmonic and bypass filters owing to RF symmetry of the rectifier structure. The entire rectenna was printed on Rogers Duroid 5880 substrate ( $\epsilon_r = 2.2$ , thickness = 1.575 mm and  $\tan \delta = 0.0009$ ). However, the measured rectenna efficiencies is 52% at

relatively high power density of  $150 \mu\text{W}/\text{cm}^2$  which is due to the use of bridge topology where four diodes are operating simultaneously increasing the rectification loss.

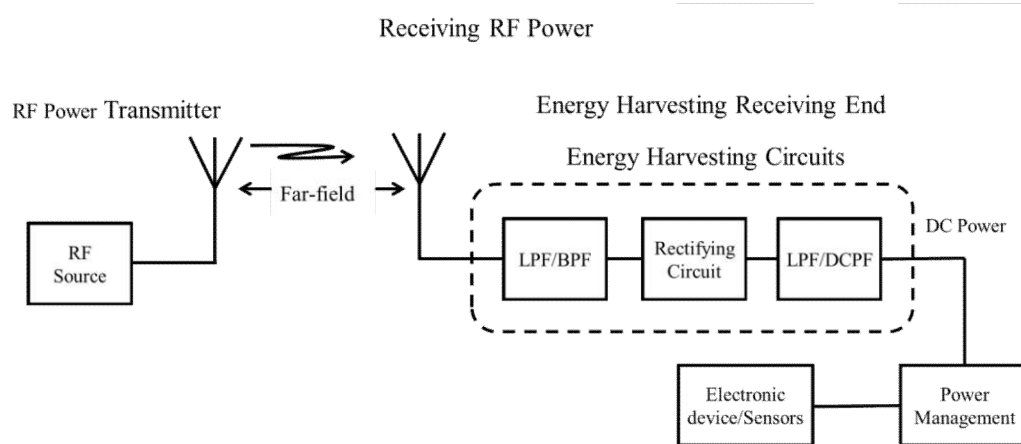


Figure 2.12. General block diagram of an energy harvesting for powering low power sensors.

#### 2.4.1 Stacked Rectenna for Low Power Application

A compact rectenna structure using stacked layer was investigated in [23]. The rectenna designed to operate at the frequency of 2.45 GHz with a series diode rectifier circuit at the back side of antenna in which both antenna and rectifier share the same ground plane as shown in Figure 2.13. The analytical model was used to provide the matching condition to the rectification circuit. The radial stubs were used to terminate the generated harmonics and a shorted stub to provide the DC loop. The design is fabricated on low-cost FR4 laminate and a RF-to-DC efficiency of 52% at 0 dBm is reported.

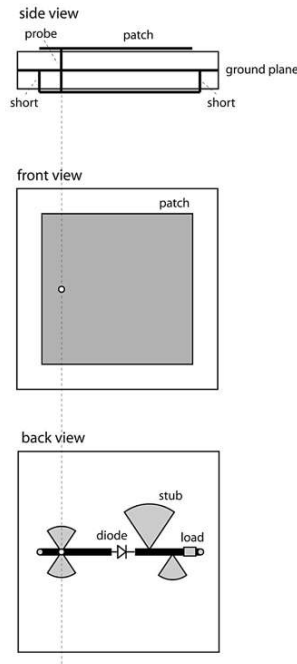


Figure 2.13. Configuration of the stacked rectenna designed by Akkermans et al. [23].

#### 2.4.2 Decoupled Dual-dipole Rectennas for Wireless Battery Charging

Antenna decoupling or isolation is commonly adopted to reduce the spacing between antennas in array structures. The authors in [94] proposed a decoupled dual-dipole rectenna aiming to achieve a rectenna with a small form factor as shown in Figure 2.14. The final structure is printed on 20-mil thick Rogers RT/duroid 5880 with dielectric constant of  $\epsilon_r = 2.2$ , resulting in overall footprint of  $62.5 \times 55 \text{ mm}^2$  which is 37% smaller than two standard patch antennas located on the same substrate without a decoupling structure. A Villard voltage doubler rectifier is incorporated to charge a standard 4.8 V NiMH battery to 5.1 V. It is reported that this rectenna could fully charge the battery in 5 hours over a distance of 23 cm.

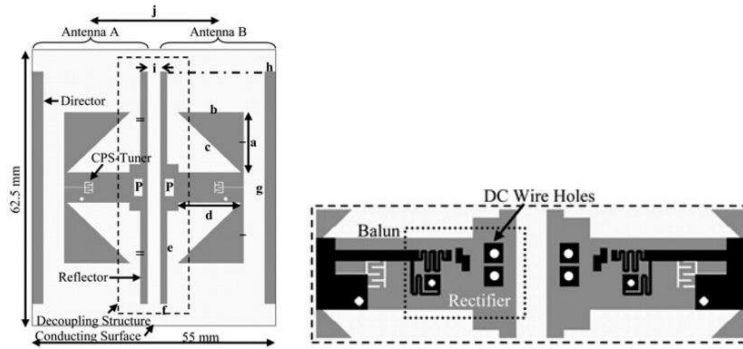


Figure 2.14. Decoupled Dual-dipole Rectennas layout presented in [94].

### 2.4.3 Compact Fractal Loop Rectenna

Employing fractal antennas is an interesting approach to realize a compact rectennas. This method employs an iterative transformation effected on the segments of some simple starting shape which can result in more efficient use of space and larger antenna electrical size. In [41], a Koch fractal loop antenna was proposed with an in-loop ground plane to facilitate the antenna impedance matching at GSM1800 frequency band. The rectifier circuit is a two-stage full-wave Greinacher circuit with two  $90^\circ$  radial stub employed to block the second harmonic at the output and an open stub at the input terminating third harmonic as shown in Figure 2.15. An efficiency of 61% and an output DC voltage of 1.8 V over  $12 \text{ k}\Omega$  resistor for  $10 \mu\text{W}/\text{cm}^2$  power density has been achieved. It is reported that the rectenna is capable of powering up a battery-less LCD watch at a distance of 10 m from the cell tower.

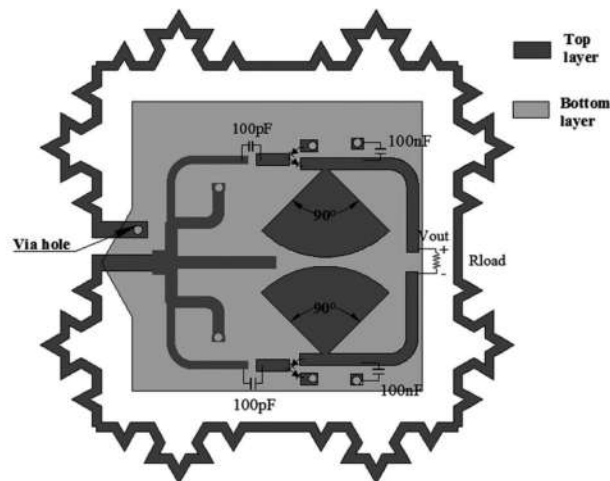


Figure 2.15. Compact fractal loop antenna by Zeng et al. [41]

#### 2.4.4 Circularly Polarized Shorted Ring-Slot Rectenna

The authors in [33] presented an efficient rectenna based on a printed shorted annular ring-slot antenna with circular polarization properties operating at 2.45 GHz. The layout of the designed rectifier is shown in Figure 2.16. In order to have compact size, the rectifier part is placed at the back side of the antenna configuration. The antenna has a 3-dB axial ratio (AR) bandwidth of 200 MHz and a maximum gain of 4.7 dBi. Furthermore, the input filter is avoided by providing the mismatch condition at the harmonic frequencies (i.e. 4.9 and 7.35 GHz), thus preventing harmonics re-radiation. In order to increase the antenna and rectifier coupling level, the microstrip lengths ( $L_5$  and  $L_6$ ) is adjusted and a quarter wavelength long radial stub is also utilized to suppress the second harmonic generated from the series diode. The overall dimensions are  $95 \times 95 \times 1.5 \text{ mm}^3$ . For an optimized load of  $2.5 \text{ k}\Omega$ , a maximum voltage of 1.1 V corresponding to efficiency of 69% at the power density of  $20 \text{ mW/cm}^2$  is reported.

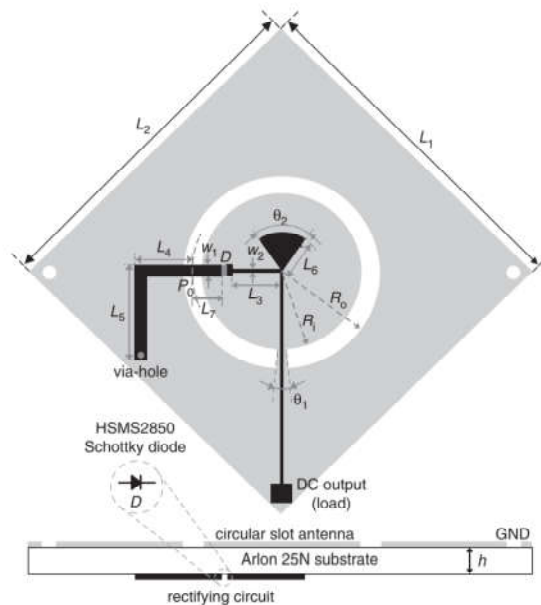


Figure 2.16. Circularly polarised shorted ring-slot rectenna [33].

#### 2.4.5 Rectennas with All Polarization Reception Properties

Aiming to collect incident waves from any arbitrary polarization, several rectennas with DCP [24, 26, 38], DLP [25, 31, 67, 68] as well as monopole [77] rectennas have also been proposed. For example, authors in [24] proposed a rectenna with all

polarization reception property. The configuration of the rectenna is shown in Figure 2.17. The rectenna consists of two different layers; a radiating square patch at the top layer, and system ground plane placed at the optimized distance with the rectifier circuit being at the back side of ground layer. The antenna itself is a dual-circularly polarized achieving its circular polarization from T-shape slot etched on the ground layer with a bandwidth of approximately 100 MHz. Since the harmonic generation of the diode can be a major source of loss, the second harmonic noise is reflected when feeding into the T-shape slot as it fails to create a current resonance around the slot. In addition, by embedding a U-shape resonator within the T-shape slot the third harmonic is blocked. Such a structure can receive waves in all polarizations while occupying an area of  $100 \times 100 \times 3.8 \text{ mm}^3$ . This rectenna is capable of providing up to 11.42 V at an input power level of 22 dBm where the efficiency reaches up to 82.3%.

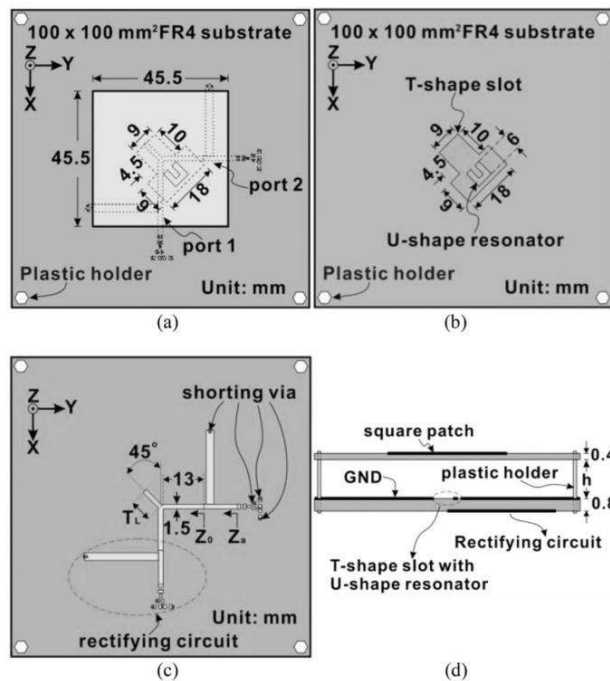


Figure 2.17. Circularly polarized all polarization receiving rectenna with harmonic rejection property [24].

Furthermore, in [31] a dual linearly-polarized rectenna is presented where the 3-dB polarization mismatch of CP rectenna was avoided. The rectenna structure is shown in Figure 2.18.

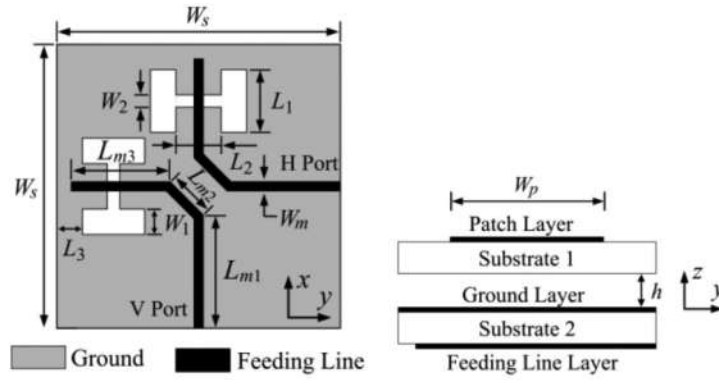


Figure 2.18. Rectenna with all-polarization-receiving capability[31].

The antenna part is an aperture coupled structure where the radiating patch and feeding layer are properly spaced for the optimum performance. Both substrates are 20-mil-thick Rogers RO4350B substrates with substrate dielectric and loss tangent of 3.38 and 0.0031, respectively. The feeding line layer is placed on the backside of the second substrate, while the ground layer is inserted in between the two substrates. The overall bandwidth of approximately 100 MHz and a gain of about 7.54 dBi is obtained. A dual shunt rectifier circuit is utilized to combine the output power from each feeding structure as shown in Figure 2.19.

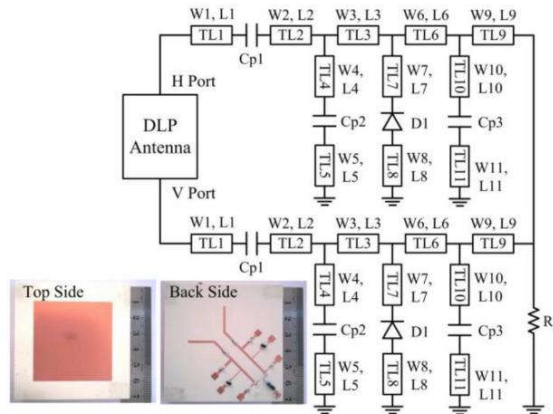


Figure 2.19. The photograph of fabricated rectenna and its dual shunt rectifier circuit employed in [31].

The overall structure occupies an area of  $70 \times 70 \times 5 \text{ mm}^2$  where an efficiency of 78% at the power density of  $295.3 \mu\text{W} / \text{cm}^2$  has been obtained.

## 2.4.6 Broadband and Multiband Rectennas

Another approach for the design of energy harvesters is to take advantage from multiple source of power spread in various frequency channels. Since the power available in a single band may not be adequate or inconsistent within a period of time, employing a multiband or broadband rectenna can be beneficial to improve the performance and reliability of the system. Following this concept, the authors in [74] proposed a compact wireless energy harvester that is able to harvest power from a 915 MHz and a 2.45 GHz ISM bands.

The rectenna is composed of a slot-loaded dual-band folded dipole antenna fabricated on Arlon 25N substrate that has relative permittivity of 3.38 and loss tangent of 0.0025. The dual band characteristic is provided from a semi-planar half-wave folded dipole operating at the 915 MHz and an etched slot at the center of the antenna introducing the resonance at 2.45 GHz as shown in Figure 2.20. The final size of fabricated rectenna is  $60 \times 60 \times 60 \text{ mm}^3$  where the measured antenna gains are 1.87 and 4.18 dBi at 915 MHz and 2.45 GHz, respectively. The evaluated RF-to-DC conversion efficiency at the power density of  $1 \mu\text{W} / \text{cm}^2$  are 37% and 20% at 915 MHz and 2.45 GHz, respectively.

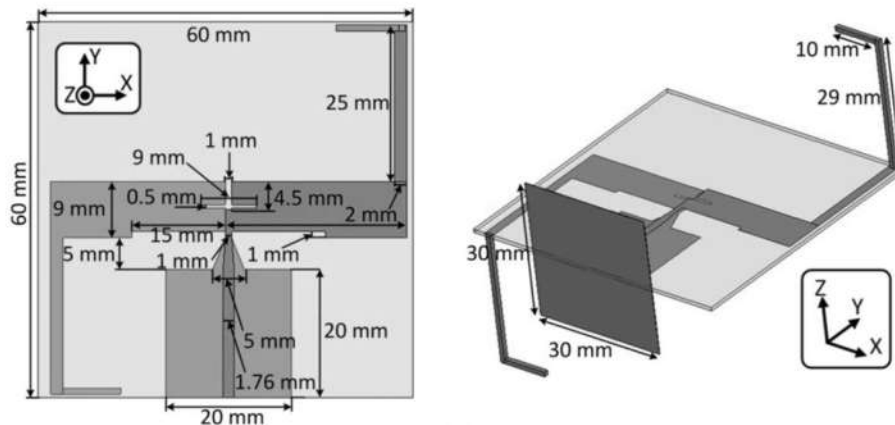


Figure 2.20. Dual band energy harvester proposed in [74].

A dual-port triple-band L-probe microstrip patch rectenna design for ambient RF energy harvesting at GSM-900, GSM-1800, and UMTS-2100 bands is proposed in [96]. The antenna used for this work consists of two single-port L-probe patch antennas

stacked back to back with adjacent grounds as shown in Figure 2.21(a). By tuning the gap between the each radiating patch and ground plane the bandwidth has been optimized resulting on a total antenna dimensions of  $200 \times 175 \times 49.4 \text{ mm}^3$ . The antenna is printed on Rogers 3003 material with dielectric constant of 3. Moreover, in order to achieve the triple band operation at the low power level, a single series rectifier with a matching network comprised of triple stub tuning and an 18 nH SMD inductor have been utilized as shown in Figure 2.21 (b). The overall size of the rectifier circuit is nearly  $84 \times 35 \text{ mm}^2$  printed on a 62-mil-thick RT/Duroid 5880.

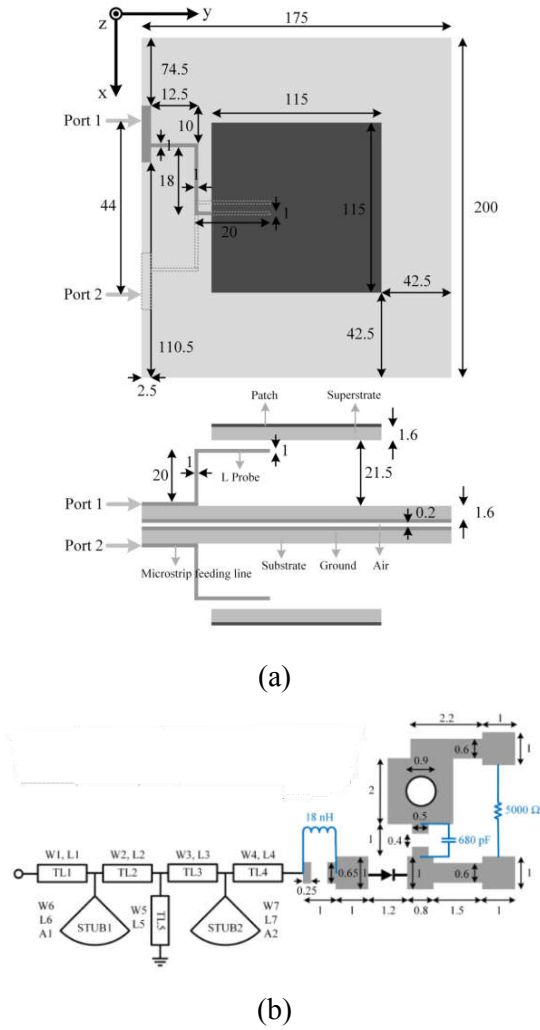


Figure 2.21. (a) the configuration of the dual port stacked antenna and (b) the rectifier topology employed in [96].

The authors have evaluated the performance of resultant rectenna under three-tone condition demonstrating the advantage of multi-band rectennas. Using DC power combining, an efficiency of greater than 40% and an output voltage of greater than 600 mV (over a load of 5 k $\Omega$ ) when the power density is more than 500  $\mu W / m^2$  is reported.

**2.4.7 Array Configuration for Energy Harvester**

Array configuration has also been used for the purpose of energy harvesting. For example in [39], a dual frequency energy harvester using 1  $\times$  4 quasi-Yagi array was presented for the ambient RF harvesting at GSM-1800 and UMTS-2100 bands. The antenna array is printed on 62-mil-thick RT/Duroid 5870 substrate with a dielectric constant of 2.33 where the gains of 10.9 and 13.3 dBi at the frequencies of 1.85 and 2.15 GHz have been obtained. A dual band rectifier using dual stub matching network and a stepped impedance microstrip low pass filter was constructed. The photograph of constructed antenna array and rectifier are presented in Figure 2.22.

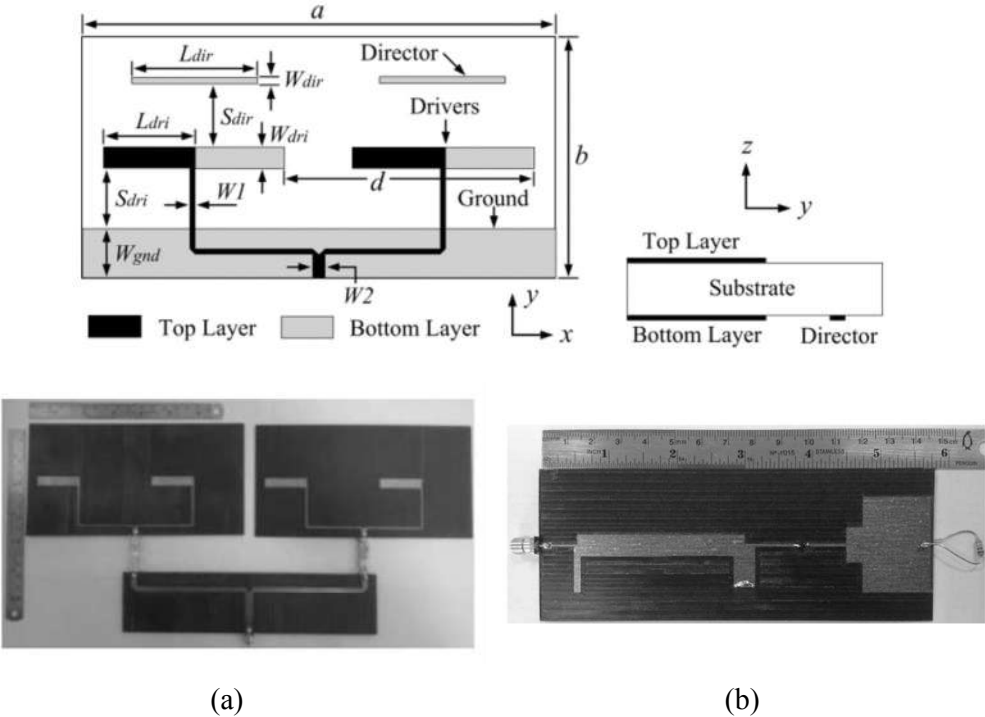


Figure 2.22. (a) The configuration of quasi-Yagi array rectenna and (b) dual band rectifier from [39].

The rectenna's capability of recycling ambient RF power has been tested on the rooftop at a direct line of sight. The output dc voltage was measured to vary between 300 to 400 mV most of the time, and it could also reach more than 400 mV sometimes due to the variation of ambient. The corresponding efficiency of this dual-band rectenna is estimated to be above 16.6–43%. Measurement results show that a power conversion efficiency of 40% and an output DC voltage of 224 mV have been achieved over a 5 k $\Omega$  resistor when the dual-tone input power density is 455  $\mu W / m^2$ . Although the overall dimensions of this rectenna is not given at the paper, but, the dimensions of each 1  $\times$  2 quasi-Yagi array is about 190  $\times$  100 mm<sup>2</sup> which can result in a total length of approximately half a meter when it is in 1  $\times$  4 array form which is unfavorably huge.

To accommodate for the narrow beamwidth characteristic of conventional antenna arrays a technique was introduced in [32] where two axillary antennas were placed at a certain angle and distance from 1  $\times$  4 patch antenna array resulting in a beamwidth twice than that of antenna array with uniform excitation distribution as shown in Figure 2.23.

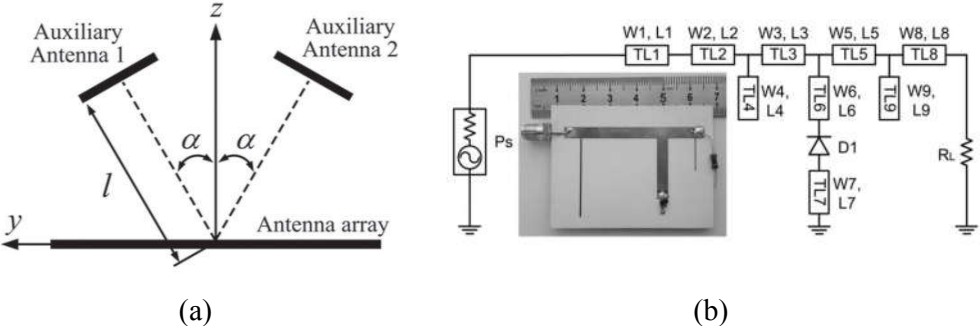


Figure 2.23. Beamwidth-enhanced rectenna (a) antenna array structure with two axillary antenna for beamwidth enhancement (b) single shunt rectifier proposed by Sun et al. in [32].

For the measurement a single shunt rectifier is connected to the new beamwidth-enhanced antenna resulting in efficiency higher than 50% when the wave incident angle is between  $-38^\circ$  and  $35^\circ$  at the H-plane under the power density of 1276  $\mu W / cm^2$ .

In [16], an array of 64 printed spiral antenna elements is proposed in which each antenna element is directly connected to a Schottky diode keeping the non-directive characteristic of spiral antennas. The configuration of the rectenna array is demonstrated in Figure 2.24. This experiment was done over the frequency range of 2-18 GHz. The series and parallel connections made between the properly oriented array elements allows for a flat response from both left-hand circularly polarized (LHCP) and right-hand circularly polarized (RHCP) illuminations at the cost of 3-dB loss for every possible polarization scenarios. The authors also examined different DC combinations and the best performance obtained when all 4-element sub-arrays were connected in parallel resulting in an overall efficiency of 20% at the power density of  $63 \mu W / cm^2$ . The footprint of this rectenna array is  $185 \times 185 mm^2$ .

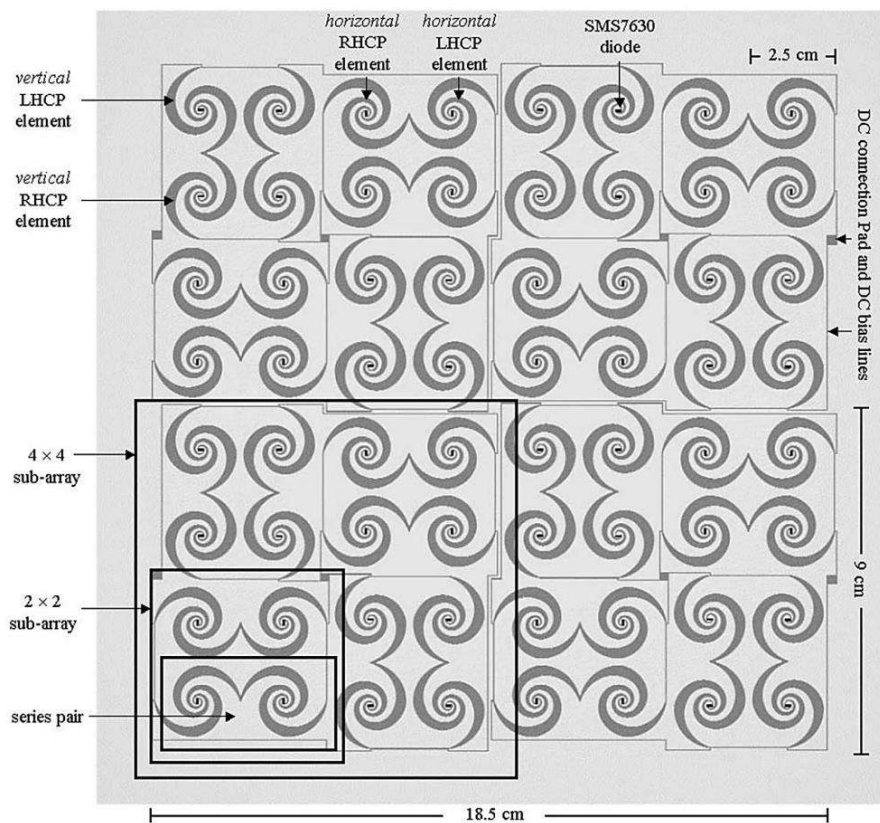


Figure 2.24. Rectenna array of 64 elements presented in [16].

### 2.4.8 Broadband Bent Triangular Omnidirectional

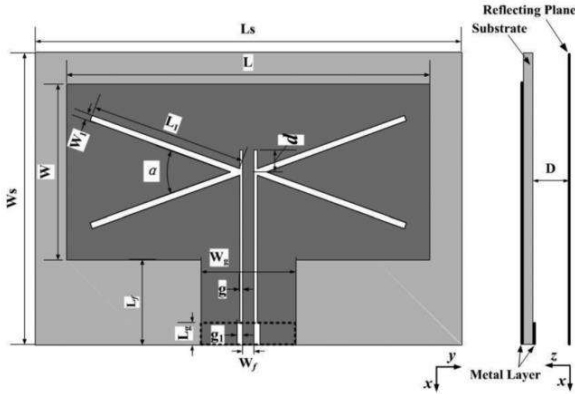
A broadband bent triangular monopole antenna has been proposed in [77] to receive both horizontal and vertical polarized waves from a single port. The antenna has a stable radiation pattern over a decent impedance bandwidth of 1.09 GHz from 850 MHz to 1.94 GHz. For the process of rectification, a simple voltage doubler charge pump is used where the input impedance of antenna and rectifier is optimized to be  $100 \Omega$  for the best possible performance eliminating the use of matching network. The structure of the rectenna and photograph of fabricated prototype are shown in Figure 2.25. Nevertheless, relatively poor peak efficiency of 60% and 17% is obtained for a load of  $500 \Omega$  at 980 and 1800 MHz when the power reception is nearly 7.2 dBm. Furthermore, the authors employed an array of two elements where a voltage of 3.76 V for open circuit and 1.38 V across a 4.3 K $\Omega$  load at a distance of 25 m from a cell site is reported.



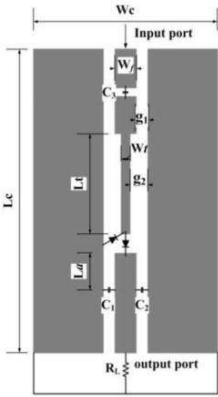
Figure 2.25. Broadband bent triangular monopole presented in [77].

A rectenna operating at 2.45 GHz using grounded coplanar waveguide (GCPW) is proposed in [78]. Such a structure has the advantage of wide bandwidth and simple integration of impedance matching network. The rectenna is composed of a CPW-fed antenna backed by a metallic reflector forming a GCPW structure with unidirectional radiation pattern, impedance bandwidth of 600 MHz (2-2.6 GHz) and average gain of 10 dBi. A simple rectifier circuit comprised of a capacitor, a series pair Schottky diode model HSMS-2862, a dc-pass filter and a resistive load as shown in Figure 2.26. A pair of capacitors,  $C_1$  and  $C_2$ , is shunted across the GCPW line to act as the dc-pass

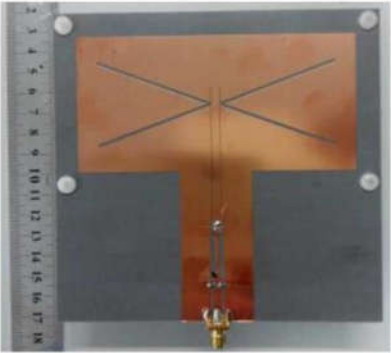
filter and the capacitor  $C_3$  is used to prevent the direct current path from being short-circuited. The rectifier design takes advantage from the natural impedance characteristics of diode pairs. The efficiency remains above 50% over the range of 2.2 to 2.6 GHz for the received power level of 13 dBm (20 mW). The overall structure dimensions are  $150 \times 135 \times 22 \text{ mm}^3$  where a maximum efficiency of 72.8% at the power level of 18 dBm is reported.



(a)



(b)



(c)

Figure 2.26. The configuration of broadband GCPW rectenna presented in [78], (a) antenna structure; (b) rectifier circuit and (c) photograph of the fabricated prototype.

## 2.5 Literature Review Summary

Generally, the antenna element of a rectenna is application specific, which can be directional or omnidirectional antenna, with either linear or circular polarization [94]. Different approaches have been pursued aiming to improve the performance of rectennas based on sense of polarization, gain improvement using array configuration, employing dual-/multi-band rectennas as well as broadband rectennas. An overview and a summary of current works available in the literature are presented in Table 2.2 and Table 2.3, respectively.

Table 2.2. Overview of integrated rectifier antennas and rectifiers described in the literature.

Ref.	f (GHz)	Bandwidth	$P_{RF,in}$ , $\mu W/cm^2$	Antenna Conf.	Rectifier Topology	PCE (%)
[23]	2.45	< 100 MHz	53.2	Stacked Rectangular	Single series	52%
[41]	1.85	100 MHz	10	Fractal loop	Dual-stage Voltage doubler	61%
[33]	2.45	NA	20E3	Shorted-slot (CP)	Single series	69%
[24]	2.45	100 MHz	158 mW	Aperture Coupled (DCP)	2 × Voltage doubler	82.3%.
[31]	2.45	100 MHz	295.3	Aperture Coupled (DLP)	2 × shunt rectifier with common output	78%
[77]	0.98 & 1.8	1090 MHz (850-1940)	5.2 mW	Bent- Triangle monopole	Voltage doubler	60 & 17%
[74]	Dual-band	45 & 150 MHz	1	slot-loaded dual-band	Single series	37 & 20%

	0.915 & 2.45			folded dipole		
[96]	Triple- band GSM-900, GSM- 1800, and UMTS- 2100	< 100 at each band	5E-2	dual-port triple-band L-probe microstrip patch	Single series DC - combined	40% (three- tone)
[39]	Dual-band GSM- 1800, and UMTS- 2100	Narrowband Covers the bands	45E-3	1 × 4 quasi- Yagi array	Single series	16.6%– 43% (two- tone)
[32]	5.8	NA	1276	1 × 4 Beamwidth- enhanced	Single shunt	50%
[78]	Broadband 2.45	400 MHz (2.2-2.6)	20 mW	GCPW	Voltage doubler	50%
[38]	Broadband 2-18	2-18	62	Printed spiral array	Single series (direct connection)	20%
[79]	Broadband	1.24-2.14	16 mW	NA (R.O)	Distributed Single shunt	< 60%
[80]	Ultra- Wideband	0.04-4.74	200 nW	NA (R.O)	Inductive loaded Single shunt	< 40%
[81]	Broadband	0.78-1.43	25 mW	NA (R.O)	Single Shunt	< 50%

This work	2.45	270 MHz (2.3-2.57)	1	(R.O)	Voltage doubler	61.9%
	Broadband	1.85-2.6	3	(R.O)	Voltage doubler	70.3%
	2.45	270 MHz (2.3-2.57)	5.28	ZOR antenna	Voltage doubler	>30% (2-15 k $\Omega$ )
	Broadband Combined	1.85-2.6	5.13	ZOR antenna	Voltage doubler	37.57% (Mono-tone at 2.15 GHz)
	Broadband Integrated		5.13	ZOR antenna (HTA)	Voltage doubler	46.9% (Mono-tone at 2.15 GHz)
			3.16			50.4% Multi-tone (three tone)

PCE: Power conversion efficiency

R.O: Rectifier only

N.A: Not available

Table 2.3. Summary of the reviewed works in the literature

Ref.	f (GHz)	Pros.	Cons.
[23]	63 × 63 × 3.2	<ul style="list-style-type: none"> <li>• Compact</li> <li>• Harmonic termination</li> </ul>	<ul style="list-style-type: none"> <li>• Narrowband</li> <li>• Unidirectional</li> <li>• Not efficient at the low power levels</li> </ul>
[41]	45 × 45 × 0.8	<ul style="list-style-type: none"> <li>• Low profile</li> <li>• High efficiency</li> </ul>	<ul style="list-style-type: none"> <li>• Narrowband</li> </ul>
[33]	95 × 95 × 1.5	<ul style="list-style-type: none"> <li>• Low profile</li> <li>• Inherent harmonic termination</li> <li>• Design simplicity</li> </ul>	<ul style="list-style-type: none"> <li>• Narrowband</li> <li>• High efficiency only at high power levels</li> </ul>
[24]	100 × 100 × 3.8	<ul style="list-style-type: none"> <li>• Dual circularly polarized</li> <li>• Inherent harmonic termination</li> </ul>	<ul style="list-style-type: none"> <li>• Narrowband</li> <li>• Unidirectional</li> <li>• suffers from 3-dB loss of received LP incidents of arbitrary polarization</li> <li>• limited axial ratio beamwidth</li> <li>• High efficiency only at high power levels</li> </ul>
[31]	70 × 70 × 5	<ul style="list-style-type: none"> <li>• Dual linearly polarized</li> <li>• much lower power loss when compared with its DCP counterpart</li> </ul>	<ul style="list-style-type: none"> <li>• Unidirectional</li> <li>• Narrowband</li> <li>• Considering the common DC output load rectifier topologies used, the loss can be significantly increased if the difference on the power received on one</li> </ul>

			polarization increases, preventing the secondary rectifier with lower received power to operate.
[77]	94×82×1.5	<ul style="list-style-type: none"> <li>• Decent omnidirectional radiation performance</li> <li>• Broadband antenna performance</li> </ul>	<ul style="list-style-type: none"> <li>• Rectifier is not optimized</li> <li>• Narrowband rectifier ( acceptable efficiency only at a single frequency band)</li> <li>• Efficient at high power levels only</li> </ul>
[74]	60×60×60	<ul style="list-style-type: none"> <li>• Dual band</li> <li>• Efficient at low power levels</li> </ul>	<ul style="list-style-type: none"> <li>• Occupies large cubic area (hard to implement)</li> <li>• Narrowband operation at each band</li> <li>• Single frequency dominance problem</li> </ul>
[96]	200×175×49.5	<ul style="list-style-type: none"> <li>• Triple band</li> <li>• Bi-directional operation</li> <li>• High gain</li> </ul>	<ul style="list-style-type: none"> <li>• Very large size</li> <li>• Arbitrary radiation properties at each frequency band</li> <li>• Not clear on the measurement</li> </ul>
[39]	N.A (190×100 for a single 1×2 element)	<ul style="list-style-type: none"> <li>• Dual band</li> <li>• High gain</li> </ul>	<ul style="list-style-type: none"> <li>• Extremely large size</li> <li>• Unidirectional</li> <li>• Narrowband band rectifier</li> </ul>
[32]	129×30×5	<ul style="list-style-type: none"> <li>• High gain</li> </ul>	<ul style="list-style-type: none"> <li>• Large size</li> </ul>

		<ul style="list-style-type: none"> <li>• Beamwidth enhanced radiation</li> </ul>	<ul style="list-style-type: none"> <li>• Unidirectional</li> <li>• Narrowband band rectifier</li> <li>• Efficient at high power levels only</li> </ul>
[78]	150×125×22	<ul style="list-style-type: none"> <li>• High gain</li> <li>• Simple structure</li> <li>• Broadband</li> </ul>	<ul style="list-style-type: none"> <li>• Unidirectional</li> <li>• Large size</li> <li>• Takes advantage from diodes natural impedance behavior which dictates the power level of operation to be 20 mW.</li> </ul>
[38]	185×185×1.57	<ul style="list-style-type: none"> <li>• Broadband</li> <li>• Flat polarization response</li> <li>• Dual circularly polarized</li> </ul>	<ul style="list-style-type: none"> <li>• Large size</li> <li>• suffers from 3-dB loss of received LP incidents of arbitrary polarization</li> <li>• No matching network</li> </ul>
[79]	35×10×0.7	<ul style="list-style-type: none"> <li>• Broadband</li> </ul>	<ul style="list-style-type: none"> <li>• Efficient only at the high power levels</li> <li>• No harmonic termination</li> <li>• Not suitable for Energy harvesting application</li> </ul>
[80]	N.A	<ul style="list-style-type: none"> <li>• Ultra-Wideband</li> </ul>	<ul style="list-style-type: none"> <li>• Efficient only at the high power levels</li> <li>• Not suitable for Energy harvesting application</li> </ul>
[81]	36×11×0.7	<ul style="list-style-type: none"> <li>• Broadband</li> </ul>	<ul style="list-style-type: none"> <li>• Efficient only at the high power levels</li> </ul>

			<ul style="list-style-type: none"> <li>• Not suitable for Energy harvesting application</li> </ul>
This Work	$53.5 \times 40.5 \times 0.508$	<ul style="list-style-type: none"> <li>• Broadband</li> <li>• Dipole-like radiation</li> <li>• Compact</li> <li>• High efficiency</li> </ul>	<ul style="list-style-type: none"> <li>• Single polarization</li> </ul>

Different approaches have been undertaken in order to overcome the low efficiency and output voltage of the rectenna systems. The antenna array configurations [32, 38, 39] have been utilized to increase the amount of captured power by enlarging the antenna aperture. Nonetheless, the large size of the structure significantly limits their application where energy harvesting system is meant to be a replacement for the small size batteries. As an example, although the exact footprint of the  $1 \times 4$  quasi-Yagi array in [39] has not given in the paper, however, from the individual dimensions given, its length is approximately 1 meter. The rectenna presented in [23], presents an efficiency of 52% at relatively high power density level of  $53.2 \mu W / cm^2$ .

Furthermore, the CP and DCP antennas [24, 33, 38] where used to mitigate the orientation problem of rectennas. However, even a DCP antenna not only suffers from 3-dB loss of received LP incidents of arbitrary polarization but also the CP performance is only attained within the limited axial ratio beamwidth characteristics of the antenna. On the other hand, DLP antenna presented in [31] can receive any waves of arbitrary polarization at a much lower power loss when compared with its DCP counterpart. However, the signal reception is restricted within certain angle limits due to its directional nature. This is the main reason that directional antennas are not used in any portable and handheld devices i.e. cell phones, lap-top computers as well as Wi-Fi routers.

Generally speaking, in ambient RF energy harvesting, due to uncertainty of the receiving signal direction, an omnidirectional antenna would be a more desirable choice [77]. Hence, a triangular bent rectenna has been presented in [77], which demonstrates broadband antenna performance with omnidirectional radiation pattern.

However, the rectenna efficiency is only acceptable at a single frequency of 1.8 GHz and considerably drops as low as 17% at the lower band (915 MHz) when the input power is 5.2 mW. This is caused by alternating input impedance of the complex antenna structure that pushes the rectenna system largely out of tune. The rectenna presented in [41] exhibits decent sensitivity of 61% when the power density is just  $10 \mu\text{W} / \text{cm}^2$  with a dipole-like radiation properties. However, the presented antenna and rectifier designs are both suffering from narrow bandwidth operation of nearly 100 MHz only. While the dual band rectenna presented in [74] presents a good efficiency at low power density levels, however it requires a cubic space area of  $60 \times 60 \times 60 \text{ mm}^3$  and the bandwidth at the lower band is as narrow as 45 MHz only. It is important to notice that, since the design of these rectennas is performed under some predefined power and load conditions, even slight deviation on output load values can downgrade the performance in some bands due to sensitive non-linear behavior of diode at different frequencies. In the reality, this can be a serious issue as the rectenna requires to maintain the high performance over large range of power and against various external circuitries with different/alternating impedance characteristics.

Furthermore, in order to increase the reliability of the energy harvesting system, the broadband rectifiers are highly needed for the energy harvesting application as the available power is spread over a large span of spectrum. By harvesting power over a large frequency band, higher amount of power can be scavenged leading to a higher resultant output voltage. Unfortunately there are only a few broadband rectennas/rectifiers available in the literature [38, 78-81] where most of them operate at high power levels (i.e. 20-100 mW). For instance, the rectenna presented in [78] takes advantage from diodes natural impedance behavior which dictates the power level of operation to be 20 mW. Moreover, the rectenna loses its orientation independency due to its high gain unidirectional characteristic implied by GCPW structure. In [38], a single diode has been connected in series with the spiral antenna structure without any consideration on the matching network and harmonic impacts.

The focus of previous efforts have mostly been on the RF to DC conversion efficiency improvement. No special attention have been paid for the simultaneous achievement of system reliability, overall sensitivity and dimensions which are crucial requirements

of energy harvesting systems. On the next chapter, the rectenna components will be presented and discussed in details that are essential to the context of energy harvesting systems.

## CHAPTER 3

### RESEARCH METHODOLOGY

#### 3.1 Introduction

Semiconductor devices are the vital and inseparable part of modern electronics. The importance of semiconductor devices lie in their instant change on optical and conducting properties allowing for the realization of core component electronics in a compact size and affordable price. In most cases this is done through the use of junctions between dissimilar materials. Junctions can form between n-type materials, in which the electrons are the majority carriers and holes are the minority carriers. In contrast, for p-type materials, the holes are the majority carriers and electrons are the minority carriers.

The p-n junction is of paramount importance in solid-state electronics. The p-n junction is the essential part of the bipolar transistors that can provide non-linear behavior of the device. This non-linearity is a key factor for the design of some applications such as rectifiers, detectors and amplifiers.

#### 3.2 Schottky Diode Characteristics

Different from p-n junctions that have a bipolar characteristic, Schottky-barrier diodes achieve their non-linear behavior from metal-semiconductor junction resulting in unipolar characteristic. Figure 3.1 shows the commonly used semiconductor junctions in diodes. However, for a p-n device, the current is controlled by the diffusion current of minority carriers that is highly temperature sensitive. Both the p-n diode and the Schottky diode can be used for rectification and non-linear I-V response.

The Schottky diode junction is made by plating highly pure metal by evaporation or sputtering under the vacuum on a doped semiconductor layer commonly referred as wafer. The doped semiconductor is made by introducing either n-type or p-type dopant atoms to the semiconductor forming n-type or p-type wafer, respectively. Once the contact between metal and semiconductor is made and the temperature between the materials becomes equal (known as temperature equilibrium condition) their Fermi

level become equal. This band diagrams are explained more in details in [97]. Under this condition, the electrons flow from semiconductor into the metal at the contact surface until the electron movement is blocked due to change on the energy levels between semiconductor and metal that is known as Schottky barrier.

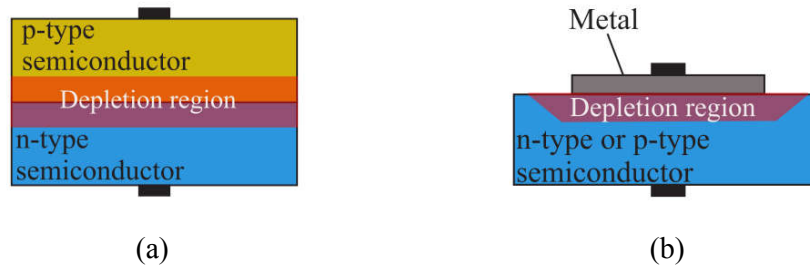


Figure 3.1. Common semiconductor junction types (a) p-n diode and (b) metal-semiconductor junction used in Schottky diodes.

When a voltage of similar polarity is applied to the diode, the energy level is increased and the electrons that happen to have much larger thermal energy than the average energy level, also known as “hot electrons”, escape and create forward current from semiconductor into the metal. Since in the case of metal-semiconductor, there is no recombination occurring at the depletion region (the basis principal of p-n junction operation), within the region where metal-semiconductor contact is made, the forward current stops in a matter of picosecond as the forward voltage is dropped [98]. This unique characteristic of Schottky diodes is vital for a system operating at a very high frequency which makes them superior choice when compared to the junction diodes.

On the other hand, unlike the p-n junction diodes that have a fixed barrier height, Schottky barrier height can be adjusted to achieve a considerably lower barrier height. For a Schottky diode with a low barrier height a much lower forward voltage is needed for a given current that is critical for the sensitive rectification process of energy harvesting systems at low power levels. As a consequence, while a p-n diode requires a minimum voltage of 0.7 V to turn on, the voltage requirement of a low barrier Schottky diode is somewhere around 0.3 V (i.e., the current is  $\sim 1$  mA) which is quite low. A comparison between p-n and Schottky diode characteristics is provided in Table 3.1.

Table 3.1. A comparison between p-n and Schottky diode characteristics.

p-n diodes	Schottky diodes
Recombination occurs at the depletion region (Ideality factor ranging from 1.2 to 2)	No recombination in the depletion region (ideality factor close to 1)
Low switching speed due to minority injection recombination/elimination	Switching speed is extremely fast in the range of nanoseconds
Requires external bias to make the device conducting (i.e. Bipolar transistors)	Design controllable low barrier height (i.e. Zero bias schottky diodes)
Forward current from minority carriers	Forward current from majority carriers
Highly sensitive to the temperature	Low sensitivity to the temperature
Easily adoptable into integrated circuit components	Difficult to implement into integrated circuits due to stringent manufacturing requirements

### 3.2.1 Schottky Diode Circuit Model

The cross section view of a typical Schottky diode is shown in Figure 3.2. As is observed, there are two layers of semiconductors in which, the base layer (substrate layer) is typically made from lightly doped semiconductor necessary for Schottky diode operation. Since the substrate layer normally possesses weak conduction properties, a second layer of highly doped semiconductor (epitaxial layer) is raised on top of substrate layer to accommodate for increased conduction with cathode. The impact of each of these layers including the metal-semiconductor contacts on the diode performance can be viewed in the form of an equivalent circuit model as shown in Figure 3.3. It consists of a non-linear resistor  $R_j$  and a non-linear capacitor  $C_j$  in parallel, representing the rectifying metal-semiconductor junction, along with a series resistor  $R_s$ . There are also an inductance  $L_p$  and capacitance  $C_p$  that represent the

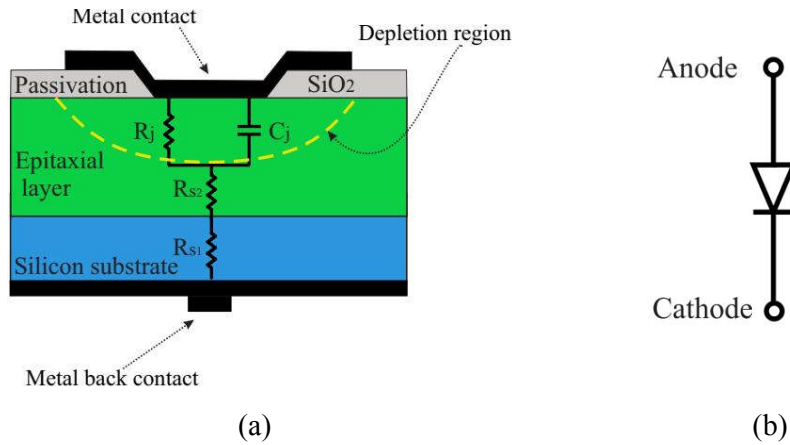


Figure 3.2. (a) Cross section view of a schottky diode, (b) graphical symbol of a diode.

parasitic components of the diode model including the packaging and inevitable fabrication parasitics such as capacitance resulted from extending of metal plate over the passivation layer. However, the parasitic component of the diode have constant values and can be easily absorbed by a properly designed matching network without having any significant impact on the circuit performance.

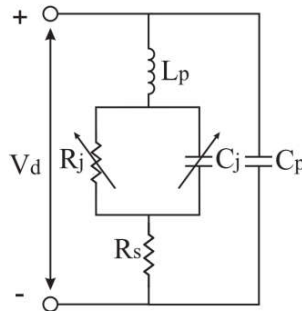


Figure 3.3. Equivalent circuit model of a Schottky diode.

### 3.2.2 Current versus Voltage Relation

The current versus voltage relationship of a Schottky diode is described following the Richardson equation as [97]

$$i_d = I_s \left( e^{\frac{qv}{n_k T}} - 1 \right) \tag{Equation (3.1)}$$

where  $I_s$  is the saturation current;  $q$  is the electronic charge and is equal to  $1.6 \times 10^{-16}$  Coulomb;  $n_i$  is the ideality factor/emission coefficient ranging between 1 to 2 (an ideal diode has an ideality factor of unity), and  $T$  is the absolute temperature in Kelvins. The saturation current can be calculated as [99]

$$I_s = UU^*T^2 e^{-\frac{q\Phi_B}{kT}} \quad \text{Equation (3.2)}$$

where  $U$  is the contact junction area;  $U^*$  is the modified Richardson constant (determined by dopant and material of diode) and  $\Phi_B$  is the barrier height in volt. The barrier height can be empirically determined by fitting the measured I-V curve of the diode into Richardson equation.

### 3.2.3 Diode Series Resistance ( $R_s$ )

The series resistance of the diode  $R_s$  is the result of several resistances including intrinsic resistance of substrate, epitaxial layers as well as the ohmic resistivity of the metal contacts. Although  $R_s$  exhibits non-linear behavior following the power change on the circuit, however, it is considered as a linear component due to its low variation under the forward condition [99]. It is generally preferred to have a low value of  $R_s$  since the signal power passing through the diode is dissipated as of heat and negatively impacts the circuit output.

### 3.2.4 Diode Junction Capacitance ( $C_j$ )

In order to have a realistic Schottky diode model, the I-V characteristic of the diode model HSMS2850 is presented in Figure 3.4. This data is obtained by using the vendor model from the ADS library under the DC condition. The equivalent model diode used here is the same as the one given in Figure 3.3, where the parasitic components ( $L_p$  and  $C_p$ ) have been neglected. Referring to Figure 3.3, one can find that the junction potential of the diode is the result of parallel combination of junction resistance  $R_j$

and junction capacitance  $C_j$  giving raise to the nonlinearity of the diode. The diode junction resistance as a function of voltage is presented in Figure 3.5.

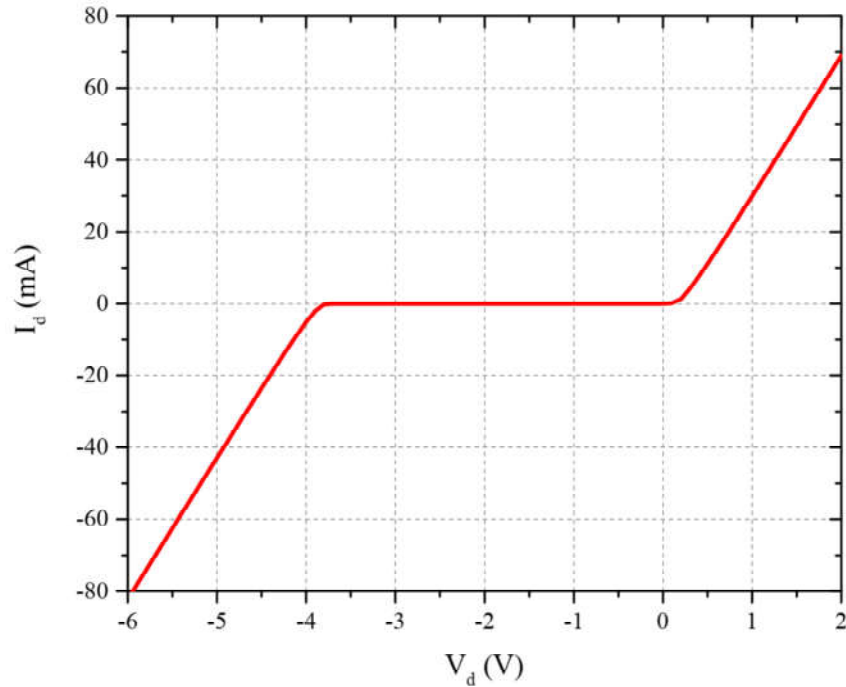


Figure 3.4. Simulated I-V curve of diode model HSMS2850 extracted from vendor model in Advanced Design System (ADS) components library.

Generally, the depletion capacitance of the junction is caused by the junction potential barrier [100]. As the diode's bias voltage is altered to reverse bias, both electrons and holes are dragged away from the barrier region resulting on the change on charge quantity and barrier width. This change on the width and concentration of the electrons and holes on each sides of the region is similar to the voltage controlled distance of parallel plate capacitors [101], where the value of the capacitance can be evaluated as

$$C = \frac{\epsilon A_u}{d} \quad \text{Equation (3.3)}$$

where  $A_u$  is the cross section junction area of the diode;  $d$  is the distance corresponding to the region width of diode and  $\epsilon$  is the permittivity of the dielectric semiconductor . As the voltage changes from reverse to forward bias the capacitance increases following the region width reduction. However, this condition is no longer

valid at the forward bias, where the capacitance becomes a function of more variables such as doping level and depth of active layer. The non-linear junction capacitance is then calculated as

$$C_j(V) = C_{j0} \left( 1 - \frac{V}{\phi_{bi}} \right)^{-m_g} \quad \text{Equation (3.4)}$$

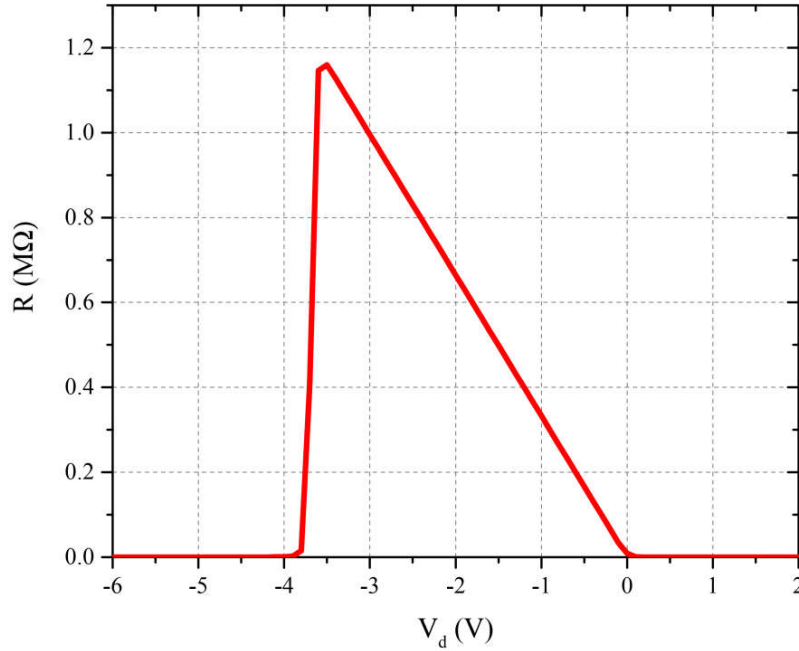


Figure 3.5. Diode junction resistance versus voltage for diode model HSMS-2850.

where  $m_g$  is the grading coefficient which is 0.5 and 0.3 for abrupt and linearly graded junctions, respectively.  $C_{j0}$  is the junction capacitance at zero bias voltage and defined as [98]

$$C_{j0} = \left( \frac{q\epsilon N_D}{2V_f} \right)^{0.5} A_a \quad \text{Equation (3.5)}$$

where  $N_D$  is donor density in n-layer and  $V_f$  is the forward voltage of diode. The approximate values of junction capacitance using equation Equation (3.4) is plotted in Figure 3.6.

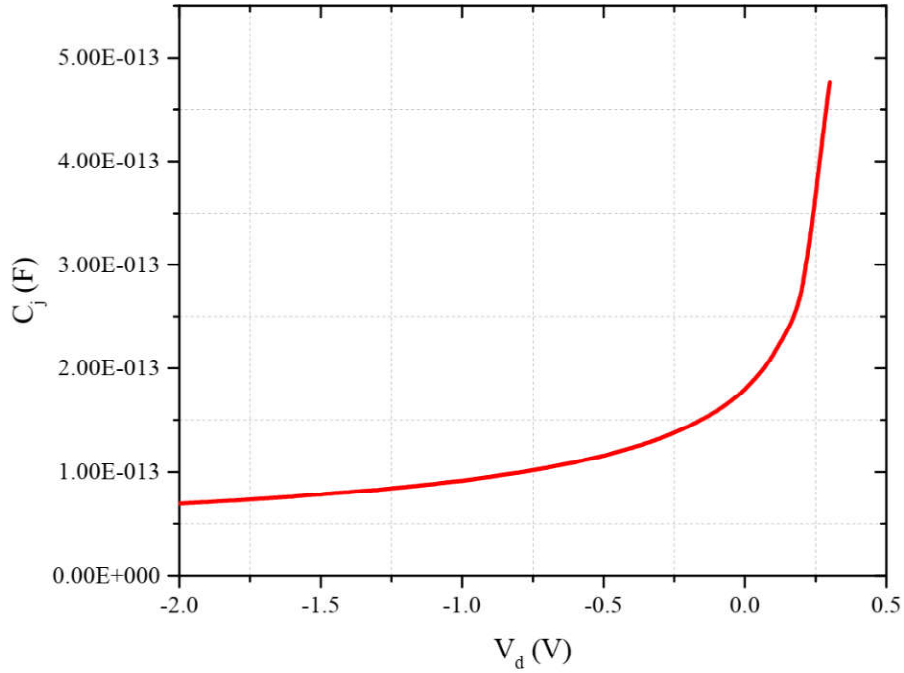


Figure 3.6. The junction capacitance of diode model HSMS-2850 derived from Equation (3.4).

The impact of junction capacitance is essentially destructive to the output power of energy harvesters as it bypasses the non-linear resistance and the power is dissipated on the series resistance without any contribution on the output voltage. This effect becomes more significant at the higher frequencies or when the value of junction capacitance is large. Figure 3.7 shows the effect of junction capacitance on the output voltage as a function of  $R_j$  using Equation (3.6) from [102]

$$M = \frac{1}{1 + \omega^2 C_j^2 R_s R_j} \quad \text{Equation (3.6)}$$

here,  $M$  is a multiplication factor for output voltage and  $\omega = 2\pi f$  is the radial frequency. Notice that while this equation is an approximation, however, it can provide a good quantitative insight on the output performance of an energy harvester.

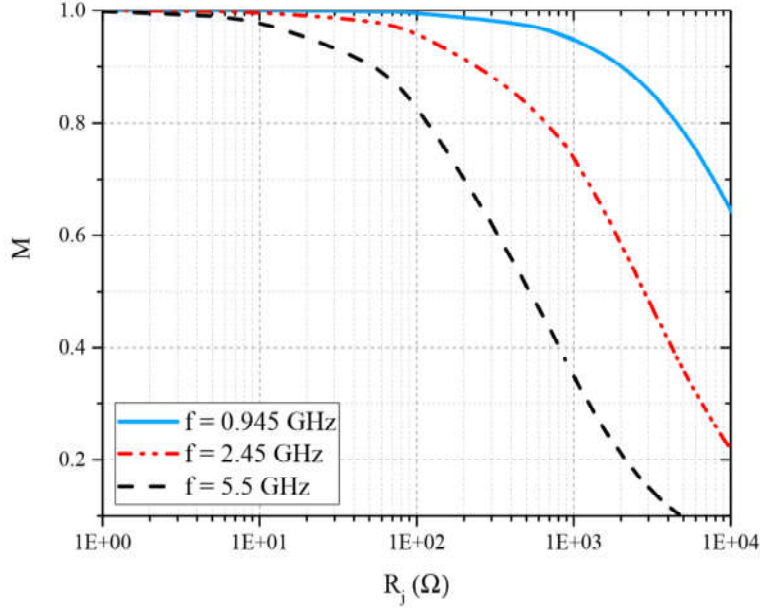


Figure 3.7. The impact of junction capacitance on the output voltage using Equation (3.6).

### 3.2.5 Harmonic Generation in Non-Linear Devices

In any circuit containing non-linear element, the values of voltage and current are limited to the device threshold. Once the value of injected input signal exceeding those limits, the wave form in the time domain is clipped and the clipped content will be observed in the form of harmonics in the frequency domain. As an example, if the non-linear element is a diode in Figure 3.3, by ignoring parasitics and phase variation on the output signal, the current of the diode follows the relation

$$I_d = A_0 + A_1 \cos(\omega t) + A_2 \cos(2\omega t) + A_3 \cos(3\omega t) + A_4 \cos(4\omega t) + A_5 \cos(5\omega t) + \dots \quad \text{Equation (3.7)}$$

Using Equation (3.1) and after some mathematical simplification the values of unknown variables are found as

$$A_0 = \frac{1}{1920} (30a^4 V_0^4 + 480a^2 V_0^2) I_s \quad \text{Equation (3.8)}$$

$$A_1 = \frac{1}{1920} (10a^5 V_0^5 + 240a^3 V_0^3 + 1920a V_0) I_s$$

$$A_2 = \frac{1}{48} V_0^2 a^2 (a^2 V_0^2 + 12) I_s, \quad A_3 = \frac{1}{384} a^3 V_0^3 (a^2 V_0^2 + 16) I_s$$

$$A_4 = \frac{1}{192} V_0^4 a^4 I_s, \quad A_5 = \frac{1}{1920} a^5 V_0^5 I_s$$

where  $a = q / nkT$ ,  $\omega = 2\pi f$ ,  $A_0$  is the DC component and  $A_1$  to  $A_5$  are the magnitudes of fundamental to fifth harmonics, respectively. These harmonics are spread in the frequency domain in the multiples of the incident input signal frequency at the output in which first harmonic carries the highest power and the power is reduced as the harmonic increases. Since these harmonic contents are carrying part of the power, the termination of harmonics is essential so that they can be recycled and participate in the next period of operation leading to a higher efficiency.

### 3.2.6 Analytical Model of Non-Linear Rectifier

Recently with the advances in the numerical simulation software packages along with the high speed computer processors available, the design of an electronic circuit has become a much simpler task than before. However, this would delimit the complete insight into the principal operation of the intended circuit. In general, to analyze a circuit under low power operation, typically less than -20 dBm, containing non-linear element such as rectifier, small signal model is utilized since the non-linear element performs at its “square law” region. Such an analyses has been made in [103]. Nevertheless, this model losses its accuracy as the level of power is increased and the circuit behavior is pushed more into its non-linear performance. Hence, a more accurate model to predict the behavior of the rectification process is essential. A numerical method is proposed in [104], where a closed-form solution for the entire range of operation is provided considering “square-law” and “linear” behavior simultaneously. A drawback of the analyses given in [104] is the over simplification of output contents in which only the DC terms are considered and harmonic contents are discarded. In this section, due to the importance of created harmonics on the process of rectification at the microwave frequencies the analysis presented in [104] is expanded to achieve a closed-form solution with more precise insight on the operation. To do so, we begin with a rectifier circuit containing an ideal exponential diode with series resistance  $R_s$  and junction capacitance  $C_j$ , an ideal bias current source, a load

resistor  $R_L$  and output capacitor  $C_{lo}$  all connected to an AC voltage source with series resistance  $R_g$ . The schematic of the proposed circuit is shown in Figure 3.8.

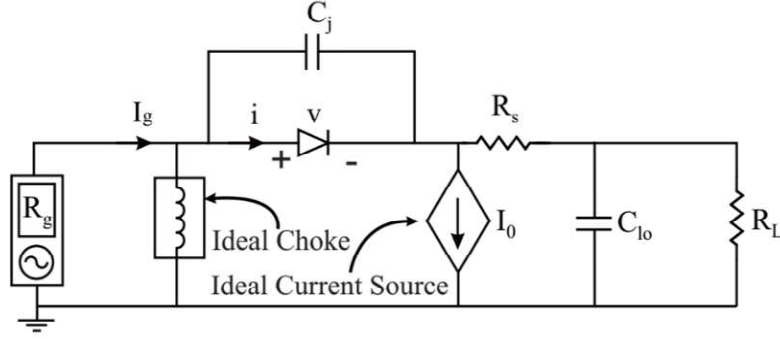


Figure 3.8. Circuit schematic of a detector circuit.

The diode presented here is an ideal diode following the relation

$$i = I_s (e^{\gamma v} - 1) \quad \text{Equation (3.9)}$$

Where  $i$  is the current through the diode,  $I_s$  is the diode saturation current and  $v$  is the voltage across non-linear diode. In Equation (3.9),  $\gamma = q / nkT$ ,  $n$  is the diode ideality factor,  $k$  is the Boltzmann constant,  $q$  is the electronic charge and  $T$  is temperature in Kelvin.

By applying the Kirchhoff laws on the circuit given in Figure 3.8, the differential equation is found as

$$\alpha \zeta + y + y' = \alpha \left[ \exp \left\{ (x - y) - \mu (y' + y) - k \zeta \right\} - 1 \right] + \zeta \left[ (x' - y') - \mu (y'' + y') \right] \quad \text{Equation (3.10)}$$

Where  $x = \gamma v_g$  is the normalized input function (also referred as forcing function), and  $y = \gamma v_o$  is the normalized output function (also referred as video output). The symbols

“'” and “''” denotes  $\partial/\partial\tau$  and  $\partial^2/\partial\tau^2$ , respectively, where  $\tau = t/(R_L C_{l0})$ . Other parameters are:  $\alpha = \gamma R_L I_s$ ,  $\zeta = I_o/I_g$ ,  $\varsigma = C_j/C_{l0}$ ,  $\mu = (R_g + R_s)/R_L$ ,  $k = \gamma I_g R_s$ . Since our aim is to perform analyses for energy harvesting systems by employing zero-bias schottky diodes, it is proper to assume that no bias current exists on the system (i.e.  $I_o = 0$ ). Therefore, the circuit schematic in Figure 3.8 is modified to Figure 3.9 and Equation (3.10) is rewritten as follow

$$y + y' = \alpha \left[ \exp\{(x - y) - \mu(y' + y)\} - 1 \right] + \varsigma \left[ (x' - y') - \mu(y'' + y') \right] \quad \text{Equation (3.11)}$$

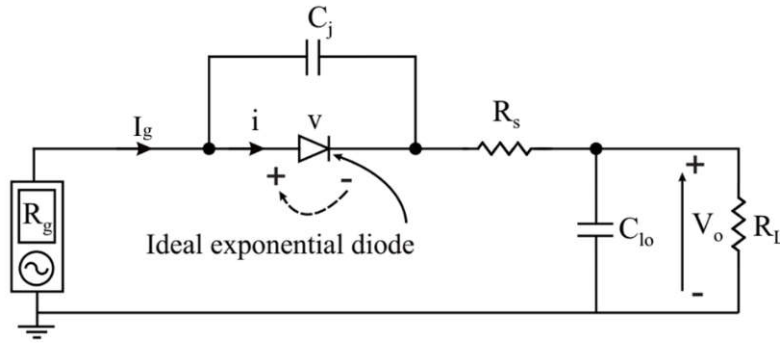


Figure 3.9. Simplified diode detector circuit with an ideal zero-bias diode.

Considering an input of angular frequency  $\omega$  we can write

$$x(\tau) = X \sin(\nu\tau) \quad \text{Equation (3.12)}$$

where  $X = \gamma V_g$  and  $\nu = \omega R_L C_{l0}$ .

In order to find a closed-form solution for the Equation (3.11), the Ritz-Galerkin (R-G) is employed where the differential equation is represented as

$$\xi \left[ \partial^2/\partial\tau^2, \partial/\partial\tau, y, x \right] \equiv 0 \quad \text{Equation (3.13)}$$

Where  $\xi$  is a non-linear operator. Then, the exact solution can be approximated as

$$\tilde{y}(\tau) = \sum_{k=1}^N \alpha_k \psi_k(\tau) \quad \text{Equation (3.14)}$$

Where  $\alpha_k$  are adjustable coefficients and  $\psi_k(\tau)$  are linearly independent functions containing DC and harmonic contents. In order to minimize the error introduced by approximation used in Equation (3.14), it is desirable to consider an error function as

$$\varepsilon(\tau) = \xi[\partial^2 / \partial \tau^2, \partial / \partial \tau, \tilde{y}, x] \neq 0 \quad \text{Equation (3.15)}$$

As shown in [105], the magnitude of residual  $\varepsilon(\tau)$  is minimized by satisfying  $N$  Rits conditions as follows

$$\int_{\tau_1}^{\tau_2} \xi[\partial^2 / \partial \tau^2, \partial / \partial \tau, \tilde{y}, x] \psi_k(\tau) d\tau = 0 \quad \text{Equation (3.16)}$$

$$k = 1, \dots, N$$

Hence, a series of  $N$  unknown coefficient,  $\alpha_k$ , and  $N$  algebraic equations are obtained simultaneously that can be used to find any unknown coefficient presented in Equation (3.16). Taking into account the periodic function  $x(\tau)$ , one can set

$$\tilde{y}(\tau) = \sum_1^m \alpha_k \psi_k(\tau) = Y_0 + Y_1 \sin(\nu\tau + \theta) + Y_2 \sin(2\nu\tau + \theta) + \dots \quad \text{Equation (3.17)}$$

Where  $Y_0$  and  $Y_{(N)}$  are the amplitude of the DC and harmonic terms, respectively, and  $\theta$  is the phase of harmonics. A valid assumption that can be made on Equation (3.17) is to neglect higher harmonic components (i.e. harmonics higher than fundamental term). This can be further justified as the power distribution reduces by increasing the harmonic orders, thus, the complexity can be noticeably reduced without losing much on the accuracy of final solution as will be shown later (see Figure 3.10).

Nevertheless, as the phase of harmonic content is of arbitrary value and simply assigning zero to that ( $\theta=0$ ) can lead to a significant error. Therefore, another modification has to be made on the equation Equation (3.17) as follows

$$\tilde{y}(\tau) = \sum_1^3 \alpha_k \psi_k(\tau) = Y_0 + Y_1^* \sin(v\tau) + Y_2^* \cos(v\tau) \quad \text{Equation (3.18)}$$

Where  $Y_1^*$  and  $Y_2^*$  are magnitudes of fundamental harmonic of an arbitrary phase and  $Y_0$  is the DC term. Consequently, from Equation (3.11), Equation (3.12) and Equation (3.18) the residual function can take the form

$$\begin{aligned} \varepsilon(\tau) = & \left( \left[ \{(-\mu-1)Y_1 + X\} \zeta - Y_1 \right] v - Y_2 \right) \cos(v\tau) \\ & + \alpha \left( \exp\{S(\tau)\} - 1 \right) + \cos(v\tau) \mu Y_2 \zeta v^2 + \\ & \left[ \mu Y_1 \zeta v^2 + \{(\mu+1)Y_2 \zeta + Y_2\} v - Y_1 \right] \sin(v\tau) - Y_0 \end{aligned} \quad \text{Equation (3.19)}$$

Where

$$\begin{aligned} S(\tau) = & -Y_2 \cos(v\tau) + (X - Y_1) \sin(v\tau) \\ & - \mu \left[ (vY_1 + Y_2) \cos(v\tau) + (-vY_2 + Y_1) \sin(v\tau) + Y_0 \right] - Y_0 \end{aligned} \quad \text{Equation (3.20)}$$

Therefore, three Ritz conditions can be established as

$$\int_0^{2\pi} \varepsilon(\tau) d(v\tau) = 0 \quad \text{Equation (3.21)}$$

$$\int_0^{2\pi} \varepsilon(\tau) \sin(v\tau) d(v\tau) = 0 \quad \text{Equation (3.22)}$$

$$\int_0^{2\pi} \varepsilon(\tau) \cos(v\tau) d(v\tau) = 0 \quad \text{Equation (3.23)}$$

After some trigonometric simplification on Equation (3.20) and substituting Equation (3.19) into Equation (3.21), Equation (3.22) and Equation (3.23) the resulting equations are presented as

$$-2\pi(\alpha + Y_0) + \alpha e^{-Y_0(1+\mu)} \times \int_0^{2\pi} \exp(\Lambda \sin(v\tau + \phi)) d(v\tau) = 0 \quad \text{Equation (3.24)}$$

$$\pi \left[ Y_1(\mu v^2 \zeta - 1) + Y_2 v(1 + \zeta(\mu + 1)) \right] + \alpha e^{-Y_0(1+\mu)} \times \int_0^{2\pi} \exp(\Lambda \sin(v\tau + \phi)) \sin(v\tau) d(v\tau) = 0 \quad \text{Equation (3.25)}$$

$$\pi \left[ Y_2(\mu v^2 \zeta - 1) - Y_1 v(1 + \zeta(\mu + 1)) + X \zeta v \right] + \alpha e^{-Y_0(1+\mu)} \times \int_0^{2\pi} \exp(\Lambda \sin(v\tau + \phi)) \cos(v\tau) d(v\tau) = 0 \quad \text{Equation (3.26)}$$

And

$$\tan(\phi) = \frac{-\mu v Y_1 - Y_2(1 + \mu)}{\mu v Y_2 - Y_1(1 + \mu) + X} \quad \text{Equation (3.27)}$$

$$\Lambda = \sqrt{(-\mu v Y_1 - Y_2(1 + \mu))^2 + (\mu v Y_2 - Y_1(1 + \mu) + X)^2} \quad \text{Equation (3.28)}$$

The integration in Equation (3.24), Equation (3.25) and Equation (3.26) can be obtained based on modified Bessel function definition and are expressed as

$$-2\pi(\alpha + Y_0) + 2\pi\alpha e^{-Y_0(1+\mu)} I_0(\Lambda) = 0 \quad \text{Equation (3.29)}$$

$$\pi \left[ Y_1(\mu v^2 \zeta - 1) + Y_2 v(1 + \zeta(\mu + 1)) \right] + 2\pi\alpha e^{-Y_0(1+\mu)} I_1(\Lambda) \cos(\phi) = 0 \quad \text{Equation (3.30)}$$

$$\begin{aligned} & \pi \left[ Y_2 (\mu v^2 \zeta - 1) - Y_1 v (1 + \zeta (\mu + 1)) + X \zeta v \right] \\ & + 2\pi \alpha e^{-Y_0(1+\mu)} I_1(\Lambda) \sin(\phi) = 0 \end{aligned} \quad \text{Equation (3.31)}$$

where  $I_0$  and  $I_1$  are zero-order and first-order modified Bessel functions of the first kind and argument  $\Lambda$ . Using Equation (3.27), Equation (3.30), Equation (3.31) and after some manipulations, one can find

$$\begin{aligned} Y_1 = & \frac{-v\Lambda(\zeta(\mu+1)+1)\sin(\phi)}{(\mu(v^2+1)+1)} + \\ & \frac{2\alpha I_1(\Lambda)e^{-Y_0(1+\mu)}(\mu+1)\cos(\phi)}{(\mu(v^2+1)+1)} \end{aligned} \quad \text{Equation (3.32)}$$

$$Y_2 = \frac{\Lambda(\mu v^2 \zeta - 1)\sin(\phi) - 2\alpha I_1(\Lambda)e^{-Y_0(1+\mu)}\mu v \cos(\phi)}{(\mu(v^2+1)+1)} \quad \text{Equation (3.33)}$$

$$\phi = \arctan \left( \frac{v(-\zeta(\mu(v^2+1)+1)\Lambda + 2\alpha I_1(\Lambda)e^{-Y_0(1+\mu)})}{(1+(\zeta+1)v^2)\Lambda + 2\alpha I_1(\Lambda)e^{-Y_0(1+\mu)}(\mu(v^2+1)+1)} \right) \quad \text{Equation (3.34)}$$

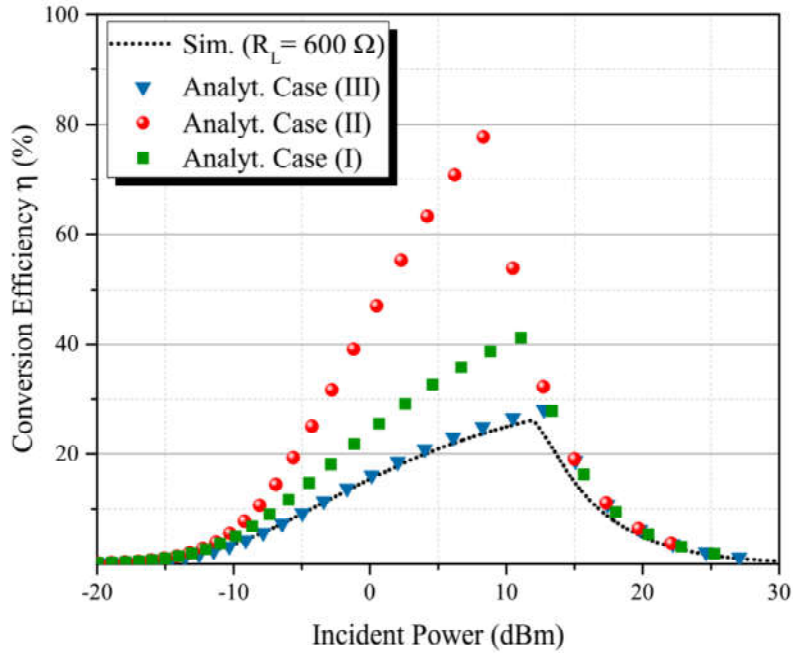
In order to find a closed-form solution for the above mentioned equations, one should find an initial value of the DC output,  $Y_0$  and modified Bessel function of the first kind of order zero,  $I_0$ , so that the Equation (3.29) is satisfied. This can be done by calculating  $Y_0$  at the absence of input power. Subsequently, the argument  $\Lambda$  value of modified Bessel functions are found by employing suitable root finding method. It is worth noting that, due to the uniqueness of the argument of the modified Bessel functions, a root finding method for a single root such as fixed point iteration, Secant method and Newton method can be used. The only difference between these methods is in their rate of convergence  $\delta$ . A sequence  $(X_k)$  is said to converge to a constant  $\xi$  with the order of  $\delta$  if there exist a positive constant  $p_{const}$  such

$$\lim_{k \rightarrow \infty} \frac{|x_{k+1} - \xi|}{|x_k - \xi|^\alpha} = \lim_{k \rightarrow \infty} \frac{e_{k+1}}{e_k^\alpha} = p_{const} \quad \text{Equation (3.35)}$$

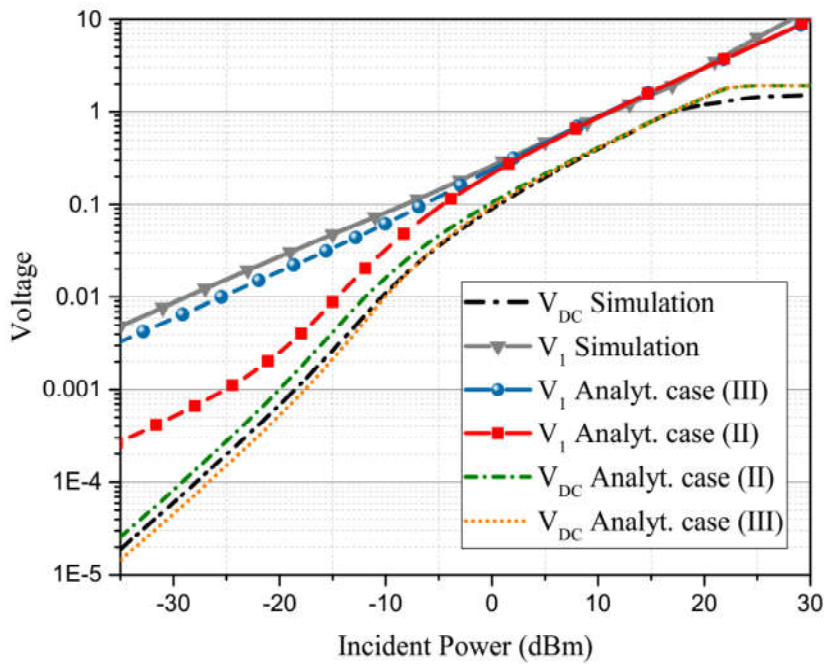
The rate on convergence is said to be linear, superlinear or quadratic if  $\delta = 1$ ,  $1 < \delta < 2$  or  $\delta = 2$ , respectively. Indeed, the rate of convergence determines the increased accuracy of the operation after each iteration. For example, Newton method has a quadratic rate of convergence (i.e.  $\delta = 2$ ) which means the precision on the convergence becomes roughly doubled after each operation leading to a faster and more precise result. However, this precision comes at the cost of calculating the derivatives of the functions at each approximation. Therefore, one may find a superlinear method such as Secant method more convenient as it does not require to calculate derivatives but with the lower convergence rate. In our case, we have adopted a modified Secant method as

$$x_{k+1} = x_k - \frac{f(x_k)(x_k - x_{k-1})}{f(x_k) - f(x_{k-1})} \quad \text{Equation (3.36)}$$

Under the condition that  $f_x \cdot f_{x-1} < 0$  to ensure that the final outcome falls within the specified interval. By implementing Equation (3.32), Equation (3.33) and Equation (3.34) in any numerical computing software such as MATLAB or Apache Open Office, and using Equation (3.36) as the solving method, the conversion efficiency can be calculated. Figure 3.10 compares the accuracy of the proposed analytical model under different output conditions where in case (I);  $Y_1 = Y_2 = 0$ , in case (II);  $Y_2 = 0$  and in case (III) all terms has been taken into account.



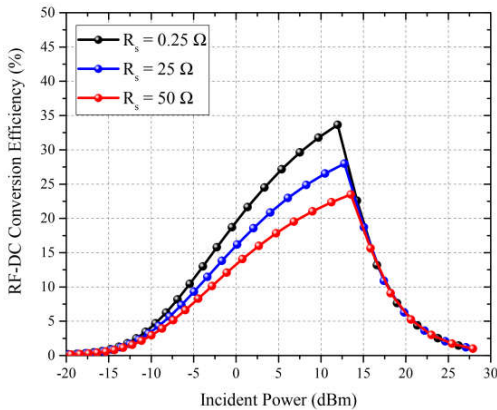
(a)



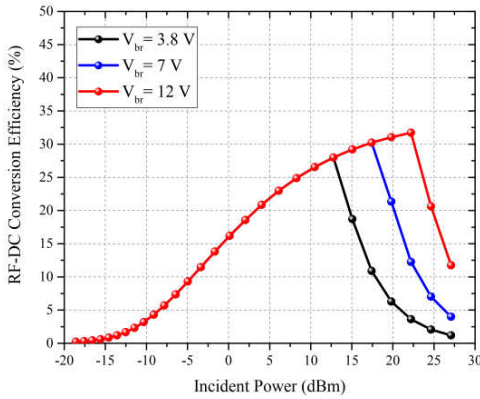
(b)

Figure 3.10. Comparison between calculated and simulated conversion efficiency. (a) Conversion efficiency and (b) output DC voltage. The outputs are for different cases using Equation (3.18).

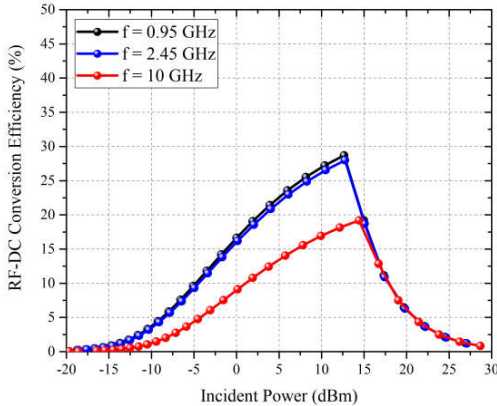
Using the same analytical model, the impact of variation on different diodes' parameters on the resultant RF-to-DC conversion efficiency is demonstrated in Figure 3.11(a)-(d). Figure 3.11(a) demonstrates the reduction on the rectifier efficiency caused by increasing series resistance. It can be noticed that, as the input power increases the loss on the semiconductor junction becomes more significant and power conversion is reduced. Figure 3.11(b) shows that the larger breakdown voltage supports for the operation of diode over larger power range. If the power level increases beyond



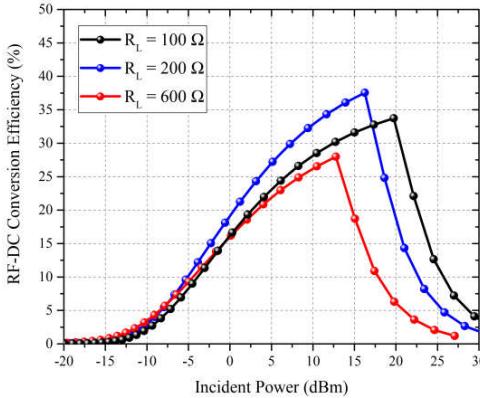
(a)



(b)



(c)



(d)

Figure 3.11. Impact of different diode's parameters on the overall efficiency; (a) series resistance, (b) breakdown voltage, (c) frequency and (d) output load.

the voltage breakdown point, the output voltage does not increase anymore, thus, the RF-DC conversion efficiency is reduced. Figure 3.11(c) demonstrates the dominance of junction capacitance as the frequency increases. While there is no significant difference between 0.95 and 2.45 GHz power conversion efficiency, but the filtering

impact of series resistance and junction capacitance at higher frequencies such as 10 GHz is obvious (see Figure 3.7). The impact of junction capacitance is essentially destructive to the output power of energy harvesters as it bypasses the non-linear resistance and the power is dissipated on the series resistance without any contribution on the output voltage. Referring to Equation 3.6 and Figure 3.7, it is observed that the voltage multiplication factor is inversely proportional to the frequency, thus, destructively impacting the overall system efficiency. Finally, Figure 3.11(d) shows an interesting and important characteristic of rectifiers on the variation of output load. The output load value is directly related to the diode's overall resistance. The increase on the output load can raise the rectifier efficiency particularly at the low power levels. However, if the load value becomes too high, the accepted input power reduces as a consequence of increased diode resistance, indicating the requirement for selecting the optimal load, which is  $200 \Omega$  in this case, for the best performance. It is worth noting that, the difference on diodes manufacturing technology as well as its physical properties, which can cause the trap state at the semiconductor depletion region, mobility fluctuation and parasitic resonances are all contributing to the natural input impedance of a diode at a certain frequency. Moreover, the latter one is more pronounced at higher frequencies due to shortening of the wavelength following the increase on the frequency. The analysis presented in this section provides us with a much clearer view on the fundamental limits on the conversion efficiency and impact of every individual diode parameter to the rectification process. These information can be greatly advantageous in design of low power rectifiers.

### **3.3 Microwave Rectifiers**

The general block diagram for the common scenario of the rectification for energy harvesting systems is presented in Figure 3.12. As is seen, it consists of a BPF, a matching network, a rectifying element, a DC-pass filter and a load resistor. There are various topologies for the design of rectifiers based on the number of rectifying element used. Some of the common rectifier topologies employed for energy harvesting applications are shown in Figure 3.13. A half-wave rectifier has a simple structure consisting of a single diode, a DC pass capacitor and a load resistor. Figure 3.13 demonstrate the two possible configurations of half-wave rectifiers.

Owing to the employment of only a single diode, half-wave rectifiers possess the lowest possible loss during the rectification process. Although, theoretically, half-wave rectifiers are limited to a maximum efficiency of 50% (as it passes only a half cycle of the input voltage), at the high frequencies such as microwave range of frequency, the efficiency is significantly increased and it can be treated as a resonant structure [106]. However, despite the fact that RF signal in a half-wave rectifier experiences less losses, there is a large amount of harmonics generated on the circuit. These harmonics have to be terminated for achieving high conversion efficiency which can lead to a significantly large footprint of the overall circuit. On the other hand, considering the typical DC voltage requirement of available low power ICs in the market (typically 0.35-3.5V), the limited supplied voltage by a single diode may not be sufficient. In another words, the issue is not only how efficient a wireless energy harvester is in converting RF-to-DC power, but also what the output DC voltage and current of the energy harvester are at the RF input power level [107]. As a consequence, voltage multipliers in the form of a full-wave voltage doubler (Figure 3.13 (c)) or a cascade of several stages as well as bridge rectifiers (Figure 3.13 (d)) are used to provide sufficient output power determined by the intended application. Moreover, rectifiers with bridge topologies have also been used for energy harvesting applications such as the one presented in [33] . However, when compared to the bridge rectifier, multi-staged voltage doubler may provide additional degree of freedom for the low power operation.

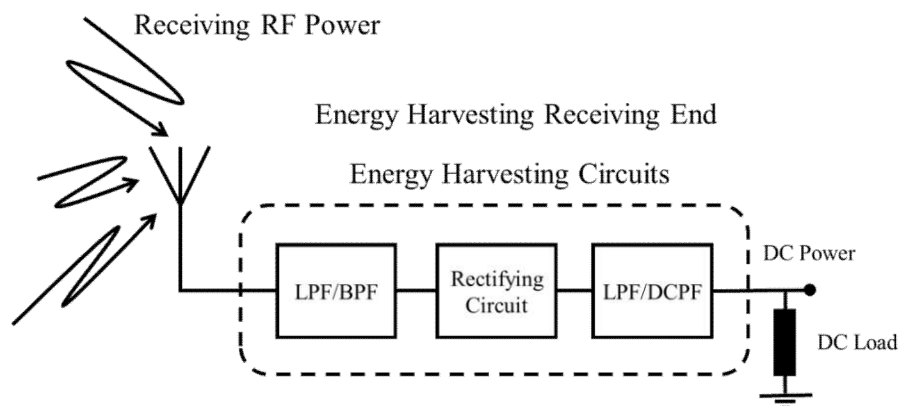


Figure 3.12. General block diagram of the rectification circuit.

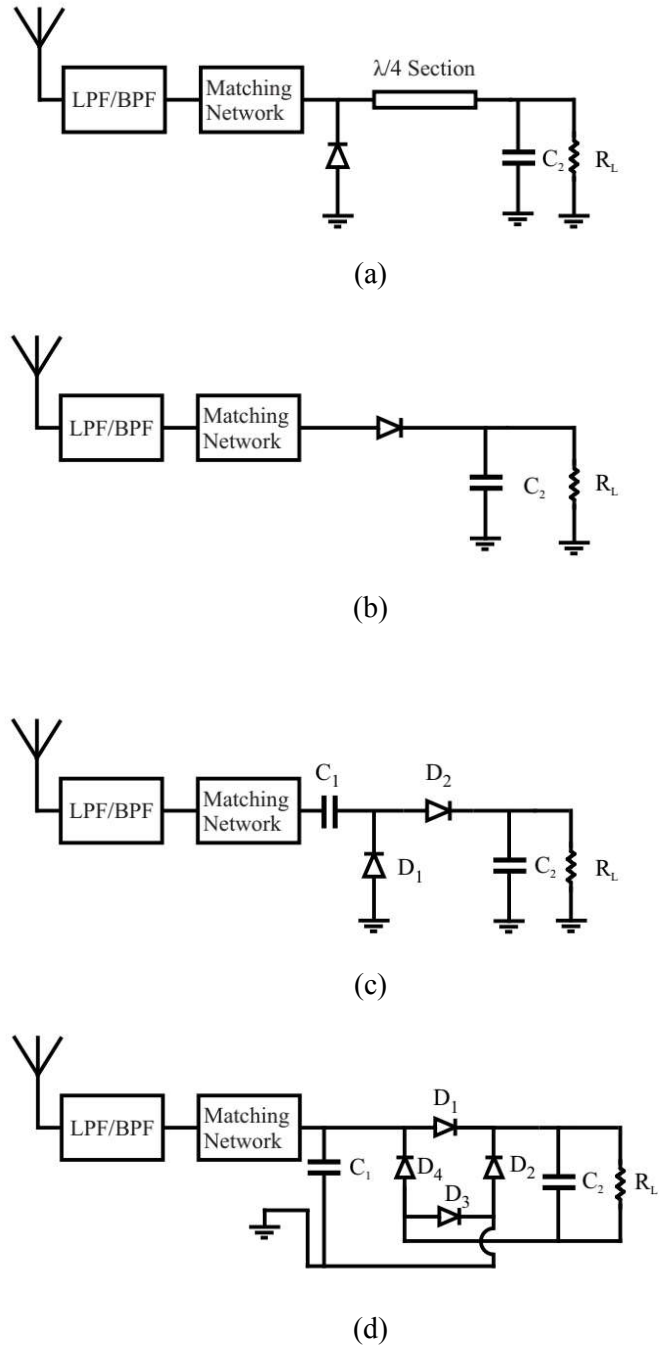


Figure 3.13. Rectenna topologies, rectenna with single shunt (a), single serial (b), voltage doubler (c) and bridge rectifier (d).

### 3.3.1.1 Voltage Multipliers for Microwave Rectification Circuits

As mentioned earlier, a single diode rectifier in the microwave range of frequency can provide a high efficiency but restricted in terms of output voltage for the low power operation. Hence, in order to generate adequate amount of voltage, one should consider

more than one diode or a voltage multiplier. This is obviously achieved at the cost of higher loss as in the case of voltage multiplier the loss through the diodes is at least doubled. Being aware of low available power that is less than 1mW at a distance of just a few meters away from the transmitter, the design of rectifier can become a highly challenging task. Aiming to increase the overall output voltage, several configuration is widely used for this purpose such as single and multi-stage Dickson charge pump, modified Greinacher and Villard charge pump as presented in Figure 3.14.

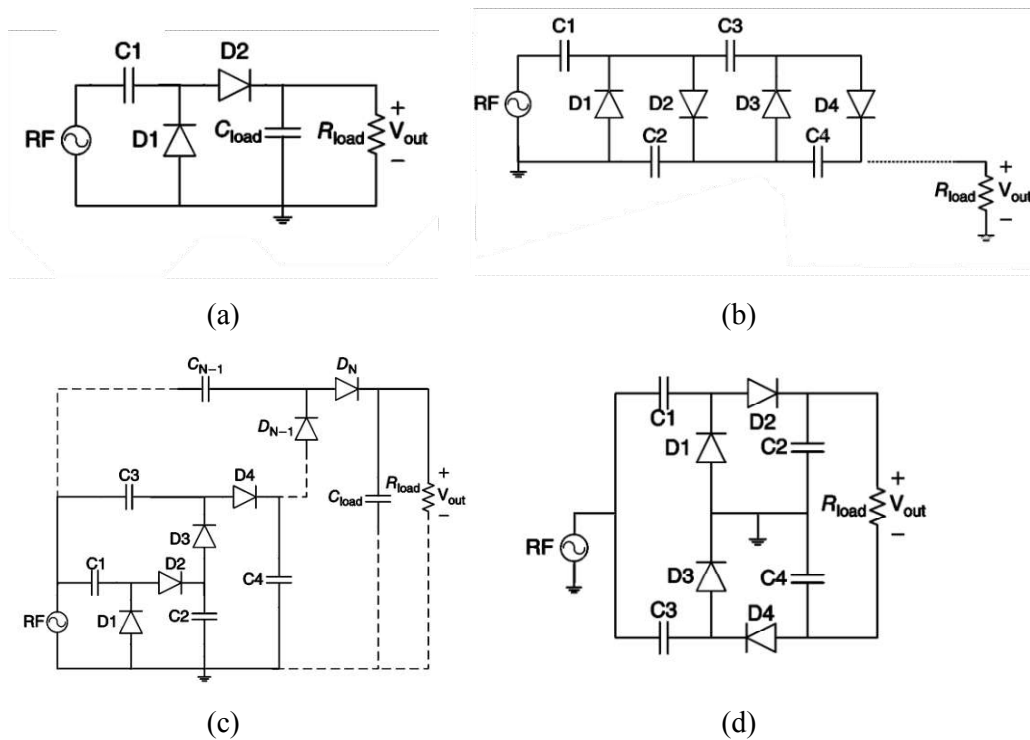


Figure 3.14. Some commonly used voltage multiplier topologies (a) single stage Dickson charge pump, (b) Villard charge pump, (c) Multi-stage Dickson charge pump, (d) modified Greinacher voltage quadrupler.

The principle of operation of a voltage doubler is shown in Figure 3.15. When the injected input signal is at its positive cycle, the series diode ( $D_2$ ) behaves as a closed switch and conducts the current coming from the positive node of the source (Figure 3.15 (a)). Under this condition the output capacitor ( $C_2$ ) is charged in which the resultant voltage across the capacitor is a subtraction of input voltage and the diode forward threshold with respect to the ground. Furthermore, the shunt diode ( $D_1$ )

behaves as a closed switch during the negative cycle and the series diode ( $D_2$ ) is open, causing the charges to be stored on the input capacitor ( $C_1$ ) with the same amount of voltage as the output capacitor considering both diodes to be identical (Figure 3.15 (b)). It should be noticed that, the resultant output DC voltage is increased but is not exactly doubled as the input signal needs to overcome the voltage threshold of diodes.

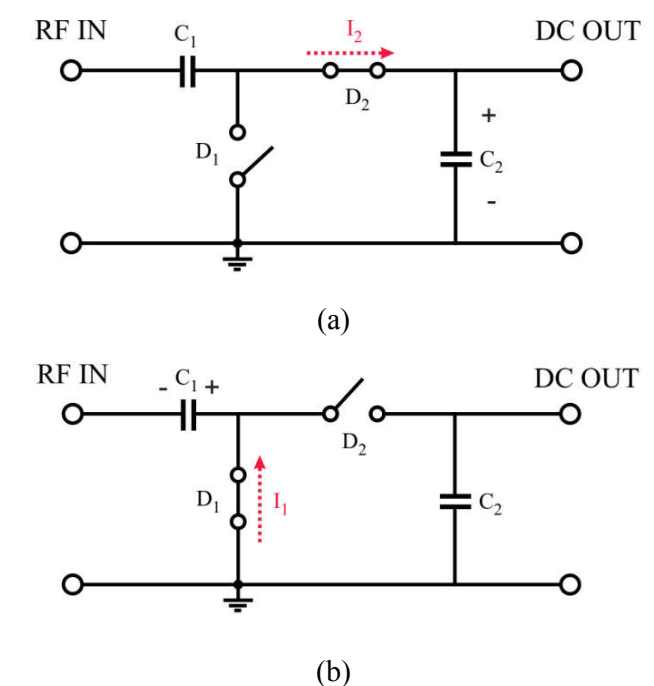


Figure 3.15. Principle of operation of a voltage doubler at (a) positive cycle, (b) negative cycle.

This problem has been significantly reduced by introducing Zero-bias Schottky diodes resulting in an output voltage nearly close to twice the input voltage. The unwanted effects and the cost impact of two single diode can also be minimized by employing two diodes in a single small package such as SOT-323 and SOT-23. There is also another advantage when using voltage doubler in terms of harmonic generation and will be discussed in the next section.

### 3.3.1.2 Voltage-Doubler/Multiplier Harmonic Analysis

The schematic of a N stage voltage doubler in the form of Dickson charge pump is shown in Figure 3.16. To begin with the harmonic analysis of the voltage doubler based rectifier it is necessary to have the IV expression of the Schottky diode as

$$I = I_s \left( e^{v/V_T} - 1 \right) + C_d \frac{dV_d}{dt} \quad \text{Equation (3.37)}$$

Assuming the input voltage provided by antenna is in the form of  $\pm V_0 \cos(\omega_0 t)$ , the voltage across each diode composed of DC and RF components can be written as

$$V_d = V_{RF} + V_{DC} = \pm V_0 \cos(\omega_0 t) - \frac{V_{Tot}^{DC}}{2N} \quad \text{Equation (3.38)}$$

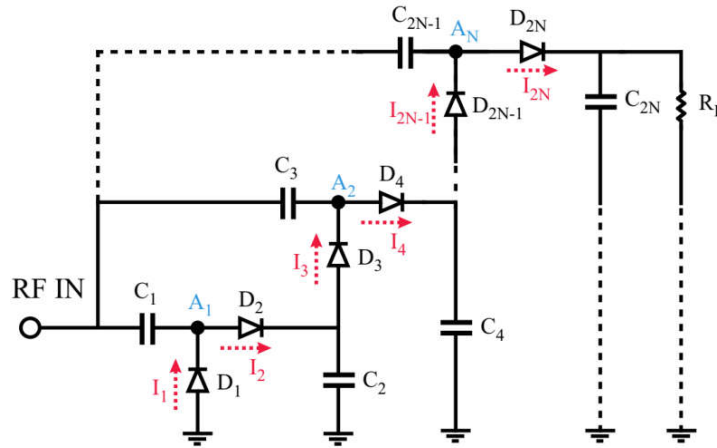


Figure 3.16. Schematic of a N stage voltage doubler in the form of Dickson charge pump.

where  $V_{Tot}^{DC}$  presents the total DC voltage provided from N stage cascaded voltage doublers. By casting Equation (3.38) into Equation (3.37) it yields

$$I = I_s \left( e^{\frac{\pm V_0 \cos(\omega_0 t) - \frac{V_{Tot}^{DC}}{2N}}{V_T}} - 1 \right) \pm C_d V_0 \omega_0 \sin(\omega_0 t) \quad \text{Equation (3.39)}$$

Here,  $C_d$  is the diode's junction capacitance and the signs indicate the direction of the current flow. To find the total current at the input of the voltage multiplier, it is sufficient to calculate the current at one node (i.e.  $A_1$ ) and multiply that by  $N$  as

$$I_{RF} = NI_s \left[ e^{-\frac{V_{Tot}^{DC}}{2NV_T}} \left( e^{\frac{V_0 \cos(\omega_0 t)}{V_T}} - e^{-\frac{V_0 \cos(\omega_0 t)}{V_T}} \right) \right] \quad \text{Equation (3.40)}$$

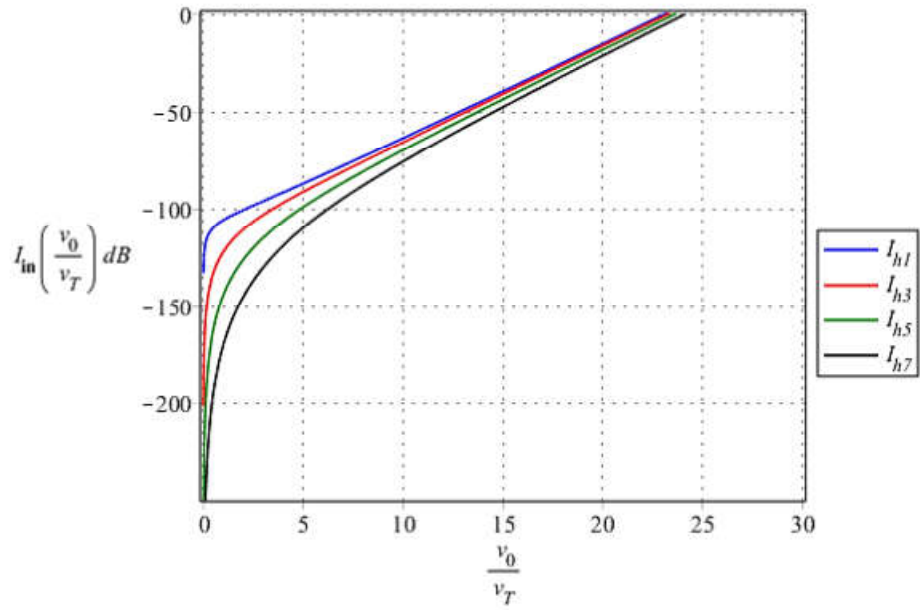
$$-2NC_d V_0 \omega_0 \sin(\omega_0 t)$$

By taking the Fourier transform of the periodic signal in Equation (3.40), the harmonic current generated from a voltage doubler can be written as

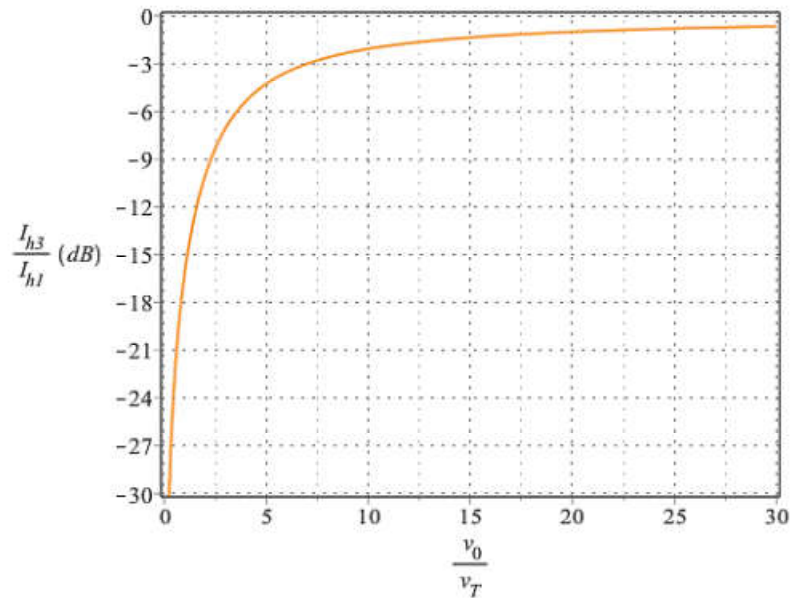
$$I = 4NI_s e^{-\frac{V_{Tot}^{DC}}{2NV_T}} \sum_{n=1}^{\infty} J_m \left( \frac{V_0}{V_T} \right) \cos(m\omega_0 t) \quad \text{Equation (3.41)}$$

$$-2NC_d V_0 \omega_0 \sin(\omega_0 t)$$

In the above equation  $J_m$  is the Bessel function of the first kind and order  $m$  where  $m = 2n - 1$ . It is worth mentioning that, while the analysis provided here involves some simplifications (such as multiplying a single stage by  $N$  and ignoring additional capacitance of higher stages in Equation Equation (3.40)), however, it can vividly emphasize on the advantage of their reduced harmonic contents due to cancellation of the even harmonics. It can be noticed that the odd harmonics are the only existing harmonics in the case of voltage multipliers where the even harmonics are cancelled due to their opposite flow direction. There are also rich information in Equation (3.41) that can be observed by plotting the dominant and harmonic contents of the voltage multiplier as shown in Figure 3.17. As is seen, increasing the output voltage can lead to increment on the harmonic levels where the influence becomes more considerable when  $V_0/V_T > 10$ . To better demonstrate this phenomena, a comparison between fundamental and third harmonics in a logarithmic scale is demonstrated in Figure 3.17 (b). It can observed that, when  $V_0/V_T$  reaches to around 7, the third harmonic current is nearly half of fundamental harmonic signifying the importance of odd harmonic terminations for achieving more efficient voltage multiplier.



(a)



(b)

Figure 3.17. (a) The impact of output voltage on the harmonic current generation of a voltage multiplier. (b) Comparison of the third to the fundamental harmonic currents of a voltage multiplier in a logarithmic scale.

### 3.3.2 Rectifier Efficiency

The efficiency of a rectifier is calculated as of the ratio between output DC power and accepted RF power by the rectifier as [97]

$$\eta = \frac{\int_0^t P_{DC} d\tau}{P_{RF-Acc} d\tau} \quad \text{Equation (3.42)}$$

However, for the energy harvesting system the transferred power from the harvester to the rectifier is of paramount importance and the efficiency is calculated as

$$\eta_{EH} = \frac{P_{outDC}}{P_{inEH}} \quad \text{Equation (3.43)}$$

Where  $P_{inEH}$  is the total amount of power delivered to the input of the system. The difference between these two equations is that, due to non-linearity of the rectifying element, part of the harvested energy is reflected back to the harvester resulting in a lower amount of power delivered to the rectifying element. Therefore, the maximum efficiency of an energy harvesting system is achieved when the amount of reflected power is minimized. This can be done by properly designing a matching network taking into account the input impedance of the rectifying element, power and load conditions. Hence, it is to be said that the maximum efficiency for an energy harvesting system is obtained when  $P_{inEH} = P_{RF-Acc}$ .

#### 3.3.2.1 Matching Network

For a rectifier circuit to operate effectively and provide high efficiency rate during the rectification process, the role of a high quality matching network is vital. A well dimensioned matching network can also absorb the parasitic effects of the diodes and allows the efficiency reaches to its extreme. The design of matching network is performed under the harmonic balanced (HB) analysis. HB is a frequency-domain analysis technique developed to take into account distortions in nonlinear circuits and systems. During the analysis, the circuit is divided into linear and nonlinear sub-circuits in which the linear sub-circuit is analyzed similar to any other passive circuits

in the frequency domain, while the nonlinear sub-circuit is analyzed differently and in the time domain. Once the results of the time domain analysis are accomplished they are transformed into the frequency domain following the Fourier Transformation. A solution is then found if the currents through the interconnections between the two sub-circuits are the same. The analysis gains its name since, the currents in the linear and nonlinear sub-circuits through these interconnections have to be balanced at every harmonic. The HB analysis is usually performed in any compatible software such as ADS.

### 3.3.2.2 Rectifier Filter Considerations

Harmonic generation of the rectifying component can be a huge source of loss as each harmonic component carries a fraction of injected power that has not converted into DC form. The employment of low pass/ band pass filter at the input can suppress the harmonics and re-inject them back to participate into another rectification cycle. Furthermore, in some cases, these harmonics can be detrimental to the consumer device particularly at the higher power levels. Hence, a low pass filter, typically made from quarter wave-length stub resonators, is used to terminate any outgoing harmonics and protect the consumer device.

### 3.3.2.3 Diode Selection

The choice of diode plays an important role on the performance of the rectifier and needs to be chosen based on requirements of the intended application. For the energy harvesting systems a diode with low built-in voltage is preferred as the available power to run the circuit is inherently low. Moreover, the efficiency of a diode is tightly related to the series resistance  $R_s$  and junction non-linear capacitance  $C_{j0}$ . While the series resistance  $R_s$  is a linear component and increases the ohmic loss on the diode, the junction capacitance  $C_{j0}$  contributes to the generation of the harmonic currents and its influence becomes more significant as the frequency increases. Basically, diodes in the smaller package can considerably reduce the junction capacitance since its value is directly related to the wafer area. The breakdown voltage  $V_{br}$  is also another important factor as it determines the power handling capability of the diode. Ideally, a diode with high breakdown voltage, low junction capacitance and low series resistance

is desirable. However, due to physical trade-offs and manufacturing constraints such diode is not feasible. The HSMS28XX family of zero-bias Schottky diodes from BROADCOM technology are attractive candidates as they do not require any external bias voltage and are capable of operating at microwave frequencies with a very low turn-on power. Although HSMS282X is the most recommended diode for the operation around 2 GHz, but the built-in voltage is relatively high (350 mV) which is not the best choice when available power is extremely low. On the other hand, HSMS285X and HSMS286X possess a built-in voltage of 150 mV and 250 mV, respectively, which makes them more suitable for our application. A comparison between HSMS285X and HSMS286X reveals that, while HSMS285X has the lowest built-in voltage, but the series resistance and break down voltage are 25  $\Omega$  and  $V_{br} = 3.6$  V. On the contrary, the HSMS286X possesses a much lower series resistance of 6  $\Omega$  and the break down voltage of  $V_{br} = 7$  V which is almost double to that of HSMS285X. A complete comparison between different parameters of the aforementioned diodes are given in Table 3.2. Since the focus of this thesis is on the

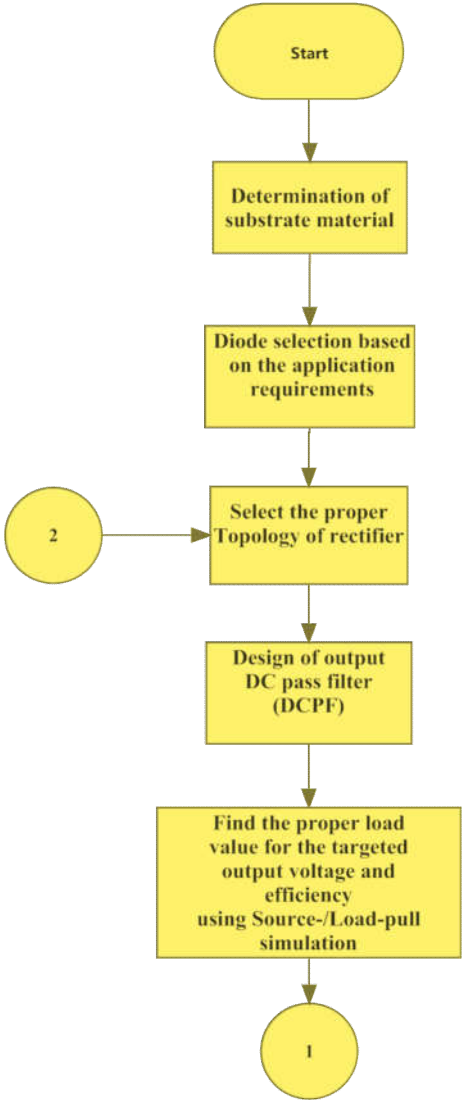
Table 3.2. Comparison of typical Schottky diode values from HSMS-28XX family.

Diode Type	HSMS-281X	HSMS-282X	HSMS-285X	HSMS-286X
$BV$ (V)	25	15	3.8	7
$I_{BV}$ (A)	1.00E-04	1.00E-03	1.00E-03	1.00E-04
$C_{j0}$ (pF)	1.1	0.7	0.18	0.18
$E_G$ (eV)	0.69	0.69	0.69	0.69
$I_s$ (A)	4.8E-09	2.20E-08	3.00E-06	5.00E-08
$N$	1.08	1.08	1.06	1.08
$R_s$ ( $\Omega$ )	10	6	25	5
$V_j$ (V)	0.65	0.65	0.35	0.65
$X_{TI}$	2	2	2	2
M	0.5	0.5	0.5	0.5
$V_f$	400 mV ( $I_f = 1$ mA) 1 V ( $I_f = 35$ mA)	340 mV ( $I_f = 1$ mA) 500 mV ( $I_f = 10$ mA) 700 mV	150 mV ( $I_f = 0.1$ mA) 250 mV ( $I_f = 1$ mA)	350 mV ( $I_f = 1$ mA) 0.6 V ( $I_f = 30$ mA)

energy harvesting application at the low power levels the diode model HSMS285C with the lowest available built-in voltage ( $V_f = 150 \text{ mV}$ ) in the HSMS-28XX family is chosen and will be considered in this thesis work.

### 3.3.3 Rectifier Design

The general methodology flowchart for the design of rectifiers is demonstrated in Figure 3.18. Notice that all the fabrication is done through the standard photo etching process.



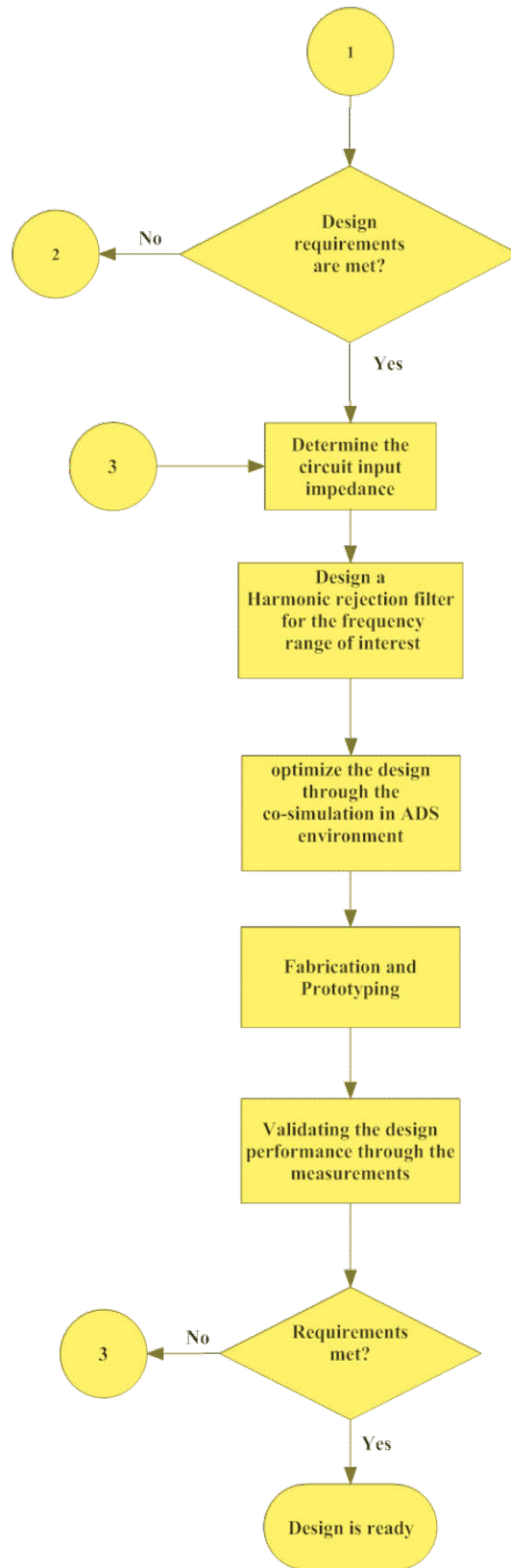


Figure 3.18 The methodology flowchart for the design of rectifiers.

For the design of a half-wave rectifier and aiming to determine the optimum output load, a Load/source pull setup is established inside the ADS environment as demonstrated in Figure 3.19. It can be observed that a shunt inductor has been used to Filter DC content at the input, while, a shunt capacitor provides a DC pass condition required at the output. In order to find the optimum load, the value of the output load has been swept 0.1 to 10 k $\Omega$  in which the impedance tuner box at the input iteratively calculates different possible impedance points and their resultant power conversion efficiency as demonstrated in Figure 3.20. It can be observed that the best efficiency

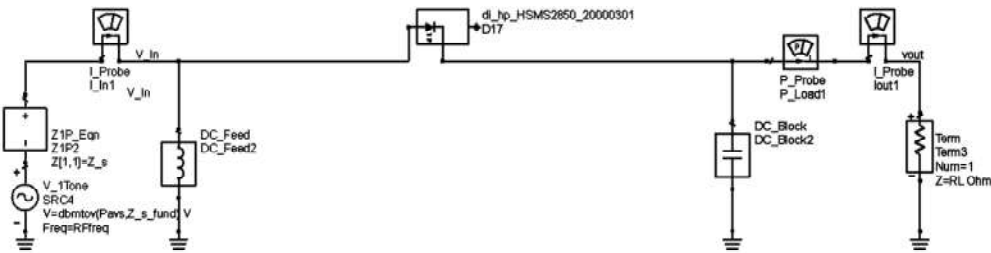


Figure 3.19. Load/Source pull simulation setup of the half-wave rectifier.

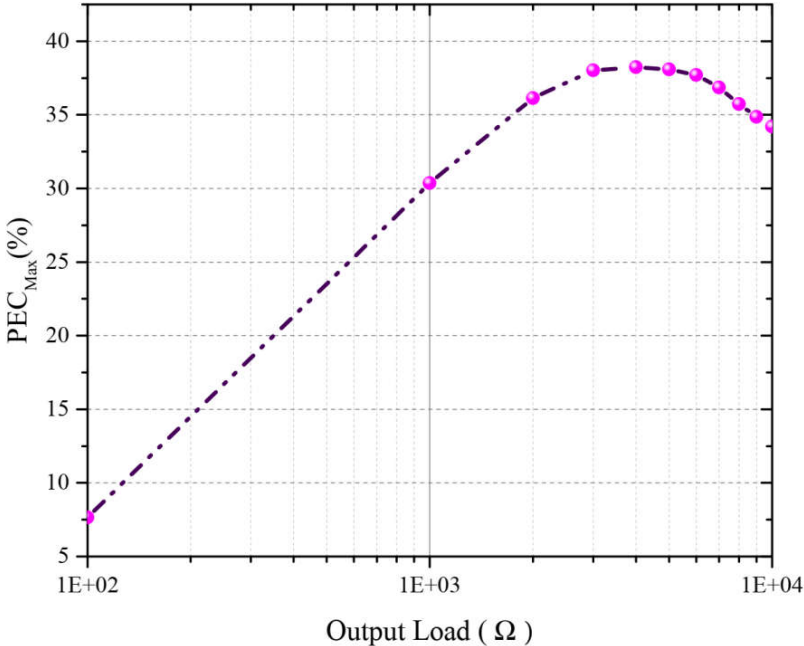


Figure 3.20 Maximum power conversion efficiency as a function of output load at 2.45 GHz and -15 dBm power level.

value is achieved for the output load range of 3 to 6 k $\Omega$  under the initial power and frequency conditions of -15 dBm and 2.45 GHz, respectively. Figure 3.21 depict the load/source pull efficiency contours for the output load value of 5 k $\Omega$  where the

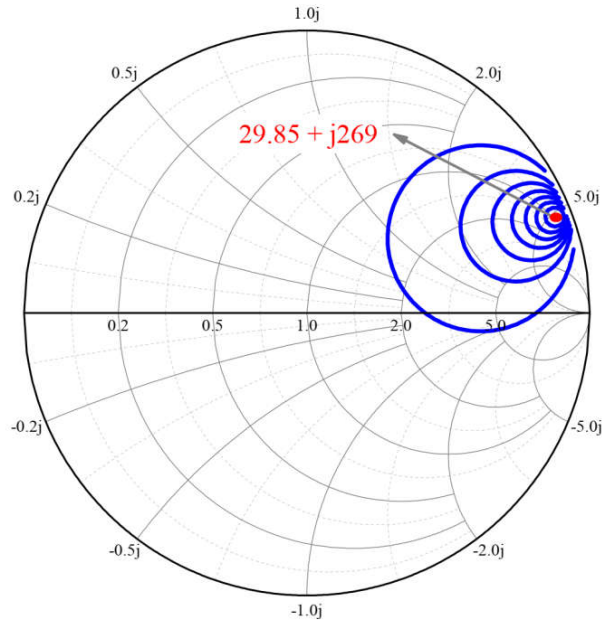


Figure 3.21. The simulated load/source pull contours on the Smith chart at 2.45 GHz and for power level of -15 dBm extracted from ADS.

maximum possible efficiency is about 38% and marked in red on the graph. It is worth noting that, in the given graph, the efficiency is reduced by 5% as the contours are expanded, in which, the efficiency inside the largest contour (if not overlapped by higher efficiency contours) is no more than 3%. Hence, a matching network can be simply constructed by providing the converse conjugate of the presented impedance. The simulated efficiency of the half-wave rectifier for various output load values are presented and discussed in the next section.

### 3.3.4 Design of Voltage Doubler Rectifier for Microwave Energy Harvesting System

The design of an efficient rectifier follows by determination of complex input impedance of the diodes which is a function of several variables such as power, frequency, harmonic termination and output load. Since, the values of junction capacitance and diodes inherent resistance is extremely non-linear, the analysis of the

diodes must be performed under the large signal and HB conditions. In order to have a better understanding about the performance of different rectifier topologies, a comparison is made between power conversion efficiency and DC output voltage of half-wave rectifier, full-wave and two stage voltage doubler for different output loads of 1 k $\Omega$ , 5 k $\Omega$  and 10 k $\Omega$  presented in Figure 3.23. As is observed, the half-wave rectifier achieves its best performance under the low load condition ( $R_L = 1$  k $\Omega$ ) with an efficiency better than 40% from -10 to 7.5 dBm. As the value of load increases to 5 k $\Omega$ , the efficiency drops at the high power levels while the efficiency at the low power levels  $P_{inc} \leq -10$  increases. Under this condition the peak efficiency of 42.4% at -11 dBm is obtained. However, the efficiency is noticeably reduced for the output load of 10 k $\Omega$  in which the achieved efficiency becomes lower or equal to that of the

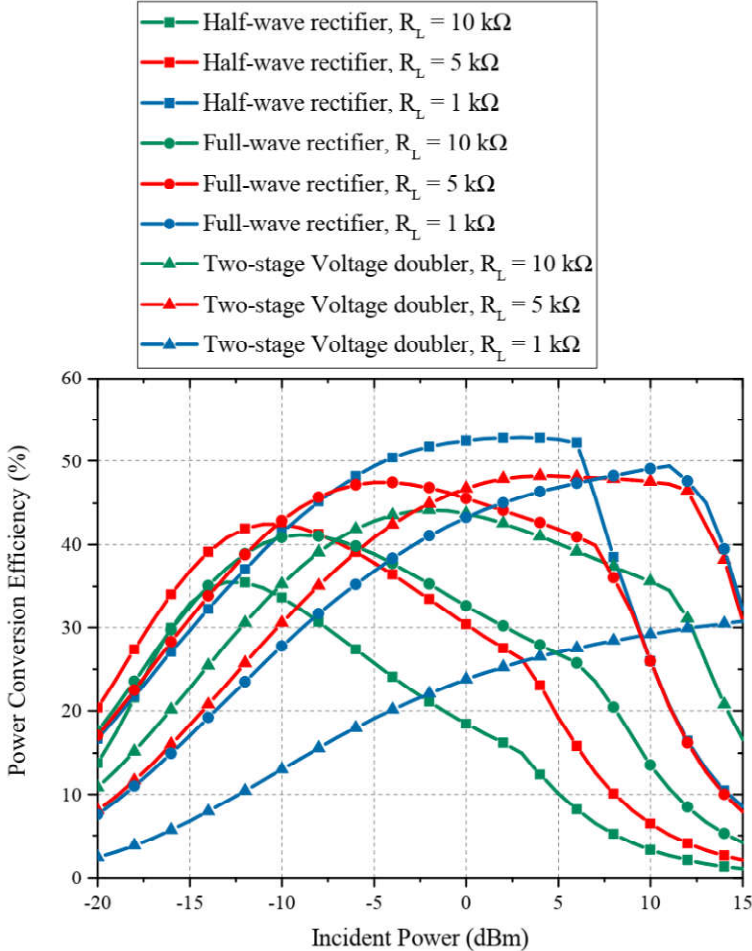


Figure 3.22. Power conversion efficiency for different output load values.

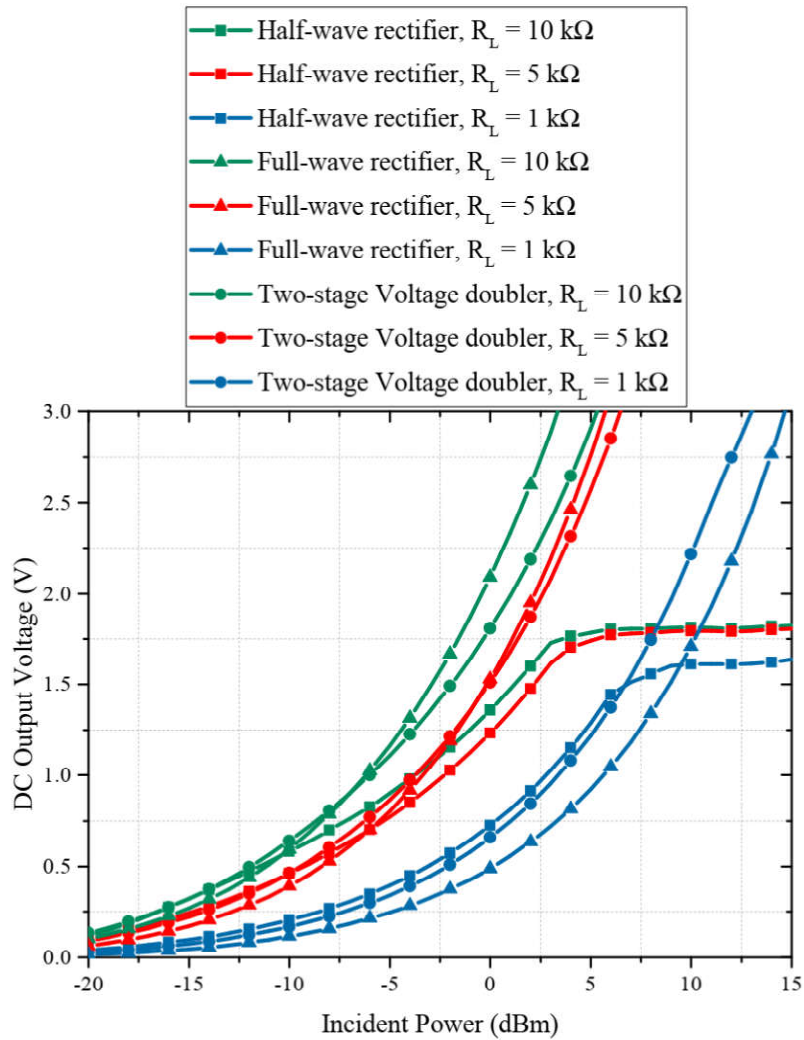


Figure 3.23. Output voltage results for various output load values.

voltage doubler all over the power levels. In oppose to a half-wave rectifier, both single and two-stage voltage doubler exhibit better efficiency performance for the high output loads, nonetheless, due to the lower loss caused by the increasing of the diodes, the voltage doubler outperforms the two-stage rectifier particularly at the low power levels. A summary of different rectifier topologies and their performance is given in Table 3.3.



Table 3.4 The optimal dimensions of the designed rectifier

Parameter	Length (mm)	Parameter	Length (mm)
$L_1$	3.06	$L_8$	7.8
$L_2$	2.85	$L_9$	19.09
$L_3$	4.46	$W_f$	1.18
$L_4$	4.68	$W_1$	0.49
$L_5$	7.7	$W_2$	0.3
$L_6$	6.05	$W_3$	1.18
$L_7$	6.04		

A DC pass filter from quarter-wavelength resonating stubs are designed to provide short up to 6<sup>th</sup> order harmonics. The DC filter used here exhibits good harmonic termination characteristic where the first quarter-wavelength stub achieves short circuit at the fundamental, and all odd harmonic frequencies where the second resonating stub ( $\lambda/4@2f_0$ ) provides short at any frequency that is the odd multiple of the second harmonic. Lastly, by adding the third quarter-wavelength stub half a wavelength away from the diodes plane ( $\lambda/2@4f_0$ ), continues termination up to 7<sup>th</sup> harmonic is obtained. The simulated harmonic terminating characteristic of the designed DC pass filter is illustrated in Figure 3.25. The advantage of employing the DC pass/ RF block filter is to terminate the generated harmonics while protecting the output device. It can be seen that, the first four harmonic frequencies present decent shorting termination to the incoming signal while the fifth termination is slightly inductive ( $0.018 + j0.06 \Omega$ ). However, this value of termination is adequate as the harmonic power generated at fifth harmonic is fairly small.

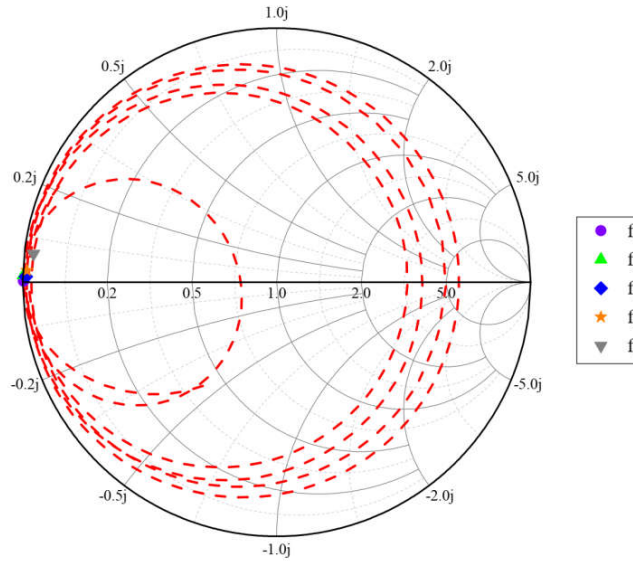


Figure 3.25. Simulated return loss of the DC pass filter providing short to the fundamental and harmonic frequencies.

To find the optimum load value for the best efficiency over large range of power levels, the source/load pull setup established and harmonic balance analysis is performed in the ADS software as shown in Figure 3.26.

Using the source pull technique, the simulator iteratively sweeps the magnitude and phase of the port at the given power and frequency, where the values of current and voltages at each node is iteratively calculated. The resultant DC output voltage is then quantified for each value of the DC output power and the efficiency contours are plotted on the Smith chart where the region of maximum efficiency can be determined.

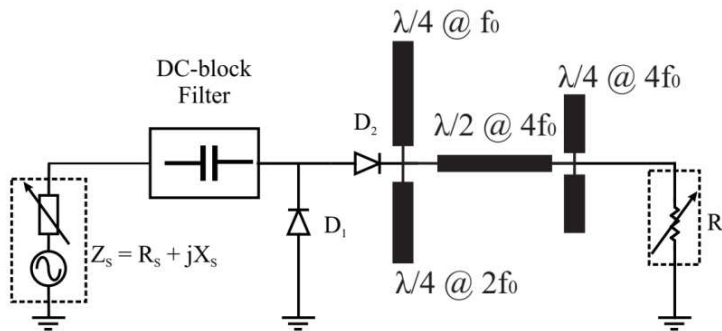


Figure 3.26. The basic test setup used for the source/load pull measurement in ADS software.

Figure 3.27 demonstrates the efficiency contours obtained for the efficiency higher than 40% at different power levels. It is observed that the efficiency contours under the medium load condition (4.3 k $\Omega$ ) presents a much larger efficiency region when compared with that of higher load (10 k $\Omega$ ) which can greatly simplify the design of matching network. Moreover, for a high load value it can be noticed that, the efficiency contours are not harmonized that reduces the possibility of achieving high RF-to-DC conversion efficiency over large power dynamic range. This effect can be better shown by plotting the two graphs on the same Smith chart as shown in Figure 3.28. As is seen, there are several possible scenarios where some important matching regions are highlighted.

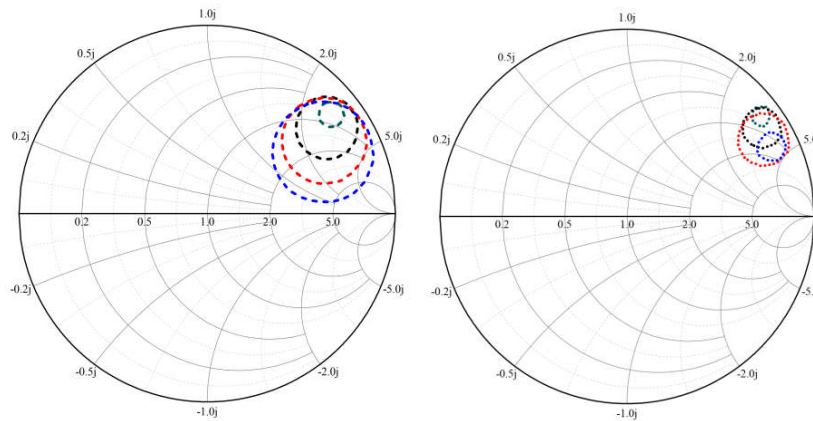


Figure 3.27. The efficiency contours obtained from source/load pull analysis to realize efficiency higher than 40% for the load values of: (a) 4.3 k $\Omega$  and (b) 10 k $\Omega$ . The dark cyan, black, red and blue colour lines indicate the power levels of -10, -5, 0 and 5 dBm, respectively.

It can be noticed that, if a matching network is properly designed within the region (A), it can provide power conversion efficiency better than 40% for the power range of -10 to 5 dBm under the output load value of 4.3 k $\Omega$ . Same condition applies for region (B) and (C) where the power conversion efficiency better than 40% can be obtained from -5 to 5 dBm and -10 to 0 dBm, respectively. There are also, two important regions that encompass wide dynamic range for both output load cases denoted as region (E) and region (D) that can provide matching for the high and low power levels, respectively. Notice that the region (D) is the overlap of region (C) and (A).

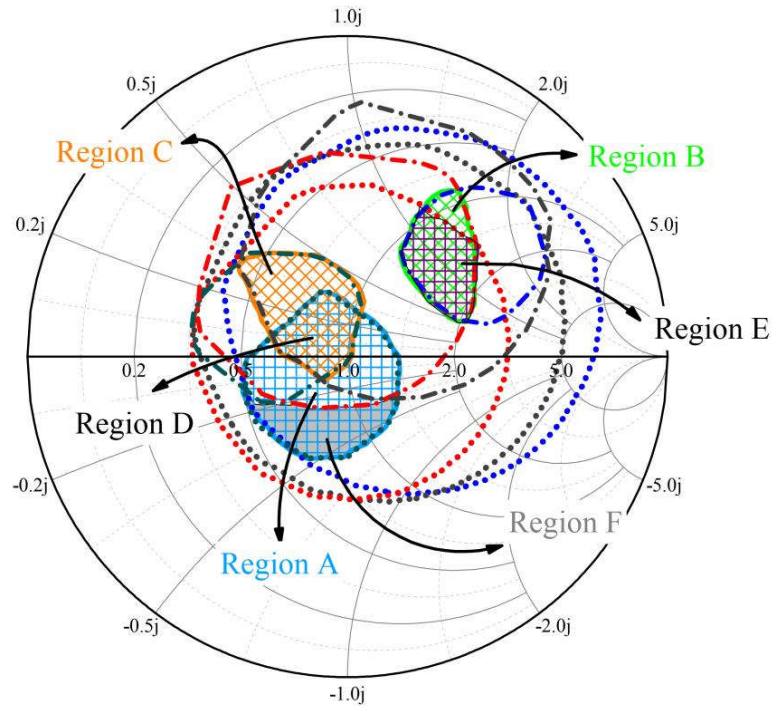


Figure 3.28. Simulated 40% efficiency contours for the output values of 4.3 k $\Omega$  (dotted lines) and 10 k $\Omega$  (dash-dotted lines). For the better demonstration, the values are normalized to  $Z_0 \times (0.8 - j2.81)$  on the Smith chart. The dark cyan, dark gray, red and blue colour lines indicate the power levels of -10, -5, 0 and 5 dBm, respectively.

The simulated power conversion efficiency by providing the matching condition at region (E), (D) and (F) are plotted in Figure 3.29. As is observed, for the rectifier matched at region (E), the highest efficiency of 73.6% has been obtained for the power level of 5 dBm. However, while the efficiency remains high for the power levels above -5 dBm, it significantly reduces as the power level drops to -10 dBm. On the other hand, the rectifier matched to region (F) shows the worst performance, since the rectifier can only provide acceptable efficiency within a very limited output load for all power levels. Lastly, the rectifier matched at region (D) exhibits the best performance for the operation at low power levels for various output load values which is very suitable for energy harvesting applications. However, the efficiency obtained is not entirely satisfactory. A further investigation into the rectifier performance reveals the high value of harmonics generated by diodes at the input terminal. Hence, a harmonic rejection filter (HRF) in the form of low pass filter is designed and placed at the input of the signal source to ensure the rejection of all the harmonics generated from the diodes. By providing such a condition, the generated harmonics are

terminated and forced to participate on another cycle of rectification leading to increased efficiency of the overall system. It is extremely important to notice that, prior to the design of the matching network, the input impedance of the rectifier (including the all the components) must be experimentally determined such as Thru-Reflect Line (TRL) method. The acquired data can then be used as a black-box for the final matching network design. A co-simulation is then performed to make sure that all the circuit component performance including the substrate and metal losses of the overall circuit have been taken into account. The proposed modified rectifier is fabricated on a 20-mil-thick RO4003C substrate with a relative permittivity of 3.38 and loss tangent of 0.0029. The photograph of fabricated modified rectifier is depicted in Figure 3.30.

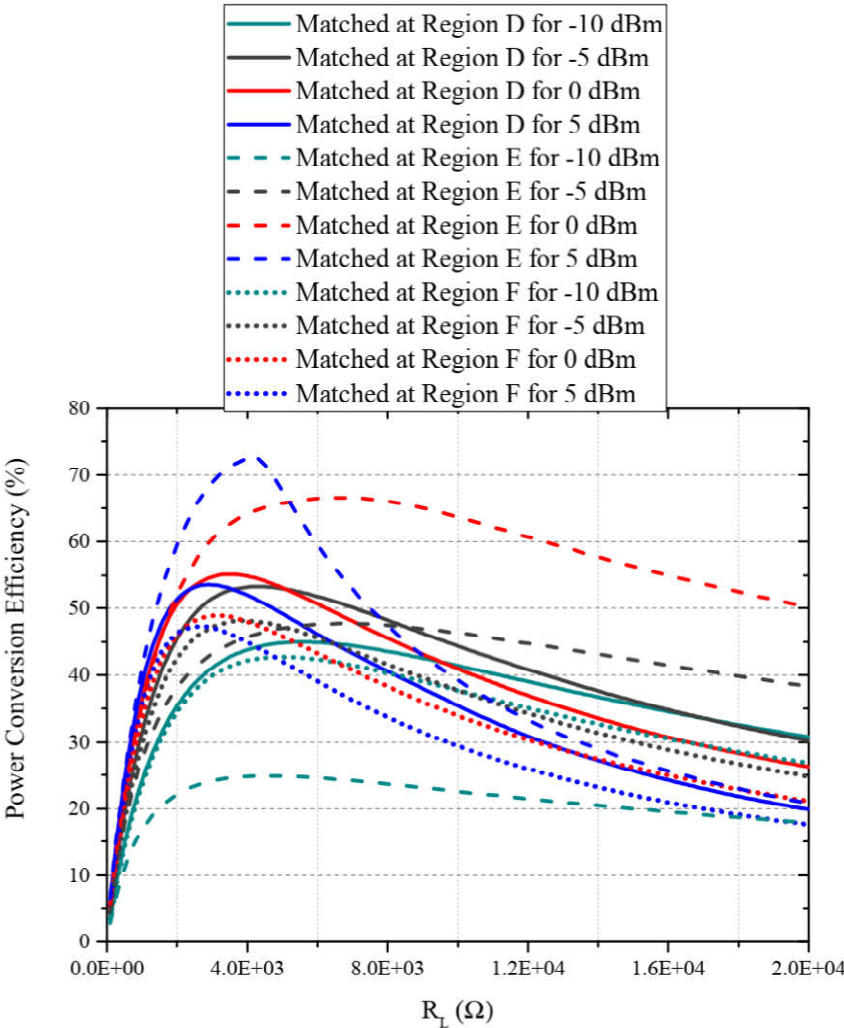


Figure 3.29. Simulated power conversion efficiency as a function of output load value.

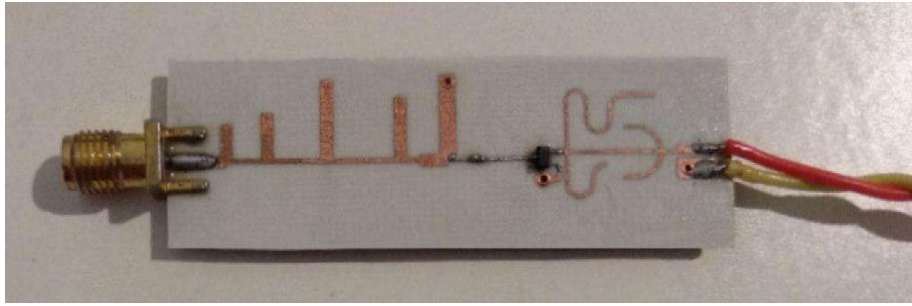
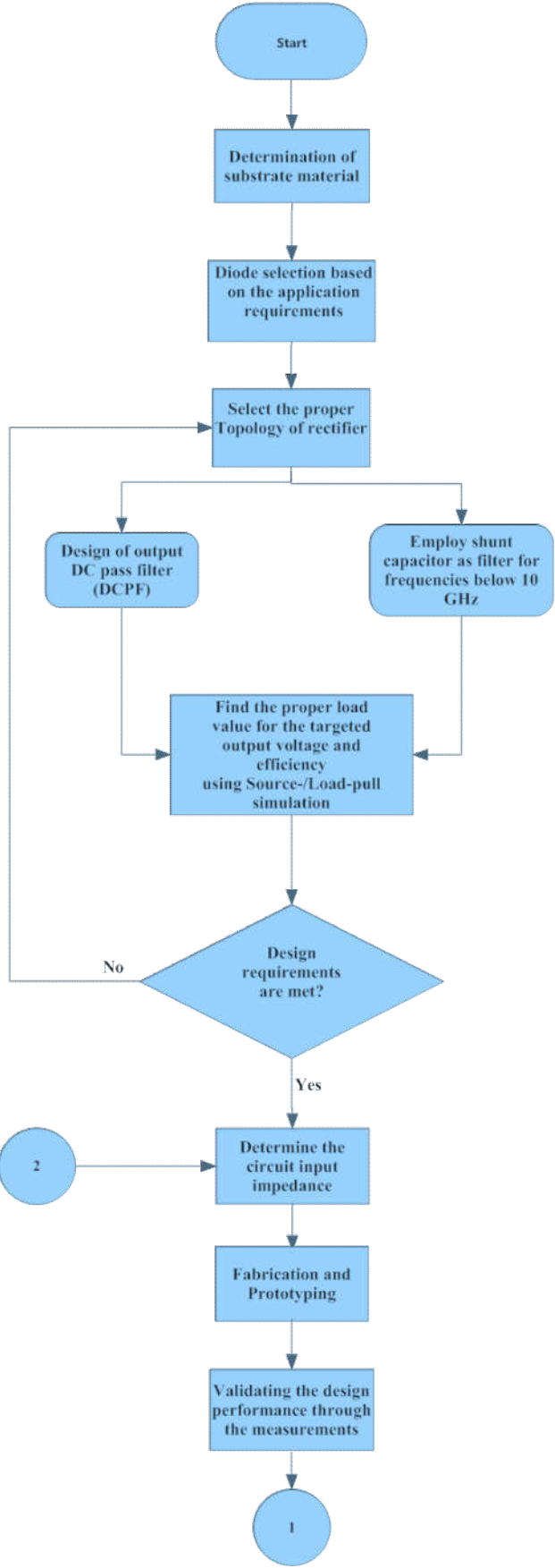


Figure 3.30. The photograph of the fabricated modified rectifier.

### 3.3.6 High Efficiency and Broadband Rectifier for Energy Harvesting System

Conventional rectifiers generally suffer from narrow band operation and low dynamic power range caused by nonlinearity of the rectifying element [31]. Unlike the previous case that the high efficiency at a single frequency was the only concern of the design, in a more realistic case, the level of receiving power at a single frequency may not be adequate for the energy harvester operation.

In this section, a method for the design of a compact and broadband rectifier based on dual mode switching configuration is proposed, which can effectively enhance the efficiency and input power dynamic range of the rectifier, simultaneously. The design methodology of the proposed broadband rectifier is illustrated in Figure 3.31.



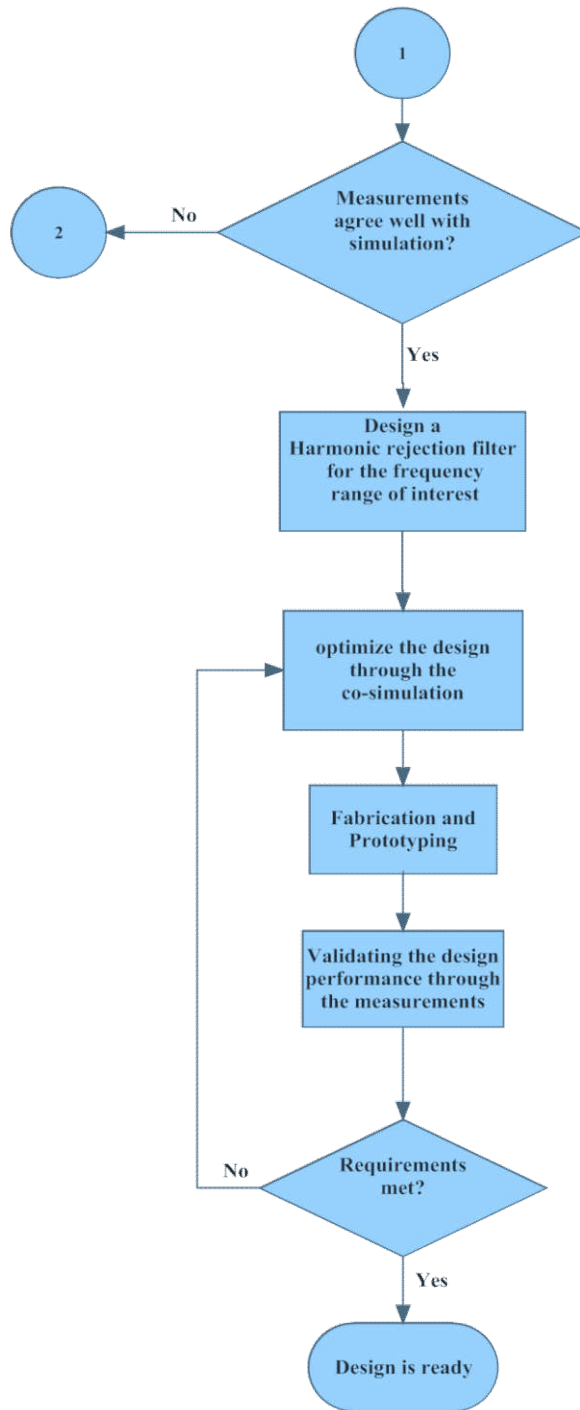


Figure 3.31. The methodology flowchart for the design of broadband rectifiers.

### 3.3.6.1 Broadband Rectifier Design

As shown in the previous section a single rectifier is limited in terms of power range and the bandwidth. In [108] an idea was introduced to employ a high frequency low power active switch at the input of rectifiers so that each rectifier with different output

load values could operate depending on the power conditions. Nevertheless, it requires biasing and some power would dissipate on the switch itself that restricts its performance. Here, to compensate for this issue, we introduce a secondary rectifier operating at a frequency around the primary rectifier. By adjusting the resonance frequencies to be close enough while taking into account the power level condition the performance bandwidth can be effectively improved. Such a technique allows for much smaller rectifier footprint which is critical to energy harvesting applications while avoiding highly complex matching network in which even slight deviation from the targeted resonant frequencies can result in large power leakage and deteriorating the rectifier performance. Figure 3.32 shows the general block diagram of the proposed broadband rectifier. As is observed, it composed of a DC-block filter ( $C_1$  and  $C_3$ ), a matching network to deliver the maximum power to the rectification circuit, rectifying elements in the form of voltage doubler, DC pass filter ( $C_2$  and  $C_4$ ) and output load resistor ( $R_{L1}$  and  $R_{L2}$ ). A T-junction power divider is employed to feed the two rectifiers matched to their respective input transmission line impedances at the targeted frequency  $f_0$  and input power level. The frequency dependent characteristic of the feeding T-junction is vanished by eliminating commonly used quarter-wavelength

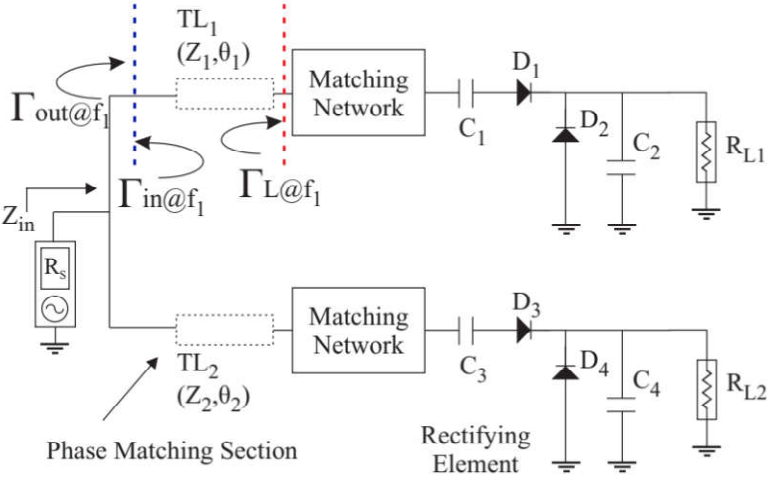


Figure 3.32. General block diagram of the proposed broadband rectifier.

transformers which also results in more compact size of the overall rectifier. Hence, under the same power condition, the entire matching network and the rectifier can be treated as a resonant load at the frequencies  $f_1$  and  $f_2$  where the magnitude of  $\Gamma_{out}$  equates  $\Gamma_{in}$  with an arbitrary phase value  $\theta$ . Since the rectifiers are initially matched to their corresponding transmission line impedances, the required electrical length to achieve phase matching for each branch at  $f_1$  and  $f_2$  is then determined as

$$Z_{in} = Z_1 \left( \frac{1 - |\Gamma_{L_{-f1}}| e^{-2j\theta_1}}{1 + |\Gamma_{L_{-f1}}| e^{-2j\theta_1}} \right) \quad \text{Equation (3.44)}$$

where  $Z_1$ , is the characteristic impedance of the transmission line and  $\theta_1$  is the electrical length of the line at the frequency of  $f_1$ . Here,  $\Gamma_{L_{-f1}}$  is the reflection coefficient of the complex load at the input of the matching network and defined as

$$\Gamma_{L_{-f1}} = \frac{Z_{L_{-f1}} - Z_1}{Z_{L_{-f1}} + Z_1} \quad \text{Equation (3.45)}$$

The same procedure is applied on the second rectifier to provide matching at  $f_2$ . As an example, Figure 3.33 demonstrates the simulated return loss response of an L-matched rectifier in which the rectifier is matched to the 100  $\Omega$  transmission line at 2.45 GHz and under 0 dBm power level. It is worth noting that, since the diode is non-linear, the impedance characteristics of the rectifier is changed depending on the input power level such that at 6 dBm below the designed power condition, the designed matching network provides no matching to the targeted frequency range being 2.4 to 2.5 GHz. Since our aim is to use a 3-dB power divider, the two potential frequency points  $f_1$  and  $f_2$  are located at 2.36 and 2.52 GHz in this case as marked on the figure. Figure 3.3 shows the two potential frequency points of 2.36 and 2.52 GHz for the phase matching as they both are located on the  $\Gamma_L = 0.33$  circle while having different phase value.

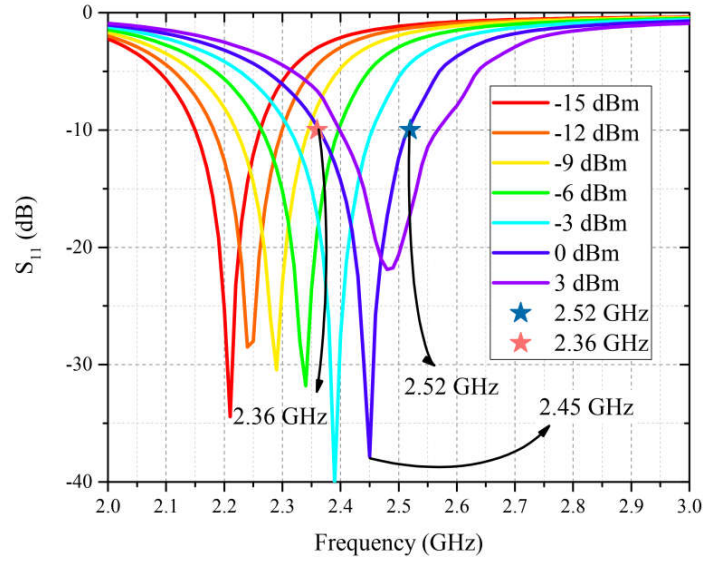


Figure 3.33. Simulated return loss of a single L-matched rectifier at different power levels for  $R_L = 10 \text{ k}\Omega$ .

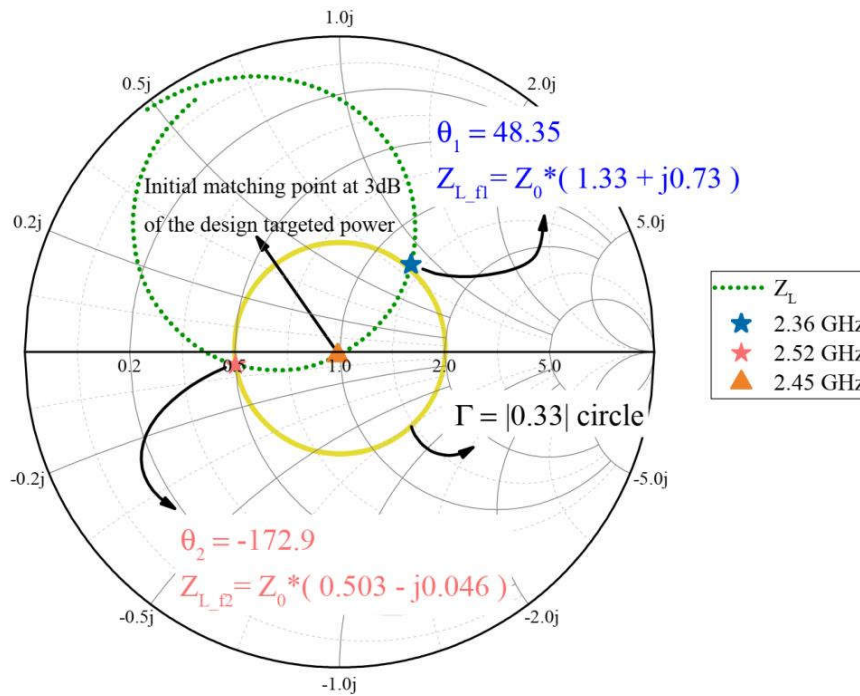


Figure 3.34. The simulated input impedance  $Z_L$  seen at the input of the matching network. The matching network provides matching at 2.45 GHz to the  $100 \Omega$  line. All the values are normalized to  $100 \Omega$ .

Hence, by increasing/reducing the length of the feeding transmission line (each arms of the T-junction), the phase matching condition can be provided. Alternatively, one can find the required length of the line as

$$t = \frac{X_L Z_1}{R_L^2 + X_L^2 - \frac{R_L Z_1}{\alpha}} \quad \text{Equation (3.46)}$$

where  $\alpha$  is the ratio of input to the line impedance ( $Z_0 / Z_1 = 1/2$ ). Thus, the exact electrical length for the phase matching ( $d_{P.M}$ ) is determined as

$$d_{P.M} = \begin{cases} \frac{\tan^{-1} t}{2\pi} \lambda & t \geq 0 \\ \frac{1}{2} + \frac{\tan^{-1} t}{2\pi} \lambda & t < 0 \end{cases} \quad \text{Equation (3.47)}$$

Here  $\lambda$  is the wavelength at its corresponding frequency point.

Based on the above analysis, a rectifier is designed operating at 2.45 GHz using commercial Schottky diode HSMS-285C from BROADCOM with built-in voltage  $V_f = 150$  mV, breakdown voltage  $V_{br} = 3.8$  V, series resistance  $R_s = 25$   $\Omega$ , and junction capacitance  $C_{j0} = 0.18$  pF. The proposed rectifier is simulated through co-simulation using harmonic balance analysis in ADS. Figure 3.35 shows the configuration of the broadband rectifier where the transmission and return loss responses of the designed harmonic rejection filter is plotted in Figure 3.36. It can be observed that, the designed filter has a rejection band from 5 to 12.5 GHz with a small band notch around 9.3-9.87 GHz which can reject all the third and fifth order harmonics. The 3-dimensional view of the  $S_{11}$  as a function of frequency and input power under the large signal condition is illustrated in Figure 3.37.

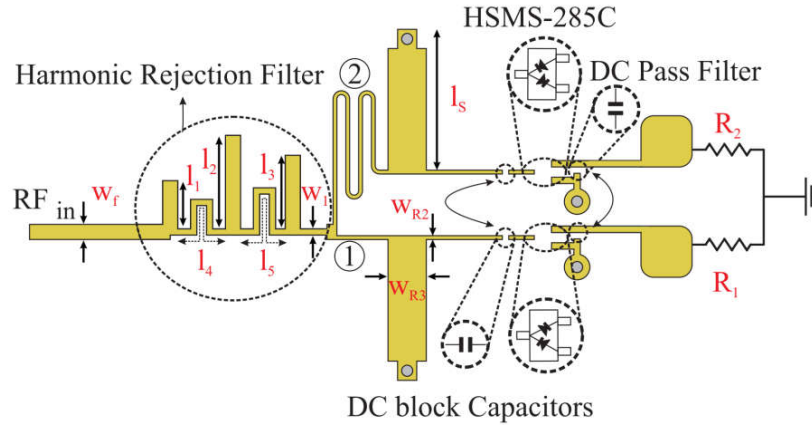


Figure 3.35. Layout of the broadband dual output rectifier.

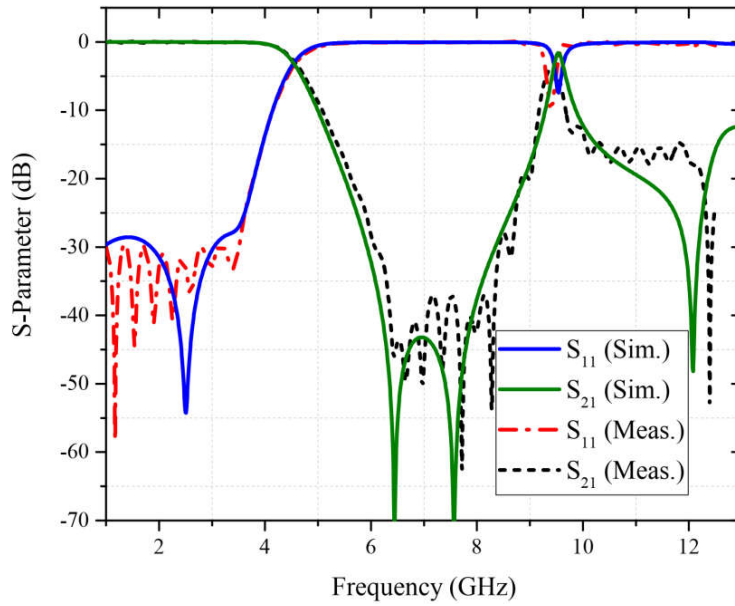


Figure 3.36. The transmission and return loss responses of the designed harmonic rejection filter.

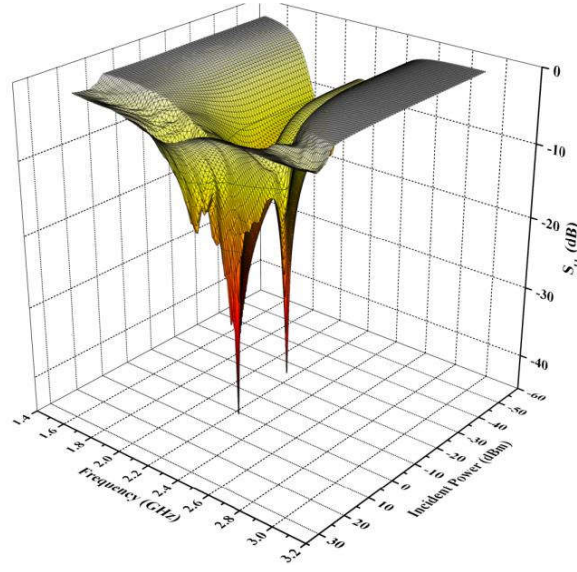


Figure 3.37. Simulated 3-D view of the return loss versus frequency and power level.

The proposed broadband rectifier is fabricated on a 20-mil-thick RO4003C substrate with a relative permittivity of 3.38. The length of the short and long arms are  $11.7^\circ$  and  $102^\circ$ , respectively, and diameter of all via holes are 0.8 mm.

Table 3.5 The optimal parameter values of the proposed rectifier design.

Parameter	Length (mm)	Parameter	Length (mm)
$l_1$	3.4	$W_1$	0.5
$l_2$	7.3	$W_f$	1.18
$l_3$	5.74	$l_s$	9.5
$l_4$	7.3	$W_{R2}$	0.3
$l_5$	8.9	$W_{R3}$	2.8

The photograph of the fabricated prototype is depicted in Figure 4.5. The footprint of the proposed rectifier is  $0.38 \lambda_0 \times 0.25 \lambda_0$ , where  $\lambda_0$  is the free space wavelength at 2.45 GHz. The return loss is measured using vector network analyzer (VNA) where

the measured and simulated results is demonstrated in Figure 4.6. The variation on the rectifier return loss response is the impact of junction capacitance which imposes change on the input impedance of diodes as the power varies. The RF-to-DC power conversion efficiency is evaluated by

$$\begin{aligned}\eta(\%) &= \frac{(P_{DC1}) + (P_{DC2})}{P_{in}} \times 100 \\ &= \frac{(V_{DC1})^2 + (V_{DC2})^2}{P_{in} \times R_L} \times 100\end{aligned}\quad \text{Equation (3.48)}$$

where  $V_{DC1}$  and  $V_{DC2}$  are the DC output voltage measured across the load resistor  $R_1$  and  $R_2$ , respectively, and  $R_1 = R_2 = R_L = 10 \text{ k}\Omega$ .

### 3.4 Metamaterial-Based Miniaturized Wideband Antennae for Energy Harvesting Systems

Microstrip patch antennas are extensively used in wireless communications due to the advantages of low profile, light weight, and low cost [109, 110]. In principle, the radiation on the antenna is caused from impedance discontinuities within the antenna structure where the type of polarization and phase of scattered electromagnetic fields depends on the location of source and antenna geometry. Hence, the total radiated power from an antenna is the sum of source radiation and the scattered fields from the antenna discontinuities. An efficient antenna must have identical and in-phase harmonic polarity at each discontinuity to produce maximum radiation. To provide such condition the following equation must be satisfied as [109]

$$|\varphi_n - \varphi_{n-1}| = \frac{2\pi l}{\lambda_p} = \pi \quad \text{Equation (3.49)}$$

where  $\varphi_{n-1}$  and  $\varphi_n$  are the radiation phase at two consecutive time instance,  $l$  is the resonator length and  $\lambda_p$  is the wavelength. Therefore, for a resonant type antenna such as microstrip patch antennas, the size of antenna is determined by frequency of operation to be half a wavelength. Owing to the requirements on small antennas,

different approaches have been introduced to overcome this problem by employing the shorting pins [44] and etching slots [45]. Nevertheless, miniaturizing antenna size via traditional miniaturization methods often result in narrow bandwidth, low radiation efficiencies and undesired radiation patterns. In addition to the aforementioned approaches, the antenna miniaturization can be achieved by dividing the transmission line into small segments as shown in Figure 3.38.

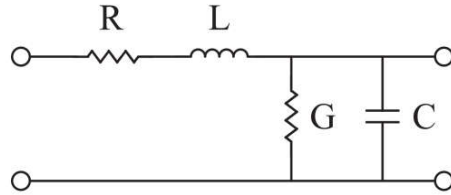


Figure 3.38. Equivalent circuit model corresponding to a small section of traditional TL.

Where the characteristic impedance ( $Z_c$ ) and phase velocity ( $v_p$ ) of this small segment can be determined as

$$Z_c = \sqrt{\frac{R + j\omega L}{G + j\omega C}} \quad \text{Equation (3.50)}$$

$$v_p = \frac{1}{\sqrt{LC}} \quad \text{Equation (3.51)}$$

Therefore, by increasing the effective capacitance and inductance of the transmission line segment, the phase velocity of constructed transmission line can be reduced allowing for realization of an antenna with much smaller size than conventional half-wavelength antenna while the constructive radiation is maintained. Such condition can be simply provided by using high dielectric substrates [109]. However, the drawback of this method is the strong dependence of the transmission line on the physical properties of the material used which can unfavorably increase the overall cost of design. A novel and effective technique for the antenna miniaturization is to employ the metamaterial structures. By constructing an artificial transmission line it is possible to realize a structure with predefined physical properties such as anti-parallel phase velocity independent of the material properties.

### 3.4.1 Composite Left/Right-Handed (CRLH) Transmission Line

The transmission line (TL) approach is a simple yet effective way of modeling and analysis of CRLH metamaterial structures [116]. Assuming the TL to be lossless, a small section can reveal the overall characteristic of the media. By employing the LC model of purely left-handed material proposed by Brillouin and Pierce, and combining that with purely right-handed model a composite LC circuit model is realized that commonly referred as CRLH material. The general homogenous LC circuit per unit length of purely RH, purely LH and their combined equivalent model for CRLH are shown in Figure 3.39 (a)-(c).

Referring to the circuit model of LH material, the propagation constant, phase velocity and group velocity can be derived as [116]

$$\gamma = \alpha + j\beta = \sqrt{Z'Y'} = -\frac{j}{\omega\sqrt{C_L L_L}} \quad \text{Equation (3.52)}$$

$$v_p = \frac{\omega}{\beta} = -\omega^2 \sqrt{C_L L_L} \quad \text{Equation (3.53)}$$

$$v_g = \frac{d\omega}{d\beta} = \omega^2 \sqrt{L_L C_L} \quad \text{Equation (3.54)}$$

It is interesting to notice that, for the LH media, the phase velocity ( $v_p$ ) takes the negative sign in opposed to the RH media given in Equation (3.51). This indicates the antiparallel phase and group velocity propagation in LH media as the direction of energy flow (pointing vector (S)), determined by group velocity ( $v_g$ ), is not changed and remained forward. As a matter of fact, CRLH transmission line possesses all the characteristics of both LH and RH materials. Notice that, there are also resistance  $R$  and conductance  $G$  to account for the conductor and substrate losses. Thus, a more generalized circuit model can be presented as shown in Figure 3.40.

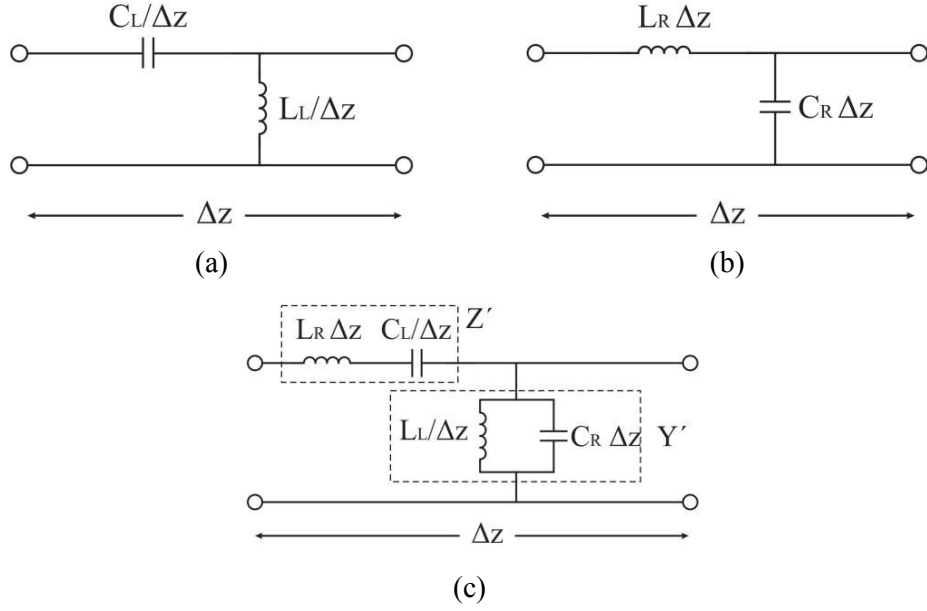


Figure 3.39. Equivalent circuit model for (a) purely left-handed; (b) purely right-handed transmission lines and (c) homogenized CRLH transmission line.

In this model, the series capacitance and shunt inductance  $C_L$  and  $L_L$  contribute to the left-handed characteristic, while shunt capacitance and series inductance  $C_R$  and  $L_R$  provide the right handed property of the CRLH-TL.

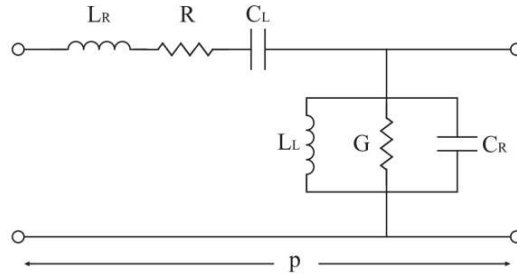


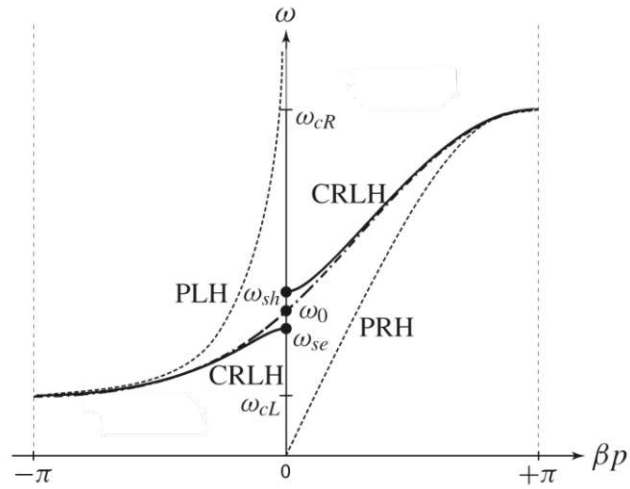
Figure 3.40. Generalized circuit model of CRLH-TL unit-cell.

Therefore, the characteristic impedance  $Z_c$  and propagation constant  $\beta$  of the periodic structure are determined as [116]

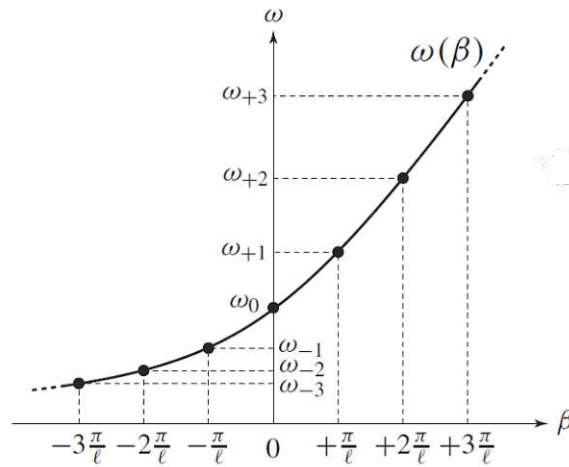
$$Z_c = \sqrt{\frac{Z'_{series}}{Y'_{shunt}}} = \left( \frac{R + j \left( \omega L_R - \frac{1}{\omega C_L} \right)}{G + j \left( \omega C_R - \frac{1}{\omega L_L} \right)} \right)^{1/2} \quad \text{Equation (3.55)}$$

$$\beta = \frac{1}{p} \cos^{-1} \left[ 1 - \frac{Z'_{series} Y'_{shunt}}{2} \right] \quad \text{Equation (3.56)}$$

where  $p$  is the physical length of the unit cell. A comparison between the dispersion diagram of purely left-handed (PLH), purely right-handed (PRH) and CRLH transmission lines are demonstrated in Figure 3.41.



(a)



(b)

Figure 3.41. Dispersion diagram of CRLH transmission line (a) unbalanced and (b) balanced case.

From Figure 3.41(a), it is observed that in the case of PLH the propagation constant  $\beta$  takes the negative values which is in contrast with the conventional PRH with the

propagation constant being always positive ( $\beta > 0$ ). Moreover, it can be seen that the CRLH structure exhibits both LH and RH properties in which the propagation constant becomes zero at two frequency points denoted by  $\omega_{sh}$  and  $\omega_{se}$ . Such a condition where  $\omega_{sh} \neq \omega_{se}$  is called unbalanced condition. On the other hand, as shown in Figure 3.41(b), by adjusting the LC values of CRLH transmission line,  $\omega_{sh}$  and  $\omega_{se}$  can become equal ( $\omega_{sh} = \omega_{se} = \omega_0$ ) which is referred as balanced condition. Balanced condition is extremely important for the design of CRLH filters as well as leaky-wave antennas as it can guarantee the continuous operation of design over a large frequency span by combining both RH and LH bands. It can also be noted that, while the same amount of resonances occur at the LH band, these resonances are in a much lower frequencies than that of RH bands. Since these resonances within the LH band have a negative propagation constant, they are referred as negative order resonances. Notice that unlike the resonances within the RH band that are in exact harmonics, negative order resonances are spread in a non-linear fashion.

### 3.4.2 CRLH Leaky-Wave Antenna

For over than a decade Meta-material antennas have earned significant attention. Various types of metamaterials have been invented such as split ring resonator (SRR), chiral metamaterials and composite right/left-handed (CRLH) structures. However, the broadband characteristic, strictly planar structure, lower loss and integration of passive elements makes CRLH more attractive compared with other aforementioned structures [116, 117]. An application of CRLH structures is to design a leaky wave antenna (LWA). LWA are a class of antennas that use a traveling wave on a guiding structure as the main radiating mechanism [109]. Some of the interesting advantages of LWA's are their beam scanning capability and reduced feed network complexity when compared with typical array antennas. A LWA is characterized by dispersion  $\beta$  and attenuation constant  $\alpha$  forming the propagation factor  $k$  [118, 119]. Considering direction of propagation to be y-axis, the propagation factor can be written as:

$$k_y = \beta_y - \alpha_y \quad \text{Equation (3.57)}$$

As a wave propagates through a LWA structure, the energy partially leaks from the discontinuity introduced on the structure. The radiation properties of the LWA is restricted to  $\alpha$  and  $\beta$  in which if  $\alpha$  is large, the power strongly leaks out at the beginning of the LWA forming a short effective antenna aperture and a wide beam pattern is achieved. On the other hand, if the value of  $\alpha$  is adequately small, the power leaks slowly along the LWA leading to the realization of long aperture and a narrow beam-width pattern consequently.

Leaky wave antenna (LWA) is of significant interest due to their beam scanning ability and has been used for many communication systems [117]. However, in conventional LWA, the antenna operates in the right-handed region only, hence the scanning is delimited from nearly bore-sight up to nearly end-fire direction [117, 120].

Figure 3.42 depicts the general concept of back-fire to end-fire radiation of the CRLH LWA in which the antenna is excited from port 1 and port 2 is assumed to be terminated to the line impedance.

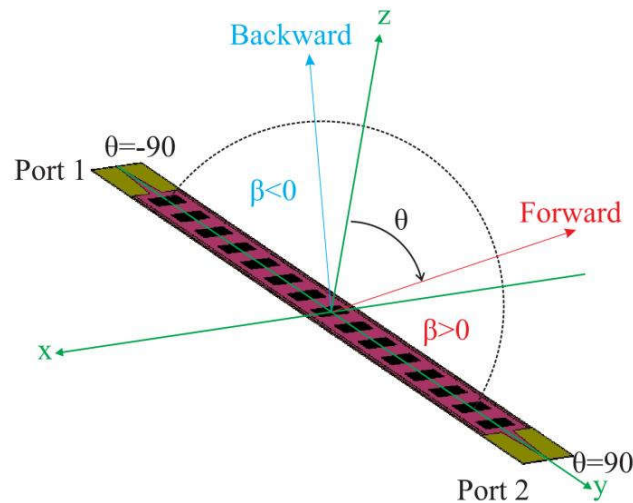


Figure 3.42. Back-fire to end-fire radiating characteristics of the CRLH LWA. Notice the backward radiation of LWA occurring at  $\beta < 0$  that is unique to left-handed property of metamaterials.

Assuming fundamental modes to be guided through the LWA structure and under the condition that  $\beta_y \gg \alpha_y$  which leads to  $k_y \approx \beta_y$  and following the split components of free-space number, one can write:

$$k_0^2 = \beta_y^2 - k_z^2 \quad \text{Equation (3.58)}$$

According to the above relation, the radiation only occurs if  $|\beta_y| < |k_0|$  which commonly known as radiating or fast wave region where the speed of wave travelling within the structure exceeds the speed of light. On the contrary, when  $|\beta_y| > |k_0|$ , the  $k_z$  component of travelling wave decays exponentially which is known as guiding or slow-wave region. Furthermore, the angle of radiation is determined by  $\beta$  and follows the equation [109, 116]

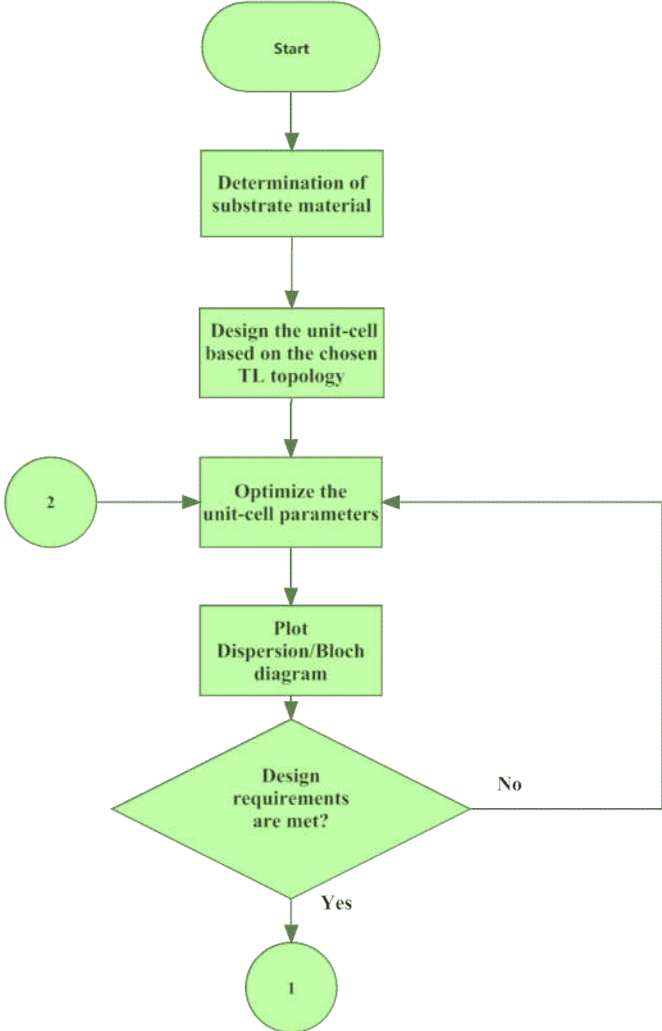
$$\theta = \sin^{-1} \left( \frac{\beta + \frac{2n\pi}{p}}{k_0} \right) \quad \text{Equation (3.59)}$$

where  $\theta$  and  $n$  are the radiation angle and space harmonic number, respectively. Hence, it is obvious that a CRLH LWA is capable of continuous back-fire to end-fire radiation under the balanced condition that could not be achieved previously. Thus, CRLH structure with the capability of supporting both forward and backward wave radiations possesses an extra advantage of wider beam steering [116, 121]. Moreover, unlike the conventional LWA, with CRLH LWA, broadside radiation is possible.

### 3.4.2.1 Unit Cell Design

Various types of CLRH LWA has been proposed on Coplanar Waveguide (CPW) [122-124], Coplanar Strip (CPS) [125] and microstrip topologies [121]. Nevertheless, most of these structures are lossy in nature due to presence of parasitic antiparallel currents. Substrate Integrated Waveguide (SIW) is superior to all aforementioned technologies owing to its unique structure exhibiting the same behavior as of the rectangular waveguide but in a very compact volume. The idea of SIW CRLH LWA

was first introduced in [126]. The high quality factor, high power handling and ease of fabrication has made SIW structure very popular for the design of microwave and millimeter wave applications [127-129]. It has also been used and combined with other topologies to reduce the cross polarization and enhance the radiation properties of various antennas [130, 131]. The flowchart of the methodology undertaken for the design of metamaterial-based antennas is presented in Figure 3.43.



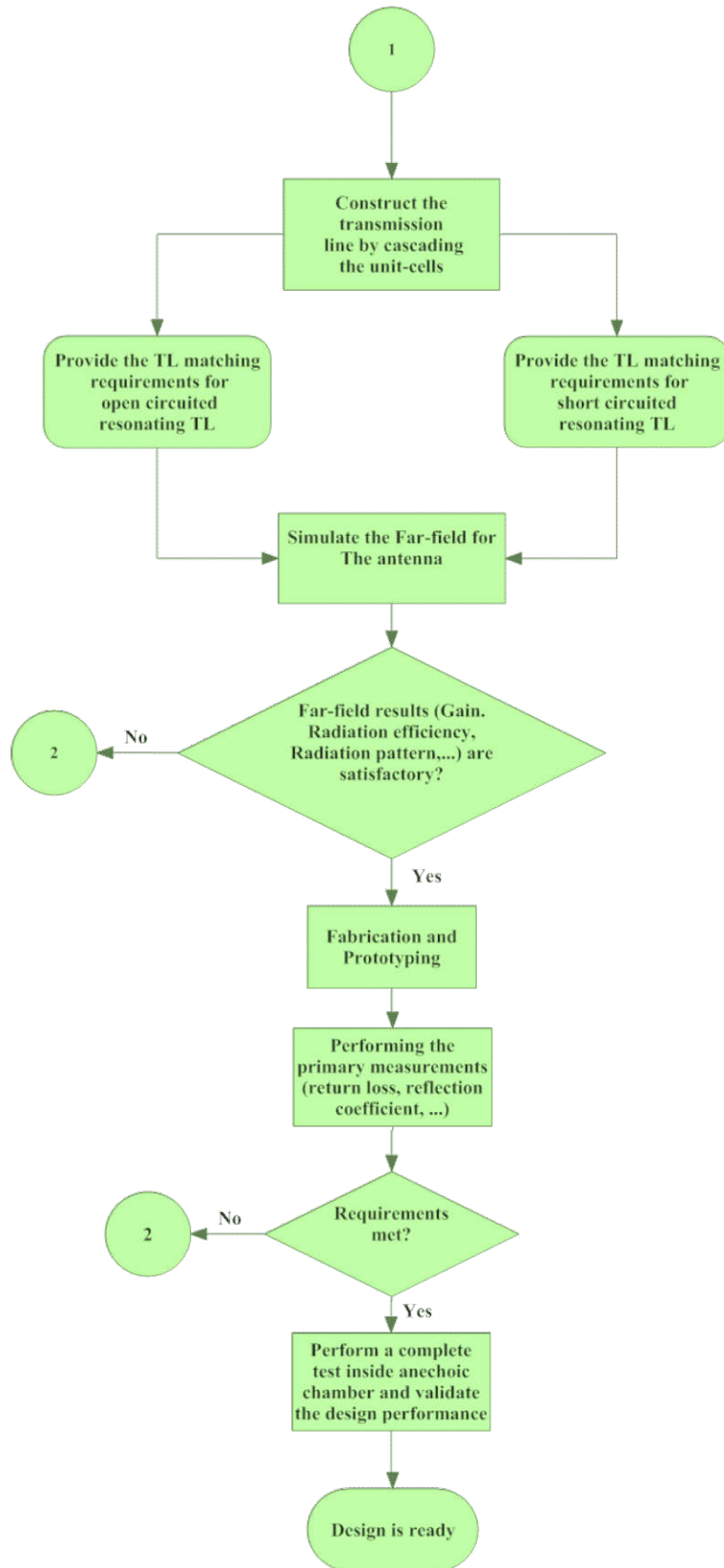


Figure 3.43 Design methodology flowchart of metamaterial-based antenna.

To design the proposed structure, the SIW topology was used as a standard host transmission line. The SIW unit cell is composed of a double layer PCB where the top and bottom metal plates are shorted using arrays of metallic vias forming a dielectric filled waveguide. The proper values of SIW parameters are found as [130]

$$W = \sqrt{\epsilon_r} \left( W_s - \frac{1.08d^2}{s} + \frac{0.1d^2}{W_s} \right) \quad \text{Equation (3.60)}$$

where  $W$  is the width of air-filled rectangular waveguide with a cut-off frequency equivalent to that of SIW for the dominant  $TE_{10}$  mode. The other parameters are relative dielectric constant of SIW ( $\epsilon_r$ ), center to center via distance ( $s$ ) and via's diameter ( $d$ ). It is also recommended to select the values of  $s$  and  $d$  to be  $s/d < 2$  and  $d/W_s < 1/8$  in order to minimize leakage from the side walls [130].

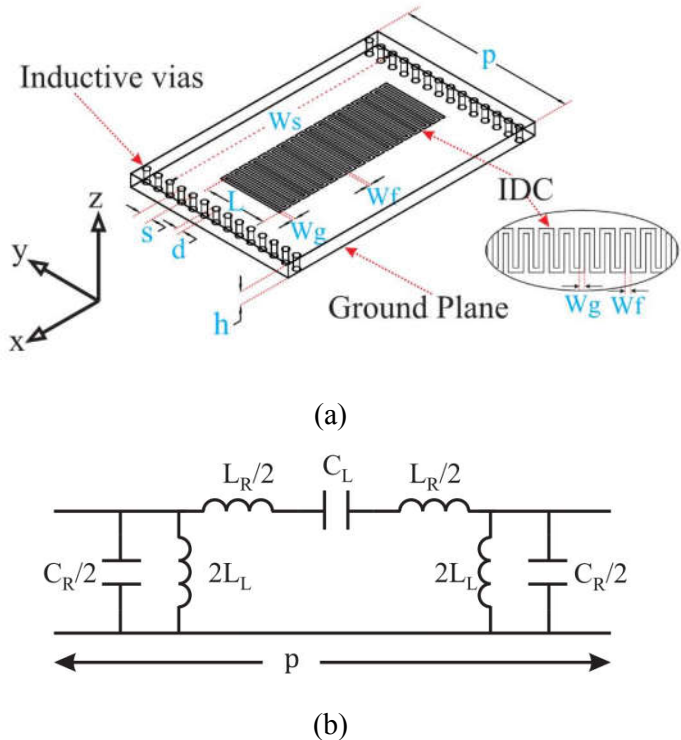


Figure 3.44. (a) The layout of proposed SIW unit cell. (b) The equivalent circuit model of the structure.

Figure 3.44 (a) and (b) show the configuration and the equivalent Pi-circuit model of the proposed unit cell, respectively. An interdigital capacitor (IDC) with 36 fingers is etched on the top layer of SIW to create an adequate series capacitance ( $C_L$ ) required for the CRLH structure. The capacitive value of IDC is changed by varying the gap  $W_g$  between two adjacent fingers. Note that the IDC also plays the role of radiating element where the EM energy is radiated through its slots. Referring to the equivalent circuit model, series inductance ( $L_R$ ) is associated with the length of the fingers  $L$  as well as the waveguide distributed inductance while the shunt inductance ( $L_L$ ) contributes to the metallic vias on the either sides of structure. Moreover, shunt capacitance ( $C_R$ ) is realized from the gap between the parallel metal plates. The right-handed property of the unit cell relates to both series inductance and shunt capacitance where the left handed property is caused by shunt inductance and series capacitance, respectively. As a result, the dispersion relation can be obtained as [116]

$$\beta(\omega) = \frac{1}{p} \cos^{-1} \left( 1 - \frac{\omega^2}{2\omega_R^2} + \frac{\omega_L^2}{2} \left( \left( \frac{1}{\omega_{sh}^2} + \frac{1}{\omega_{se}^2} \right) - \frac{1}{\omega^2} \right) \right) \quad \text{Equation (3.61)}$$

where  $\omega_{se}$  and  $\omega_{sh}$  are the resonance frequencies of the series and shunt tanks, respectively, and are defined as

$$\omega_{se} = \frac{1}{\sqrt{C_L L_R}} = 2\pi f_{se} \quad \text{Equation (3.62)}$$

$$\omega_{sh} = \frac{1}{\sqrt{L_L C_R}} = 2\pi f_{sh} \quad \text{Equation (3.63)}$$

Correspondingly,  $\omega_L$  and  $\omega_R$  are given by

$$\omega_L = 1/\sqrt{C_L L_L} \quad \text{Equation (3.64)}$$

$$\omega_R = 1/\sqrt{C_R L_R} \quad \text{Equation (3.65)}$$

Furthermore, in order to achieve closed-stop band condition (balanced condition), it is required to have both LH and RH impedances to be equal at the transition. This can be accomplished when the following relation is satisfied

$$\frac{L_L}{C_L} = \frac{L_R}{C_R} \quad \text{Equation (3.66)}$$

During the design process, the balanced condition was obtained by forcing series and shunt tanks to resonate at 2.45 GHz. In order to obtain the dispersion diagram, a full-wave simulation was carried out using CST microwave studio and is presented in Figure 3.45. The proposed unit cell was designed on RO4003C laminate with a thickness of  $h = 0.508\text{mm}$ , dielectric constant of  $3.36 \pm 0.05$  and loss tangent of 0.0027. The values obtained for the circuit model parameters are:  $C_L = 1.82\text{ pF}$ ,  $L_R = 2.3\text{ nH}$ ,  $L_L = 0.33\text{ nH}$ ,  $C_R = 12.9\text{ pF}$ . To better demonstrate the effect of alternated IDC on the dispersive behavior of the cells, an unbalanced case is also considered. The parameter values for both cases of balanced and unbalanced conditions are presented in Table 3.6.

Table 3.6 The SIW unit cell parameter values.

Balanced Case		Unbalanced Case	
Parameter	Length (mm)	Parameter	Length (mm)
$W_s$	29.6	$W_s$	29.6
$L$	7.95	$L$	7.17
$W_f$	0.26	$W_f$	0.24
$W_g$	0.25	$W_g$	0.15
$s$	1.54	$s$	1.54
$d$	0.8	$d$	0.8
$p$	20.2	$p$	20.2

It is observed that for the unbalanced case, the conventional right-handed band achieved for the frequencies  $f_{U\_sh} < f < f_{U3}$  while the anti-parallel phase and group velocity occurs for the frequencies from  $f_{U0}$  to  $f_{U\_se}$  exhibiting the left-handedness characteristic. Apparently, there is a band gap for the unbalanced case from 2.25 GHz to 2.56 GHz ( $f_{U\_se} < f < f_{U\_sh}$ ). Hence, the value of series inductance is increased by lengthening the fingers ( $L$ ) and the gap between the fingers ( $W_g$ ) is widened to reduce series capacitance so that the balanced condition is achieved. Note that the physical length of a single unit cell ( $p$ ) has a direct impact on the radiation properties as it defines the fast wave region limits ( $f_{B1} < f < f_{B2}$ ) following the relation  $|\beta p| < k_0 p$ ,  $k_0$  being free space wave number. In this work, the physical length of the proposed design is more than six times smaller than the free-space wavelength ( $\lambda_0 = 122$  mm) at the transition frequency so that the overall structure composed of this unit cell can be considered as quasi-uniform.

As is seen from the figure, for the balanced case, the LH pass band lies in the range of 1.72 GHz and goes to 2.45 GHz while RH-region initiates from 2.45 GHz and goes to 4.25 GHz. The fast-wave region ( $\beta < k_0$ ), where the phase velocity of the wave inside the media exceeds the speed of light, is in the frequency range from 2.05 to 3.25 GHz ( $f_{B1} < f < f_{B2}$ ) with a transition at  $f_0$  (2.45 GHz).

The circuit parameter values and the dispersion characteristic inferred from circuit model are also compared. As is seen from the figure, there is a slight inconsistency between full-wave simulation and the circuit model that can be referred to parasitic resonant behavior of IDC and the host line. Moreover, to demonstrate the degree of miniaturization of CRLH SIW configuration and its SIW counterpart, a four-stage balanced CRLH SIW is designed and a comparison is made in Figure 3.46. Note that, the dimensions of both structures are identical. It is observed that the cut-off frequency of the SIW occurring at 2.78 GHz is shifted down to 1.77 GHz. A quick comparison between Figure 3.46 and Figure 3.45 reveals a miniaturization of 12% for the RH pass

band and a total of 36% for its equivalent CRLH SIW. An insertion loss better than -5 dB achieved for the entire band.

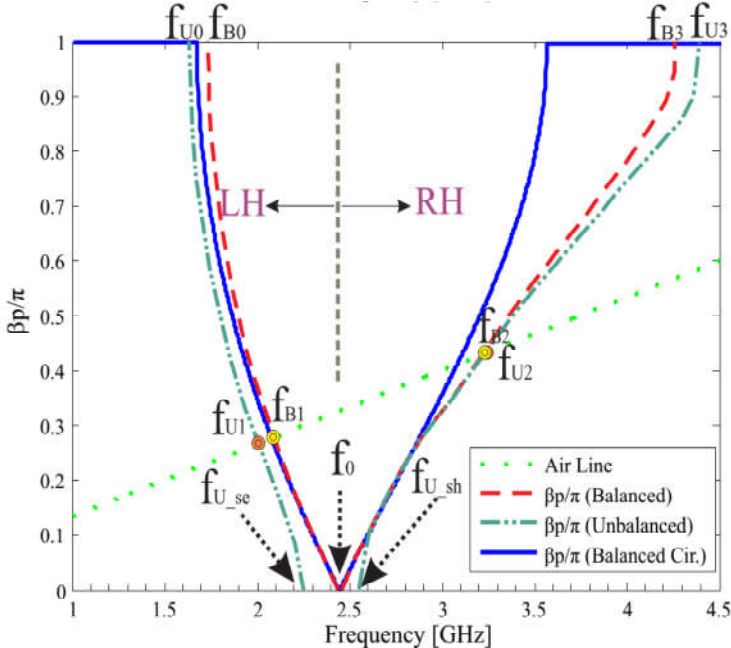


Figure 3.45. Dispersion diagram of the proposed unit cell.

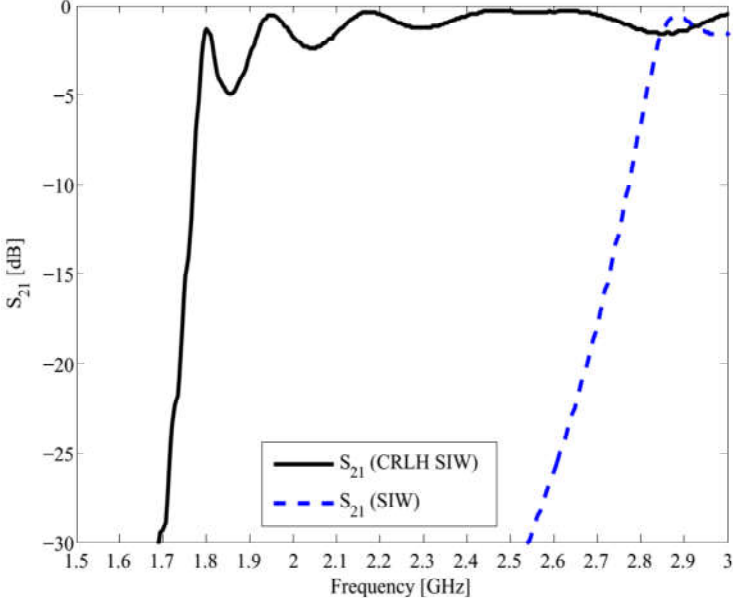


Figure 3.46. Simulated transmission coefficient of the four-stage CRLH SIW and its equivalent SIW structure.

Generally for a travelling wave structure such as LWA, it is more desirable to have more number of unit cells that could in turn increases the overall directivity of the antenna [118]. Furthermore, according to [117], in order to have more than 90% of the power radiated the following relation should be satisfied,

$$\frac{L}{\lambda_0} \approx \frac{0.18}{\alpha / k_0} \quad \text{Equation (3.67)}$$

where  $\alpha$  is the attenuation constant;  $L$  is the length of the antenna;  $k_0$  and  $\lambda_0$  are the wave number and the wave-length in the air. However, in this work the choice of 15 unit cells was made considering our limitations on the manufacturing equipment. Hence, an antenna composed of 15 cascaded unit cells was designed and a photograph of the fabricated design is depicted in Figure 3.47.

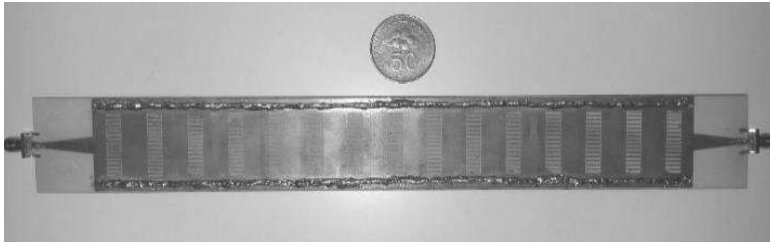


Figure 3.47. The photograph of the fabricated LWA.

### 3.4.3 CRLH Zeroth Order Resonant Antenna

A very interesting characteristic of CRLH structure is the existence of zeroth order resonances where the propagation constants becomes zero (i.e.  $\omega_{sh}$ ,  $\omega_{se}$  or  $\omega_0$ ). A CRLH TL can be realized by cascading  $N$  number of CRLH unit cells in which each unit cell possesses a periodicity  $p$  where the resonance can be calculated as

$$\theta = \beta_n p = \frac{np\pi}{l} = \frac{n\pi}{N} \quad \text{Equation (3.68)}$$

$$n = 0, \pm 1, \pm 2, \pm 3, \dots$$

where  $n$ ,  $l$  and  $N$  are mode number, the total length of the resonator and number of unit cells, respectively. From equation Equation (3.68) it can be noticed that if an antenna operates at zeroth order resonance, its electrical length becomes independent from frequency of operation, thus, an antenna with arbitrary size can be developed.

Such an antenna is called zeroth order resonance (ZOR) antenna. The resonance condition of CRLH is determined by the type of open/short-circuited termination in which series tank resonance  $\omega_{se}$  is defined by the values of series capacitance and series inductance for a short-ended ZOR antenna and can be found from Equation (3.62). On the contrary, the resonance of an open-ended ZOR antenna is determined by shunt tank resonance  $\omega_{sh}$  defined by the values of shunt inductance and shunt capacitance following the Equation (3.63). Furthermore, for an open-ended lossless CRLH-TL the input impedance can be defined as

$$Z_{in} \stackrel{\beta \rightarrow 0}{\cong} Z_c \frac{1}{j\beta l} = \frac{1}{Y'_{shunt}(Np)} \quad \text{Equation (3.69)}$$

Evidently, in this case the resonance is merely determined by shunt resonating tank  $\omega_{sh}$ . Therefore the quality factor of the shunt resonance under the condition that the stored magnetic energy in  $L_L$  ( $W_m$ ) and stored electrical energy in  $C_R$  ( $W_e$ ) to be equal [59], can be given by

$$Q_o = \frac{2\omega_h W_m}{P_{loss}} = \frac{1/G}{\omega_{sh} L_L} = \frac{1}{G} \sqrt{\frac{C_R}{L_L}} \quad \text{Equation (3.70)}$$

Following the same procedure the quality factor for a short-ended CRLH-TL can be found to be

$$Q_s = R \sqrt{\frac{C_L}{L_R}} \quad \text{Equation (3.71)}$$

Since the impedance bandwidth of the antenna is inversely proportional to  $Q$ , it is found from Equation (3.70) that increasing shunt inductance and/or reducing shunt capacitance can lead to a larger bandwidth. However, according to the Chu limits [132, 133], for the electrically small antennas, the maximum realizable bandwidth is restricted and follows the relation

$$FBW_{\max} = \frac{s'-1}{\eta\sqrt{s}} \left( \frac{1}{k^3 a^3} + \frac{1}{ka} \right)^{-1} \quad \text{Equation (3.72)}$$

where  $k$  is the wave-number of the air,  $a$  is the radius of the sphere enclosing maximum dimension of the antenna and  $s'$  is the voltage standing wave ratio (VSWR). The design of a novel center-fed CPW ZOR antenna loaded with a folded dipole-like parasitic element is presented in the following section which can effectively improve the bandwidth and efficiency of the miniaturized antenna simultaneously.

### 3.4.3.1 ZOR Antenna Design

The CRLH unit cell can be constructed from either lump components such as surface mount capacitors and inductors or by employing the distributed elements. Since the lump components are lossy in general and available within a limited range, distributed structures such as interdigital capacitors and via holes are typically used constituting the series capacitance and shunt inductance, respectively.

Figure 3.49 illustrates the configuration of the proposed antenna. The antenna composed of dual CRLH-TL symmetrically oriented with respect to the CPW feed line and a parasitic element proximity coupled to the signal patch. Each CRLH-TL composed of two unit cells where the left-handed parameters  $C_L$  and  $L_L$  are realized from the gap between square patches and the thin shorted meandered line, respectively. The gap between signal trace and ground plane contributes to the shunt capacitance  $C_R$  while the length of the unit-cell line determines the series inductance  $L_R$  giving rise to the right-handed property of the TL. In order to increase the bandwidth of the ZOR antenna, according to Equation (3.70), the unit cell is designed in a fashion that the quality factor is initially reduced by increasing the length of the thin meandered line ( $L_L$ ) and minimizing  $C_R$  by increasing the gap between the unit cell and ground plane. Furthermore, to compensate for the reduced efficiency caused by reduced quality factor, an identical CRLH-TL is added symmetrical to the CPW feeding line to form a center-fed CPW CRLH-TL. The optimized parameter values of the structure are given in Table 3.7. The proposed configuration allows for evenly distribution of

the surface current through the structure leading to a symmetric and more stable radiation pattern compared with its asymmetrical counterpart, thus the cross polarization is also reduced. The circuit parameter values of the CRLH-TL unit cell are obtained through the two-port parameter extraction [116] by performing full-wave simulation using CST microwave studio software [134]. The antenna is initially designed to target GSM-1800 downlink frequency span (1805.2-1879.8 MHz) at the ZOR frequency. Figure 3.48 demonstrates the configuration of the CPW CRLH unit cell inside the CST environment. It should be noticed that, while the ports are extended to the edges of the proposed unit cell, the length of the extended CPW line (TL-Extension) should be minimized for a better accuracy.

Table 3.7. The optimized parameter values of the designed ZOR antenna.

Parameter	Length (mm)	Parameter	Length (mm)	Parameter	Length (mm)
$W$	40.5	$g_2$	0.3	$l_2$	14
$W_1$	1	$g_3$	0.5	$l_3$	5.3
$W_2$	5.3	$g_i$	0.3	$l_4$	4.5
$W_t$	0.7	$g_f$	0.5	$l_5$	3.55
$W_i$	0.2	$L$	50.5	$l_6$	34.6
$W_f$	2.5	$l_t$	21.25	$l_i$	8.2
$g_1$	0.2	$l_1$	11.6	$p$	8.62

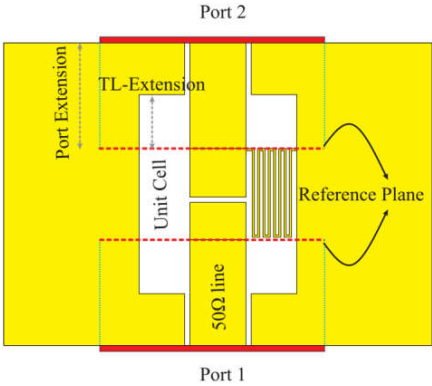


Figure 3.48. CPW-CRLH unit cell design setup in CST software.



According to the dispersive characteristic of CRLH-TL, the first negative order resonance ( $f_{-1}$ ) and zeroth-order resonance are found to occur at 1.13 GHz and 1.815 GHz, respectively. In order to extend the bandwidth of the proposed antenna a thin folded microstrip line as a parasitic element is loaded to the structure.

The purpose of using the parasitic element is twofold. One is to provide an additional resonance to overcome the low bandwidth drawback of the antenna. The other is to provide a path for the trapped power on the square signal patch caused by the high impedance within the band-gap region of CRLH-TL that, in turn, effectively improves the efficiency of the proposed antenna. The resonant length of the parasitic element is calculated by

$$\lambda_g = \sqrt{\frac{2}{\epsilon_r + 1}} \lambda_0 \quad \text{Equation (3.74)}$$

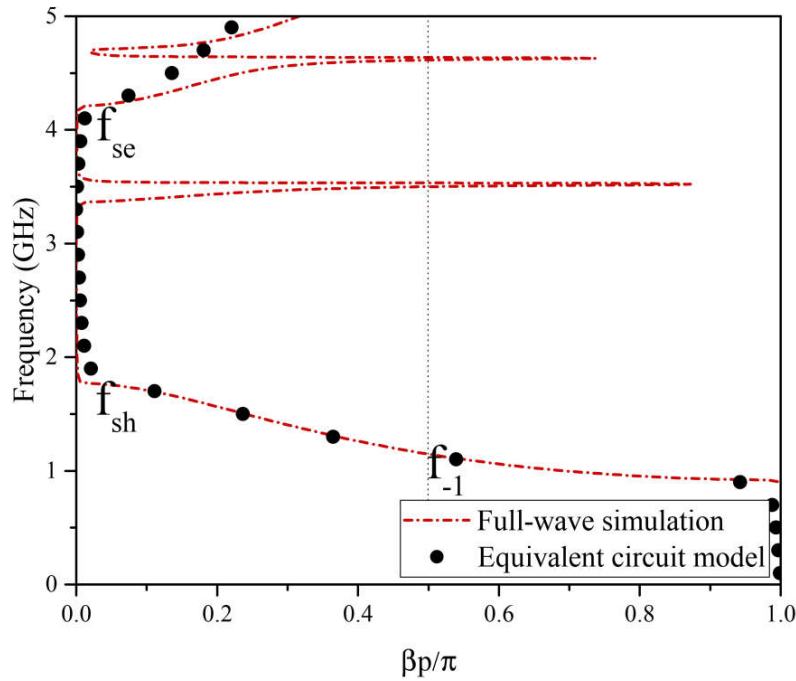


Figure 3.50. Dispersion diagram of the proposed CRLH unit cell.

where  $\lambda_g$  is the guided wavelength on a low-thickness substrate, and  $\epsilon_r$  is the relative permittivity. Using Equation (3.74), the guided wavelength on a low-thickness

substrate ( $h = 0.508$  mm) with  $\epsilon_r = 3.38$  at 3.08 GHz is found to be 65.8 mm that is very much close to the total length of parasitic element being 67 mm. Due to the high input impedance introduced by the loaded parasitic element, a CPW-tapered line is used to transform the impedance to the standard 50  $\Omega$  end. A prototype of the proposed ZOR antenna was fabricated on RO4003C substrate with a low thickness of 0.508 mm, dielectric constant of 3.38 and loss tangent of 0.0029. The overall dimensions of the proposed antenna is  $0.303 \lambda_0 \times 0.248 \lambda_0 \times 0.003 \lambda_0$ , where  $\lambda_0$  is the free space wavelength at frequency of the dominant resonance ( $f_0 = 1.84$  GHz). Figure 3.51 shows the photograph of the fabricated prototype.

Figure 3.51. Photograph of the fabricated antenna.

#### **3.4.4 Miniaturized Antenna Design for Integrated Energy Harvesting System**

The combination of antenna and rectifier can be advantageous as it allows for the easier diagnosis of the energy harvester at each segment of the system. However, there are some drawbacks with those configurations such as increased overall occupied area of the energy harvester as well as increased losses resulting from employment of SMA ports and adapters that can negatively impact the overall rectification performance of

the system. Therefore, to accommodate these issues, the ZOR antenna is redesigned in which the harmonic rejecting filter is included as part of antenna aiming to achieve better return loss and filtering performance at the harmonic frequencies, thus, forming a harmonic terminating antenna (HTA). To do so, the length of the CPW ground plane was re-adjusted to implement a CPW-microstrip transition. In this manner, the compact dimensions of the antenna was preserved while additional degree of freedom was provided to connect the antenna input to the LPF and rectifier circuit subsequently. The CPW ground plane was connected to the microstrip ground plane using 6 via holes of diameter 0.8 mm. Figure 3.52 illustrate the configuration of the HTA.

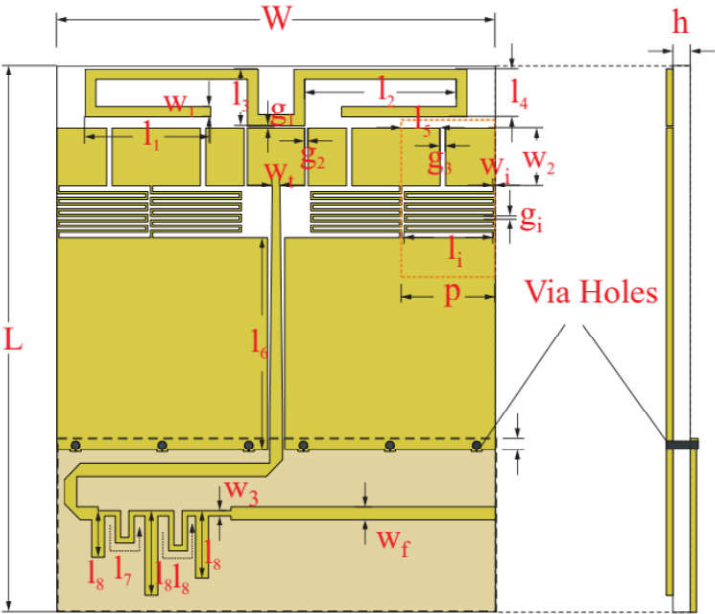


Figure 3.52. The layout of harmonic terminating ZOR antenna (HTA).

The optimized parameters of HTA are presented in Table 3.8. The antenna is printed on 20-mil-thick RO4003C and a photograph of the fabricated antenna is presented in Figure 3.53(a). The photograph of HTA under the test inside anechoic chamber also presented in Figure 3.53(b).



(a)

(b)

Figure 3.53. (a) Photograph of the fabricated HTA and (b) HTA under the test.

The simulated and measured S-parameters of the proposed HTA are demonstrated in Figure 4.20.

Table 3.8. The optimized parameters of the ZOR HTA.

Parameter	Length (mm)	Parameter	Length (mm)	Parameter	Length (mm)
$W_1$	1	$p$	8.65	$l_8$	7.3
$W_2$	5.3	$l_1$	11.6	$l_9$	5.74
$W_3$	0.49	$l_2$	14	$l_{10}$	7.9
$W_i$	0.2	$l_3$	5.3	$l_{11}$	6.75
$W_t$	0.7	$l_4$	4.5	$l_{12}$	2.08
$g_2$	0.3	$l_5$	3.55	$W$	40.5
$g_3$	0.5	$l_6$	18.6	$L$	53.5
$g_i$	0.3	$l_7$	3.41	$g_1$	0.2

Moreover, the broadband rectifier is redesigned to fit within the HTA geometry. The layout of broadband rectifier is demonstrated in Figure 3.54.

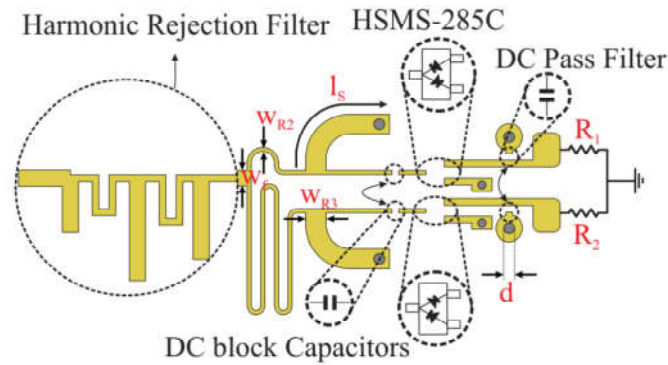


Figure 3.54. The layout of compact broadband rectifier.

The optimized dimensions are:  $W_{R2} = 0.3$  mm,  $W_{R3} = 1.5$  mm,  $d = 0.8$  mm,  $l_s = 7.2$  mm and  $W_f = 1.18$  mm.

### 3.5 Summary

In summary, this chapter presents a detailed description on the diode and the impact of its different components on its performance. The harmonic generation on the non-linear device is discussed and its importance is demonstrated through the development of an analytical model that is an extension of the method presented in [104]. An excellent agreement between the analytical and simulation results clearly justifies the accuracy of the analytical model presented. Next, different common topologies for the design of microwave rectifiers are studied. An analysis on the harmonic generation of evenly multiplied rectifiers is presented demonstrating the advantage these topologies on the reduced harmonic contents. The design process of a rectifier with increased output tolerance using harmonic balanced analysis and source pull technique is presented. Furthermore, a novel method for the design of a compact and broadband rectifier based on dual mode switching configuration is presented, which can effectively enhance the efficiency and input power range of the rectifier, simultaneously. Lastly, different antenna structures such as CRLH LWA and CPW ZOR antennas loaded with a parasitic element have been presented and discussed. The antenna is initially designed to target GSM-1800 downlink frequency span (1805.2-1879.8 MHz) at the ZOR frequency. The simulated and experimental results of the presented designs are presented and discussed in the next chapter.

## CHAPTER 4

### RESULTS AND ANALYSIS

In the previous chapter, various structures of rectifier for microwave range of applications are studied and the design of miniaturized and broadband ZOR antenna is then presented. In the sequel, the individual and combination results of the final rectenna and its achieved performance are presented and discussed.

#### 4.1 Modified Rectifier with Increased Output Tolerance Results

The simulated performance of proposed rectifier and the rectifier without HRF are shown in Figure 4.1. It can be seen that, the efficiency of the proposed rectifier is significantly improved particularly at the power levels above -10 dBm and reaches to 62.9% at the 5 dBm which is almost 10% higher than that of rectifier without HRF.

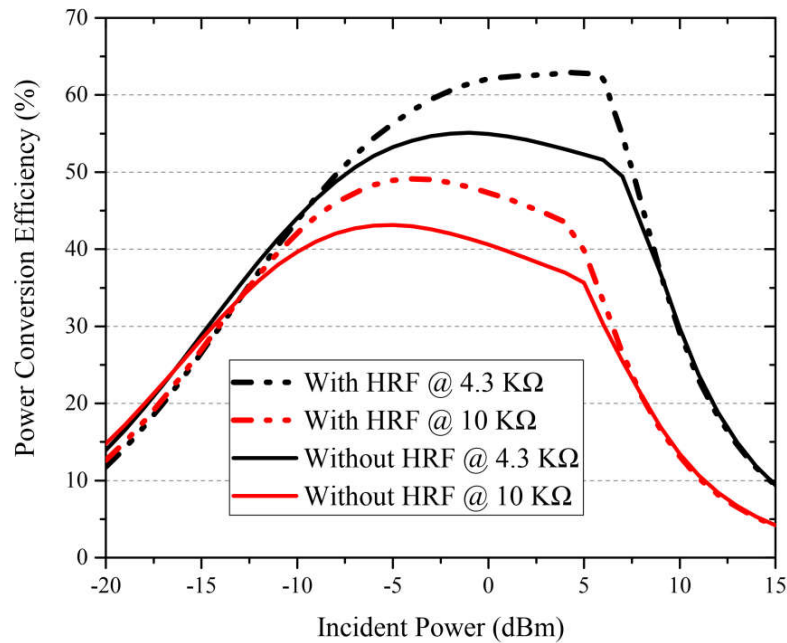


Figure 4.1. Comparison between the simulated results of modified rectifier and the rectifier without HRF.

The simulated and measurement  $S_{11}$  of the modified rectifier are demonstrated in Figure 4.2. Good agreement between the simulation and measurement has been

achieved validating the effectiveness of the method used. The simulated and measured RF-to-DC power conversion efficiency and achieved output voltage are presented in Figure 4.3. As is observed, the efficiency of the proposed rectifier is significantly

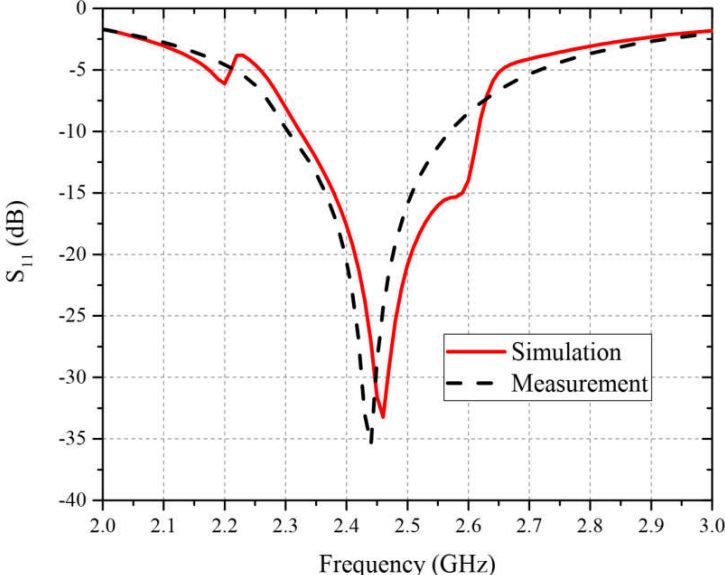


Figure 4.2. Simulated and measured return loss of the modified rectifier at the input power of -10 dBm and the load of 4.3 k $\Omega$ .

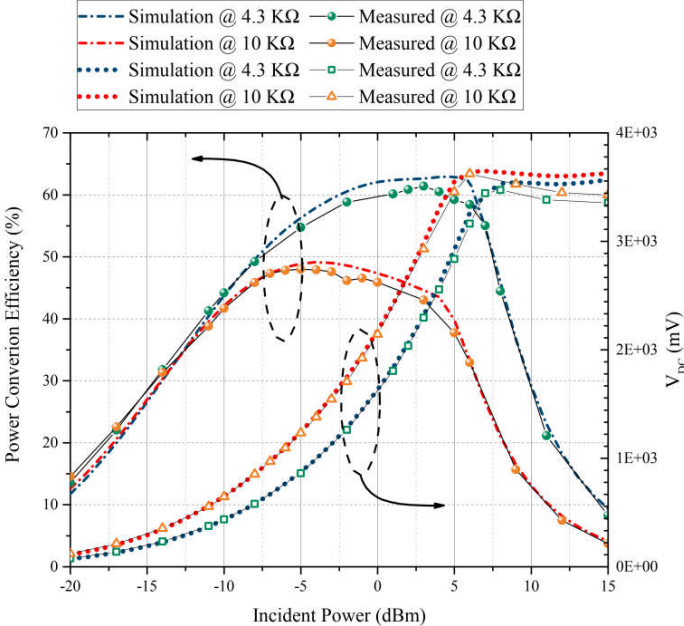


Figure 4.3. Simulated and measured results of the proposed modified rectifier.

improved with the maximum efficiency of 61.9% occurring at the 3 dBm. It is worth noting that, even at the low power level of -20 dBm, the efficiency remains above 13%

where the output voltage is 76 and 120 mV for the load values of 4.3 and 10 k $\Omega$ , respectively.

Moreover, the efficiency of the rectifier is also evaluated by varying the value of output load from 1 to 12 k $\Omega$  as demonstrated in Figure 4.4. It can be observed that, the measured values follow well the simulation at the lower power level (-10 dBm) where diode behavior is relatively linear. However, as the power level increased to 5 dBm, the diode is pushed more into non-linear state and the matching condition is reduced. It is worth noting that, since the impedance of diodes is a function of frequency, input power level and output load, the matching network may perform less effective if any of these conditions are changed. For example, the power level for the design of the modified rectifier is ranging from -10 to 5 dBm while the power level for the full-wave rectifier presented in Figure 3.22 is set -15 dBm leading to a different matching network design, thus, different efficiency values obtained.

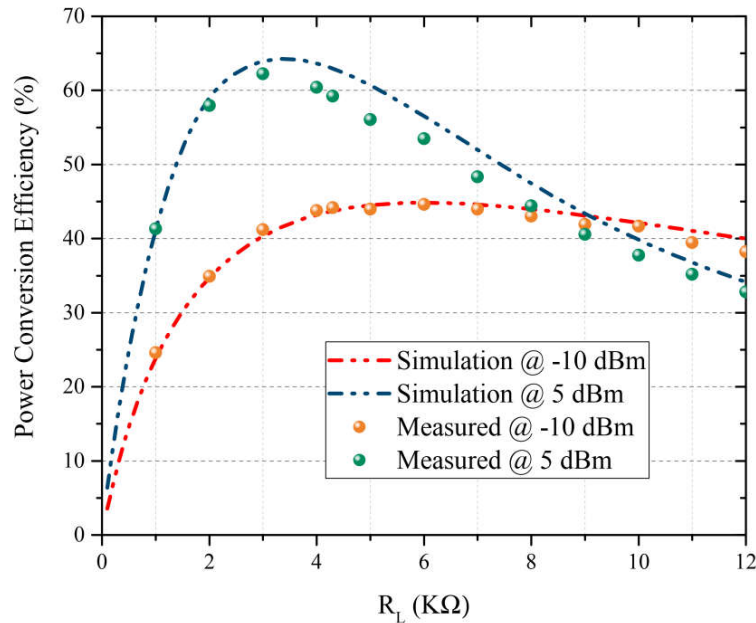


Figure 4.4. Simulated and measured RF-to-DC power conversion efficiency of the modified rectifier as a function of output load.

## 4.2 Broadband Rectifier Results and Analysis

Figure 4.7 shows the measured and simulated efficiency for three different input power values over 10 k $\Omega$  loads. As is observed, good efficiency over wide range of frequency

(1.9 to 2.6 GHz) has been achieved. The efficiency drops as the input power value reduces from 3 dBm down to -17 dBm. However, even at the low input power of -17 dBm, an efficiency better than 10% from 1.85 to 2.5 GHz is obtained. The simulated and measured efficiency as a function of input power at different frequency of 2, 2.15, 2.3 and 2.45 GHz are shown in Figure 4.8. There is an overall good agreement between the simulation and measured results where the simulated efficiency is slightly better than the measured ones. However, a very good power dynamic range of 14 dBm from -8 to 6 dBm is obtained in which the efficiency remains above 40% at all sampled frequencies.

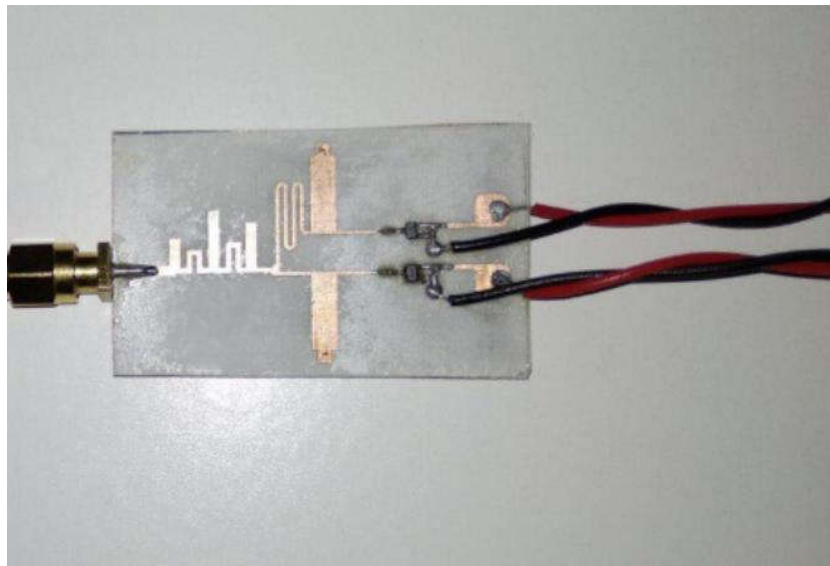


Figure 4.5. Photograph of the fabricated broadband rectifier.

The highest measured efficiency is 70.3% obtained at 2.3 GHz. The slight difference between simulation and measurement is mainly due to the inaccuracy of diode modeling, connector losses as well as the fabrication tolerances.

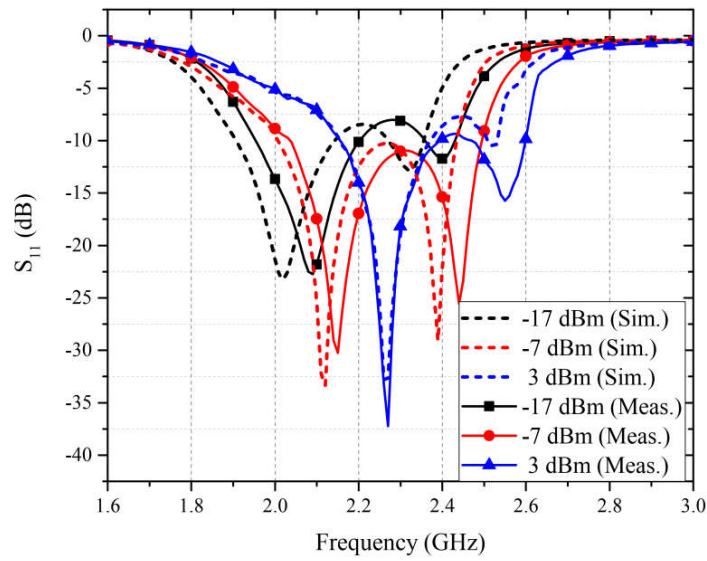


Figure 4.6. Simulated and measured return loss of the fabricated broadband rectifier under various power conditions.

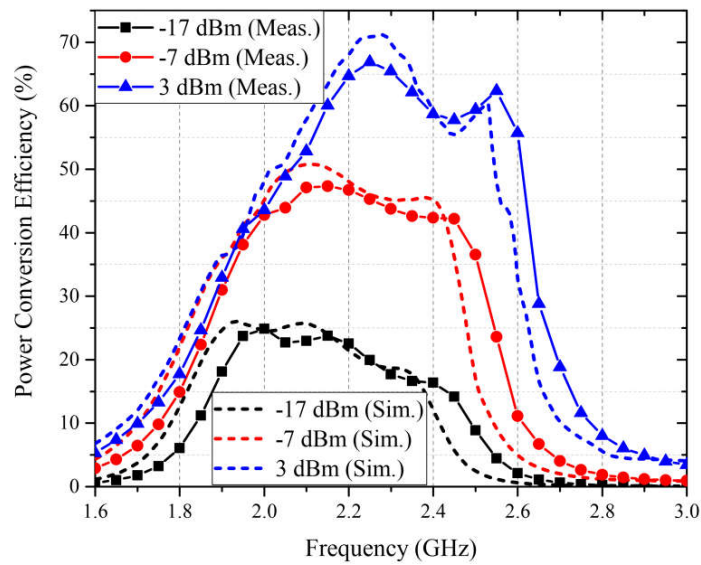


Figure 4.7. Measured and simulated power conversion efficiency as a function of frequency at three power levels of 3, -7 and -17 dBm.

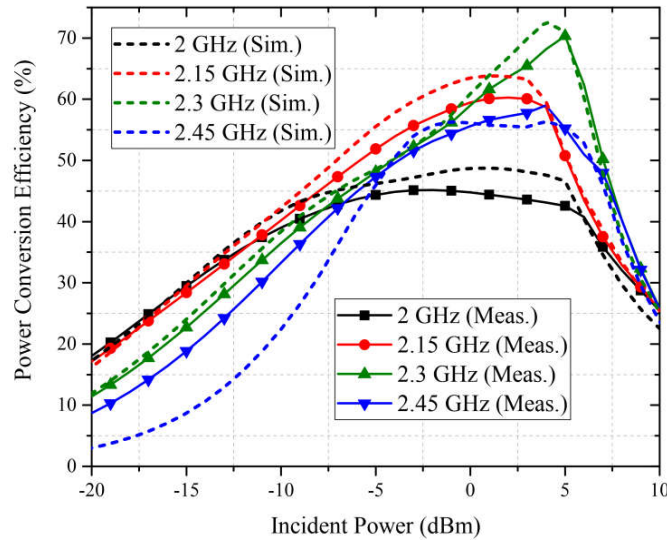
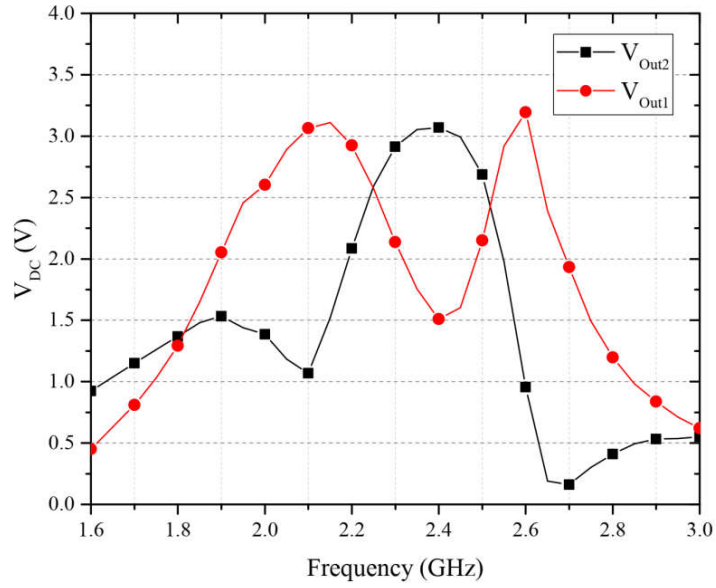
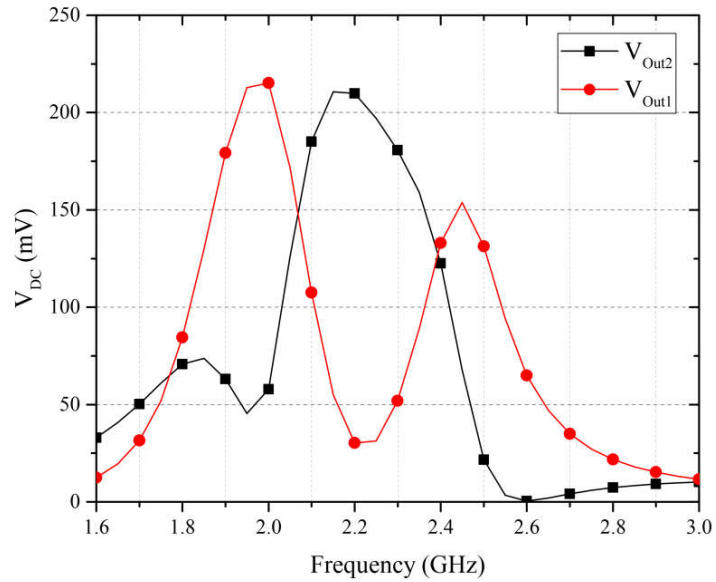


Figure 4.8. Measured and simulated power conversion efficiency as a function of power at different frequencies.

Figure 4.9(a) and (b) demonstrate the output DC voltage obtained under 3 and -17 dBm incident power levels versus frequency. It can be observed that, under 3 dBm power level, each rectifier output is maximized around 2.1 and 2.4 GHz in which each rectifier is L-matched at about 2.27 GHz where the output DC voltages become equal. Thanks to the non-isolated connection between arms of the T-junction, there is an additional DC voltage peak around 2.66 GHz resulted from extreme mismatched condition from second rectifier at the higher frequencies, thus, driving the first rectifier with higher power. The maximum obtained under 3 dBm power level, is 3.2 V at 2.66 GHz. Similar scenario is observed for the achieved output DC voltages at -17 dBm in which the highest achieved output DC voltage is 216 mV at 2 GHz. It is worth noting that, even at the low power level of -17 dBm, the output DC voltage of better than 100 mV is achieved from at least one rectifier output for the frequency range of 1.85 to 2.6 GHz. While this amount of voltage appears to be relatively low, however, it is fairly sufficient to drive a step up boost converter and a low power consumer device, subsequently.



(a)



(b)

Figure 4.9. Measured output DC voltage versus frequency of the broadband rectifier for an incident power levels of (a) 3 dBm and (b) -17 dBm.

### 4.3 CRLH LWA Results and Analysis

In order to feed the proposed LWA, a microstrip taper is used in order to match the antenna with the standard 50 ohm microstrip line. The length and width of microstrip taper are 27 and 7.7 mm, respectively, and the width of the lower side of the taper is

the same as the width of  $50 \Omega$  microstrip line. The overall size of structure without considering the feeding structure is  $2.46 \lambda_0 \times 0.25 \lambda_0 \times 0.004 \lambda_0 \text{ mm}^3$ .

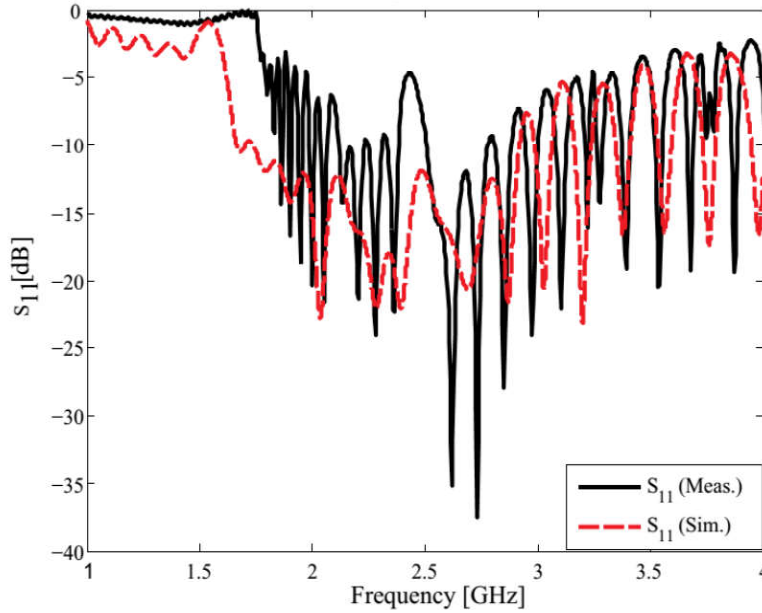


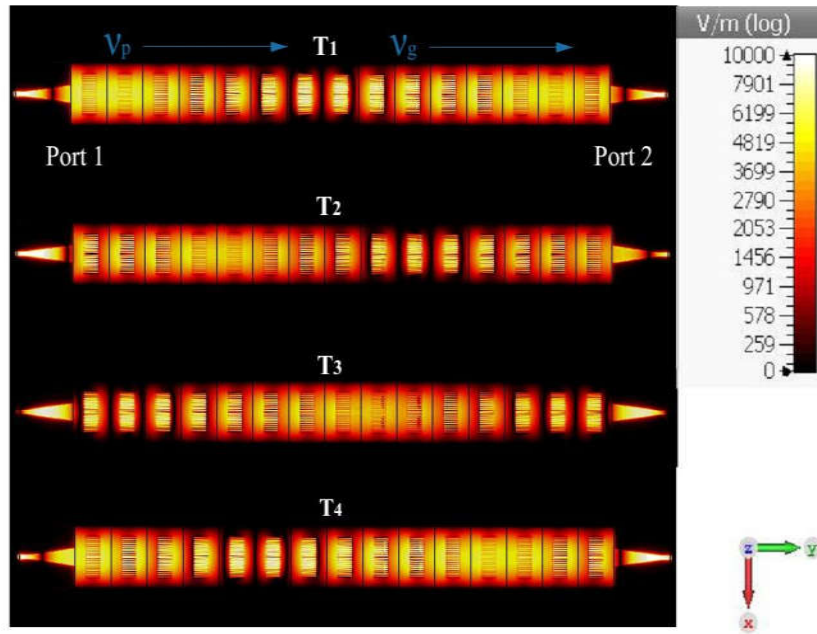
Figure 4.10. Simulated and measured return loss of the proposed design.

The antenna scattering parameters were measured using Agilent 8722ES Vector Network Analyzer (VNA). Figure 4.10(b) shows the simulated and measured return loss of the antenna. It can be observed that, the left-handed and right-handed regions are separated by a band notch occurring around 2.45 GHz. Referring back to the dispersion diagram extracted from the designed unit-cell properties as given in Figure 3.45, the return loss follows the expected dispersion behavior fairly well. However, an impedance mismatching is observed around 2.45 GHz indicating the existence of a very narrow band gap within the transition frequency that may be referred to fabrication tolerances such as via drilling and soldering involved. To demonstrate the backward and forward wave propagation of the proposed design, the transient E-field distribution at three different frequencies of 2.3 GHz, 2.45 GHz and 2.7 GHz for different time instants are depicted in Figure 4.11(a)-(c). Note that in all cases, the antenna is fed from port 1 while port 2 is terminated by  $50 \Omega$ .

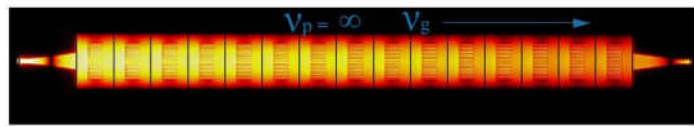
As is seen from Figure 4.11(a), for the RH region the wave propagation is forward at 2.7 GHz. It can also be noticed that both phase velocity ( $v_p$ ) and group velocity ( $v_g$ )

are parallel as is the case for the conventional LWAs. Figure 4.11(b) shows the field distribution at 2.45 GHz where the phase constant becomes zero leading the phase velocity toward infinity. It is also seen that the field variation is almost constant within the longitude of the overall structure. At the frequency of 2.3 GHz the phase velocity and group velocity become antiparallel indicating that the antenna is operating at LH region where the wave propagation is backward as shown in Figure 4.11(c).

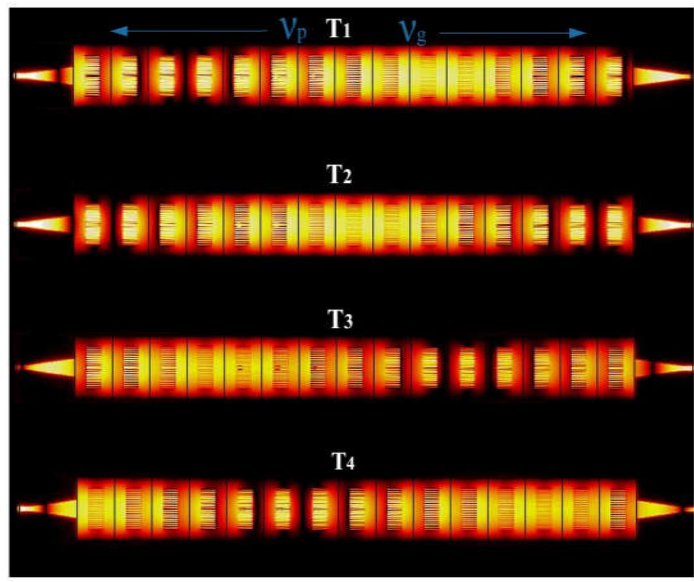
The 3-D farfield view at 2.55 GHz are illustrated in Figure 4.12(a). For a LWA, the scanning angle ( $\theta$ ) is the angle of the beam steered from the normal to the structure at the elevation-plane and is defined as the relationship of phase shift between two adjacent unit cells within the fast wave following Equation (3.59). From Figure 4.12(b), it is clearly observed that for the radiation pattern of the antenna at E-plane (zy-plane), the main lobe moves from backfire toward endfire as frequency increases, validating the scanning capability of the structure. The normalized simulated radiation patterns of the antenna at both E-plane (zy-plane) and H-plane (zx-plane) are displayed in Figure 4.13. The cross-polarization level at E-plane and H-plane are well below -58 and -40 dB, respectively, for the entire band. The evaluated scanning angle is almost 133 degrees from -68 at 2.05 GHz and steers to +65 degree at 3.25 GHz in which  $\theta$  is measured from the broadside direction and presented in Figure 4.14.



(a)

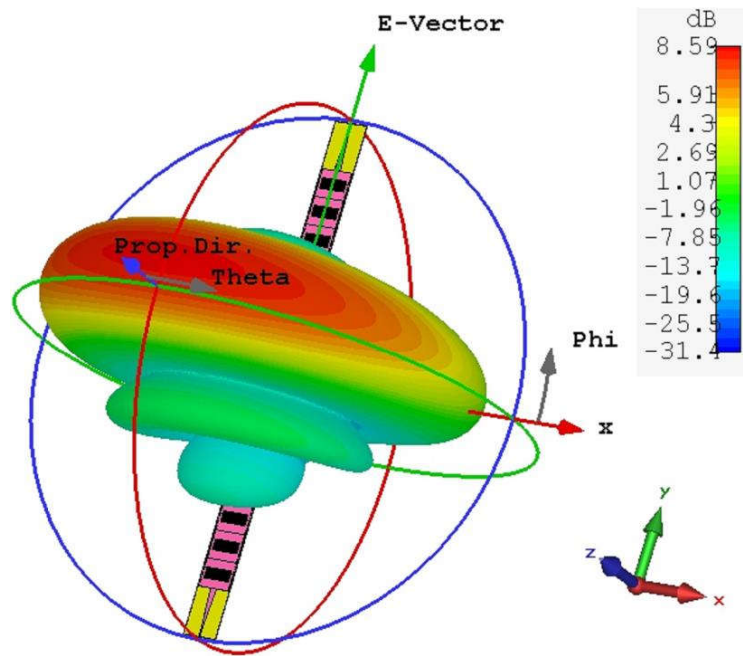


(b)

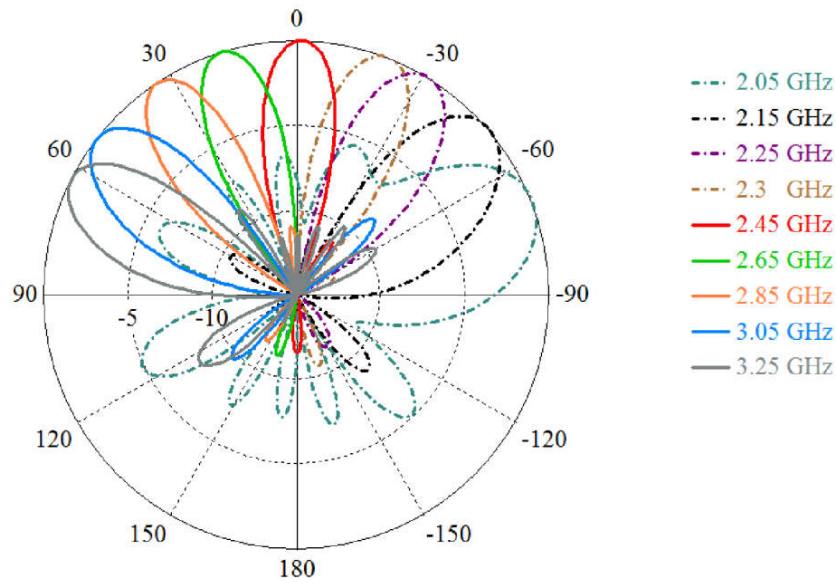


(c)

Figure 4.11. E-field distribution of the LWA for different time instants on the x-y plane. (a) Transient E-field at 2.7 GHz, (b) transient E-field at 2.45 GHz, (c) transient E-field at 2.3GHz.



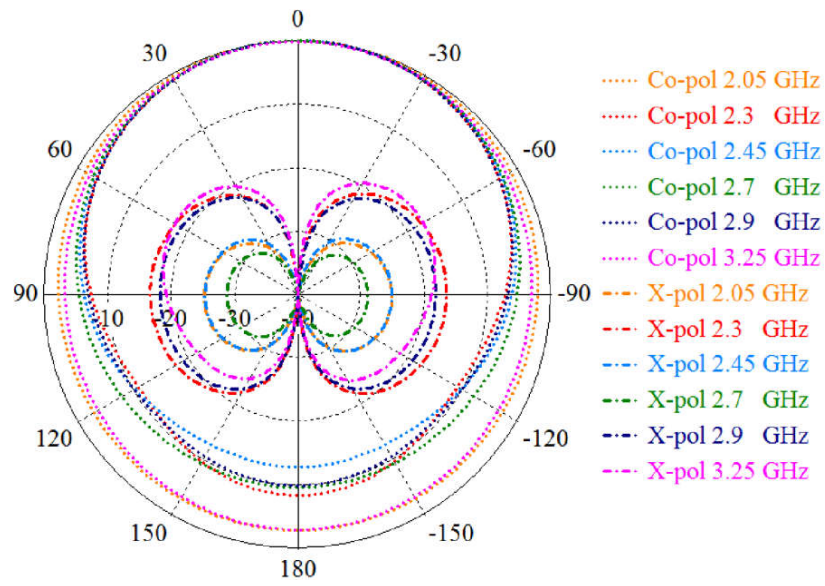
(a)



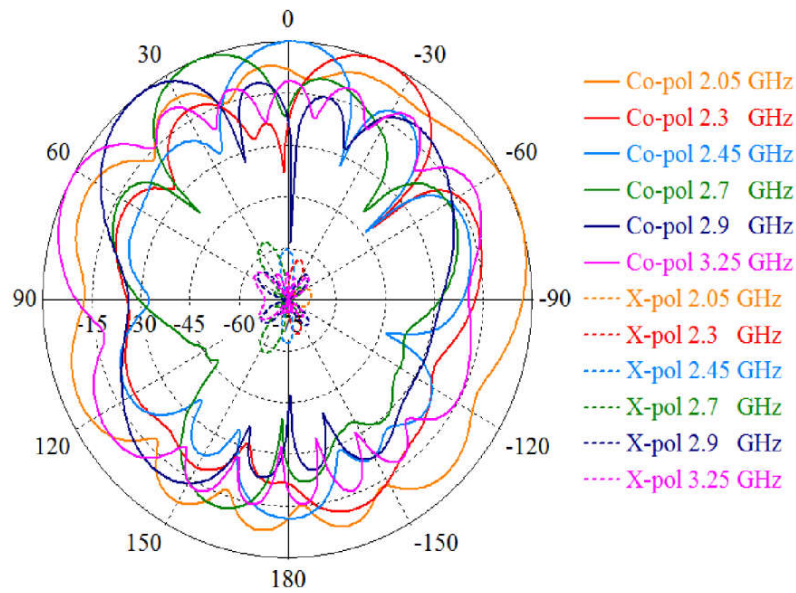
(b)

Figure 4.12. (a) 3-D farfield view at 2.55GHz and (b) normalized radiation patterns of the antenna at E-plane (zy-plane).

As is perceived, the gain in forward region is higher than the backward with the highest gain of 8.6 dB occurring at 2.55 GHz while the highest gain value in backward region is 8.3 dB at 2.15 GHz. A slight drop on the gain is apparent around 2.45GHz (6.2 dB) where the transition occurs with the radiation at broadside direction ( $\theta = 0$ ).



(a)



(b)

Figure 4.13. Normalized simulated radiation patterns at (a) H-plane (zx-plane) and (b) Elevation plane (zy-plane).

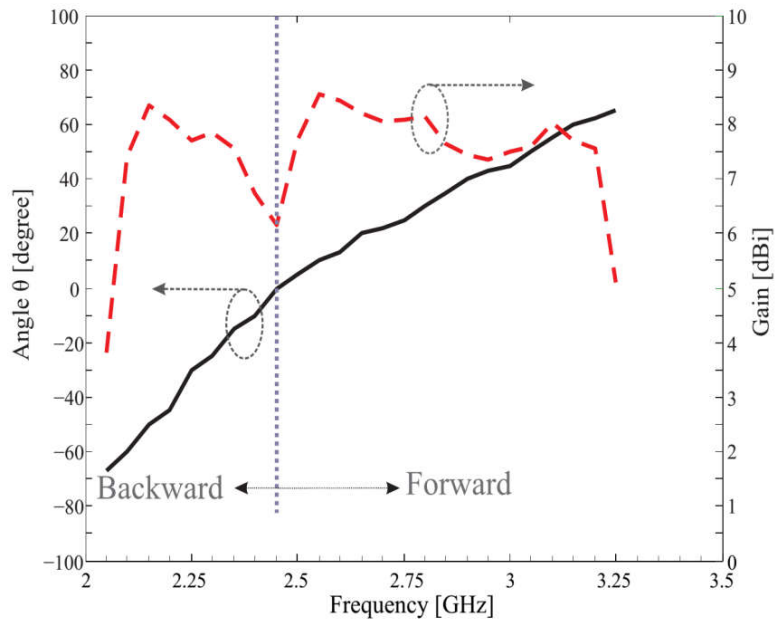


Figure 4.14. Simulated scanning angle (black solid line) and antenna gain (red dashed line) versus frequency.

The measured gain and efficiency of the proposed LWA is presented in Figure 4.15. Unfortunately, the measured gain is much lower than expected with the peak gain of 6.1 and 1.05 dBi at the frequency of 2.1 and 2.4 GHz, respectively. The highest gain achieved at the RH region is 4.6 dBi occurring at 2.5 GHz.

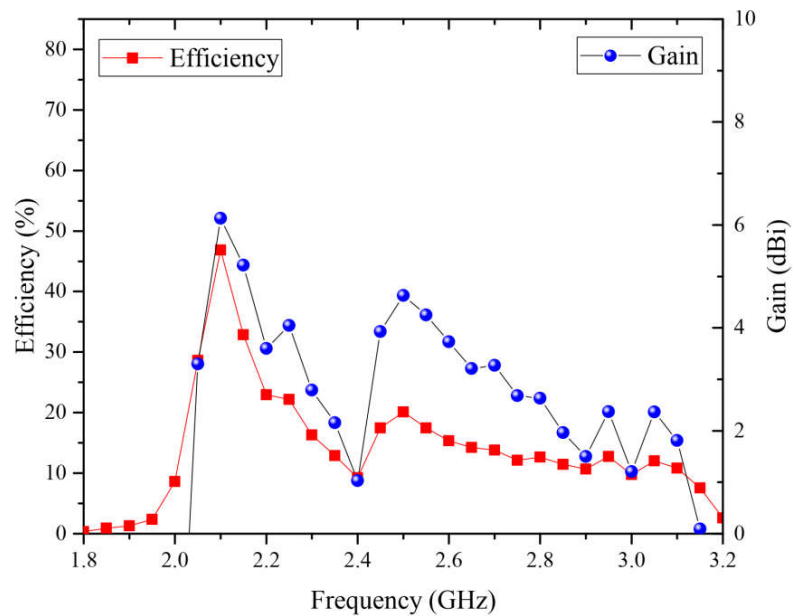


Figure 4.15. Measured gain and efficiency of the designed LWA.

Furthermore, the measured LWA efficiency, that is an important factor for the EH systems, is lower than 30% for most of the covered band with the highest efficiency of 47% at 2.1 GHz. Since the attenuation constant is a function of frequency, both the gain and radiation efficiency may vary depending on frequency and radiation angle. According to [117] While a solution to this problem can be the increase on the number of cascaded unit cells, which can indeed increase both gain and efficiency of the LWA, however, due to our constrains in terms of fabrication and computational memory limits, a different approach is undertaken and is presented through the rest of this thesis work.

#### **4.4 ZOR Antenna Experimental Results**

Figure 4.16 demonstrates the effect of parasitic element on the antenna return-loss. As is seen, the -10 dB bandwidth for the ZOR antenna without parasitic element is 120 MHz for the frequency range of 1.75 to 1.87 GHz corresponding to 6% of the fractional bandwidth, while it has been significantly improved to 1.6 GHz covering the frequency range of 1.7 to 3.3 GHz corresponding to the fractional bandwidth of 87%. Compared with the measurement results, an excellent agreement is observed for the ZOR frequency but the second resonance at the higher frequencies is slightly deviated from 3.08 GHz to 3.13 GHz. This can be attributed to the length dependent resonant nature of the parasitic element and its sensitivity to the permittivity of the substrate as well as the fabrication tolerances. Notice that, although the first negative-order resonance  $f_{-1}$  shows a reflection coefficient better than -10, but there is no radiation from the antenna

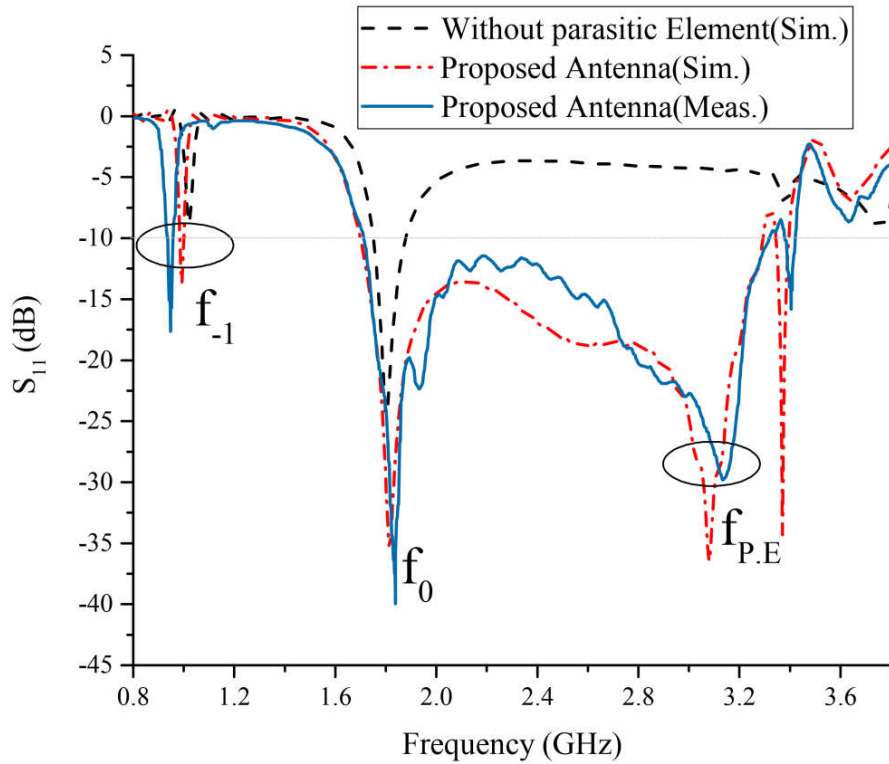


Figure 4.16. Simulated and measured reflection coefficients of the proposed antenna.

as it operates within the guiding wave region  $|\beta p| > |kp|$ . The measured operational bandwidth of the antenna is 1.6 GHz from 1.715 to 3.318 GHz with a dominant resonant frequency  $f_0$  at 1.84 GHz related to the ZOR frequency. A standard 50  $\Omega$  SMA connector was included through all the simulations to take into account its effect on the overall performance of the antenna.

The surface current distribution at 1.84 and 3.15 GHz are demonstrated in Figure 4.17. As expected for the ZOR frequency, strong current exists on the meandered lines while at the second resonance (3.08 GHz) much stronger current is observed on the parasitic element.

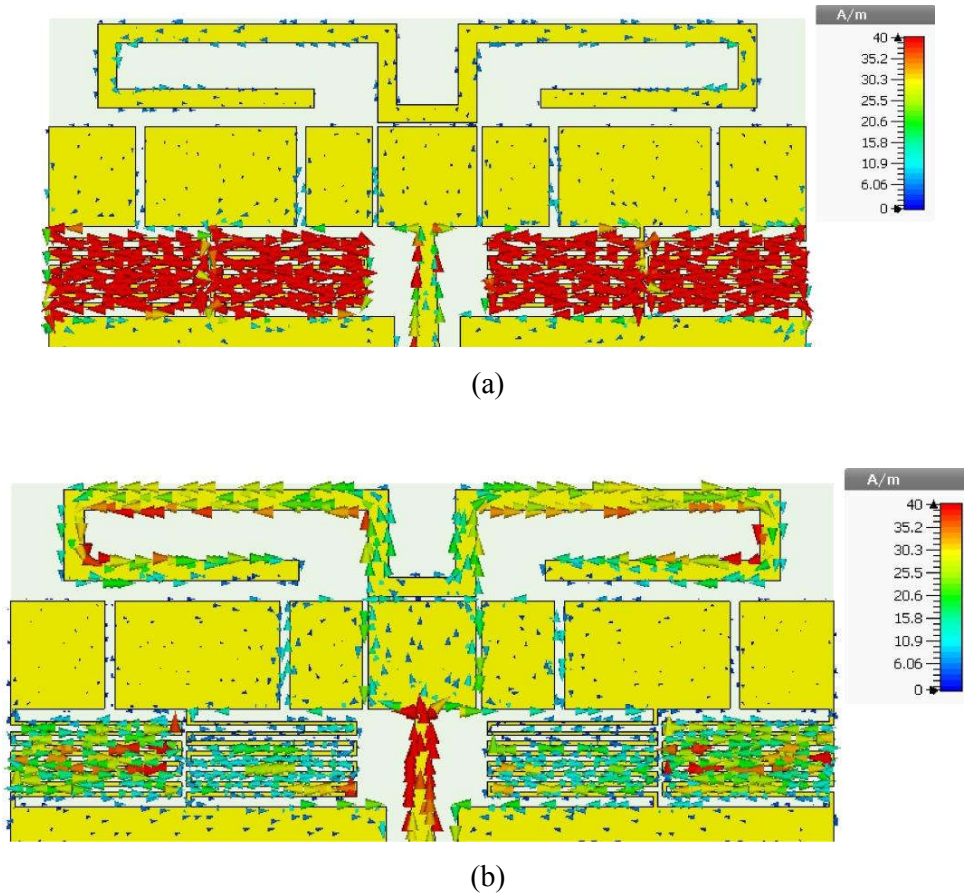
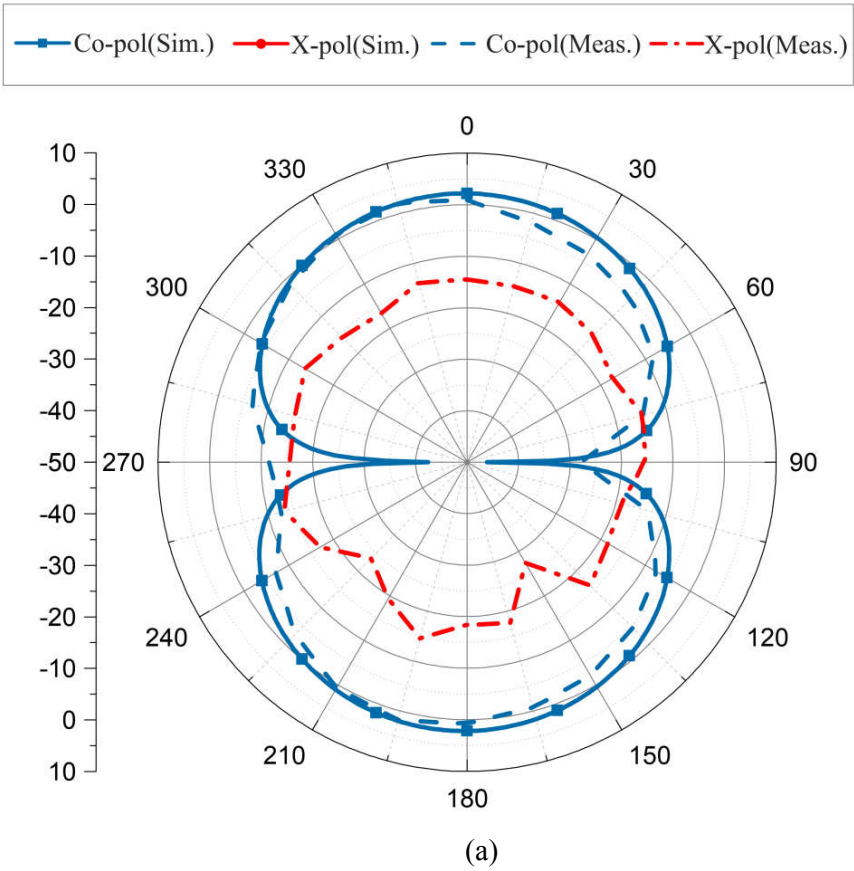
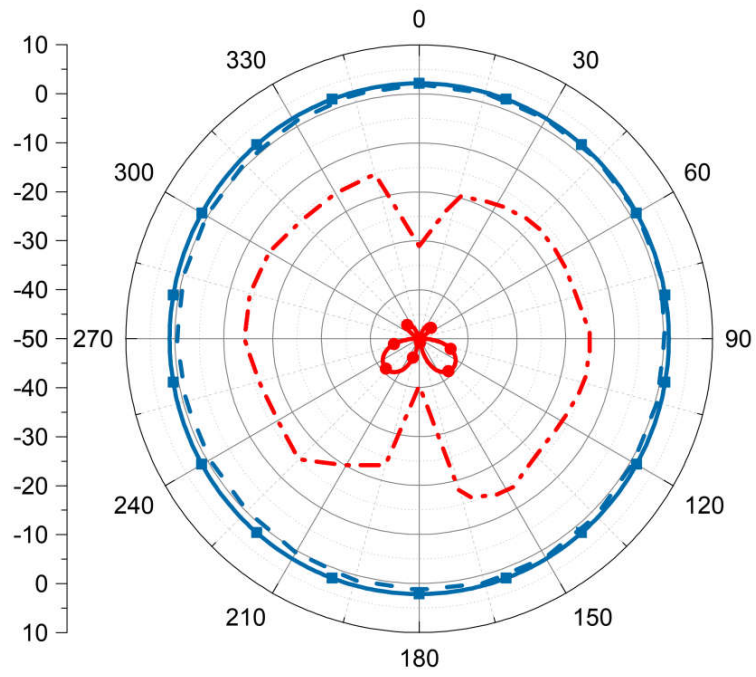


Figure 4.17. Simulated results of surface current distribution at (a)  $f = 1.84$  GHz and (b)  $f = 3.1$  GHz obtained from CST software.

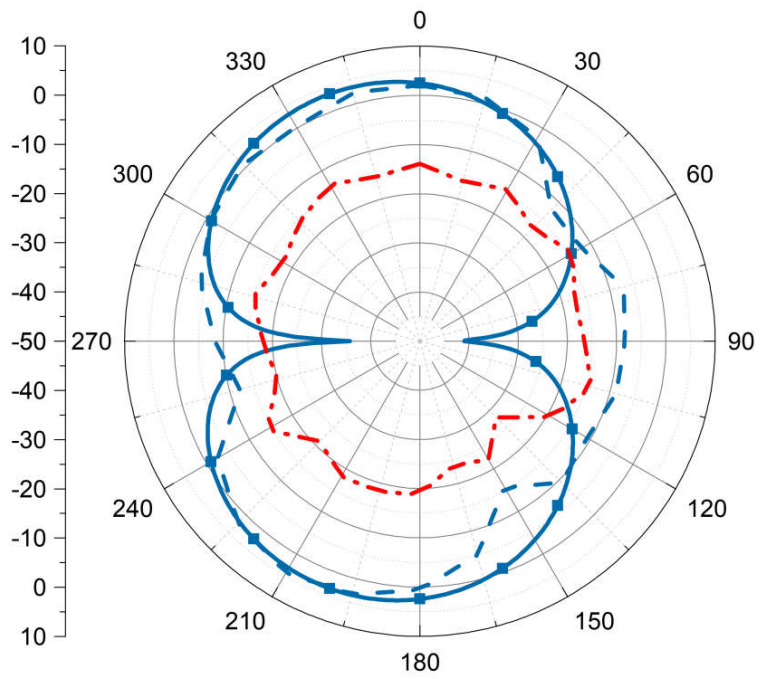
Furthermore, the radiation characteristic of the proposed antenna was measured in an anechoic chamber and are compared with the simulation at the resonance frequencies ( $f_0 = 1.84$  GHz and  $f_{P,E} = 3.08$  GHz) demonstrated in Figure 4.18. As is observed in the two principal planes, E-plane (yz-plane) and H-plane (xz-plane) the radiation is approximately dipole-like. From the measured results, an isolation ratio better than 14 dB between co and cross polarization are achieved that contributes to symmetrical configuration of the antenna. The measured gain and radiation efficiency of the antenna are presented in Figure 4.19. The efficiency was evaluated using the measurement system as of the ratio between the received radiated power of the antenna under the test to the power transmitted from the standard horn antenna. Normally, the antenna efficiency is measured by feeding a certain amount of power to the antenna while the strength of the radiated electromagnetic field in the surrounding space is precisely evaluated in the anechoic chamber. Having in mind the strict calibration

policy of the anechoic chamber, the radiation efficiency has been measured inside a closed-door fully automated anechoic chamber without any external interferences. The value of the gain is 2.1 and 3.35 dBi at the resonance frequencies 1.84 GHz and 3.08 GHz, respectively. The values of the gain varies from 1.85 to 3.35 dBi as the frequency increases. An efficiency better than 80% is achieved for the entire band and reaches as high as 95.7% at 3 GHz. The overall performance of the proposed ZOR antenna is compared with the recently reported metamaterial antennas and tabulated in Table 4.1. It is observed that the proposed ZOR antenna exhibits reasonable bandwidth and efficiency enhancement while fabrication simplicity and relatively compact size is maintained.





(b)



(c)

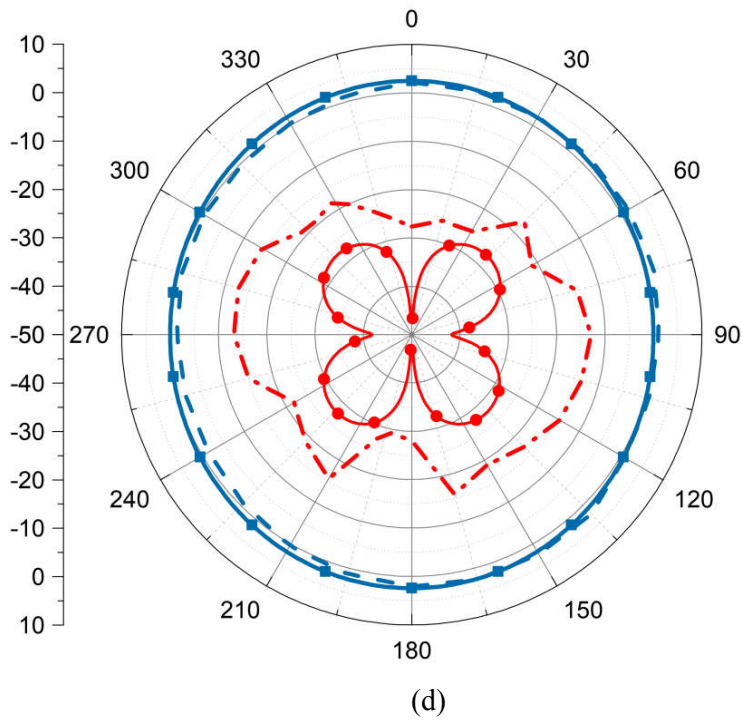


Figure 4.18. Simulated and measured radiation patterns of the proposed antenna: (a) zy-plane (E-plane) at 1.84 GHz; (b) xz-plane (H-plane) at 1.84 GHz; (c) zy-plane (E-plane) at 3.08 GHz; (d) xz-plane (H-plane) at 3.08 GHz. Symbol lines indicate the simulated results where the blue and red colour lines show the co-pol and X-pol, respectively.

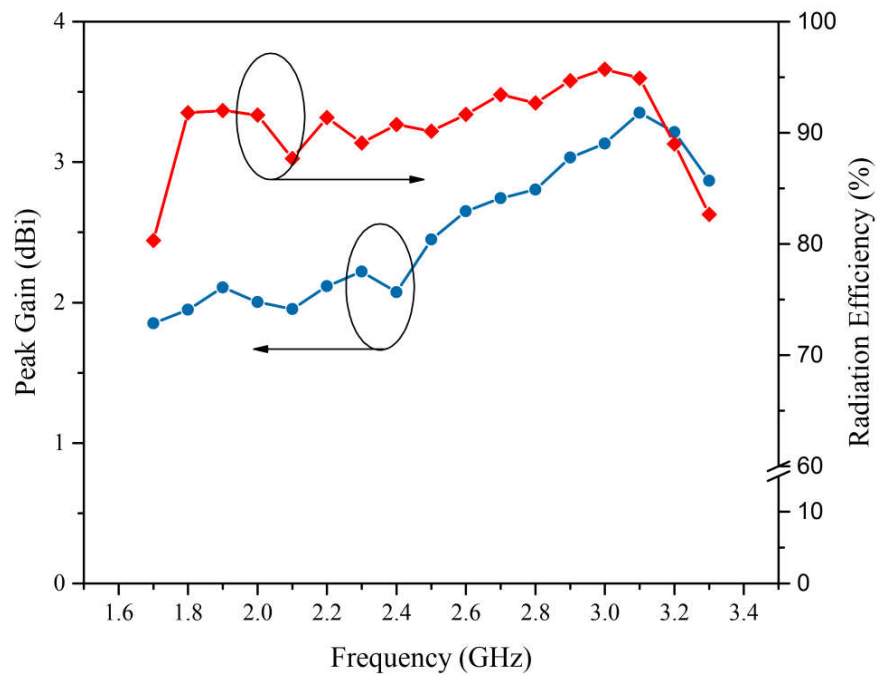


Figure 4.19. Measured Gain and radiation efficiency of the proposed antenna.

Table 4.1. Comparison results of the proposed and reference antennas.

	This Work	[58]	[62]	[61]
f (GHz)	1.84	2.16	1.99	3.8
Area ( $\lambda_0^2$ )	$0.30 \times 0.24$	$0.14 \times 0.22$	$0.33 \times 0.17$	$0.41 \times 0.25$
B.W. (%)	87.1	15.1	67.4	109.1
Gain (dBi)	3.35	1.62	2.77	3.37
$\eta$ (%)	95.7	72	90.08	98.01
Via process	No	No	No	Yes
Fabrication Type	Single-Sided	Single-Sided	Double-Sided	Double-Sided

#### 4.5 Miniaturized Antenna Design for Integrated Energy Harvesting System Results and Analysis

The simulated and measured S-parameters of the proposed HTA are demonstrated in Figure 4.20.

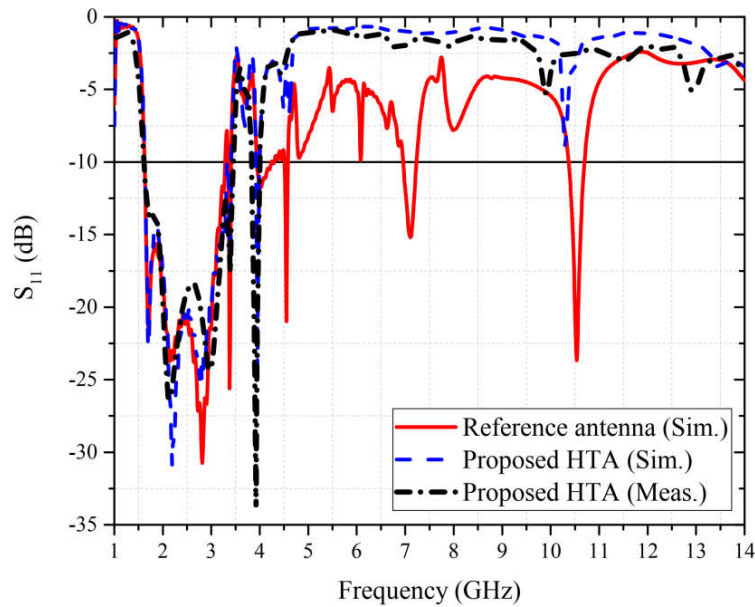
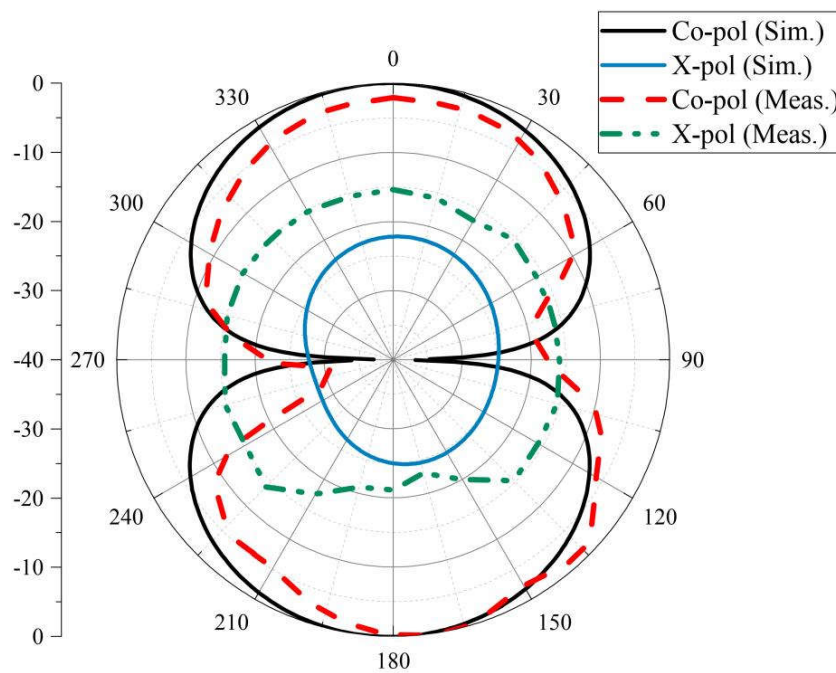


Figure 4.20. Measured and simulated reflection coefficient of the proposed HTA and the reference modified ZOR antenna without the harmonic rejecting filter.

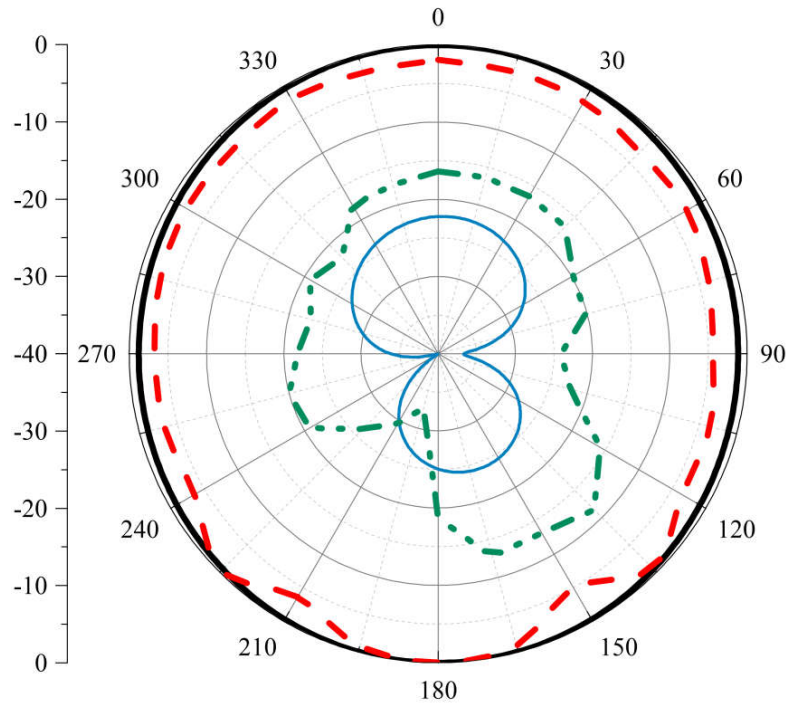
As is observed, the proposed HTA presents very good return loss performance with -10 dB bandwidth from 1.65 to 3.25 GHz covering most of highly populated modern wireless communication bands such as GSM1800, UMTS/3G, WiMAX, WLAN and LTE. It can also be seen that,  $|S_{11}| \geq -2.5$  dB achieved from 4.55 GHz up to 9.8 GHz providing a good rejecting band to the third harmonics while  $|S_{11}| \geq -5.2$  dB is obtained up to 14 GHz.

The antenna radiation pattern was measured inside an anechoic chamber. As was expected, the radiation characteristics of the filtering antenna is fairly similar to the reference antenna.

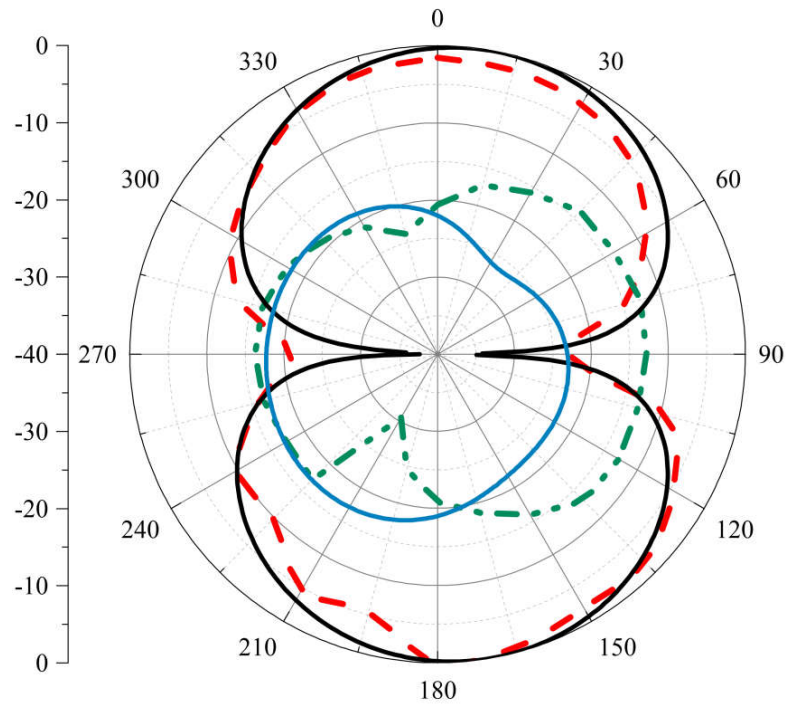
The measured and simulated radiation patterns of the HTA at E- and H-plane for three frequency points of 1.85, 2.45 and 3 GHz are presented in Figure 4.21. As is observed, the measured radiation patterns follow well the simulation results exhibiting dipole-like radiation pattern. The slight discrepancy on the measurement results is believed to be the impact of SMA connector and cables caused from side feeding of filtering antenna as well as fabrication tolerances.



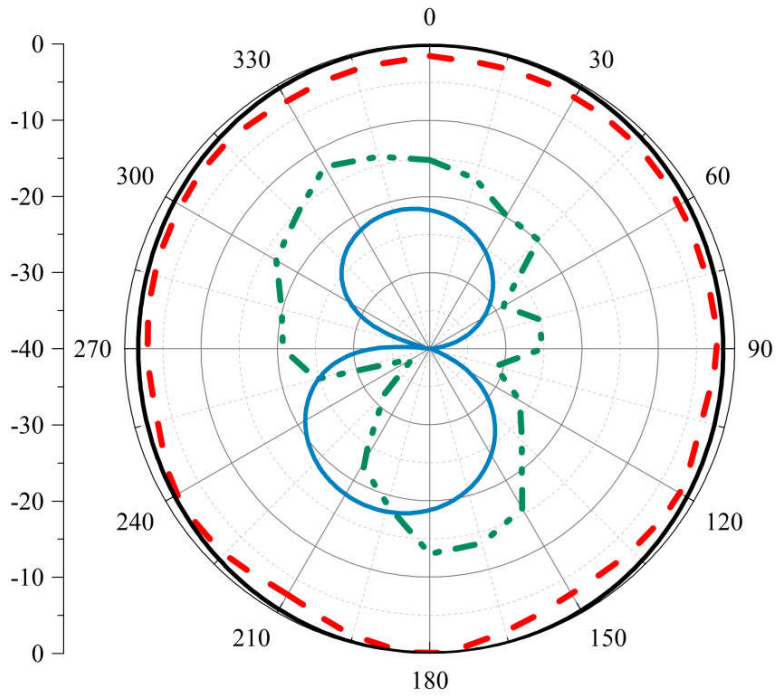
(a)



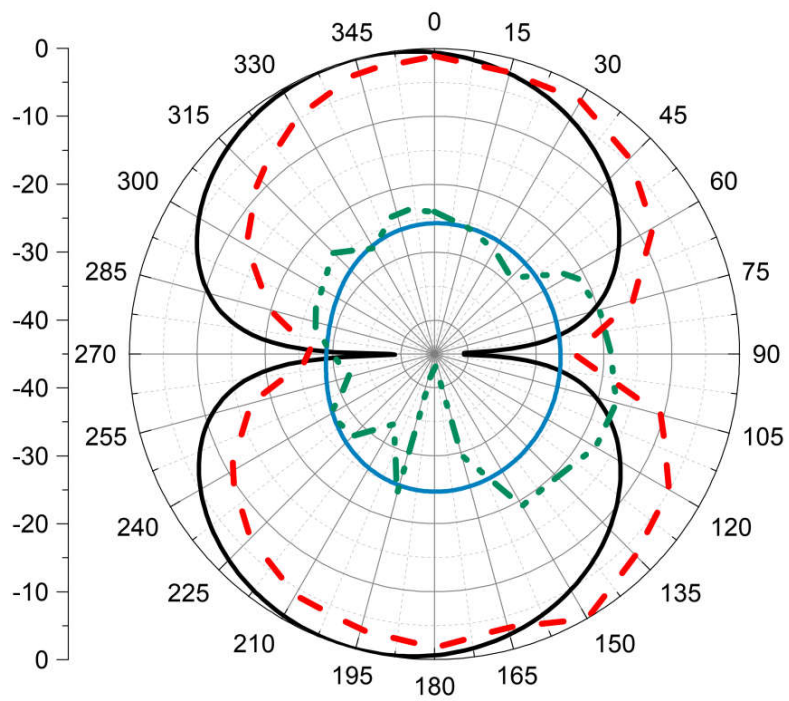
(b)



(c)



(d)



(e)

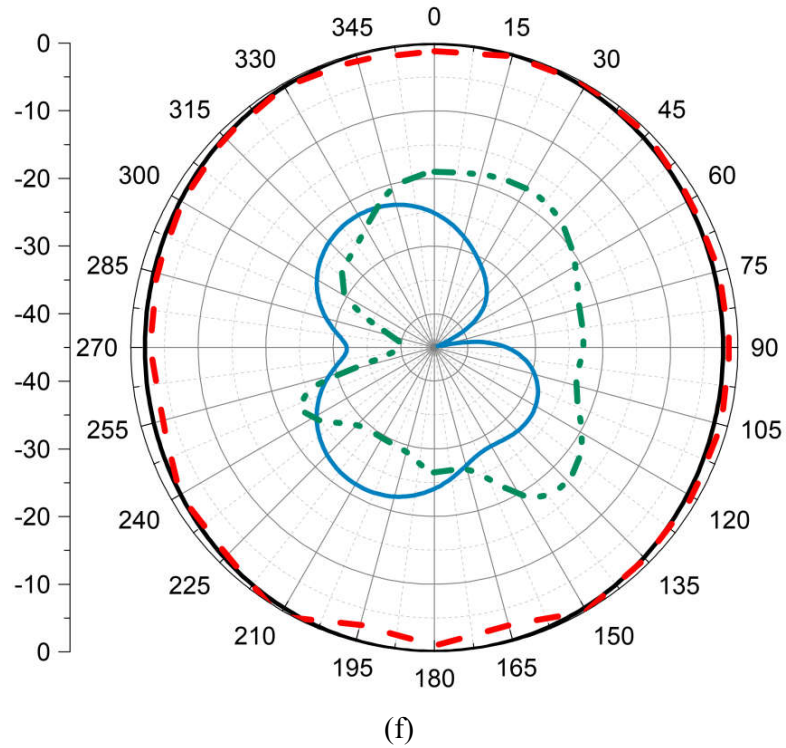


Figure 4.21. Simulated and measured radiation patterns of the HTA: (a) zy-plane (E-plane) at 1.85 GHz; (b) xz-plane (H-plane) at 1.85 GHz; (c) zy-plane (E-plane) at 2.45 GHz; (d) xz-plane (H-plane) at 2.45 GHz; (e) zy-plane (E-plane) at 3 GHz; (f) xz-plane (H-plane) at 3 GHz.

The measured and simulated realized gain of the filtering ZOR antenna is presented in Figure 4.22 . The measured gain varies from 1.83 to 3.4 dBi, with 2.34, 2.43 and 2.52

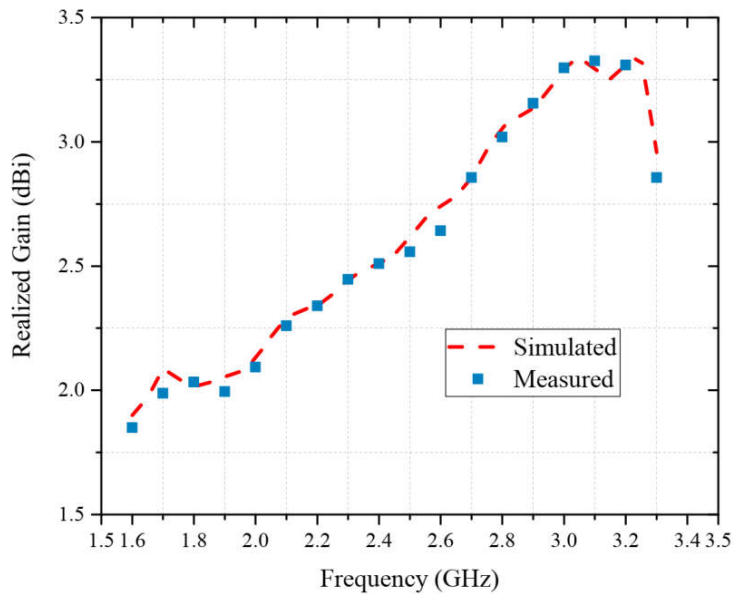


Figure 4.22. Measured and simulated gain of the HTA.

dBi at 2.15, 2.3 and 2.45 GHz, respectively.

#### 4.6 Rectenna Measurements Setup

After complete characterization of the designed rectifiers and antenna, a test setup is established to evaluate the performance of the rectenna in whole. The ad hoc measurement setup used for the experiment is shown in Figure 4.23. A double ridged standard horn antenna is used to transmit the RF power at the frequency of 2.45 GHz. The distance between the transmitter and receiving antenna is set and the calibration for the power density level is performed using the well-known Friis equation as:

$$S(\theta, \varphi) = \frac{4\pi P_{Cal}}{G_{Cal} \lambda^2} \quad \text{Equation (4.1)}$$

where the  $G_{Cal}$  is the known measured gain of the receiving antenna and  $P_{Cal}$  is the power measured at the receiving part which is set to be our reference plane.

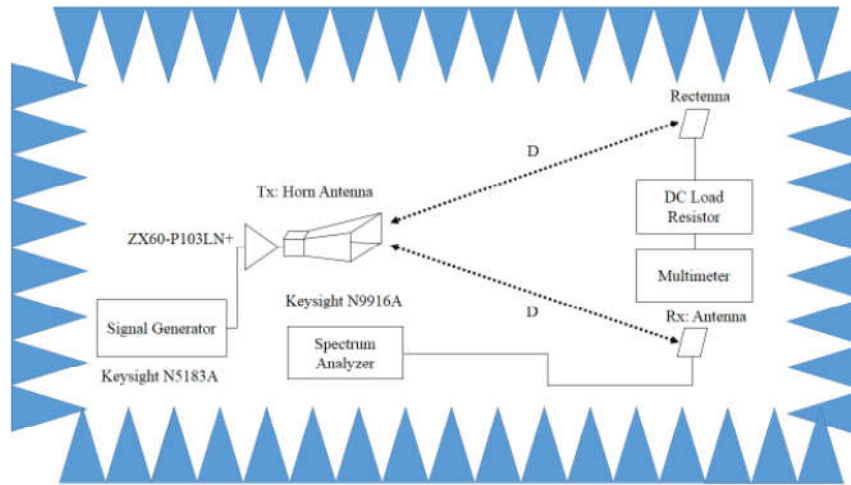


Figure 4.23. The ad hoc measurement test setup used for rectenna performance evaluation inside an anechoic chamber.

In order to evaluate the performance of the rectenna under the far-field condition, the Fraunhofer distance from the transmitting antenna is initially satisfied as

$$D = R_f = \frac{2D_a^2}{\lambda} \quad \text{Equation (4.2)}$$

where  $D_a$  is the largest dimension of the antenna and  $\lambda$  is the wavelength at the frequency of interest. Since our aim is to determine the efficiency over large range of frequency, it is necessary to define the distance with respect to the highest frequency of interest that is 2.6 GHz in our case. Furthermore, the Ferris transmission equation is used to estimate the amount of receiving power from the emitting antenna at the receiving point (receiving antenna) as a function of incident power density as

$$S(\theta, \varphi) = \frac{G_t P_t}{4\pi D^2} \quad \text{Equation (4.3)}$$

where  $G_t$  and  $P_t$  are the gain (with respect to an isotropic radiator) and transmitted power of emitting antenna and  $D$  is the distance between transmitting and receiving antennas (rectenna in this case). As is noticed from Equation (4.3), the value of power density is a function of gain and transmitted power from emitting antenna where the impact of radiation properties of the receiving antenna is entirely neglected. To include this effect, the received power is determined by an effective aperture area of the receiving antenna. The effective area is indeed a measure of how effective an antenna is at the power of radio waves. Hence, the received power available at the antenna terminal is calculated as a product of the effective aperture area of the receiving antenna times the power density as

$$P_{RX} = S(\theta, \varphi) \cdot A_{eff} = \frac{G_t P_t}{4\pi R^2} \times G_r \left( \frac{\lambda^2}{4\pi} \right) \quad \text{Equation (4.4)}$$

where  $G_r$  is the realized gain of the receiving antenna. It is worth noting that the effective aperture area of an antenna does not merely depends on the physical size of the antenna as the shape, coupling effects and the excited modes can also contribute to the overall performance of antenna. In this measurement, the distance  $D$  is set to be 1.45 m, which guarantees the far-field condition over the frequency range of interest. During the measurement, the system efficiency is calculated as

$$\eta_{EH} (\%) = \frac{1}{P_{RX}} \left( \sum_{n=1}^m P_{DC\_n} \right) \times 100 = \frac{1}{P_{RX}} \left( \frac{V_{out1}^2 + V_{out2}^2}{R_L} \right) \times 100 \quad \text{Equation (4.5)}$$

where  $P_{DC}$  is the DC power measured from the achieved voltage across each output load of rectifier and  $n$  is the number of outputs. The power is transmitted wirelessly to the rectenna via a horn antenna with an average gain of 9 dBi. Hence, first the transmitting power is measured using the antenna element only. Since the gain of the receiving antenna is already known, the value of receiving power is calculated, taking into account the power loss through the connections. Once the power level is set from the transmitter, the output voltage across the optimum load at the rectenna end is recorded using a multi-meter and the efficiency is calculated from Equation (4.5). Furthermore, through the process of rectenna measurement, it was noticed that, Due to fluctuation on both transmitting antenna gain and amplified power, the calculation of power density needs to be carried out independently at each frequency point. Taking into account the gain of transmitting antenna that is 9.12, 8.93 and 9.22 dBi at the frequency points of 2.15, 2.3 and 2.45 GHz, respectively, the value of amplified power (using amplifier model ZX60-P103LN+) is measured at the cable end before connecting to the transmitting antenna. The power is measured using a spectrum analyzer model N9916A where the recorded power values are 22.2, 21.9 and 22.23 dBm at the frequency points of 2.15, 2.3 and 2.45 GHz, respectively.

#### 4.7 Antenna and Modified Rectifier Combination Measurement Results

In order to evaluate the preliminary performance of the rectenna, the designed ZOR antenna is connected to the modified rectifiers using an SMA adapter as illustrated in Figure 4.24, and the DC voltage is measured across the resistive load at the output of rectifier. Figure 4.25 shows the measured efficiency and output voltage of the modified rectifier antenna under two different load values of 4.3 and 10 k $\Omega$ .

It can be observed that, in both cases, the efficiency of the rectenna remains almost the same, particularly for the power densities lower than 2  $\mu W / cm^2$ . However, as the power density increases, the rectenna with 4.3 k $\Omega$  load achieves better efficiency reaching to 40% at power density level of 5.28  $\mu W / cm^2$ . On the other hand, it can

also be observed that the rectenna with 10 kΩ load condition provides much higher DC voltage over all measured power density levels. The maximum voltage achieved

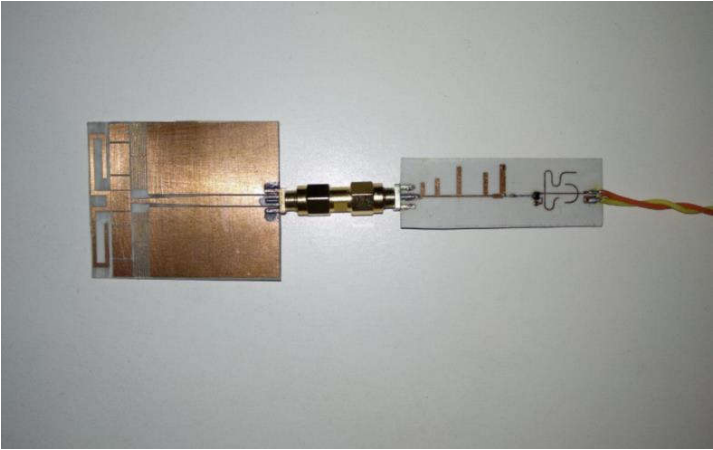


Figure 4.24. Photograph of rectenna from combination of modified rectifier and ZOR antenna.

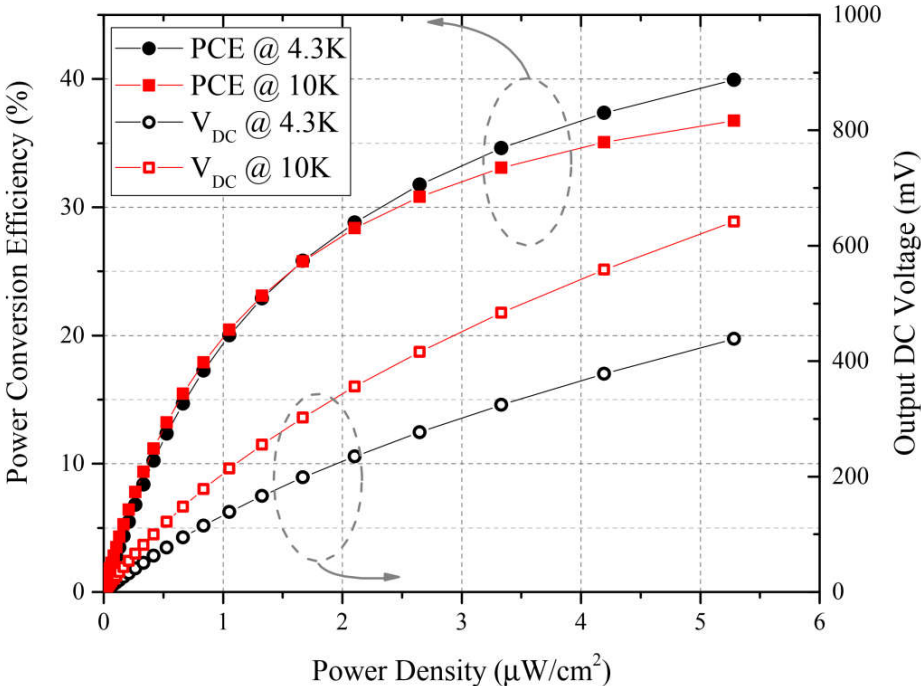


Figure 4.25. Measured RF-to-DC power conversion efficiency of the modified rectifier.

is 640 mV that is almost 46% higher than that of rectifier with 4.3 kΩ load condition being 438 mV. The RF-to-DC power conversion efficiency of the modified rectifier

as a function of output load is demonstrated in Figure 4.26. It is seen that, at the higher power density level ( $5.28 \mu\text{W}/\text{cm}^2$ ) the efficiency is more sensitive to the output load while as the power density drops to  $1.05 \mu\text{W}/\text{cm}^2$ , the variation is considerably reduced. Notice that, for a large range of output load of 2 to 15 K $\Omega$ , the power conversion efficiency remains better than 30% and 15% at the power densities of 5.28 and  $1.05 \mu\text{W}/\text{cm}^2$ , respectively. The peak efficiency is 39.8% at  $5.28 \mu\text{W}/\text{cm}^2$  for a load value of 5 k $\Omega$  while at the power density of  $1.05 \mu\text{W}/\text{cm}^2$  maximum efficiency of 21% over a load of 7 k $\Omega$  is obtained.

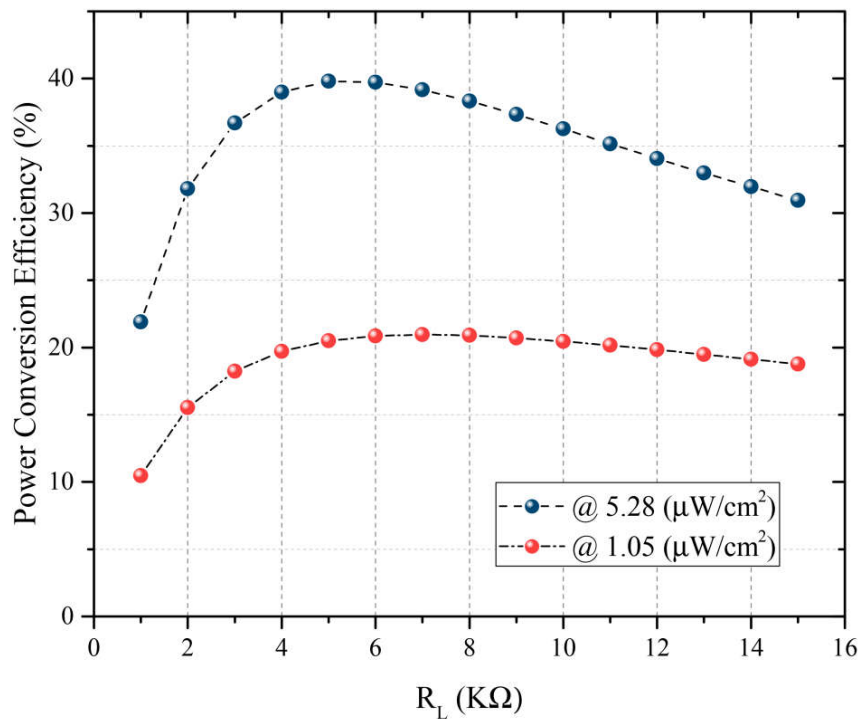


Figure 4.26. Measured RF-to-DC efficiency as a function of output load.

#### 4.8 Antenna and Broadband Rectifier Combination Measurement Results

Similar to the previous case, the performance of the combined broadband rectifier and antenna is evaluated as presented in Figure 4.27. The photograph of the antenna and broadband rectifier is demonstrated in Figure 4.28. During the measurement, the value of power density is calculated independently at each frequency point. It can be seen that, as the power density level increases the efficiency is also increased at all three frequency points of 2.15, 2.3 and 2.45 GHz. However, at 2.45 GHz, the maximum

achieved efficiency is 29.6% which is nearly 6% lower than that of rectenna with modified rectifier under the same load ( $10k\Omega$ ) and power density level ( $5.28 \mu W / cm^2$ ). The reason may be due to the impact of re-injected harmonics and higher sensitivity of the broadband rectifier to the coupling between antenna and rectifier. In addition, losses caused by secondary rectifier may also affect the overall efficiency. It can also be noticed that the efficiency is increased all over the power densities as the frequency reduced. When the power density is around  $1 \pm 0.05 \mu W / cm^2$  the efficiencies are 12.6%, 17% and 22.8% corresponding to the frequencies of 2.45, 2.3, 2.15 GHz, respectively. The maximum efficiency is 37.6% obtained at 2.15 GHz under the power density of  $5.13 \mu W / cm^2$ .

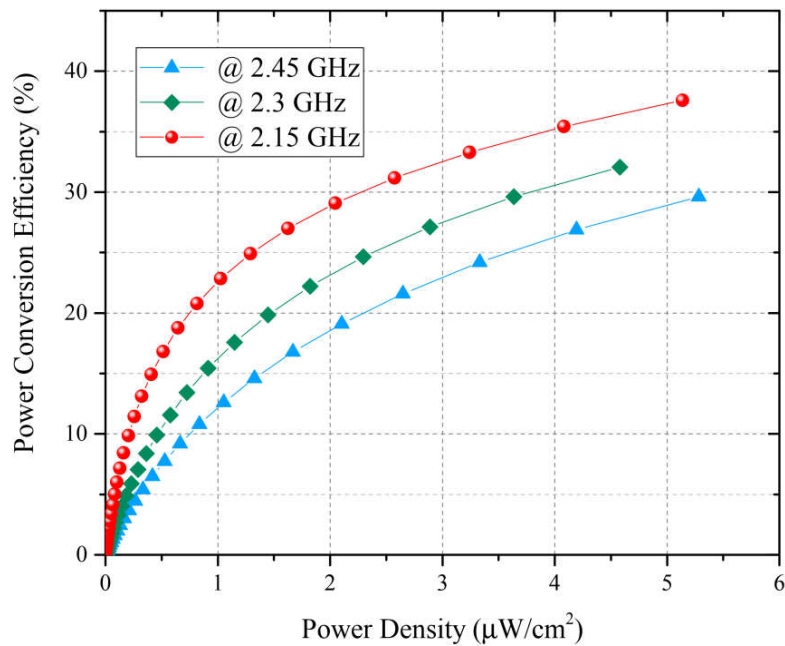


Figure 4.27. Measures RF-to-DC power conversion efficiency of the broadband rectenna versus power density.

Figure 4.28. Photograph of rectenna from combination of broadband rectifier and ZOR antenna.

The measured DC output voltage at each port as a function of power density is demonstrated in Figure 4.29. As is observed, maximum measured voltage is 597 mV corresponding to the power density level of  $5.13 \mu\text{W}/\text{cm}^2$  achieved at 2.15 GHz. The

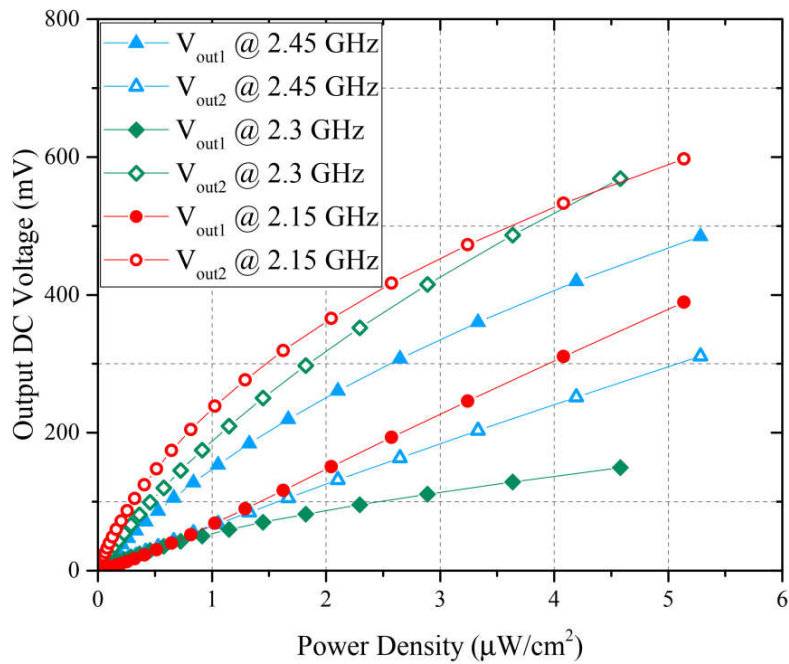


Figure 4.29. Measured DC output voltage at each port as a function of power density.

output voltage better than 100 mV achieved at least from one rectenna output at the power densities of 0.32, 0.66 and 0.46  $\mu W / cm^2$  at the frequencies of 2.15, 2.3 and 2.45 GHz, respectively. It is also interesting to notice that, while the second terminal is the dominant rectifier output at 2.15 and 2.3 GHz, the first rectifier output becomes dominant at 2.45 GHz due to the phase matching of the rectifier outputs around the same frequencies.

#### **4.9 Miniaturized Integrated Rectenna Results**

In order to evaluate the RF power received at the rectenna plane the carefully controlled power is transmitted through the horn antenna and the power received at the receiving point is monitored using the same exact antenna connected to the spectrum analyzer. The received RF power at the input of the rectenna and recorded rectified DC power for three frequency points of 2.15, 2.3 and 2.45 GHz are demonstrated in Figure 4.30. The photograph of fabricated integrated rectenna and its achieved RF-to-DC conversion efficiency are shown in Figure 4.31 and Figure 4.32, respectively. As is observed, the integrated rectenna shows better conversion efficiency at all frequencies and power density levels when compared with the combined antenna and rectifier using connectors demonstrating the advantage of integrated rectennas. The best efficiency for the low power level is achieved at the frequency of 2.15 GHz where the efficiency exceeds 20% (22.06%) at only 0.52  $\mu W / cm^2$ .

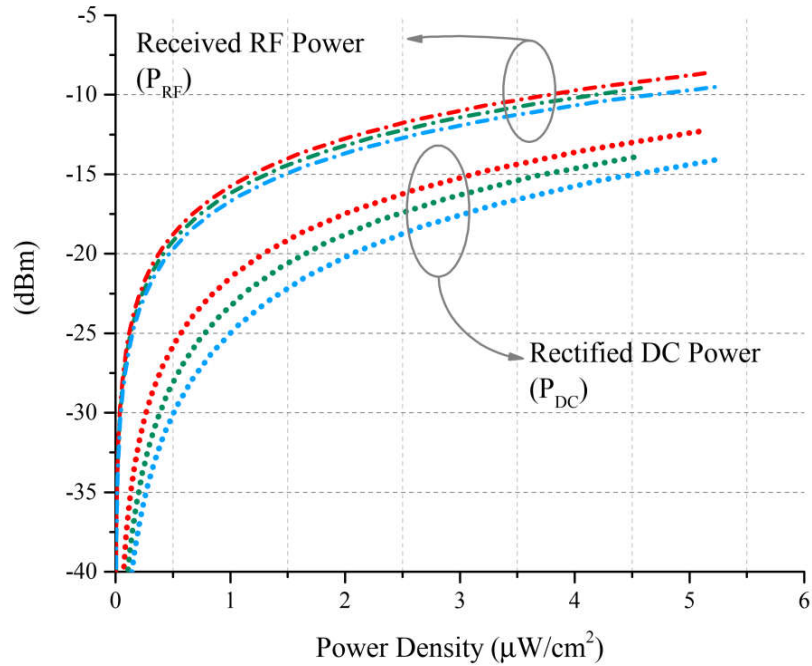


Figure 4.30. Measured received RF power and rectified DC power at 2.15 (Red lines), 2.3 (Green lines) and 2.45 GHz (Blue lines) for different power density levels.

The maximum recorded efficiency is 46.9% achieved at 2.15 GHz where the power density is  $5.13 \mu W / cm^2$ . The measured output DC voltage of the integrated broadband rectifier is demonstrated in Figure 4.33. It can be seen that, at the power density of  $0.51 \mu W / cm^2$  the voltage of 100 mV is obtained from at least one output terminal at all the measured frequency points. The maximum voltage is 657 mV obtained from second output of rectenna at 2.15 GHz. It is worth noting that, the highest output isolation obtained at 2.3 GHz where the output voltage from first ( $V_{Out1}$ ) and second output ( $V_{Out2}$ ) terminals are 171 and 650 mV, respectively, at the power density of  $4.58 \mu W / cm^2$ . Figure 4.34 depicts the photograph of the integrated antenna under the test and the summary of the measured results are tabulated in Table 4.2. Furthermore, although crosstalk is an important effect that can cause serious performance degradation, however, the low power level operation of presented energy harvester, which is typically in the range of micro Watts, ensures the negligible impact of crosstalk on the system performance [136-138].

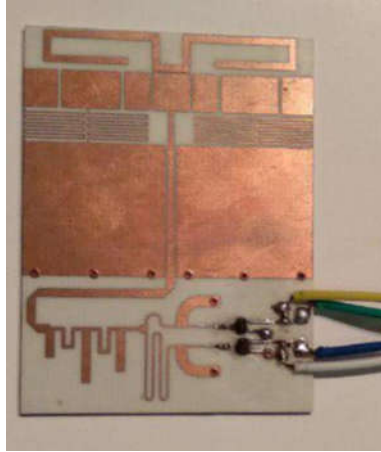


Figure 4.31. Fabricated prototype of compact integrated rectenna.

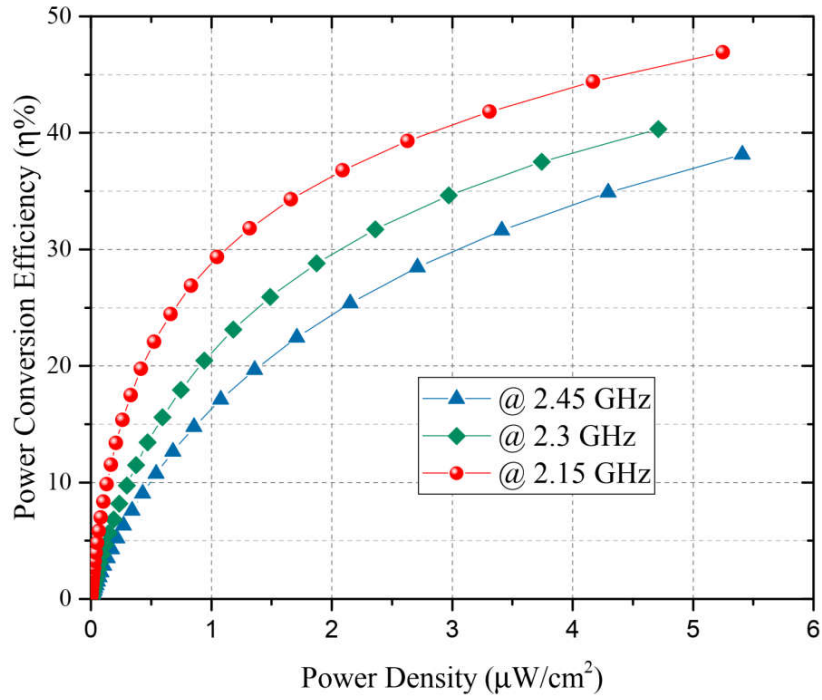


Figure 4.32. Measured RF-to-DC efficiency of the integrated Rectenna.

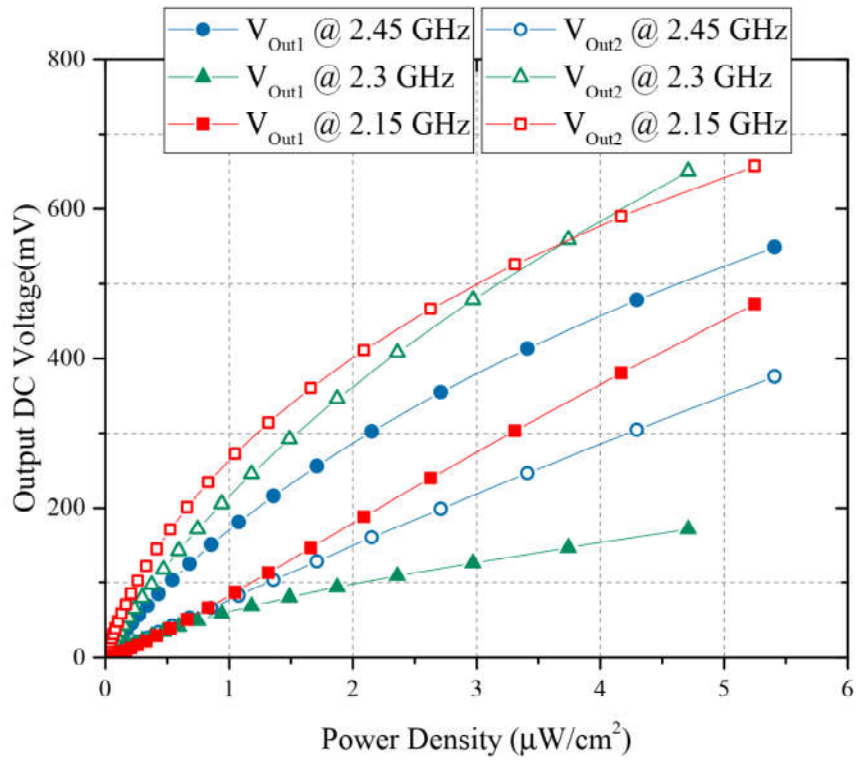


Figure 4.33. Measured output DC voltage at different power density levels.

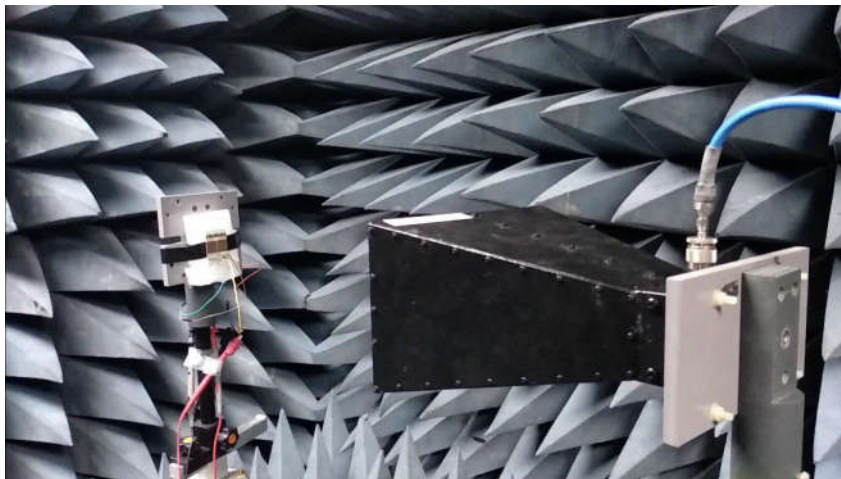
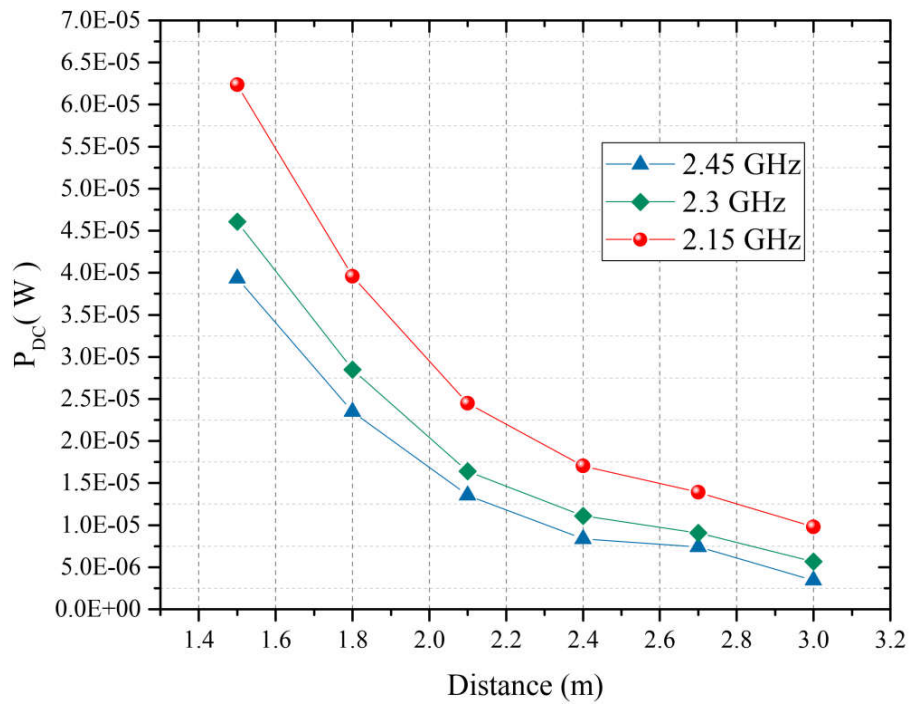


Figure 4.34. Rectenna under test inside an anechoic chamber.

Table 4.2. Performance comparison of the presented rectenna combinations.

Rectenna Configuration	Freq.	Eff. > 10 @ $\mu W / cm^2$	Voltage (mV)	Max. Efficiency @ $\mu W / cm^2$	Voltage (mV)
Antenna and Rectifier Combination	2.45	10.8% @ 0.8	127@V1	29.62 @ 5.28	485 @ V1
			54 @V2		311 @V2
	2.3	11.57% @ 0.57	35 @V1	32 @ 4.58	150 @V1
			120@V2		568 @V2
	2.15	11.43@ 0.25	13@ V1	37.57 @ 5.13	390 @ V1
			87@ V2		596 @ V2
Integrated Rectenna	2.45	10.74@ 0.54	103@V1	38.14 @ 5.28	550 @ V1
			42@ V2		375 @ V2
	2.3	11.48@ 0.37	28@ V1	40.3 @ 4.58	171 @ V1
			97@ V2		650 @ V2
	2.15	11.52@ 0.16	9@ V1	46.9 @ 5.13	472 @ V1
			70@ V2		657@ V2

Furthermore, the measured harvested power and output DC voltage of the integrated rectenna as a function of distance are plotted in Figure 4.35 (a) and Figure 4.35 (b), respectively. The value of harvested DC power is around 24.5, 16.4 and 13.55  $\mu W$  at the distance of 2.1 meter away from the transmitter. The value of the harvested power drops swiftly as we go further away from the transmitter achieving an output power of 9.8, 5.66 and 3.45  $\mu W$  at the frequency points of 2.15, 2.3 and 2.45 GHz, respectively, for a distance of just 3 meter away from the transmitter. The highest output DC voltage is 656 mV obtained at the frequency of 2.3 GHz when the distance between the rectenna and transmitter is just 1.5 m. It is worth noting that, considering the low level of transmitting power of only  $150 \pm 20$  mW, signifies the excellent performance of the proposed rectenna at such a compact form. The impact of increased harvested power at lower frequencies are due to the lower FSPL as well as the increased rectifier sensitivity at those lower power levels.



(a)

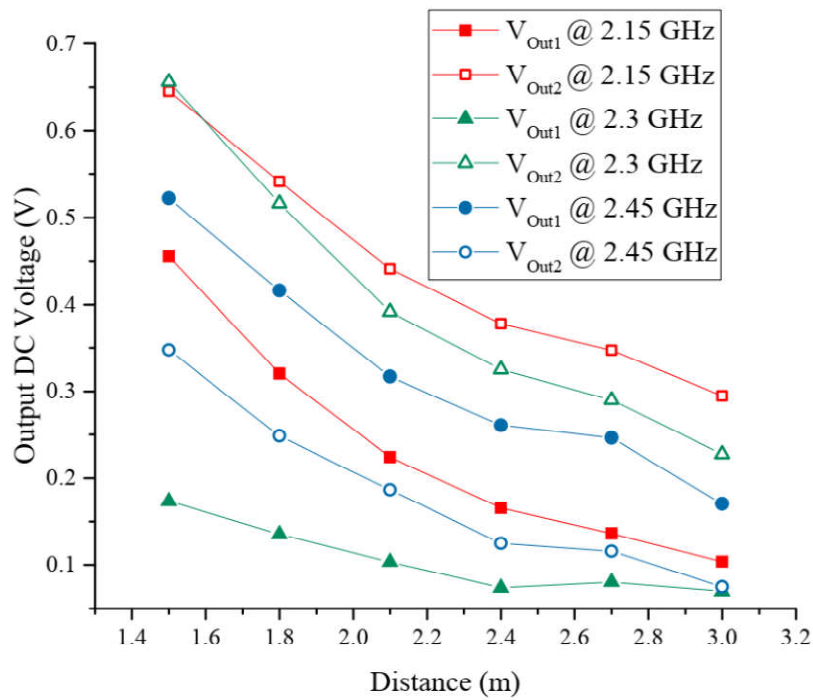


Figure 4.35. Measured harvested (a) DC power and (b) achieved output DC voltage as a function of distance.

#### 4.10 Broadband Rectenna performance on the open Field

For outdoor measurements, the rectenna output voltage has been measured in the balcony of an office environment at approximately 30 m away from a cell tower in which the antenna is directly connected to a spectrum analyzer. Through the measurements, it was noticed that the highest range of measured power corresponds to the commonly used frequency bands of GSM-1800, UMTS-2100 and WiFi frequency that are presented in Table 4.3.

Table 4.3 The range of measured available power at approximately 30 m away from cell tower.

Band	Frequency Range (MHz)	Antenna Gain (dBi)	Received Power (dBm)
GSM-1800	1805 - 1880	2.03	-25 to -40
UMTS-2100/3G	2110 - 2170	2.31	-30 to -40
WiFi	2400 - 2500	2.5	-30 to -45

The power is measured using the same ZOR antenna that has been used in integrated rectenna. It was also found that the value of received WiFi signal is greatly improved when a high data rate communication is established between the WiFi router and any connected device such as Laptops. For example, when compared with a video of 480p resolution, the power received from the WiFi raised from -35 to -30 dBm is nearly quadrupled when a 4k video is played. By connecting the multimeters to the outputs of the integrated rectenna the amount of rectified power was measured to be ranging from -16 to -21. Obviously this amount of rectified power is larger than the measured receiving power. It is worth noting that, when the same experiment is conducted with modified rectifier, the output voltage remained less than 10 mV the entire time which can clearly reconfirm the advantage of broadband rectifiers for the purpose of energy harvesting applications. The highest voltage value recorded is 428 mV and 256 mV from port I and port II respectively. Since there was a large fluctuation on the amount of received power from each frequency band, it was decided to perform the measurements inside a more controlled environment to properly evaluate the performance of the proposed rectenna and will be presented next.

#### 4.11 Multi-Tone Analysis and Measurement Results

In order to more accurately evaluate the broadband performance of the proposed integrated rectenna under multi-tone conditions, a 2-way RF power combiner (ZN2PD2-50-S+) and 3-way RF power combiner (ZN3PD-622W-S+) are used to combine the generated signals from three individual signal generators to feed the transmitting antenna. The test setup used for the measurement is presented in Figure 4.36. During the measurements, the frequency points were kept the same which are 2.15, 2.3 and 2.45 GHz corresponding to UMTS/3G, WiMAX and Wi-Fi frequencies, respectively.

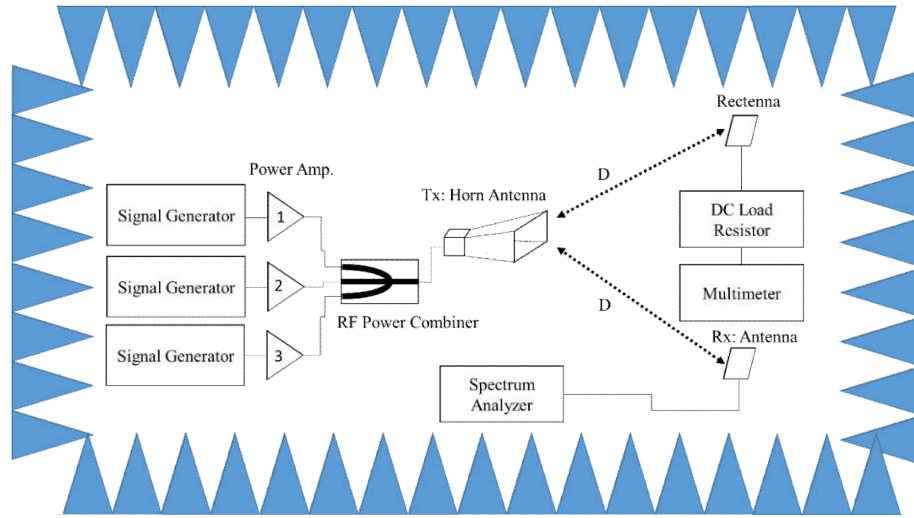


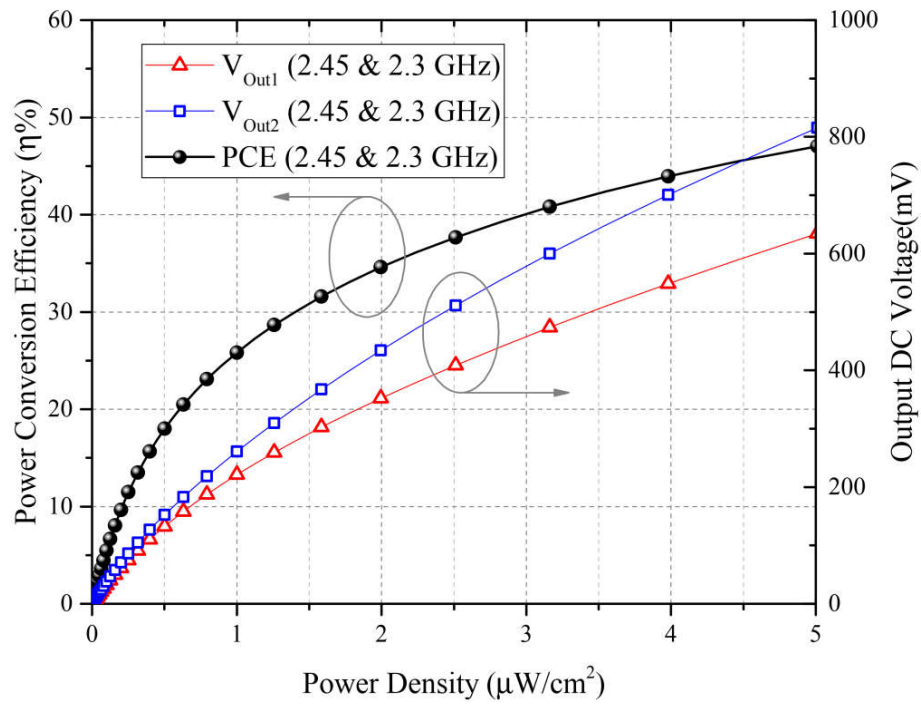
Figure 4.36. The general test setup used for multi-tone measurements inside anechoic chamber.

The measurement results of the two and three-tone power conversion efficiency of the broadband integrated rectenna are presented in Figure 4.37 (a)-(d). The power density for multi-tone measurements are evaluated as [96]

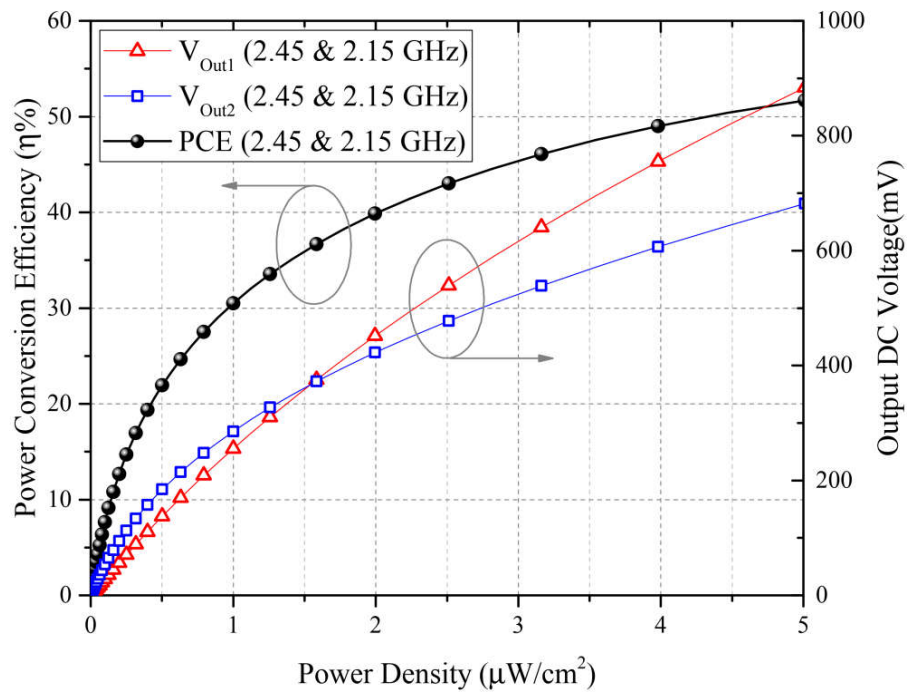
$$S = \sum_{n=1}^m \frac{P(f_n)}{A_{eff}(f_n)} = \frac{4\pi}{c^2} \sum_{n=1}^m \frac{P(f_n)}{G(f_n)/f_n^2} \quad \text{Equation (4.6)}$$

where  $P$  is the input power level,  $A_{eff}$  is antenna's equivalent aperture area,  $n$  is the tone number,  $G$  is the measured gain of the antenna at each tone and  $c$  is the speed of light in the vacuum. As is observed, under the multi-tone condition, there is a

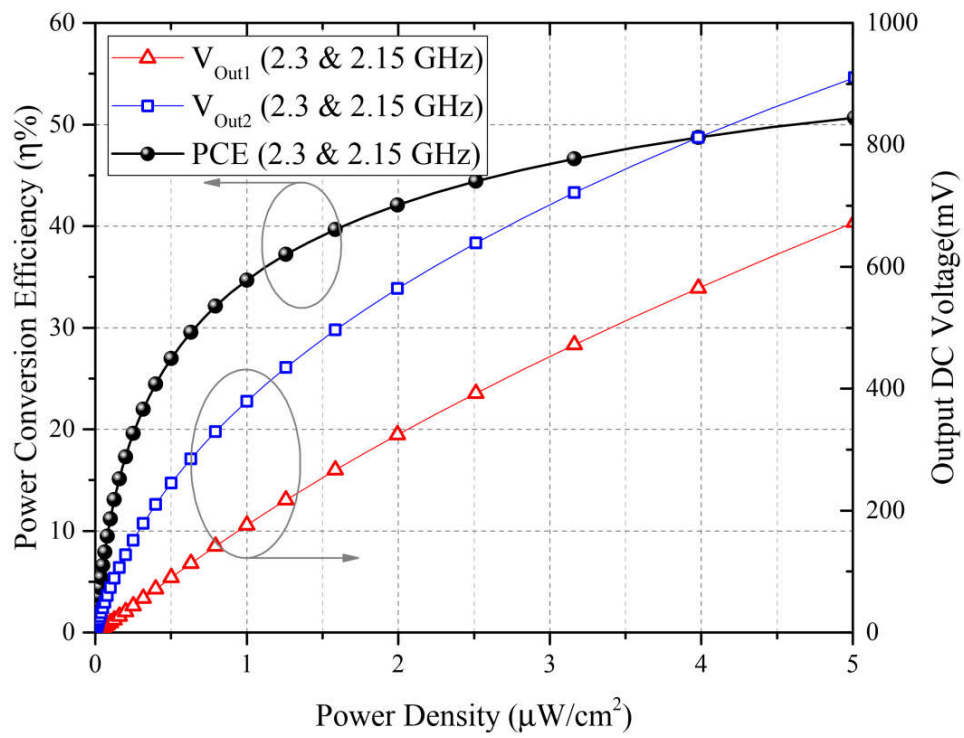
noticeable improvement on both output voltage and overall efficiency of the rectenna. For the two-tone cases, the highest sensitivity is obtained for the case of 2.3 and 2.15 GHz where an efficiency of 10.3% obtained at only  $0.09 \mu W / cm^2$ . The efficiency increases to 15.1% at the power density level of  $0.16 \mu W / cm^2$  and the output voltages of 26 and 106 mV are obtained from  $V_{Out1}$  and  $V_{Out2}$ , respectively. Moreover, an efficiency of 50.7% at the power density of  $5 \mu W / cm^2$  is obtained. On the other hand, for the case of 2.45 and 2.15 GHz, the efficiency is around 10.8% at  $0.16 \mu W / cm^2$  and increases to 51.7% at  $5 \mu W / cm^2$  achieving a DC voltage of 883 and 681 mV from



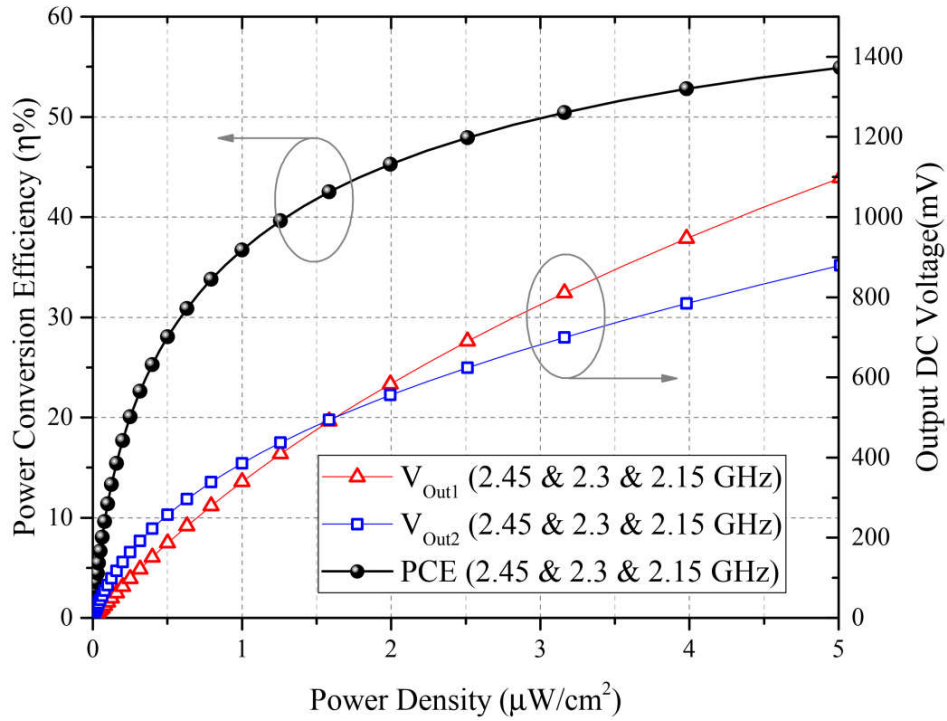
(a)



(b)



(c)



(d)

Figure 4.37. The two and three-tone performance measurements of the broadband integrated rectenna (a) 2.45 & 2.3GHz; (b) 2.45 & 2.15 GHz; (c) 2.3 & 2.15 GHz; (d) 2.45 & 2.3 & 2.15 GHz.

$V_{\text{Out1}}$  and  $V_{\text{Out2}}$ , respectively. Furthermore, the lowest two-tone combination efficiency achieved for the case of 2.45 and 2.3 GHz where the efficiency is 8.05% and 47% at the power densities of  $0.16$  and  $5 \mu\text{W}/\text{cm}^2$ , respectively. As is observed from Figure 4.37(d), the highest efficiency achieved is for the three-tone case with the measured conversion efficiency of 10.5% and 50.4% obtained at  $0.09$  and  $3.16 \mu\text{W}/\text{cm}^2$ , respectively. Moreover, as the power increases, the efficiency reaches to 54.9% corresponding to the power density level of  $5 \mu\text{W}/\text{cm}^2$ . The output voltage under the power density of  $5 \mu\text{W}/\text{cm}^2$  are 1097 and 880 mV achieved from  $V_{\text{Out1}}$  and  $V_{\text{Out2}}$ , respectively.

#### 4.12 Summary

In this chapter, the experimental performance of several designed rectifiers and antennas have been presented. The empirical results agree well with theoretical verifying the validity of the proposed design approach. Moreover, the performance of

different rectenna components and structures have been presented and discussed. It has been shown that the rectenna with increased output tolerance (antenna and modified rectifier) has the advantage of more stable output efficiency over large range of output loads which can greatly expand the applicability of the energy harvesting system over larger number of available sensors with different voltage and current requirement. The advantage of integrated rectennas has also been emphasized.

It has been shown that the efficiency of a broad band rectenna can be considerably improved under the multi-tone (two- and three-tone) conditions which has two distinguish benefits:

- 1- Compared to conventional rectennas, a broadband rectenna can remain operational by simply transmitting the reduced power over different frequency channels within the operating band of broadband rectenna without exceeding the regulatory standards.
- 2- Increased output DC power and efficiency of the broadband rectenna can alleviate the physical dimensions problem of high gain rectenna systems to some extent which can be advantageous to many space-restricted applications such as IoT devices.

## CHAPTER 5

### CONCLUSION AND RECOMMENDATIONS FOR FUTURE WORK

#### 5.1 Conclusion

This thesis work described the research that was performed to enhance the functionality of rectennas for the efficient far-field electromagnetic power harvesting in space-restricted applications. The theory of composite right-/left-handed transmission line is employed to realize a miniaturized and high efficiency antenna with broad bandwidth performance. By utilizing the zeroth order resonance of the artificial CRLH-TL a symmetrically fed two-stage metamaterial-inspired antenna was designed in which a compromise between the antenna radiation properties and overall compact size has been established.

The design of miniaturized high efficiency ZOR antenna with broad bandwidth operation is presented. The experimental results of the antenna exhibit wide operational bandwidth of 1.6 GHz from 1.715 to 3.318 corresponding to 87.1% of the fractional bandwidth and excellent radiation efficiency up to 95.7%.

Moreover, two essential harmonic terminated rectifier design have been presented aiming to improve the output load tolerance and bandwidth performance of rectifiers. The measured results indicate an efficiency better than 40% over a large load range of 3 to 9 k $\Omega$  and various incident power levels of 5 and -10 dBm, respectively.

Furthermore, the designed broadband rectifier attains a high power conversion efficiency over a broad frequency span of 1.85 to 2.6 GHz under various input power levels. A prototype has been fabricated and tested to validate the design. Measurement results indicate a peak efficiency of 70.3% obtained at 2.3 GHz. Furthermore, a very good power dynamic range of 14 dBm from -8 to 6 dBm is obtained in which the efficiency remains above 40% at all the sampled frequencies. Moreover, the harvester reliability has been further improved as targeted frequency lies within the jammed available spectrum sources such as 1.8 to 2.7 GHz frequency range encompassed by GSM-1800 (1805.2 – 1879.8 GHz), UMTS-3G (2110 – 2170 GHz), WiMAX (2.3

GHz), ISM-2.4 GHz (2.4-2.5 GHz, including Wi-Fi channels) and LTE- 4G (2.5-2.69 GHz) at the upper band.

Lastly, the advantage of broadband rectifier has been emphasised by performing open field and multi-tone (Three-tone) measurements where the overall dimensions of the entire system is as compact as  $53.5 \times 40.5 \times 0.508 \text{ mm}^3$ .

It was proven that for a miniaturized rectenna, the broad bandwidth properties could pay-off for the low gain of rectenna to some extent. We could successfully increase the performance of rectenna under the multi-tone (three-tone) condition achieving over and 50% obtained for the power density level of only  $3.16 \mu\text{W} / \text{cm}^2$ , which was fairly high considering the overall dimensions of the miniaturized rectenna. The presented rectenna can be an alternative to the bulky and high gain rectennas for the space-restricted application such as IoT devices.

## **5.2 Contribution of this Research Work**

The contribution of this research work are summarized as follows

1. A novel compact, high efficiency and bandwidth-enhanced ZOR antenna loaded by parasitic element is developed. Therefore, the narrowband and deteriorated radiation pattern of the miniaturized ZOR antenna is compensated by loading the structure with a parasitic element and providing the symmetry to the entire antenna. The antenna presents a very wide bandwidth property with stable radiation pattern and fairly high radiation efficiency.
2. A novel technique is presented as an efficient approach to increase the output load tolerance of the low power rectifier circuits. In order to validate the idea, a rectifier is designed operating at 2.45 GHz. The rectifier can maintain the high performance over large range of power and the conversion efficiency remains high against external circuitry, thus, the same rectifier can be utilized for various external circuitries with different/alternating impedance characteristics. The measurement results show that the output load sensitivity is considerably reduced.

3. In order to increase the bandwidth of the rectifiers under low power condition, an original idea is put forward to take advantage from a phase matched and identical complementary rectifier. To increase the reliability, the targeted frequency is chosen to be within the jammed available spectrum sources including GSM-1800, UMTS-3G, WiMAX, ISM-2.4 GHz and LTE-4G. As a consequence, through the measurements, much larger and consistent output DC power is obtained with a considerable improvement than conventional rectifiers. The measured results show the broadband performance under low power condition with increased power dynamic range, thus, increasing both output power and system mobility.
4. A compact integrated energy harvesting system with broadband performance is presented. To validate the broadband harvester performance, it has been tested under multi-tone condition demonstrating increased achieved efficiency and output power which can make up for the reduced size/gain of the implemented harvesters antenna.

### **5.3 Future Works**

The process of energy harvesting requires precise scaling of power at every single stage of the process down to consumer device. Currently, most of the designs are focused on the overall RF-to-DC efficiency of the harvesters only entirely ignoring the external circuit requirements for the optimum performance. For example, the integration of the rectenna with energy management unit imposes some restriction on the load condition such as cold start requirements of the management circuits. Unfortunately, most of ultra-low power management ICs are built for the purpose of energy harvesting using the solar or thermal harvesters which are substantially low current/high voltage harvesters. In opposed to that, RF and microwave energy harvesters are preferred to be high current/low voltage harvesters so that the usage of several diodes in the harvester can be avoided resulting in both more cost effective and low loss harvesters.

There is also the need for the design of dual polarized antennas with broadband and omnidirectional radiation characteristics for the purpose of energy harvesting. Currently almost all of dual polarized antennas used for energy harvesting are

unidirectional with typically narrowband characteristic which makes them less intriguing for the real-life applications.

There is still the need for more research on the broadband rectifier designs to extend their bandwidth somewhere close to that of broadband rectifiers at the high power levels.

Complementary metal–oxide–semiconductor (CMOS) technology has shown great potential on the realization of ultra-low power integrated circuits. While the power handling of the CMOS technology is lower than its Schottky diode counterpart, it can deliver low-loss and tunable diode properties which can be engineered according to the application requirements.

## REFERENCES

- [1] H. S. Kim, J.-H. Kim, and J. Kim, "A review of piezoelectric energy harvesting based on vibration," *International journal of precision engineering and manufacturing*, vol. 12, pp. 1129-1141, 2011.
- [2] I. Kosmadakis, V. Konstantakos, T. Laopoulos, and S. Siskos, "Vibration-based energy harvesting systems characterization using automated electronic equipment," *Sensors & Transducers*, vol. 187, pp. 75-76, 2015.
- [3] M. Hassanaliheragh, A. Page, T. Soyata, G. Sharma, M. Aktas, G. Mateos, "Health monitoring and management using Internet-of-Things (IoT) sensing with cloud-based processing: Opportunities and challenges," in *IEEE International Conference on Services Computing*, 2015, pp. 285-292.
- [4] S. Feng, P. Setoodeh, and S. Haykin, "Smart home: Cognitive interactive people-centric Internet of Things," *IEEE Communications Magazine*, vol. 55, pp. 34-39, 2017.
- [5] M. Diaz-Cacho, E. Delgado, P. Falcon, and A. Barreiro, "IoT integration on industrial environments," in *2015 IEEE World Conference on Factory Communication Systems (WFCS)*, 2015, pp. 1-7.
- [6] L. Atzori, A. Iera, and G. Morabito, "The internet of things: A survey," *Computer networks*, vol. 54, pp. 2787-2805, 2010.
- [7] D. Lund, C. MacGillivray, V. Turner, and M. Morales, "Worldwide and regional internet of things (IoT) 2014–2020 forecast: A virtuous circle of proven value and demand," *International Data Corporation (IDC), Tech. Rep.*, vol. 1, 2014.
- [8] Q. Liu, J. Wu, P. Xia, S. Zhao, and L. Hanzo, "Distributed laser charging for mobile wireless power transfer-Will it work," *IEEE transactions on vehicular technology*, vol. 65, pp. 9457-9470, 2016.

- [9] K. Wu, D. Choudhury, and H. Matsumoto, "Wireless power transmission, technology, and applications," *Proceedings of the IEEE*, vol. 101, pp. 1271-1275, 2013.
- [10] A. Kurs, A. Karalis, R. Moffatt, J. D. Joannopoulos, P. Fisher, and M. Soljačić, "Wireless power transfer via strongly coupled magnetic resonances," *science*, vol. 317, pp. 83-86, 2007.
- [11] G. Landis, M. Stavnes, J. Bozek, and S. Oleson, "Space transfer with ground-based laser/electric propulsion," in *28th Joint Propulsion Conference and Exhibit*, 1992, pp. 3213-3214.
- [12] R. M. Dickinson, "Performance of a high-power, 2.388-GHz receiving array in wireless power transmission over 1.54 km," in *1976 IEEE-MTT-S International Microwave Symposium*, 1976, pp. 139-141.
- [13] A. S. Andrenko, X. Lin, and M. Zeng, "Outdoor RF spectral survey: A roadmap for ambient RF energy harvesting," in *TENCON 2015-2015 IEEE Region 10 Conference*, 2015, pp. 1-4.
- [14] M. Piñuela, P. D. Mitcheson, and S. Lucyszyn, "Ambient RF energy harvesting in urban and semi-urban environments," *IEEE Transactions on microwave theory and techniques*, vol. 61, pp. 2715-2726, 2013.
- [15] R. Vyas, H. Nishimoto, M. Tentzeris, Y. Kawahara, and T. Asami, "A battery-less, energy harvesting device for long range scavenging of wireless power from terrestrial TV broadcasts," in *IEEE/MTT-S International Microwave Symposium Digest*, 2012, pp. 1-3.
- [16] T. Haumann, U. Münzenberg, W. Maes, and P. Sierck, "HF-Radiation levels of GSM cellular phone towers in residential areas," in *2nd International Workshop on Biological effects of EMFS*, 2002, pp. 327-33.

- [17] D. Willkomm, S. Machiraju, J. Bolot, and A. Wolisz, "Primary users in cellular networks: A large-scale measurement study," in *3rd IEEE Symposium on New Frontiers in Dynamic Spectrum Access Networks*, 2008, pp. 1-11.
- [18] IEEE Standards Coordinating Committee, "IEEE standard for safety levels with respect to human exposure to radio frequency electromagnetic fields, 3kHz to 300GHz," *IEEE C95*, 2005.
- [19] J. C. Lin, "A new IEEE standard for safety levels with respect to human exposure to radio-frequency radiation," *IEEE Antennas and Propagation Magazine*, vol. 48, pp. 157-159, 2006.
- [20] Guideline, I. C. N. I. R. P., "Guidelines for limiting exposure to time-varying electric, magnetic, and electromagnetic fields (up to 300 GHz)," *Health phys*, vol. 74, pp. 494-522, 1998.
- [21] International Commission on Non-Ionizing Radiation Protection. "ICNIRP statement on the "Guidelines for limiting exposure to time-varying electric, magnetic, and electromagnetic fields (up to 300 GHz)", " *Health Physics*, vol. 97, pp. 257-258, 2009.
- [22] W. C. Brown, "The history of power transmission by radio waves," *IEEE Transactions on microwave theory and techniques*, vol. 32, pp. 1230-1242, 1984.
- [23] J. Akkermans, M. Van Beurden, G. Doodeman, and H. Visser, "Analytical models for low-power rectenna design," *IEEE Antennas and Wireless Propagation Letters*, vol. 4, pp. 187-190, 2005.
- [24] J.-H. Chou, D.-B. Lin, K.-L. Weng, and H.-J. Li, "All polarization receiving rectenna with harmonic rejection property for wireless power transmission," *IEEE Transactions on Antennas and Propagation*, vol. 62, pp. 5242-5249, 2014.

- [25] A. Georgiadis, G. V. Andia, and A. Collado, "Rectenna design and optimization using reciprocity theory and harmonic balance analysis for electromagnetic (EM) energy harvesting," *IEEE Antennas and Wireless Propagation Letters*, vol. 9, pp. 444-446, 2010.
- [26] Z. Harouni, L. Cirio, L. Osman, A. Gharsallah, and O. Picon, "A dual circularly polarized 2.45-GHz rectenna for wireless power transmission," *IEEE Antennas and Wireless Propagation Letters*, vol. 10, pp. 306-309, 2011.
- [27] T. Matsunaga, E. Nishiyama, and I. Toyoda, "5.8-GHz stacked differential rectenna suitable for large-scale rectenna arrays with DC connection," *IEEE Transactions on Antennas and Propagation*, vol. 63, pp. 5944-5949, 2015.
- [28] B. L. Pham and A.-V. Pham, "Triple bands antenna and high efficiency rectifier design for RF energy harvesting at 900, 1900 and 2400 MHz," in *Microwave Symposium Digest (IMS), IEEE MTT-S International*, 2013, pp. 1-3.
- [29] Y.-J. Ren and K. Chang, "5.8-GHz circularly polarized dual-diode rectenna and rectenna array for microwave power transmission," *IEEE Transactions on Microwave Theory and Techniques*, vol. 54, pp. 1495-1502, 2006.
- [30] Y.-H. Suh, C. Wang, and K. Chang, "Circularly polarised truncated-corner square patch microstrip rectenna for wireless power transmission," *Electronics Letters*, vol. 36, pp. 1-2, 2000.
- [31] H. Sun and W. Geyi, "A new rectenna with all-polarization-receiving capability for wireless power transmission," *IEEE Antennas and Wireless Propagation Letters*, vol. 15, pp. 814-817, 2016.
- [32] H. Sun and W. Geyi, "A new rectenna using beamwidth-enhanced antenna array for RF power harvesting applications," *IEEE Antennas and Wireless Propagation Letters*, vol. 16, pp. 1451-1454, 2017.

- [33] H. Takhedmit, L. Cirio, S. Bellal, D. Delcroix, and O. Picon, "Compact and efficient 2.45 GHz circularly polarised shorted ring-slot rectenna," *Electronics letters*, vol. 48, pp. 253-254, 2012.
- [34] H. Takhedmit, B. Merabet, L. Cirio, B. Allard, F. Costa, C. Vollaire, *et al.*, "A 2.45-GHz low cost and efficient rectenna," in *Antennas and Propagation (EuCAP), Proceedings of the Fourth European Conference on*, 2010, pp. 1-5.
- [35] J. Zbitou, M. Latrach, and S. Toutain, "Hybrid rectenna and monolithic integrated zero-bias microwave rectifier," *IEEE Transactions on Microwave Theory and Techniques*, vol. 54, pp. 147-152, 2006.
- [36] F. Xie, G.-M. Yang, and W. Geyi, "Optimal design of an antenna array for energy harvesting," *IEEE Antennas and Wireless Propagation Letters*, vol. 12, pp. 155-158, 2013.
- [37] D. Bouchouicha, M. Latrach, F. Dupont, and L. Ventura, "An experimental evaluation of surrounding RF energy harvesting devices," in *The 40th European Microwave Conference*, 2010, pp. 1381-1384.
- [38] J. A. Hagerty, F. B. Helmbrecht, W. H. McCalpin, R. Zane, and Z. B. Popovic, "Recycling ambient microwave energy with broad-band rectenna arrays," *IEEE Transactions on Microwave Theory and Techniques*, vol. 52, pp. 1014-1024, 2004.
- [39] H. Sun, Y.-x. Guo, M. He, and Z. Zhong, "A dual-band rectenna using broadband Yagi antenna array for ambient RF power harvesting," *IEEE Antennas and Wireless Propagation Letters*, vol. 12, pp. 918-921, 2013.
- [40] U. Olgun, C.-C. Chen, and J. L. Volakis, "Investigation of rectenna array configurations for enhanced RF power harvesting," *IEEE antennas and wireless propagation letters*, vol. 10, pp. 262-265, 2011.

- [41] M. Zeng, A. S. Andrenko, X. Liu, Z. Li, and H.-Z. Tan, "A compact fractal loop rectenna for RF energy harvesting," *IEEE Antennas and Wireless Propagation Letters*, vol. 16, pp. 2424-2427, 2017.
- [42] Y.-J. Ren and K. Chang, "Bow-tie retrodirective rectenna," *Electronics Letters*, vol. 42, pp. 191-192, 2006.
- [43] P. Lu, X.-S. Yang, J.-L. Li, and B.-Z. Wang, "A compact frequency reconfigurable rectenna for 5.2-and 5.8-GHz wireless power transmission," *IEEE Transactions on Power Electronics*, vol. 30, pp. 6006-6010, 2015.
- [44] K. L. Wong, C. L. Tang, and H. T. Chen, "A compact meandered circular microstrip antenna with a shorting pin," *Microwave and Optical Technology Letters*, vol. 15, pp. 147-149, 1997.
- [45] A. A. Deshmukh and G. Kumar, "Compact broadband U-slot-loaded rectangular microstrip antennas," *Microwave and Optical Technology Letters*, vol. 46, pp. 556-559, 2005.
- [46] A. Alu, F. Bilotti, N. Engheta, and L. Vegni, "Subwavelength, Compact, Resonant Patch Antennas Loaded With Metamaterials," *Antennas and Propagation, IEEE Transactions on*, vol. 55, pp. 13-25, 2007.
- [47] F. Bilotti, A. Alu, and L. Vegni, "Design of Miniaturized Metamaterial Patch Antennas With  $\mu$  Negative Loading," *Antennas and Propagation, IEEE Transactions on*, vol. 56, pp. 1640-1647, 2008.
- [48] F. Martin, F. Falcone, J. Bonache, R. Marques, and M. Sorolla, "Miniaturized coplanar waveguide stop band filters based on multiple tuned split ring resonators," *Microwave and Wireless Components Letters, IEEE*, vol. 13, pp. 511-513, 2003.

- [49] H. Mosallaei and K. Sarabandi, "Magneto-dielectrics in electromagnetics: concept and applications," *Antennas and Propagation, IEEE Transactions on*, vol. 52, pp. 1558-1567, 2004.
- [50] H. Mosallaei and K. Sarabandi, "Antenna miniaturization and bandwidth enhancement using a reactive impedance substrate," *IEEE Transactions on Antennas and Propagation*, vol. 52, pp. 2403-2414, 2004.
- [51] L. Yousefi and O. M. Ramahi, "New Artificial Magnetic Materials Based on Fractal Hilbert Curves," in *Antenna Technology: Small and Smart Antennas Metamaterials and Applications, IWAT '07. International Workshop on*, 2007, pp. 237-240.
- [52] L. Yousefi and O. M. Ramahi, "Miniaturised antennas using artificial magnetic materials with fractal hilbert inclusions," *Electronics Letters*, vol. 46, pp. 816-817, 2010.
- [53] R. O. Ouedraogo and E. J. Rothwell, "Metamaterial inspired patch antenna miniaturization technique," in *Antennas and Propagation Society International Symposium (APSURSI), IEEE*, 2010, pp. 1-4.
- [54] C.-C. Liu, P.-L. Chi, and Y.-D. Lin, "Compact zeroth-order resonant antenna based on dual-arm spiral configuration," *IEEE Antennas and Wireless Propagation Letters*, vol. 11, pp. 318-321, 2012.
- [55] S. K. Sharma, A. Gupta, and R. K. Chaudhary, "Epsilon negative CPW-fed zeroth-order resonating antenna with backed ground plane for extended bandwidth and miniaturization," *IEEE Transactions on Antennas and Propagation*, vol. 63, pp. 5197-5203, 2015.
- [56] C. Zhou, G. Wang, Y. Wang, B. Zong, and J. Ma, "CPW-fed dual-band linearly and circularly polarized antenna employing novel composite right/left-handed transmission-line," *IEEE Antennas and Wireless Propagation Letters*, vol. 12, pp. 1073-1076, 2013.

- [57] J. Zhu and G. V. Eleftheriades, "A compact transmission-line metamaterial antenna with extended bandwidth," *IEEE antennas and wireless propagation letters*, vol. 8, pp. 295-298, 2009.
- [58] P.-L. Chi and Y.-S. Shih, "Compact and bandwidth-enhanced zeroth-order resonant antenna," *IEEE Antennas and Wireless Propagation Letters*, vol. 14, pp. 285-288, 2015.
- [59] T. Jang, J. Choi, and S. Lim, "Compact coplanar waveguide (CPW)-fed zeroth-order resonant antennas with extended bandwidth and high efficiency on vialess single layer," *IEEE Transactions on Antennas and Propagation*, vol. 59, pp. 363-372, 2011.
- [60] S.-T. Ko and J.-H. Lee, "Wideband folded mushroom zeroth-order resonance antenna," *IET Microwaves, Antennas & Propagation*, vol. 7, pp. 79-84, 2013.
- [61] H. Lee, D.-J. Woo, and S. Nam, "Compact and bandwidth-enhanced asymmetric coplanar waveguide (ACPW) antenna using CRLH-TL and modified ground plane," *IEEE Antennas and Wireless Propagation Letters*, vol. 15, pp. 810-813, 2016.
- [62] B.-J. Niu, Q.-Y. Feng, and P.-L. Shu, "Epsilon negative zeroth-and first-order resonant antennas with extended bandwidth and high efficiency," *IEEE Transactions on Antennas and Propagation*, vol. 61, pp. 5878-5884, 2013.
- [63] G. Wang and Q. Feng, "A novel coplanar waveguide feed zeroth-order resonant antenna with resonant ring," *IEEE antennas and wireless propagation letters*, vol. 13, pp. 774-777, 2014.
- [64] S.-Y. Yang and M. N. M. Kehn, "A bisected miniaturized ZOR antenna with increased bandwidth and radiation efficiency," *IEEE Antennas and Wireless Propagation Letters*, vol. 12, pp. 159-162, 2013.

- [65] W. C. Brown, "An experimental low power density rectenna," in *IEEE MTT-S International Microwave Symposium Digest*, 1991, pp. 197-200.
- [66] J. Heikkinen and M. Kivikoski, "Low-profile circularly polarized rectifying antenna for wireless power transmission at 5.8 GHz," *IEEE Microwave and wireless components letters*, vol. 14, pp. 162-164, 2004.
- [67] T. Paing, J. Morroni, A. Dolgov, J. Shin, J. Brannan, R. Zane, *et al.*, "Wirelessly-powered wireless sensor platform," in *European Microwave Conference*, 2007, pp. 999-1002.
- [68] M. Roberg, E. Falkenstein, and Z. Popović, "High-efficiency harmonically-terminated rectifier for wireless powering applications," in *IEEE/MTT-S International Microwave Symposium Digest*, 2012, pp. 1-3.
- [69] H. Sun, Y.-x. Guo, M. He, and Z. Zhong, "Design of a high-efficiency 2.45-GHz rectenna for low-input-power energy harvesting," *IEEE Antennas and Wireless Propagation Letters*, vol. 11, pp. 929-932, 2012.
- [70] H. Takhedmit, L. Cirio, F. Costa, and O. Picon, "Transparent rectenna and rectenna array for RF energy harvesting at 2.45 GHz," in *The 8th European Conference on Antennas and Propagation (EuCAP)*, 2014, pp. 2970-2972.
- [71] T. Urgan and L. Reindl, "Harvesting low ambient RF-sources for autonomous measurement systems," in *Instrumentation and Measurement Technology Conference Proceedings, IMTC. IEEE*, 2008, pp. 62-65.
- [72] G. A. Vera, A. Georgiadis, A. Collado, and S. Via, "Design of a 2.45 GHz rectenna for electromagnetic (EM) energy scavenging," in *Radio and Wireless Symposium (RWS), IEEE*, 2010, pp. 61-64.
- [73] T.-C. Yo, C.-M. Lee, C.-M. Hsu, and C.-H. Luo, "Compact circularly polarized rectenna with unbalanced circular slots," *IEEE Transactions on Antennas and Propagation*, vol. 56, pp. 882-886, 2008.

- [74] K. Niotaki, S. Kim, S. Jeong, A. Collado, A. Georgiadis, and M. M. Tentzeris, "A compact dual-band rectenna using slot-loaded dual band folded dipole antenna," *IEEE Antennas and Wireless Propagation Letters*, vol. 12, pp. 1634-1637, 2013.
- [75] Y.-J. Ren, M. F. Farooqui, and K. Chang, "A compact dual-frequency rectifying antenna with high-orders harmonic-rejection," *IEEE Transactions on Antennas and Propagation*, vol. 55, pp. 2110-2113, 2007.
- [76] R. Scheeler, S. Korhummel, and Z. Popovic, "A dual-frequency ultralow-power efficient 0.5-g rectenna," *IEEE Microwave Magazine*, vol. 15, pp. 109-114, 2014.
- [77] M. Arrawatia, M. S. Baghini, and G. Kumar, "Broadband bent triangular omnidirectional antenna for RF energy harvesting," *IEEE Antennas and Wireless Propagation Letters*, vol. 15, pp. 36-39, 2016.
- [78] M.-J. Nie, X.-X. Yang, G.-N. Tan, and B. Han, "A compact 2.45-GHz broadband rectenna using grounded coplanar waveguide," *IEEE antennas and wireless propagation letters*, vol. 14, pp. 986-989, 2015.
- [79] D. Wang, X. A. Nghiem, and R. Negra, "Design of a 57% bandwidth microwave rectifier for powering application," in *IEEE Wireless Power Transfer Conference*, 2014, pp. 68-71.
- [80] D. Wang, M.-D. Wei, and R. Negra, "Design of a broadband microwave rectifier from 40 MHz to 4740 MHz using high impedance inductor," in *Asia-Pacific Microwave conference*, 2014, pp. 1010-1012.
- [81] H. Zhang and X. Zhu, "A broadband high efficiency rectifier for ambient RF energy harvesting," in *IEEE MTT-S international microwave symposium (IMS2014)*, 2014, pp. 1-3.

- [82] W. Brown and J. Triner, "Experimental thin-film, etched-circuit rectenna," in *IEEE MTT-S International Microwave Symposium Digest*, 1982, pp. 185-187.
- [83] J. J. Schlesak, A. Alden, and T. Ohno, "A microwave powered high altitude platform," in *IEEE MTT-S International Microwave Symposium Digest*, 1988, pp. 283-286.
- [84] Y. Hao, L. Peng, H. Lu, M. Hassan, and A. Alamri, "Energy harvesting based body area networks for smart health," *Sensors*, vol. 17, pp. 1602-1603, 2017.
- [85] S. Kim, J. S. Ho, L. Y. Chen, and A. S. Poon, "Wireless power transfer to a cardiac implant," *Applied Physics Letters*, vol. 101, pp. 701-703, 2012.
- [86] M. Todd, D. Mascarenas, E. Flynn, T. Rosing, B. Lee, D. Musiani, "A different approach to sensor networking for SHM: Remote powering and interrogation with unmanned aerial vehicles," in *Proceedings of the 6th International workshop on Structural Health Monitoring*, 2007, pp. 13-15.
- [87] L. Gallucci, C. Menna, L. Angrisani, D. Asprone, R. S. L. Moriello, F. Bonavolontà, *et al.*, "An embedded wireless sensor network with wireless power transmission capability for the structural health monitoring of reinforced concrete structures," *Sensors*, vol. 17, pp. 2566-2569, 2017.
- [88] Z. J. Chew, T. Ruan, and M. Zhu, "Strain energy harvesting powered wireless sensor node for aircraft structural health monitoring," *Procedia Engineering*, vol. 168, pp. 1717-1720, 2016.
- [89] A. Sanada, M. Kimura, I. Awai, C. Caloz, and T. Itoh, "A planar zeroth-order resonator antenna using a left-handed transmission line," in *34th European Microwave Conference*, 2004, pp. 1341-1344.
- [90] S. Pyo, S.-M. Han, J.-W. Baik, and Y.-S. Kim, "A slot-loaded composite right/left-handed transmission line for a zeroth-order resonant antenna with

- improved efficiency," *IEEE transactions on microwave theory and techniques*, vol. 57, pp. 2775-2782, 2009.
- [91] H.-M. Lee, "A compact zeroth-order resonant antenna employing novel composite right/left-handed transmission-line unit-cells structure," *IEEE Antennas and Wireless propagation letters*, vol. 10, pp. 1377-1380, 2011.
- [92] W.-H. Tu, S.-H. Hsu, and K. Chang, "Compact 5.8-GHz rectenna using stepped-impedance dipole antenna," *IEEE Antennas and Wireless Propagation Letters*, vol. 6, pp. 282-284, 2007.
- [93] T. S. Almoneef, H. Sun, and O. M. Ramahi, "A 3-D folded dipole antenna array for far-field electromagnetic energy transfer," *IEEE Antennas and Wireless Propagation Letters*, vol. 15, pp. 1406-1409, 2016.
- [94] W. Yeoh, W. Rowe, and K. Wong, "Decoupled dual-dipole rectennas on a conducting surface at 2.4 GHz for wireless battery charging," *IET microwaves, antennas & propagation*, vol. 6, pp. 238-244, 2012.
- [95] P. Momenroodaki, R. D. Fernandes, and Z. Popović, "Air-substrate compact high gain rectennas for low RF power harvesting," in *Antennas and Propagation (EuCAP), 10th European Conference on*, 2016, pp. 1-4.
- [96] S. Shen, C.-Y. Chiu, and R. D. Murch, "A dual-port triple-band L-probe microstrip patch rectenna for ambient RF energy harvesting," *IEEE Antennas and Wireless Propagation Letters*, vol. 16, pp. 3071-3074, 2017.
- [97] S. M. Sze and K. K. Ng, *Physics of semiconductor devices*: John wiley & sons, 2006.
- [98] S. A. Maas, "Microwave mixers," *Norwood, MA, Artech House, Inc., 1986*, 368 p., 1986.
- [99] S. A. Maas, *Nonlinear microwave and RF circuits*: Artech House, 2003.

- [100] W. Yuan, J. Song, C. Zhongjian, and J. Lijiu, "Full parasitic capacitance model of diode-class ESD protection structures for mix-signal and RF ICs," in *Electron Devices and Solid-State Circuits, IEEE Conference on*, 2005, pp. 515-518.
- [101] R. Vogel, "Microwave On-Wafer Characterization and Modelling of Schottky Barrier Diodes," in *Microwave Conference, 1990. 20th European*, 1990, pp. 766-771.
- [102] H.-P. A. Note, "969," "The Zero Bias Schottky Detector Diode, 1994. [Online]. Available: <https://www.rf-microwave.com/app/resources/uploads/diodes/AN969.pdf>
- [103] K. Klotter, "Nonlinear vibration problems by averaging method of W. Ritz," in *Proc. 1st National Congress for Applied Mathematics*, 1951, p. 125.
- [104] R. G. Harrison, "Full nonlinear analysis of detector circuits using Ritz-Galerkin theory," in *Microwave Symposium Digest, 1992., IEEE MTT-S International*, 1992, pp. 267-270.
- [105] R. G. Harrison, "Full nonlinear analysis of detector circuits using Ritz-Galerkin theory," in *1992 IEEE MTT-S Microwave Symposium Digest*, 1992, pp. 267-270.
- [106] L. Clare and S. Burrow, "Half-wave rectifiers offer advantages for vibration energy harvesters," *Electronics letters*, vol. 46, pp. 1623-1624, 2010.
- [107] J. Joe, M. Chia, A. Marath, and C. Ang, "Zero bias schottky diode model for low power, moderate current rectenna," *DETS'97 Proc*, 1997, pp. 6-8.
- [108] M. Del Prete, A. Costanzo, D. Masotti, and A. Romani, "An alternative rectenna design approach for wirelessly powered energy autonomous

- systems," in *IEEE MTT-S International Microwave Symposium Digest*, 2013, pp. 1-4.
- [109] C. A. Balanis, *Antenna theory: analysis and design*: John Wiley & Sons, 2016.
- [110] W. L. Stutzman and G. A. Thiele, *Antenna theory and design*: John Wiley & Sons, 2012.
- [111] V. G. Veselago, "The electrodynamics of substances with simultaneously negative values of  $\epsilon$  and  $\mu$ ," *Physics-Uspeski*, vol. 10, pp. 509-514, 1968.
- [112] J. B. Pendry and D. R. Smith, "Reversing light with negative refraction," *Physics today*, vol. 57, pp. 37-43, 2004.
- [113] D. R. Smith and N. Kroll, "Negative refractive index in left-handed materials," *Physical review letters*, vol. 85, pp. 2933-2934, 2000.
- [114] D. R. Smith, J. B. Pendry, and M. C. Wiltshire, "Metamaterials and negative refractive index," *Science*, vol. 305, pp. 788-792, 2004.
- [115] C. A. Balanis, *Advanced engineering electromagnetics, 2nd Edition*: John Wiley & Sons, 2012.
- [116] C. Caloz and T. Itoh, *Electromagnetic metamaterials: transmission line theory and microwave applications*: John Wiley & Sons, 2005.
- [117] D. R. Jackson and A. Oliner, "Antenna engineering handbook," *University of Houston*, 2007.
- [118] A. Lai, T. Itoh, and C. Caloz, "Composite right/left-handed transmission line metamaterials," *IEEE microwave magazine*, vol. 5, pp. 34-50, 2004.

- [119] F. J. Villegas, D. R. Jackson, J. T. Williams, and A. A. Oliner, "Leakage fields from planar semi-infinite transmission lines," *IEEE transactions on microwave theory and techniques*, vol. 47, pp. 443-454, 1999.
- [120] J. Liu, D. R. Jackson, and Y. Long, "Substrate integrated waveguide (SIW) leaky-wave antenna with transverse slots," *IEEE Transactions on Antennas and Propagation*, vol. 60, pp. 20-29, 2011.
- [121] L. Liu, C. Caloz, and T. Itoh, "Dominant mode leaky-wave antenna with backfire-to-endfire scanning capability," *Electronics Letters*, vol. 38, pp. 1414-1416, 2002.
- [122] Y.-J. Chi and F.-C. Chen, "Novel CRLH leaky wave antenna with horizontal scanning property," in *Asia-Pacific Microwave Conference*, 2011, pp. 935-938.
- [123] A. Grbic and G. V. Eleftheriades, "Leaky CPW-based slot antenna arrays for millimeter-wave applications," *IEEE transactions on Antennas and Propagation*, vol. 50, pp. 1494-1504, 2002.
- [124] G. Zamora, S. Zuffanelli, F. Paredes, F. Herraiz-Martinez, F. Martin, and J. Bonache, "Leaky-wave antenna (LWA) based on slot line and non-bianisotropic split ring resonators (NB-SRRs) and comparison with CPW approach," in *IEEE-APS Topical Conference on Antennas and Propagation in Wireless Communications (APWC)*, 2014, pp. 48-51.
- [125] H. Nguyen, N. Yang, and C. Caloz, "Differential Bi-directional CRLH leaky-wave antenna in CPS technology," in *Asia-Pacific Microwave Conference*, 2007, pp. 1-4.
- [126] Y. D. Dong and T. Itoh, "Composite right/left-handed substrate integrated waveguide leaky-wave antennas," in *European Microwave Conference (EuMC)*, 2009, pp. 276-279.

- [127] M. Bozzi, A. Georgiadis, and K. Wu, "Review of substrate-integrated waveguide circuits and antennas," *IET Microwaves, Antennas & Propagation*, vol. 5, pp. 909-920, 2011.
- [128] Y. Dong and T. Itoh, "Substrate integrated composite right-/left-handed leaky-wave structure for polarization-flexible antenna application," *IEEE Transactions on Antennas and Propagation*, vol. 60, pp. 760-771, 2011.
- [129] Q. Yang, Y. Zhang, and X. Zhang, "X-band composite right/left-handed leaky wave antenna with large beam scanning-range/bandwidth ratio," *Electronics letters*, vol. 48, pp. 746-747, 2012.
- [130] D. Deslandes and K. Wu, "Single-substrate integration technique of planar circuits and waveguide filters," *IEEE Transactions on microwave theory and Techniques*, vol. 51, pp. 593-596, 2003.
- [131] I. Mohamed and A. Sebak, "High-gain SIW-based antipodal linearly tapered slot antenna for 60-GHz applications," in *IEEE Antennas and Propagation Society International Symposium (APSURSI)*, 2014, pp. 217-218.
- [132] L. J. Chu, "Physical limitations of omni-directional antennas," *Journal of applied physics*, vol. 19, pp. 1163-1175, 1948.
- [133] J. S. McLean, "A re-examination of the fundamental limits on the radiation Q of electrically small antennas," *IEEE Transactions on antennas and propagation*, vol. 44, pp. 672-678, 1996.
- [134] *CST, Microwave Studio Computer Simulation Technology*. 2014.
- [135] T. Liebig, S. Held, A. Rennings, and D. Erni, "Accurate parameter extraction of lossy composite right/left-handed (CRLH) transmission lines for planar antenna applications," in *Fourth International Congress on Advanced Electromagnetic Materials in Microwaves and Optics*, 2010, pp. 13-16.

- [136] G. Wang, P. Wang, Y. Tang, and W. Liu, "Analysis of dual band power and data telemetry for biomedical implants," *IEEE Transactions on biomedical circuits and systems*, vol. 6, pp. 208-215, 2011.
- [137] L. Ji, L. Wang, C. Liao and S. Li, "Crosstalk study of simultaneous wireless power/information transmission based on an LCC compensation network," *Energies*, Vol. 10, pp. 1606-1611, 2017.
- [138] J. Wu, C. Zhao, Z. Lin, J. Du, Y. Hu and X. He, " Wireless power and data transfer via a common inductive link using frequency division multiplexing," *IEEE transactions on industrial electronics*, Vol.62, pp. 7810-7820, 2015.

# APPENDIX

## HSMS-285x Series Surface Mount Zero Bias Schottky Detector Diodes



### Data Sheet



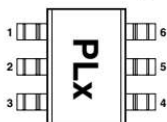
#### Description

Avago's HSMS-285x family of zero bias Schottky detector diodes has been designed and optimized for use in small signal (Pin <-20 dBm) applications at frequencies below 1.5 GHz. They are ideal for RF/ID and RF Tag applications where primary (DC bias) power is not available.

**Important Note:** For detector applications with input power levels greater than -20 dBm, use the HSMS-282x series at frequencies below 4.0 GHz, and the HSMS-286x series at frequencies above 4.0 GHz. The HSMS-285x series IS NOT RECOMMENDED for these higher power level applications.

Available in various package configurations, these detector diodes provide low cost solutions to a wide variety of design problems. Avago's manufacturing techniques assure that when two diodes are mounted into a single package, they are taken from adjacent sites on the wafer, assuring the highest possible degree of match.

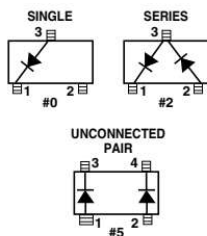
#### Pin Connections and Package Marking



Notes:

1. Package marking provides orientation and identification.
2. See "Electrical Specifications" for appropriate package marking.

#### SOT-23/SOT-143 Package Lead Code Identification (top view)



#### Features

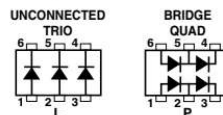
- Surface Mount SOT-23/SOT-143 Packages
- Miniature SOT-323 and SOT-363 Packages
- High Detection Sensitivity: up to 50 mV/μW at 915 MHz
- Low Flicker Noise: -162 dBV/Hz at 100 Hz
- Low FIT (Failure in Time) Rate\*
- Tape and Reel Options Available
- Matched Diodes for Consistent Performance
- Better Thermal Conductivity for Higher Power Dissipation
- Lead-free

\* For more information see the Surface Mount Schottky Reliability Data Sheet.

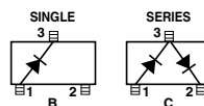


**Attention: Observe precautions for handling electrostatic sensitive devices.**  
ESD Machine Model (Class A)  
ESD Human Body Model (Class 0)  
Refer to Avago Application Note A004R: Electrostatic Discharge Damage and Control.

#### SOT-363 Package Lead Code Identification (top view)



#### SOT-323 Package Lead Code Identification (top view)



**SOT-23/SOT-143 DC Electrical Specifications,  $T_c = +25^\circ\text{C}$ , Single Diode**

Part Number HSMS-	Package Marking Code	Lead Code	Configuration	Maximum Forward Voltage $V_f$ (mV)		Maximum Reverse Leakage, $I_R$ ( $\mu\text{A}$ )	Typical Capacitance $C_T$ (pF)
2850	P0	0	Single	150	250	175	0.30
2852	P2	2	Series Pair <sup>(1,2)</sup>				
2855	P5	5	Unconnected Pair <sup>(1,2)</sup>				
Test Conditions				$I_F = 0.1 \text{ mA}$	$I_F = 1.0 \text{ mA}$	$V_R = 2\text{V}$	$V_R = -0.5 \text{ V to } -1.0\text{V}$ $f = 1 \text{ MHz}$

Notes:

- $\Delta V_f$  for diodes in pairs is 15.0 mV maximum at 1.0 mA.
- $\Delta C_T$  for diodes in pairs is 0.05 pF maximum at -0.5V.

**SOT-323/SOT-363 DC Electrical Specifications,  $T_c = +25^\circ\text{C}$ , Single Diode**

Part Number HSMS-	Package Marking Code	Lead Code	Configuration	Maximum Forward Voltage $V_f$ (mV)		Maximum Reverse Leakage, $I_R$ ( $\mu\text{A}$ )	Typical Capacitance $C_T$ (pF)
285B	P0	B	Single	150	250	175	0.30
285C	P2	C	Series Pair				
285L	PL	L	Unconnected Trio				
285P	PP	P	Bridge Quad				
Test Conditions				$I_F = 0.1 \text{ mA}$	$I_F = 1.0 \text{ mA}$	$V_R = 2\text{V}$	$V_R = 0.5 \text{ V to } -1.0\text{V}$ $f = 1 \text{ MHz}$

Notes:

- $\Delta V_f$  for diodes in pairs is 15.0 mV maximum at 1.0 mA.
- $\Delta C_T$  for diodes in pairs is 0.05 pF maximum at -0.5V.

**RF Electrical Specifications,  $T_c = +25^\circ\text{C}$ , Single Diode**

Part Number HSMS-	Typical Tangential Sensitivity TSS (dBm) @ $f = 915 \text{ MHz}$	Typical Voltage Sensitivity $g$ (mV/ $\mu\text{W}$ ) @ $f = 915 \text{ MHz}$	Typical Video Resistance $R_V$ (K $\Omega$ )
2850	-57	40	8.0
2852			
2855			
285B			
285C			
285L			
285P			
Test Conditions		Power in = -40 dBm $R_L = 100 \text{ K}\Omega$ , Zero Bias	Zero Bias

**Absolute Maximum Ratings, T<sub>C</sub> = +25°C, Single Diode**

Symbol	Parameter	Unit	Absolute Maximum <sup>[1]</sup>	
			SOT-23/143	SOT-323/363
P <sub>IV</sub>	Peak Inverse Voltage	V	2.0	2.0
T <sub>J</sub>	Junction Temperature	°C	150	150
T <sub>STG</sub>	Storage Temperature	°C	-65 to 150	-65 to 150
T <sub>OP</sub>	Operating Temperature	°C	-65 to 150	-65 to 150
θ <sub>JC</sub>	Thermal Resistance <sup>[2]</sup>	°C/W	500	150

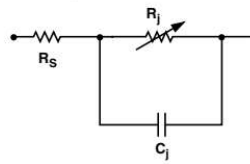
Notes:

- Operation in excess of any one of these conditions may result in permanent damage to the device.
- T<sub>C</sub> = +25°C, where T<sub>C</sub> is defined to be the temperature at the package pins where contact is made to the circuit board.

**ESD WARNING:**  
Handling Precautions Should Be Taken  
To Avoid Static Discharge.

**Equivalent Linear Circuit Model**

HSMS-285x chip



R<sub>S</sub> = series resistance (see Table of SPICE parameters)

C<sub>J</sub> = junction capacitance (see Table of SPICE parameters)

$$R_j = \frac{8.33 \times 10^{-5} \text{ nT}}{I_b + I_s}$$

where

I<sub>b</sub> = externally applied bias current in amps

I<sub>s</sub> = saturation current (see table of SPICE parameters)

T = temperature, °K

n = ideality factor (see table of SPICE parameters)

Note:

To effectively model the packaged HSMS-285x product, please refer to Application Note AN1124.

**SPICE Parameters**

Parameter	Units	HSMS-285x
B <sub>V</sub>	V	3.8
C <sub>J0</sub>	pF	0.18
E <sub>G</sub>	eV	0.69
I <sub>BV</sub>	A	3 E-4
I <sub>S</sub>	A	3 E-6
N		1.06
R <sub>S</sub>	Ω	25
P <sub>B</sub> (V <sub>J</sub> )	V	0.35
P <sub>T</sub> (XTI)		2
M		0.5

**Typical Parameters, Single Diode**

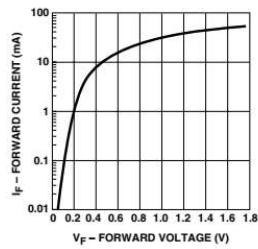


Figure 1. Typical Forward Current vs. Forward Voltage.

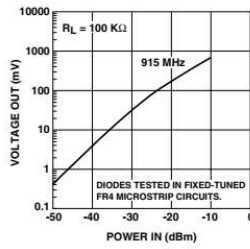


Figure 2. +25°C Output Voltage vs. Input Power at Zero Bias.

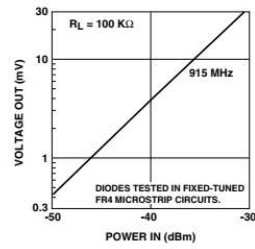


Figure 3. +25°C Expanded Output Voltage vs. Input Power. See Figure 2.

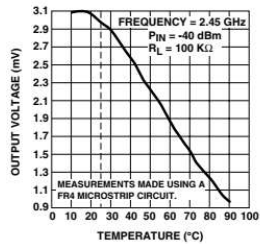


Figure 4. Output Voltage vs. Temperature.

## Certificate of Award



The certificate features a geometric background with purple, pink, and blue triangles. At the top, it displays the logos of Universiti Teknologi MARA (UTM) and IRMI. The main title 'iindex 2018' is prominently displayed, with the subtitle 'Invention, Innovation & Design Exposition 2018' below it. A quote, 'Championing Innovation Revitalizing Communities', is positioned to the right of the title. The recipient's names are listed: NORASHIDAH BINTI MD DIN, SYAMIMI BINTI MOHD NORZELI, SOBHAN SARAVANI, and CHANDAN KUMAR CHAKRABARTY. The award is for 'GOLD' in the category of 'HIGHLY SENSITIVE COMPACT METAMATERIAL-BASED ENERGY HARVESTING SYSTEM WITH WIDEBAND PERFORMANCE'. The event details are provided: 24 - 28 SEPTEMBER 2018 at DEWAN AGUNG TUANKU CANSELOR (DATC), UNIVERSITI TEKNOLOGI MARA, SHAH ALAM, SELANGOR, MALAYSIA. The certificate is signed by Professor Dr. Hadariah Bahron, Assistant Vice Chancellor (Research & Innovation) at UTM. The Bank Islam logo is visible at the bottom, and a circular seal of the UTM is located in the bottom right corner. A vertical banner on the right side of the certificate reads 'Certificate of AWARD'.

# iindex 2018

*Invention, Innovation & Design Exposition 2018*

*"Championing Innovation  
Revitalizing Communities"*

This is to certify that  
**NORASHIDAH BINTI MD DIN  
SYAMIMI BINTI MOHD NORZELI  
SOBHAN SARAVANI  
CHANDAN KUMAR CHAKRABARTY**

has/have been awarded  
**GOLD**

for the Invention/Innovation/Design of  
**HIGHLY SENSITIVE COMPACT METAMATERIAL-BASED ENERGY  
HARVESTING SYSTEM WITH WIDEBAND PERFORMANCE**

at  
INVENTION, INNOVATION & DESIGN EXPOSITION 2018

**24 - 28 SEPTEMBER 2018**  
DEWAN AGUNG TUANKU CANSELOR (DATC)  
UNIVERSITI TEKNOLOGI MARA  
SHAH ALAM, SELANGOR  
MALAYSIA

  
**PROFESSOR DR. HADARIAH BAHRON**  
ASSISTANT VICE CHANCELLOR (RESEARCH & INNOVATION)  
UNIVERSITI TEKNOLOGI MARA

Main Sponsor  
**BANK ISLAM**



*Certificate*  
**of AWARD**

# Certificate of Award



## Certificate of Award

*This is to certify that*

**DATO' PROF. IR. DR. NORASHIDAH BINTI MD DIN, SOBHAN SARAVANI,  
PROF. DR. CHANDAN KUMAR CHAKRABARTHY,  
DR. SYAMIMI BINTI MOHD NORZELI**

**UNIVERSITI TENAGA NASIONAL, MALAYSIA**

*has been awarded the*

**ITEX 2018 SILVER MEDAL**

*for the invention*

**HIGHLY SENSITIVE COMPACT METAMATERIAL-BASED ENERGY  
HARVESTING SYSTEM WITH WIDE-BAND PERFORMANCE**

*at the*

**29<sup>TH</sup> INTERNATIONAL INVENTION, INNOVATION & TECHNOLOGY  
EXHIBITION 2018**

**KUALA LUMPUR, MALAYSIA  
10 – 12 MAY 2018**



**Academician Emeritus Professor  
Tan Sri Datuk Dr Augustine Ong Soon Hock**  
President  
Malaysian Invention and Design Society

SUPPORTED BY



ENDORSED BY